STRUCTURAL SYSTEMS

RESEARCH PROJECT

Report No.
SSRP – 99/15

SEISMIC PERFORMANCE OF HOLLOW RECTANGULAR REINFORCED CONCRETE PIERS WITH HIGHLY-CONFINED BOUNDARY ELEMENTS
PHASE I: FLEXURAL TESTS
PHASE II: SHEAR TESTS

By

ERIC M. HINES

FRIEDER SEIBLE

M.J. NIGEL PRIESTLEY

Final Report on a Research Project funded by Caltrans Under Contract 59A0051

February 2002

Department of Structural Engineering
University of California, San Diego
La Jolla, California 92093-0085

University of California, San Diego
Department of Structural Engineering
Structural Systems Research Project

Report No. SSRP- 99/15

Seismic Performance of Hollow Rectangular Reinforced Concrete Piers with Highly-Confined Boundary Elements

Phase I: Flexural Tests

Phase II: Shear Tests

by

Eric M. Hines

Graduate Research Assistant

Frieder Seible

Professor of Structural Engineering

M.J. Nigel Priestley

Professor of Structural Engineering

Final Report on a Research Project funded by Caltrans under Contract 59A0051

Department of Structural Engineering
University of California, San Diego

La Jolla, California 92093-0085

February 2002

Technical Report Documentation Page

1. Report No. SSRP-99/15	2. Government Accession No.	3. Recipient's Catalog No.
4. Title and Subtitle Seismic Performance of Hollow Rectangular Reinforced Concrete Bridge Piers with Highly-Confined Corner Elements; Phase I Flexural Tests, Phase II Shear Tests		5. Report Date August 1999 – February 2002 6. Performing Organization Code UCSD
7. Author(s) Eric M. Hines, Frieder Seible, M.J. Nigel Priestley		8. Performing Organization Report No. UCSD / SSRP-99/15
9. Performing Organization Name and Address Department of Structural Engineering School of Engineering University of California, San Diego La Jolla, California 92093-0085		10. Work Unit No. (TRAIS) 11. Contract or Grant No.
12. Sponsoring Agency Name and Address California Department of Transportation Engineering Service Center 1801 30th St., West Building MS-9 Sacramento, California 95807		13. Type of Report and Period Covered Final Report - 14. Sponsoring Agency Code

15. Supplementary Notes

Prepared in cooperation with the State of California Department of Transportation.

16. Abstract

Large scale tests were conducted to investigate the integral behavior of structural walls with highly-confined boundary elements. Five test units with similar geometry and longitudinal reinforcement were loaded cyclically in single bending. Design parameters included column length, transverse reinforcement in the wall and wall thickness.

Test results are compared with predictions of deformation capacity and shear capacity. Experimental plastic hinge lengths are derived for both tall and short columns. The steel contribution to shear capacity is evaluated based both on the action of the transverse bars in the wall and on that of the boundary element spirals. Web crushing capacity is discussed in relation to the critical compression struts that transfer shear between the compression and tension boundary elements in the plastic hinge region.

17. Key Words reinforced concrete, structural wall, boundary element, hysteresis, plastic hinge length, web crushing		18. Distribution Statement Unlimited	
19. Security Classification (of this report) Unclassified	20. Security Classification (of this page) Unclassified	21. No. of Pages 286	22. Price

Form DOT F 1700.7 (8-72) Reproduction of completed page authorized

Seismic Performance of Hollow Rectangular Reinforced Concrete Piers with Highly-Confined Boundary Elements
Phase I: Flexural Tests
Phase II: Shear Tests

Eric M. Hines
Graduate Research Assistant
UCSD

Frieder Seible
Professor
UCSD

M.J. Nigel Priestley
Professor
UCSD

February 3, 2002

ABSTRACT

Large scale tests were conducted to investigate the integral behavior of structural walls with highly-confined boundary elements. Five test units with similar geometry and longitudinal reinforcement were loaded cyclically in single bending. Design parameters included column length, transverse reinforcement in the wall and wall thickness.

Test results are compared with predictions of deformation capacity and shear capacity. Experimental plastic hinge lengths are derived for both tall and short columns. The steel contribution to shear capacity is evaluated based both on the action of the transverse bars in the wall and on that of the boundary element spirals. Web crushing capacity is discussed in relation to the critical compression struts that transfer shear between the compression and tension boundary elements in the plastic hinge region.

DISCLAIMER

The authors assume responsibility for the accuracy of all information presented in this research report. All opinions, recommendations, and conclusions expressed in this report are those of the authors, and do not necessarily reflect the views of the State of California or the California Department of Transportation.

ACKNOWLEDGEMENTS

The research described in this report was funded by the California Department of Transportation (Caltrans). We would like to thank Don Lee and Gary Tolen of Caltrans for their support and input during the testing phases of this project. We would also like to thank Brian Maroney for his enthusiastic support of this preliminary work on the Bay Area Bridges.

We would like to thank Dr. Sajid Abbas and Rafael Manzanarez of T.Y.Lin Intl. and Greg Orsolini of Deleuw-Cather for their input on the design and testing of of these bridge pier subassemblages.

Special thanks are extended to Dr. Rob Dowell of Anatech Inc. who was instrumental in preparing the finite element predictions for each of the test units, and on who's moment-curvature program the section analysis studies were based. We would also like to thank Bob Dameron of Anatech for his valuable input on preparing the finite element predictions.

We gratefully acknowledge the Headed Reinforcement Company for their donation of the headed transverse bars used in test unit 1A.

The tests were conducted in the Charles Lee Powell Laboratories at UCSD, where the help of the Laboratory staff has been essential to the successful execution of the testing program. In particular we would like to thank Charlie Stearns and Alex Sherman for their excellent input on the construction of the test units, for their reliability in meeting deadlines and for their persistance in seeing the lighter side of this kind of work. Special thanks are in order for Dr. Chris Latham, Bob Parks and James Batti, without whom none of the testing would have run so smoothly. Their willingness to stay late in order to prepare a test for public viewing the next day or to complete a test is greatly appreciated. We would like to thank Larry Berman for his assistance in organizing the program to be completed in a timely manner, and we would like to thank Frank Ho for his help in ordering materials. Manu Garg, Lazaro Herrera, John Leuenberger and Wei Chi (Richard) Chen assisted in construction, setup and instrumentation of the test units. John Hermstad and Jason Bither conducted all materials testing for the program.

Certain individuals showed an enthusiasm for and personal commitment to the program which was greatly appreciated. We would like to thank Dr. Andy Budek for his advice regarding the construction and instrumentation of the test units. We would also like to extend special recognition to Karen Wilson, whom we not only quickly grew to trust in handling responsibility in the laboratory, but who also showed a distinct commitment to the project in summarizing the test results for the performance-based design database.

Finally, we would like to thank our colleagues in the department for their input on design, testing, data reduction and interpretation of results. The support of Dr. Pedro Silva, Dr. Gianmario Benzoni, Dr. Jay Holombo, Lelli Hose, Dr. Rigoberto Burgueño and Jill Patty is greatly appreciated. We would also like to thank Dr. Evan Bentz of Toronto for his input on the response of the test units based on the Modified Compression Field Theory.

Contents

1 Introduction **1**
1.1 Reinforced Concrete Piers for Long Span Bridges 1
1.2 Testing Program 3
1.2.1 Test Phase I – Flexural Test Units 6
1.2.2 UCSD Test Phase II – Shear Test Units 6
1.3 Previous Work 8
1.3.1 Wang et al. 1975, Vallenas et al. 1979 9
1.3.2 Oesterle et al. 1976-1979 11
1.3.3 Sittipunt et al. 1993 14
1.4 Issues to be Resolved by Further Testing 15
1.5 Report Outline 16

2 Test Unit Designs and Details **19**
2.1 Overview 19
2.2 Design Criteria 19
2.3 Phase I Test Units 20
2.3.1 Confinement 21
2.3.2 Load Capacity 21
2.3.3 Displacement Capacity 23
2.3.4 Shear 23
2.3.5 Other Design Considerations 24
2.4 Phase II Test Units 27

3 Construction and Material Properties **30**
3.1 Overview 30
3.2 Construction of the Phase I Test Units 30
3.3 Construction of the Phase II Test Units 31
3.4 Material Properties 40

4 Test Protocol and Instrumentation **48**
4.1 Overview 48
4.2 Test Setup 49
4.3 Instrumentation 53
4.3.1 Strain Gages 53
4.3.2 Slip of Transverse Bars 58

4.3.3 Curvature Instrumentation 59
4.3.4 Shear Deformation 64
4.4 Loading History 72
4.5 Data Acquisition and Control 74

5 Analytical Considerations and Test Predictions 75
5.1 Overview 75
5.2 Failure Mechanisms 75
5.3 Moment-Curvature Analysis 77
5.4 Web Crushing Failure 78
5.5 Shear Equations 83
5.6 Phase II Shear Capacity Envelopes 84
5.6.1 ACI 318-95 85
5.6.2 UCSD Shear Model: Priestley et al. [2000] 86
5.6.3 ACI 318-95 – Web Crushing 86
5.6.4 Oesterle et al. [1984] – Web Crushing 87
5.6.5 Paulay et al. [1992] – Web Crushing 88
5.6.6 Force-Deflection Curves and Shear Envelopes 89

6 Test Observations 92
6.1 Overview 92
6.2 Unit 1A 92
6.2.1 Summary 92
6.2.2 First Cracking ($3/4F_y$) 92
6.2.3 Steel Yield (F_y) 93
6.2.4 Propagation of Flexure/Shear Cracks ($\mu_\Delta = 1.0 - 2.0$) 93
6.2.5 Initiation of Spalling ($\mu_\Delta = 3.0$) 93
6.2.6 Growth of Spalled Region ($\mu_\Delta = 4.0$) 93
6.2.7 Full Development of Spalled Region ($\mu_\Delta = 6.0$) 93
6.2.8 Strength Loss due to Bar Fracture ($\mu_\Delta = 6.0 - 8.0$) 94
6.3 Unit 1B 94
6.3.1 Summary 94
6.3.2 First Cracking ($3/4F_y$) 94
6.3.3 Steel Yield (F_y) 95
6.3.4 Propagation of Flexure/Shear Cracks ($\mu_\Delta = 1.0 - 2.0$) 95
6.3.5 Initiation of Spalling ($\mu_\Delta = 3.0$) 95
6.3.6 Growth of Spalled Region ($\mu_\Delta = 4.0$) 95
6.3.7 Full Development of Spalled Region ($\mu_\Delta = 6.0$) 96
6.3.8 Strength Loss due to Bar Fracture ($\mu_\Delta = 6.0 - 8.0$) 96
6.4 Unit 2A 96
6.4.1 Summary 96
6.4.2 First Cracking ($3/4F_y$) 97
6.4.3 Steel Yield (F_y) 97
6.4.4 Formation of Shear Cracks ($\mu_\Delta = 1.0 - 2.0$) 97
6.4.5 Initiation of Spalling ($\mu_\Delta = 3.0$) 98

6.4.6 Growth of Spalled Region (μ_Δ .0) 98
6.4.7 Full Development of Spalled Region (μ_Δ .0) 99
6.4.8 Strength Loss due to Bar Fracture (μ_Δ .0) 99
6.5 Unit 2B 100
6.5.1 Summary 100
6.5.2 First Cracking ($3/4F_y$) 100
6.5.3 Steel Yield (F_y) 101
6.5.4 Formation of Shear Cracks (μ_Δ $.0 - 2.0$) 101
6.5.5 Initiation of Spalling (μ_Δ .0) 102
6.5.6 Growth of Spalled Region (μ_Δ .0) 102
6.5.7 Full Development of Spalled Region (μ_Δ .0) 103
6.5.8 Strength Loss due to Wall Degradation (μ_Δ .0) 103
6.6 Unit 2C 104
6.6.1 Summary 104
6.6.2 First Cracking ($3/4F_y$) 104
6.6.3 Steel Yield (F_y) 104
6.6.4 Formation of Shear Cracks (μ_Δ $.0 - 2.0$) 105
6.6.5 Initiation of Spalling (μ_Δ .0) 106
6.6.6 Growth of Spalled Region (μ_Δ .0) 106
6.6.7 Full Development of Spalled Region (μ_Δ=6.0) 106
6.6.8 Strength Loss due to Longitudinal Bar Fracture (μ_Δ=8.0) . . 107

7 Discussion of Test Results 108
7.1 Overview 108
7.2 Hysteretic Behavior 108
7.2.1 Phase I 108
7.2.2 Phase II 115
7.2.3 Comparison of Finite Element Predictions and Test Results . 122
7.2.4 Equivalent Viscous Damping 130
7.3 Plastic Hinge Length 130
7.3.1 Curvature Profiles 131
7.3.2 Longitudinal Bar Strains 141
7.3.3 Back Calculation of L_p 142
7.4 Performance in Shear 153
7.4.1 Transverse Strains 153
7.4.2 Transverse Bar Anchorage and Slip 154
7.4.3 Spiral Strains 160

8 Development of a Flexure-Shear Model for Web Crushing 164
8.1 Overview 164
8.2 Classical Models for Web Crushing 164
8.3 Concerns Raised from Test Observations 165
8.4 Flexure-Shear Approach to Web Crushing Demand and Capacity . . 166
8.5 Calibration of Concrete Strength 170
8.6 Web Crushing Parameter Study 171

9 Conclusions **177**
9.1 Overview . . . 177
9.2 Flexure . . . 177
9.2.1 Plastic Hinge Length . . . 177
9.2.2 Material Strain and Limit States . . . 178
9.3 Shear . . . 178
9.3.1 Transverse Reinforcement . . . 179
9.3.2 Axial Load Contribution to Shear Capacity, V_p . . . 180
9.3.3 Web Crushing . . . 180
9.4 Future Work . . . 181

A Photos from Tests **182**
A.1 Unit 1A Test Photos . . . 183
A.2 Unit 1B Test Photos . . . 190
A.3 Unit 2A Test Photos . . . 197
A.4 Unit 2B Test Photos . . . 204
A.5 Unit 2C Test Photos . . . 211

B Test Unit 1A Results **218**

C Test Unit 1B Results **229**

D Test Unit 2A Results **240**

E Test Unit 2B Results **250**

F Test Unit 2C Results **260**

List of Tables

1.1 Test Unit geometry and reinforcement. 6
1.2 Test Unit geometry and reinforcement. 10
1.3 Test Unit non-dimensional force and displacement capacities. 10
1.4 Test Unit geometry and reinforcement, Oesterle et al. (1976-1979) . . 12
1.5 Test Unit force and displacement capacities, Oesterle et al. (1976-1979) 12

3.1 Concrete mix design for Phase I & II units 1/2" aggregate. 41
3.2 Concrete mix design for Phase I & II units 3/8" aggregate. 41
3.3 Test unit concrete compressive strengths psi [MPa]. 42
3.4 Test unit footing concrete compressive strengths psi [MPa] 42
3.5 Test unit steel reinforcement properties 42

4.1 Initial load and displacement values. 73

5.1 General properties for the Phase II test units. 85

6.1 μ_Δ=3.0x3: Crack widths up column height. 99
6.2 μ_Δ=6.0x3: Crack widths up column height. 99
6.3 μ_Δ=6.0x3: Crack widths up column height. 103
6.4 μ_Δ=1.5x1: Crack widths up column height. 105
6.5 μ_Δ=3.0x1: Crack widths up column height. 106
6.6 μ_Δ=4.0x1: Crack widths up column height. 106
6.7 μ_Δ=6.0x1: Crack widths up column height. 107
6.8 μ_Δ=4.0x1: Crack widths up column height. 107

7.1 Equivalent viscous damping 130
7.2 Experimental calibration of L_p from UCSD test results. 147
7.3 Experimental calibration of L_p from Oesterle et al.'s test results. . . . 147
7.4 Experimental curvature and strain values for the Phase I and Phase II test units. 151
7.5 Percent difference in load capacity 155

8.1 Parameters affecting the web crushing strength of bridge piers. 169
8.2 Web crushing Capacity/Demand ratios 171
8.3 Web crushing Capacity/Demand ratios compared 172
8.4 Relative Depth Ratio parametric study: geometric properties for columns C1-C7. 174

8.5 Column web crushing properties at ultimate displacement Δ_u. 175
8.6 Column force-deflection properties. 175

List of Figures

1.1 Schematic representation of proposed Bay Area bridge piers. 2
1.2 (a) Early proposal for a typical cross section of the 2nd Benicia Martinez Bridge Piers. (b) True half section with tributary longitudinal reinforcement in the wall. (c) Test subassembly consisting of a single structural wall with boundary elements. 4
1.3 (a) Long structural wall in bridge transverse direction. (b) Short structural wall in bridge longitudinal direction. (c) Test unit section geometry generalized from Benicia Martinez prototype. 5
1.4 (a) Test Unit 1A section and side elevation with column reinforcement. (b) Test Unit 2A section and side elevation with column reinforcement. 7
1.5 Photo of test setup for Phase I tests. 8
1.6 Photo of test setup for Phase II tests. 8
1.7 Oesterle et al. test unit overall geometry [6]. 13
1.8 Oesterle et al. test unit section geometry and reinforcement [6]. . . . 13
1.9 Web crushing in Test Unit B7 (μ_Δ .8) [7]. 14
1.10 Web crushing in Test Unit F2 (μ_Δ .5) [7]. 14

2.1 Cross section of Test Phase I Units 1A and 1B with reinforcement. . . 20
2.2 Force couples in the Phase I test units. 22
2.3 Test Units 1A (a) and 1B (b) with column reinforcement. 25
2.4 Phase I force-deflection curves. 26
2.5 Cross section of Test Phase II Units 2A and 2B with reinforcement. . 27
2.6 Cross section of Test Phase II Unit 2C with reinforcement. 27
2.7 Phase II sections and elevations with column reinforcement. 28
2.8 Phase II force-deflection predictions 29

3.1 Footing longitudinal bars: No. 8 [D25] U-bars and No. 6 [D19] Z-bars. 32
3.2 Boundary element cages are tied separately. 32
3.3 Boundary element cages are lifted into place via forklift. 33
3.4 Test Unit 1A: footing and column cage. 33
3.5 Test Unit 1A: detail of footing and column reinforcement. 34
3.6 Test Units 1A and 1B in lab yard with footings cast. 34
3.7 Moving Test Unit 1A into the laboratory before casting the column and load stub. 35
3.8 Test Unit 1A: detail of boundary element curvature rod attachments. 35
3.9 Test Unit 1A: reinforcement detail 36
3.10 Test Unit 1B: reinforcement detail 36

3.11 Test Units 1A and 1B: casting the columns. 37
3.12 Test Units 1A and 1B: casting the load stubs. 37
3.13 Test Units 1A and 1B: removing column and load stub formwork. 38
3.14 Test Unit 1A: partial instrumentation and setup. 38
3.15 Test Units 2A & 2B on the casting beds, with footings cast. 39
3.16 Phase II test unit reinforcement detail. 39
3.17 Stress strain curves for Units 1A and 1B #4 [D13] longitudinal bars. . 43
3.18 Stress strain curves for Units 1A and 1B #3 [D10] spirals. 43
3.19 Stress strain curve for Unit 1A #3 [D10] transverse bars. 44
3.20 Stress strain curves for Units 1B and 2B #2 [D6] transverse bars. . . 44
3.21 Stress strain curves for Units 2A and 2B #4 [D13] longitudinal bars. . 45
3.22 Stress strain curves for Units 2A and 2B #3 [D10] spirals. 45
3.23 Stress strain curves for Units 2A and 2C #3 [D10] transverse bars. . . 46
3.24 Stress strain curve for Unit 2C #4 [D13] longitudinal bars. 46
3.25 Stress strain curve for Unit 2C #3 [D10] spirals. 47

4.1 Fluctuation in axial load as a function of displacement. 49
4.2 Test setup for Units 1A and 1B. 50
4.3 Test setup for Units 2A and 2B. 51
4.4 Test setup for Unit 2C. 52
4.5 Phase I longitudinal strain gage locations. 54
4.6 Phase I transverse and spiral strain gage locations. 55
4.7 Phase II transverse strain gage locations. 56
4.8 Phase II spiral strain gage locations. 57
4.9 Plan and elevation of transverse bars slippage instrumetation. 58
4.10 Bar slippage instrumentation mounted at 18 in. [457 mm] height. . . 58
4.11 Phases I and II curvature instrumentation. 60
4.12 Curvature and shear panel instrumentation on Unit 2A: East Face. . 61
4.13 Curvature instrumentation detail – linear potentiometer. 61
4.14 Detail of curvature instrumentation for Test Units 1A and 1B. 62
4.15 Detail of curvature instrumentation for Test Units 2A, 2B and 2C. . . 62
4.16 Phases I and II shear instrumentation. 65
4.17 Decomposition of panel deformation into five independent modes. . . 68
4.18 Panel deformation. 68
4.19 Diagonal deformations are equivalent in flexure. 69
4.20 Diagonal deformations are equivalent in horizontal and vertical expansion. 69
4.21 Diagonal deformations are used to estimate shear deformation. 70
4.22 Alternative method for calculating shear deformation. 71
4.23 Standard loading history for all test units. 72

5.1 Slippage between the boundary elements and the wall caused by shear. 76
5.2 Idealized design and overstrength force-deflection curves. 79
5.3 Free body diagram on which existing web crushing equations were developed. 81

5.4 Carquinez and East Bay Bridge pier sections. 82
5.5 V_c parameter γ as a function of μ_ϕ and μ_Δ. 84
5.6 Unit 2A: predicted force-deflection curves and shear envelopes. 89
5.7 Unit 2B: predicted force-deflection curves and shear envelopes. 90
5.8 Unit 2C: predicted force-deflection curves and shear envelopes. 91

7.1 First cycle force-displacement envelopes for Units 1A and 1B. 109
7.2 Third cycle force-displacement envelopes for Units 1A and 1B. 110
7.3 Fractured longitudinal reinforcing bars at end of Test 1A. 111
7.4 Fractured longitudinal reinforcing bars during final cycles of Test 1B. 111
7.5 Test Unit 1A hysteretic behavior. 113
7.6 Test Unit 1B hysteretic behavior. 113
7.7 Incipient spalling in Test Unit 1A at μ_Δ 114
7.8 Partial development of spalled region in Test Unit 1A at μ_Δ 114
7.9 Failure modes for Test Units 2A, 2B and 2C. 116
7.10 Third cycle force-displacement envelopes for Units 2A, 2B and 2C. . . 118
7.11 Third cycle force-displacement envelopes for Units 2A, 2B and 2C. . . 119
7.12 Test Unit 2A hysteretic behavior. 120
7.13 Test Unit 2B hysteretic behavior. 120
7.14 Test Unit 2C hysteretic behavior. 121
7.15 (a) Finite element mesh for the Phase I tests. (b) Finite element mesh for the Phase II tests. 122
7.16 Hysteretic behavior for Test Unit 1A with cyclic finite element prediction. 125
7.17 Hysteretic behavior for Test Unit 1B with cyclic finite element prediction. 126
7.18 Hysteretic behavior for Test Unit 2A with cyclic finite element prediction. 127
7.19 Hysteretic behavior for Test Unit 2B with cyclic finite element prediction. 128
7.20 Hysteretic behavior for Test Unit 2C with cyclic finite element prediction. 129
7.21 Test Unit 1A curvature profiles. 132
7.22 Test Unit 1B curvature profiles. 132
7.23 Test Unit 1A experimental displacement values. 133
7.24 Test Unit 1B experimental displacement values. 134
7.25 Test Unit 2A curvature profiles. 136
7.26 Test Unit 2B curvature profiles. 136
7.27 Test Unit 2C curvature profiles. 137
7.28 Test Unit 2A experimental displacement values. 138
7.29 Test Unit 2B experimental displacement values. 139
7.30 Test Unit 2C experimental displacement values. 140
7.31 Test Unit 1A experimental plastic hinge length values. 144
7.32 Test Unit 1B experimental plastic hinge length values. 144
7.33 Test Unit 2A experimental plastic hinge length values. 145
7.34 Test Unit 2B experimental plastic hinge length values. 145
7.35 Test Unit 2C experimental plastic hinge length values. 146
7.36 Test Unit 1B: fully developed spalled region at μ_Δ 149
7.37 Test Unit 2A: fully developed spalled region at μ_Δ 149
7.38 Flexure-shear cracks in the hinge region of Test Unit 1B. 150

7.39 Flexure-shear cracks in Test Unit 2B. 150
7.40 Slippage of and strains in the transverse bars at 18 in. [457 mm] above the footing (Test Unit 1A). 156
7.41 Slippage of and strains in the transverse bars at 36 in. [914 mm] above the footing (Test Unit 1A). 157
7.42 Slippage of and strains in the east transverse bar at 18 in. [457 mm]. (Test Unit 1A) 159
7.43 Tension boundary element cracks: 2A, 2B and 2C. 162
7.44 Spiral strains in Test Unit 2B. 163

8.1 Free body diagram for classical web crushing equations. 165
8.2 Detail of web crushing 166
8.3 Critical compression struts take shear directly into the compression toe. 166
8.4 UCSD Test Unit 2C 167
8.5 Free body diagram for critical compression strut region. 167
8.6 Effective region of longitudinal steel. 168
8.7 Variation in the ratio of web crushing strength to ultimate flexural strength V_{wc}/V_u, as a function of the relative depth ratio D_w/D_b. . . 173
8.8 Theoretical force-deflection curves for columns C1-C7 of decreasing relative depth ratio D_w/D_b. 176

A.1 1A; F_y; F=47.4kips; Δ=0.81in. 184
A.2 1A; $-F_y$; F=-47.3kips; Δ=-0.86in. 184
A.3 1A; μ_Δ=1.5x1; F=63.1kips; Δ=1.67in. 185
A.4 1A; μ_Δ=1.5x3; F=57.0kips; Δ=1.67in. 185
A.5 1A; μ_Δ=3.0x1; F=66.0kips; Δ=3.33in. 186
A.6 1A; μ_Δ=3.0x3; F=65.2kips; Δ=3.34in. 186
A.7 1A; μ_Δ=4.0x3; F=70.1kips; Δ=4.44in. 187
A.8 1A; μ_Δ=6.0x1; F=72.5kips; Δ=6.68in. 187
A.9 1A; μ_Δ=6.0x1; F=72.5kips; Δ=6.68in. 188
A.10 1A; μ_Δ=-6.0x1; F=-70.2kips; Δ=-6.68in. 188
A.11 1A; μ_Δ=-8.0x1; F=-63.8kips; Δ=-8.82in 189
A.12 1A; μ_Δ=8.0x3; F=42.8kips; Δ=8.82in 189
A.13 1B; $3/4F_y$; F=33.5kips; Δ=0.38in. 191
A.14 1B; $-F_y$; F=-47.4kips; Δ=-0.83in. 191
A.15 1B; μ_Δ=-1.0x1; F=-54.1kips; Δ=-1.11in. 192
A.16 1B; μ_Δ=1.5x1; F=62.2kips; Δ=1.67in. 192
A.17 1B; μ_Δ=-3.0x1; F=-66.3kips; Δ=-3.34in. 193
A.18 1B; μ_Δ=-3.0x1; F=-66.3kips; Δ=-3.34in. 193
A.19 1B; μ_Δ=4.0x1; F=67.4kips; Δ=4.45in. 194
A.20 1B; μ_Δ=6.0x1; F=69.6kips; Δ=6.67in. 194
A.21 1B; μ_Δ=6.0x1; F=69.6kips; Δ=6.67in. 195
A.22 1B; μ_Δ=-6.0x3; F=-65.7kips; Δ=-6.68in. 195
A.23 1B; μ_Δ=8.0x1; F=65.9kips; Δ=8.88in. 196
A.24 1B; μ_Δ=-8.0x2; F=-55.9kips; Δ=-8.82in. 196

A.25 2A; 3/4 F_y; F=70.8kips; Δ=0.14in. 198
A.26 2A; $-F_y$; F=-94.4kips; Δ=-0.26in 198
A.27 2A; μ_Δ=-1.0x1; F=-105.4kips; Δ=-0.35in. 199
A.28 2A; μ_Δ=-1.5x1; F=-121.4kips; Δ=-0.53in. 199
A.29 2A; μ_Δ=3.0x1; F=131.9kips; Δ=1.05in. 200
A.30 2A; μ_Δ=-3.0x1; F=-127.6kips; Δ=-1.06in. 200
A.31 2A; μ_Δ=-4.0x3; F=-121.2kips; Δ=-1.44in. 201
A.32 2A; μ_Δ=6.0x1; F=135.9kips; Δ=2.10in. 201
A.33 2A; μ_Δ=-6.0x1; F=-131.8kips; Δ=-2.10in. 202
A.34 2A; μ_Δ=-6.0x3; F=-125.8kips; Δ=-2.10in. 202
A.35 2A; μ_Δ=8.0x1; F=135.0kips; Δ=2.80in. 203
A.36 2A; μ_Δ=8.0x2; F=118.0kips; Δ=2.80in. 203
A.37 2B; 3/4 F_y; F=71.1kips; Δ=0.12in. 205
A.38 2B; $-F_y$; F=-94.6kips; Δ=-0.25in. 205
A.39 2B; μ_Δ=-1.0x1; F=-104.1kips; Δ=-0.35in. 206
A.40 2B; μ_Δ=1.5x3; F=112.4kips; Δ=0.53in. 206
A.41 2B; μ_Δ=3.0x1; F=130.0kips; Δ=1.05in. 207
A.42 2B; μ_Δ=-3.0x1; F=-126.5kips; Δ=-1.06in. 207
A.43 2B; μ_Δ=4.0x3; F=121.8kips; Δ=1.40in. 208
A.44 2B; μ_Δ=6.0x1; F=134.1kips; Δ=2.10in. 208
A.45 2B; μ_Δ=-6.0x1; F=-129.2kips; Δ=-2.10in. 209
A.46 2B; μ_Δ=-6.0x3; F=-121.4kips; Δ=-2.10in. 209
A.47 2B; μ_Δ=8.0x1; F=128.8kips; Δ=2.80in. 210
A.48 2B; μ_Δ=8.0x3; F=101.1kips; Δ=2.80in. 210
A.49 2C; 3/4 F_y; F=71.1kips; Δ=0.12in. 212
A.50 2C; $-F_y$; F=-94.6kips; Δ=-0.25in. 212
A.51 2C; μ_Δ=-1.0x1; F=-104.1kips; Δ=-0.35in. 213
A.52 2C; μ_Δ=1.5x3; F=112.4kips; Δ=0.53in. 213
A.53 2C; μ_Δ=3.0x1; F=130.0kips; Δ=1.05in. 214
A.54 2C; μ_Δ=-3.0x1; F=-126.5kips; Δ=-1.06in. 214
A.55 2C; μ_Δ=4.0x3; F=121.8kips; Δ=1.40in. 215
A.56 2C; μ_Δ=6.0x1; F=134.1kips; Δ=2.10in. 215
A.57 2C; μ_Δ=-6.0x1; F=-129.2kips; Δ=-2.10in. 216
A.58 2C; μ_Δ=6.0x3; F=121.4kips; Δ=2.10in. 216
A.59 2C; μ_Δ=8.0x1; F=128.8kips; Δ=2.80in. 217
A.60 2C; μ_Δ=8.0x3; F=104.5kips; Δ=2.83in. 217

B.1 Test Unit 1A hysteretic behavior. 218
B.2 Unit 1A: Curvature profiles for the wall (left) and for the total section (right). 219
B.3 Unit 1A: SBE and NBE curvatures. 220
B.4 Unit 1A: Longitudinal bar strain profiles at 6in. [152mm] below the footing surface. 221
B.5 Unit 1A: Longitudinal bar strain profiles at footing level. 222

B.6 Unit 1A: Longitudinal bar strain profiles at 6in. [152mm] above the footing. 223
B.7 Unit 1A: Longitudinal bar strain profiles at 12in. [305mm] above the footing. 224
B.8 Unit 1A: Longitudinal bar strain profiles at 24in. [610mm] above the footing. 225
B.9 Unit 1A: Strains on east transverse bars at initial and final testing stages. 226
B.10 Unit 1A: Strains on west transverse bars at initial and final testing stages. 227
B.11 Unit 1A: East and west spiral strains at final stages of loading. 228

C.1 Test Unit 1B hysteretic behavior. 229
C.2 Unit 1B: Curvature profiles for the wall (left) and for the total section (right). 230
C.3 Unit 1B: NBE and SBE curvatures. 231
C.4 Unit 1B: Longitudinal bar strain profiles at 6in. [152mm] below the footing surface. 232
C.5 Unit 1B: Longitudinal bar strain profiles at footing level. 233
C.6 Unit 1B: Longitudinal bar strain profiles at 6in. [152mm] above the footing. 234
C.7 Unit 1B: Longitudinal bar strain profiles at 12in. [305mm] above the footing. 235
C.8 Unit 1B: Longitudinal bar strain profiles at 24in. [610mm] above the footing. 236
C.9 Unit 1B: Strains on east transverse bars at initial and final testing stages. 237
C.10 Unit 1B: Strains on west transverse bars at initial and final testing stages. 238
C.11 Unit 1B: East and west spiral strains at final stages of loading. 239

D.1 Test Unit 2A hysteretic behavior. 240
D.2 Unit 2A: Curvature profiles for the wall (left) and for the total section (right). 241
D.3 Unit 2A: Longitudinal bar strain profiles at 6in. [152mm] below the footing surface. 242
D.4 Unit 2A: Longitudinal bar strain profiles at footing level. 243
D.5 Unit 2A: Longitudinal bar strain profiles at 6in. [152mm] above the footing. 244
D.6 Unit 2A: Longitudinal bar strain profiles at 12in. [305mm] above the footing. 245
D.7 Unit 2A: Longitudinal bar strain profiles at 24in. [610mm] above the footing. 246
D.8 Unit 2A: Strains on east transverse bars at initial and final testing stages. 247
D.9 Unit 2A: Strains on west transverse bars at initial and final testing stages. 248
D.10 Unit 2A: East and west spiral strains at final stages of loading. 249

E.1 Test Unit 2B hysteretic behavior. 250
E.2 Unit 2B: Curvature profiles for the wall (left) and for the total section (right). 251
E.3 Unit 2B: Longitudinal bar strain profiles at 6in. [152mm] below the footing surface. 252
E.4 Unit 2B: Longitudinal bar strain profiles at footing level. 253
E.5 Unit 2B: Longitudinal bar strain profiles at 6in. [152mm] above the footing. 254
E.6 Unit 2B: Longitudinal bar strain profiles at 12in. [305mm] above the footing. 255
E.7 Unit 2B: Longitudinal bar strain profiles at 24in. [610mm] above the footing. 256
E.8 Unit 2B: Strains on east transverse bars at initial and final testing stages. 257
E.9 Unit 2B: Strains on west transverse bars at initial and final testing stages. 258
E.10 Unit 2B: East and west spiral strains at final stages of loading. 259

F.1 Test Unit 2C hysteretic behavior. 260
F.2 Unit 2C: Curvature profiles for the wall (left) and for the total section (right). 261
F.3 Unit 2C: Strains on east transverse bars at initial and final testing stages. 262
F.4 Unit 2C: Strains on west transverse bars at initial and final testing stages. 263
F.5 Unit 2C: East and west spiral strains at final stages of loading. 264

List of Symbols

A_e	effective area of a section
A_g	gross area of a section
A_{sl}	area of longitudinal reinforcement
A_{sp}	area of spiral reinforcement
A_{tr}	area of transverse reinforcement
b_w	width of a concrete section
c	neutral axis depth
c'	vertical depth of contact between the critical compression struts and the compression boundary element
c_o	depth of concrete cover
d_{bl}	longitudinal bar diameter
d_s	minimum depth of the critical compression struts
D	section depth
D'	spiral diameter for a circular concrete section
D_b	boundary element depth
D_w	structural wall depth
E	elastic modulus of steel
E_c	elastic modulus of concrete
E_{sh}	initial strain hardening modulus for steel
f'_c	concrete ultimate compressive strength (stress)
f'_{cc}	confined concrete ultimate compressive strength (stress)
f_u	steel ultimate stress
f_y	steel yield stress
f_{yl}	steel yield stress in longitudinal reinforcement
f_{ytr}	steel yield stress in transverse reinforcement
f_{ysp}	steel yield stress in spirals
$F_{\varepsilon_c=0.004}$	theoretical lateral force on a column at which ε_c .004 in the extreme compression fiber at the column base
F_{iy}	ideal yield force
F_u	ultimate force capacity of a structural member, including overstrength
F_y	yield force capacity of a structural member
$F_{y,theory}$	theoretical yield force capacity of a structural member
h_1	height in the tension boundary element from the column base to the lower edge of the critical compression strut region

h_2	height in the tension boundary element from the column base to the upper edge of the critical compression strut region
h_i	gauge length over which a single rotation reading is taken from displacement potentiometers mounted on the side of the column. The rotation is divided by this gauge length in order to calculate the average curvature over this height.
h_s	height of the critical compression strut region in the tension boundary element
jd_b	moment arm for boundary element steel
jd_w	moment arm for structural wall steel
k	concrete strength reduction factor
K_e	elastic stiffness of a structural member
l_t	horizontal distance over which total curvature is calculated for Test Units 2A, 2B and 2C
l_w	horizontal distance over which wall curvature is calculated
L	cantilever length of a structural member (L M/V)
L'	distance from axial load application point to the base of a column
L_p	plastic hinge length
L_{pe}	experimentally calculated plastic hinge length
L_{sp}	strain penetration depth
M	moment
$M - \Phi$	abbreviation for "moment-curvature"
M_n	nominal moment
M_u	ultimate moment
M_y	yield moment
N_C	axial capacity of the critical compression strut region
N_D	axial demand on the critical compression strut region
P	axial load; exponent for the strain hardening of reinforcing steel
s_{sp}	spiral spacing
s_{tr}	transverse reinforcement vertical spacing
t_w	structural wall thickness
T_{by}	yield tensile force of the boundary element longitudinal steel
T_{bu}	ultimate tensile force of the boundary element longitudinal steel
T_{tr}	tensile force acting on the critical compression strut region as a result of the transverse reinforcement
T_{wy}	yield tensile force of the structural wall longitudinal steel
T_{wu}	ultimate tensile force of the structural wall longitudinal steel
v_{max}	maximum allowable shear stress on a reinforced concrete structural wall
v_{wc}	stress at web crushing in a reinforced concrete structural wall
V	shear force
V_c	concrete component of a column's shear capacity
V_D	column design shear force
V_{iy}	test unit ideal yield force

V_o	column overstrength shear force
V_p	axial load component of a column's shear capacity
V_s	steel component of a column's shear capacity
V_u	column ultimate shear force
$V_{u,calc}$	estimated ultimate column shear force (Oesterle et al.)
$V_{u,test}$	measured ultimate column shear force (Oesterle et al.)
V_{wc}	web crushing force on a reinforced concrete structural wall
V_y	test unit shear force at theoretical yield of the steel
α	aspect ratio factor for V_c
β	longitudinal reinforcement ratio factor for V_c
γ	ductility factor for V_c
δ	drift ratio δ $/L$ $=\Delta$
δ_u	drift ratio at ultimate displacement
Δ	test unit top displacement
Δ_e	elastic displacement
Δ_f	flexural displacement
Δ_{iy}	test unit ideal yield displacement corresponds to μ_Δ =
Δ_n	nominal yield displacement
Δ_{nb}	incremental vertical displacement on the north boundary element in Test Units 2A, 2B and 2C for calculating total section curvature
Δ_{nbn}	incremental vertical displacement on the north end of the north boundary element in Test Units 1A and 1B for calculating total section curvature
Δ_p	plastic displacement
Δ_{sb}	incremental vertical displacement on the south boundary element in Test Units 2A, 2B and 2C for calculating total section curvature
Δ_{sbs}	incremental vertical displacement on the south end of the south boundary element in Test Units 1A and 1B for calculating total section curvature
Δ_{shr}	displacement due to shear deformations
Δ_{top}	displacement measured at the top of the column
ΔT_l	net tensile force acting vertically downward on the critical compression strut region
Δ_u	column ultimate displacement
Δ_y	column top displacement at first yield
Δ_{yD}	column design yield displacement
$\Delta_{y,exp}$	experimental column displacement under the force corresponding to theoretical yield of the longitudinal steel
Δ_{yo}	column yield displacement accounting for overstrength
ε_c	concrete strain
ε_{cu}	ultimate concrete strain
ε_s	steel strain
ε_{sh}	steel strain at onset of hardening

ε_{su}	ultimate steel strain
ε_{tr}	transverse bar strain
ε_y	steel yield strain
θ	inclination angle of concrete cracks, measured from the vertical
θ_i	rotation measured over a gauge height h_i
θ_1	inclination angle of the lower edge of the critical compression strut region, measured from the vertical
θ_2	inclination angle of the upper edge of the critical compression strut region, measured from the vertical
θ_{av}	average inclination angle of the critical compression strut region, measured from the vertical
μ_Δ	displacement ductility factor
$\mu_{\Delta o}$	displacement ductility accounting for overstrength in the yield displacement
$\mu\varepsilon$	microstrains
μ_ϕ	curvature ductility ratio
ρ_h	transverse reinforcement ratio in the structural wall
ρ_l	longitudinal reinforcement ratio in the boundary elements
ρ_n	longitudinal reinforcement ratio in the structural wall
ρ_s	volumetric confinement ratio in the boundary elements
ϕ	curvature; also strength reduction factor
ϕ_b	curvature measured at the base of the column
$\phi_{i,av}$	average curvature over a given gauge height h_i
ϕ_n	nominal yield curvature
$\phi_{o,w}$	flexural overstrength factor for a structural wall
ϕ_w	curvature measured from the structural wall
ϕ_{tI}	curvature measured for the total section, Units 1A and 1B
ϕ_{tII}	curvature measured for the total section, Units 2A, 2B and 2C
ϕ_y	yield curvature

Chapter 1

Introduction

1.1 Seismic Performance of Reinforced Concrete Piers for Long Span Bridges

The current construction of three new toll bridges in the San Francisco Bay Area has made the seismic design of long span bridges a research priority for Caltrans. While designers are confident that the principles applied to the seismic design of shorter spans remain valid for all bridges, important structural details must be developed to accommodate the increase in scale. As with shorter spans, the piers which support these new structures are required to withstand large deformations with no loss of strength during an earthquake event.

Designers have proposed hollow rectangular reinforced concrete piers for the Second Benicia Martinez Bridge, the Third Carquinez Strait Bridge and the East Bay Spans of the San Francisco-Oakland Bay Bridge* that rely on highly confined boundary elements at the corners for deformation capacity, connected by structural walls for stiffness and strength. Reducing the mass of these piers by making them hollow decreases their contribution to seismic loads on the bridge. The hollow core ensures greater quality control during construction by reducing the heat of hydration on the interior of the section and hence minimizing shrinkage cracks caused by temperature differences inside the curing pier. Furthermore, the reduction in the total amount of material required to construct the piers implies a potential savings in construction cost. While circular hollow piers also address these three issues, designers have, for aesthetic reasons, preferred hollow rectangular piers for each of the three new Bay Area bridges shown in Figure 1.1. The hollow rectangular cross section can assume a number of different shapes and therefore allows designers to create, through the shape

*In this report, these bridges will be referred to as the Benicia Martinez Bridge, the Carquinez Strait Bridge and the East Bay Bridge.

of the piers, a strong visual impression that is integrated with the overall bridge form.

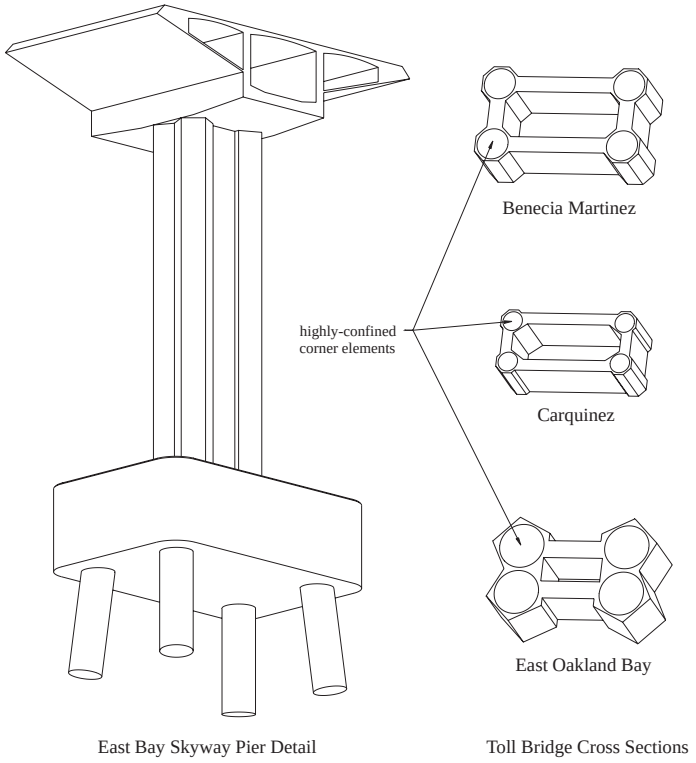

Figure 1.1: Schematic representation of proposed Bay Area bridge piers.

Since the neutral axis in such piers typically lies near or within the compression boundary elements, an interior region filled with concrete would contribute almost nothing to the flexural response. This similarity in behavior to solid columns does not imply, however, that the equivalent plastic hinge length of such bridge piers can be estimated accurately by the empirical expressions based on the existing database of tests on smaller and less complex bridge columns.

The scale and the complexity of these bridge piers also raises the question of how shear is transferred across the section under loading in both principal directions and in the diagonal direction. In the principal directions, the walls need to be strong enough to carry the shear directly across the section. Such transfer is expected to occur in the form of a truss mechanism consisting of diagonal compression struts in the wall that are held in place between the boundary elements by reinforcing steel tension ties. Therefore, the level of transverse steel and the wall thickness should be designed to support a truss mechanism that carries the maximum possible shear demand on the section without yielding the steel or crushing the wall. In the case of double bending, the wall connection between boundary elements should sufficiently restrain

parts of the section from slipping vertically against one another. With increased understanding of the cyclic behavior of these bridge piers, it may eventually become possible to modify pier design details in order to allow controlled yielding of the transverse bars or vertical slippage between section components, thus customizing a pier's force-deflection behavior to meet desired performance criteria under lateral loads. It is recommended, however, not to explore such modifications in depth until the mechanisms of shear transfer discussed above are well understood.

Under transverse loading in the diagonal direction, the compression region consists of a single boundary element and parts of the adjoining walls. In such a case, a three dimensional truss mechanism is expected to develop, with the shear forces following a more complicated path around the perimeter of the pier. Furthermore, when these diagonal loads do not act through the shear center of the pier section they place a torsional demand on the pier. The significance of shear and torsional demands on a pier implies that analytical tools must be able to evaluate the flexural, shear and torsional behavior of the piers on the member level.

Although the effect of shear on these piers is expected to be significant, for the purposes of design, section analysis predictions can be calibrated by simply modifying equivalent plastic hinge length equations to account for tension shift effects. Such simplification also requires that existing design equations for total shear capacity and for web crushing strength be recalibrated for different section geometries and reinforcement configurations.

1.2 Testing Program

In order to study in detail the seismic behavior of these bridge piers, Caltrans and the University of California, San Diego have undertaken a multi-phase, large scale testing program at the Charles Lee Powell Structural Research Laboratories at the University of California, San Diego. This report describes the first two phases of the testing program, which focus on the in-plane behavior of structural walls with boundary elements (barbell shaped sections). Such walls are the basic subassemblies for the entire pier sections introduced earlier. Later phases of testing will investigate the cyclic behavior of the entire pier under biaxial loading.

In order to study the in plane behavior of structural walls and their boundary elements, it was initially sufficient to test individual walls, extracted from the prototype rectangular section. Figure 1.2 shows in position (a) a proposed cross section for the Second Benicia Martinez Bridge and in position (c) a subassembly (barbell shape)

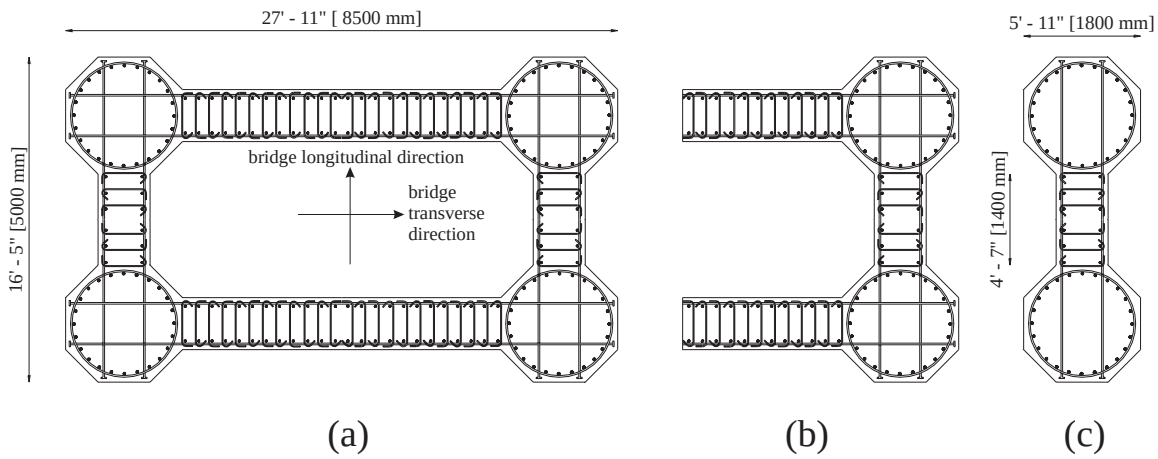

Figure 1.2: (a) Early proposal for a typical cross section of the 2nd Benicia Martinez Bridge Piers. (b) True half section with tributary longitudinal reinforcement in the wall. (c) Test subassembly consisting of a single structural wall with boundary elements.

extracted from a short side of the pier. The drawing in position (b) shows the entire area of reinforcement expected to contribute to the shear demand on the structural wall subassembly. For these initial phases of testing, however, only the reinforcement in the subassembly itself was considered. The test unit section geometry can be seen in Figure 1.3 (c) as a hybrid of the transverse (a), and longitudinal (b) walls of the proposed Benicia Martinez bridge pier. The test units themselves were designed to just under 20% scale of this hybrid geometry and are discussed in detail in Chapter 2.

Design Issues

The important design issue for the chosen subsection of these piers lies in detailing the structural wall for shear capacity under the assumption that the boundary elements provide adequate flexural capacity. The strength of the structural wall and its ability to enforce integral behavior between the tension and compression boundary elements is assumed to depend primarily on the wall thickness t_w, and the level of transverse reinforcement ρ_h, which is defined as the ratio of transverse steel area to the area of concrete in the structural wall. The ratio is calculated using the equation $\rho_h = \frac{A_{str}}{t_w s_{tr}}$, where s_{tr} is the vertical spacing between the transverse reinforcement oriented in the plane of loading. The basic geometry and reinforcement of the test units is given in Table 1.1.

Test units in the first two phases of the testing program were designed based

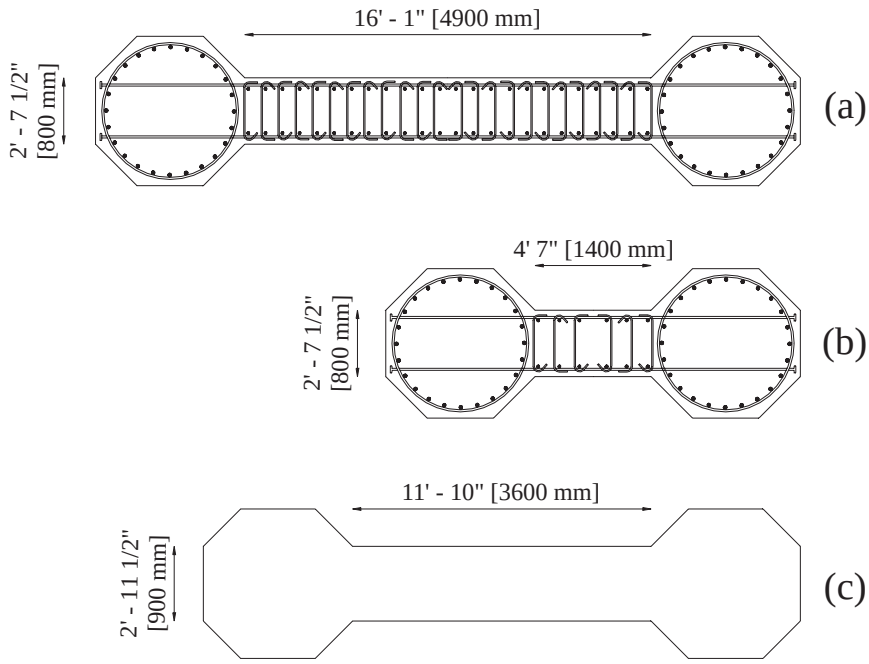

Figure 1.3: (a) Long structural wall in bridge transverse direction. (b) Short structural wall in bridge longitudinal direction. (c) Test unit section geometry generalized from Benicia Martinez prototype.

on the geometry of the subassembly introduced in Figures 1.2 and 1.3. The basic geometry and reinforcement configuration for the Phase I and Phase II test units is shown in Figure 1.4. Phase I (see Figure 1.5) investigated the flexural behavior of this subassembly in single bending for an aspect ratio of M/VD 4 in the loading direction. The aspect ratio, M/VD is defined as the moment to shear ratio (which for a cantilever in single bending is equivalent to the column length L) divided by the total section depth D. Phase II tests (see Figure 1.6) investigated the shear behavior of the same subassembly in single bending by reducing the height of the column for a reduction in aspect ratio to M/VD 2 in the loading direction.

Analysis Issues

The issues important to analysis include both (1) the extent to which the structural wall enforces integral action between the boundary elements, and (2) the spread of plasticity in the plastic hinge region. The first issue addresses the validity of the assumption that plane sections remain plane, used in the moment-curvature analysis of a section. The second addresses the relationship between plastic hinge length and column length.

Test Unit	M/VD	$P/f'_c A_g$	f'_c		t_w		Reinforcement (%)*			
			psi	MPa	in.	[mm]	ρ_l	ρ_n	ρ_s	ρ_h
1A	4	0.090	5530	40.1	6	152	1.43	1.39	1.38	0.61
1B	4	0.081	6210	42.8	6	152	1.43	1.39	1.38	0.21
2A	2	0.094	5310	36.6	6	152	1.43	1.39	1.38	0.61
2B	2	0.083	6017	41.5	6	152	1.43	1.39	1.38	0.21
2C	2	0.111	4059	31.1	4	102	1.43	2.08	1.38	0.61

* ρ_l longitudinal reinforcement ratio in boundary columns
ρ_n longitudinal reinforcement ratio in structural wall
ρ_s volumetric reinforcement ratio for confinement in boundary elements
ρ_h transverse reinforcement ratio in structural wall

Table 1.1: Test Unit geometry and reinforcement.

1.2.1 Test Phase I – Flexural Test Units

The test units in the first phase had an aspect ratio of M/VD 4 and represented two extremes in designing the structural wall of constant thickness to provide a stable shear connection between the boundary elements. The test units had identical boundary elements, but the structural wall of Unit 1A was reinforced to carry the section overstrength shear by its transverse steel alone, whereas the transverse steel in Unit 1B constituted the minimum necessary to control shrinkage.

Unit 1A contained a conservative distribution of transverse reinforcement, and Unit 1B contained an unconservative distribution of transverse reinforcement. Instead of verifying the behavior of columns designed according to existing standards [1], these tests were designed to establish the effects of extreme levels of reinforcement on column behavior and thereby reveal the relative consequences, in terms of performance issues such as crack patterns and displacement ductility, of designing conservatively and non-conservatively.

The piers in the new Bay Area bridges were designed to behave in a ductile manner, forming plastic hinges at the member ends. The first phase of this program was therefore also designed to validate the accuracy of force-deflection predictions based on a moment-curvature results and an assumed equivalent plastic hinge length.

1.2.2 UCSD Test Phase II – Shear Test Units

With an aspect ratio of M/VD 2, these units were subjected to roughly twice the shear force applied to the Phase I units. Phase II evaluated the shear strength of three units according to five shear assessment and design equations which gave a

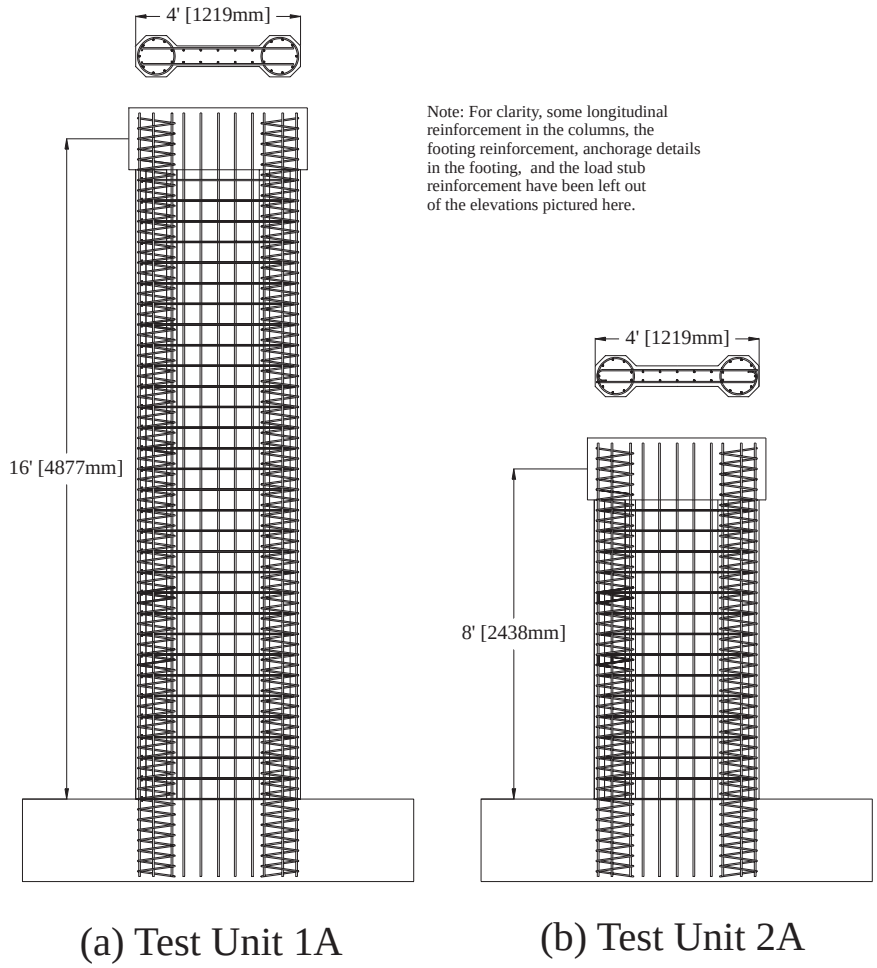

Figure 1.4: (a) Test Unit 1A section and side elevation with column reinforcement. (b) Test Unit 2A section and side elevation with column reinforcement.

wide variation in predicted shear capacity (see Chapter 5). Units 2A and 2B were designed with section geometry and reinforcement identical to Units 1A and 1B, the only difference being their aspect ratio and hence the applied shear force. With the increased shear demand on these units, both designs had inadequate shear capacity according to ACI standards, based on an effective shear area of $A_e = Dt_w$ where D is the total section depth and t_w is the wall thickness. The UCSD shear model (see Chapter 5) predicted that Unit 2A would not fail in shear but that Unit 2B would fail in shear just after μ_Δ =4. Unit 2C was designed with a 4 in. [102 mm] wall thickness as opposed to the 6 in. [152 mm] wall thickness of Units 2A and 2B. Maintaining the same transverse reinforcement ratio as Unit 2A, the total amount of transverse reinforcement in Unit 2C was two thirds that of Unit 2A. Unit 2C was designed to fail by crushing of the structural wall (see Chapter 5). The UCSD shear model predicted

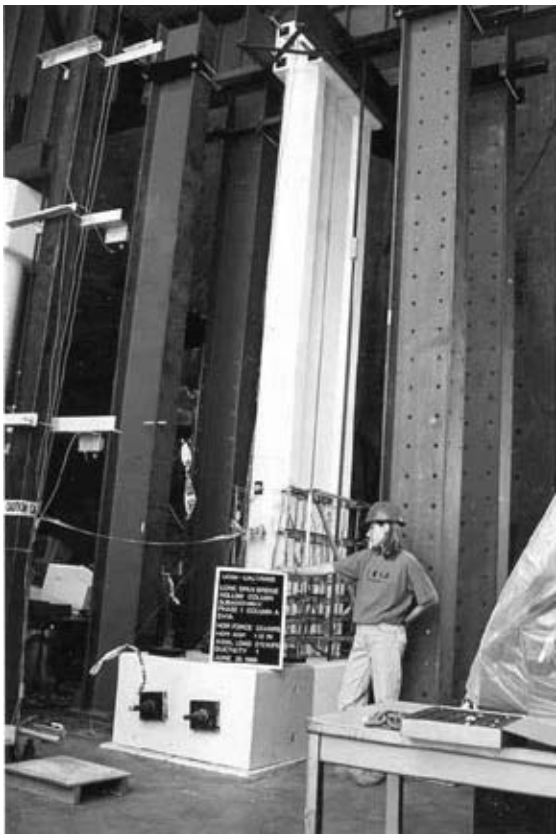

Figure 1.5: Photo of test setup for Phase I tests.

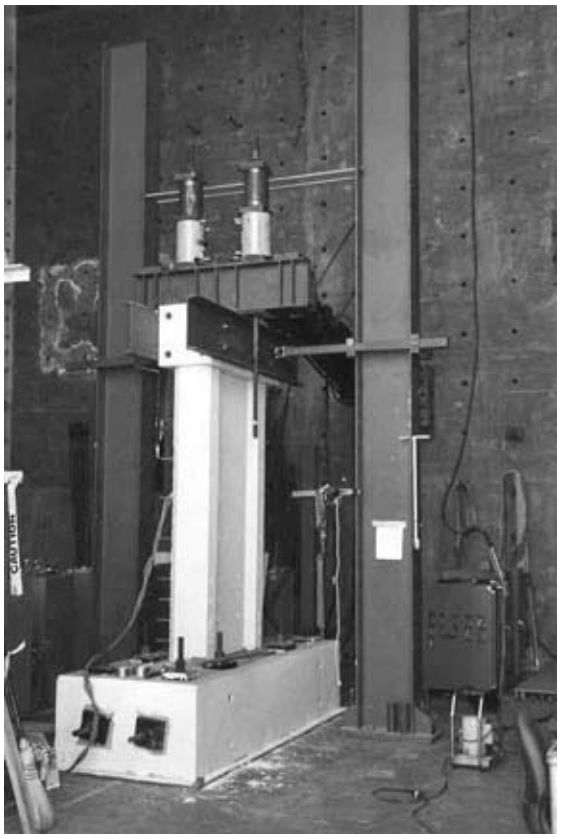

Figure 1.6: Photo of test setup for Phase II tests.

that it would not fail in shear.

The Phase II units were therefore designed to provide three specific data points for understanding shear behavior of structural walls with boundary elements.

- Unit 2A was designed to fail in flexure in spite of the high shear/flexure demand ratio.
- Unit 2B was designed to fail in shear due to inadequate transverse reinforcement.
- Unit 2C was designed to fail by web crushing due to inadequate wall thickness.

1.3 Previous Work

Wang et al. and Vallenas et al. at the University of California, Berkeley, and Oesterle et al. at the Portland Cement Association conducted extensive tests on structural walls with confined boundary elements in the late 1970's. These test programs focused on structural walls as lateral force resisting members exclusively for buildings and not

bridges. Aspects of bridge pier design that differ from the design of structural walls for buildings include

- differences in scale,
- the integral action of several walls and boundary elements as a single hollow pier,
- greater concentration of longitudinal reinforcement in the structural wall,
- increase in slenderness to flexural aspect ratios,
- the need to perform reliably under seismic loads in both single and double bending,
- the relative depth and width of the boundary elements compared to that of the structural wall (relative depth ratio D_w/D_b)
- the axial load ratio.

This report and later work on the Bay Area bridge piers will address these issues directly while drawing on results from the previous tests where appropriate. In particular, the existing work done by Oesterle et al. provides a range of data points for web crushing failures, and forms the basis for the discussion in Chapter 8 on a new flexure-shear web crushing model.

1.3.1 Wang et al. 1975, Vallenas et al. 1979

Tests performed by Wang et al. in 1975 and Vallenas et al. in 1979 at the University of California, Berkeley characterized the effect of loading history on structural walls with confined boundary elements. Of the twelve tests conducted in this experimental program, four are of interest regarding the design of bridge piers. The test units were labeled SW1, SW2 [18] SW3 and SW4 [16] and had identical cross sectional geometry, longitudinal reinforcement and transverse reinforcement. The only difference in reinforcement was that SW1 and SW2 had spiral confinement in the boundary elements, whereas SW3 and SW4 had rectangular confinement in the boundary elements. Test unit properties are given in Table 1.2.

SW1 and SW3 were loaded monotonically to failure whereas SW2 and SW4 were loaded cyclically and failed at a lower ultimate displacement. Table 1.3 gives non-dimensional ultimate load and ultimate displacement descriptions of the tests as well

Aspect Ratio M/VD	Relative Depth Ratio D_w/D_b	Axial Load Ratio P/f'_cA_g	f'_c psi	f'_c MPa	Reinforcement (%) ρ_l	ρ_n	ρ_s	ρ_h
1.28	7.4	0.075	5300	36.5	3.52	0.83	0.83	1.80

Table 1.2: Test Unit geometry and reinforcement: SW1, SW2, SW3, SW4, Wang et al. (1975), Vallenas et al. (1979)

Test Unit	Loading Pattern	v_u/f'_c	$\delta_u = \Delta_u/L$	Failure Mode
SW1	monotonic with some cycles	0.124	0.035	web crushing
SW2	cyclic	0.123	0.025	web crushing
SW3	monotonic	0.123	0.061	boundary element crushing
SW4	cyclic	0.109	0.024	web crushing

Table 1.3: Test Unit force and displacement capacities, Wang et al. (1975), Vallenas et al. (1979)

as the failure mode for each test unit. The ultimate load is reported non-dimensionally as v_u/f'_c, where v_u is the ultimate shear stress across the section. This is defined as $v_u = V_u/Dt_w$, where D is the total section depth, t_w is the wall thickness, and V_u is the ultimate shear demand on the wall. The drift ratio at ultimate displacement δ_u describes the ultimate displacement of each test unit in non-dimensional terms and is defined as $\delta_u = \Delta_u/L$.

Test Units SW2 and SW4 reached almost exactly the same ultimate displacement, although SW4 reached an 11% lower ultimate load than SW2. Test Units SW1 and SW3, loaded monotonically, reached similar ultimate loads, however SW3 reached an ultimate displacement 71% greater than SW1. The extra displacement capacity of SW3 may be attributed to the fact that it was loaded purely monotonically, whereas SW1 was cycled inadvertently just after yield because of difficulties with the control system and then again at μ_Δ because the test needed to be stopped in order to secure further the reaction blocks against uplift. After the reversal at μ_Δ, SW1 was loaded in the negative direction and cycled until it reached a point of nearly zero lateral displacement. This negative excursion into the inelastic range clearly lowered the web crushing displacement capacity of SW1.

The aspect ratio (M/VD) of these four test units was relatively low, and the relative depth ratio (D_w/D_b) was relatively high compared to the ratio values one would see in bridge piers. The differences in response under monotonic versus cyclic loading clearly indicated, however, that the web crushing displacement capacity of structural walls with boundary elements was reduced by cyclic loading. Cyclic loading

subjected the wall to large strain reversals across flexure-shear cracks in the wall and degraded the capacity of the compression struts in the truss mechanism that formed in the wall.

1.3.2 Oesterle et al. 1976-1979

The first eight walls tested by Oesterle et al. in 1976 at the Portland Cement Association consisted of three wall types: rectangular, walls with boundary elements (barbell shaped sections), and a wall with flanges. Test parameters included longitudinal reinforcement, confinement in the columns and loading history–with primarily cyclic tests and one monotonic test. One wall was repaired and retested, making a total of nine tests. In 1979 six more walls were tested, five had confined columns and the sixth had flanges. Test parameters included axial load ratio, transverse reinforcement, concrete strength and variations in the cyclic loading history. One of these walls was repaired and retested, making for a total of 7 tests. Figure 1.7 shows the basic geometry of the units tested by Oesterle et al. and Table 1.4 gives the critical material properties and reinforcement ratios for the test units. Section geometry of the different test units and reinforcement details are given in Figure 1.8. All test units were identical in height and in total section depth, giving them an aspect ratio of M/VD 2.4. The relative depth ratio for the barbell units was D_w/D_b .25.

Table 1.5 summarizes the failure modes and force-deflection characteristics of Oesterle et al.'s test units. Test units with values of $V_{utest}/V_{ucalc} < 1$ did not reach their theoretical ultimate flexural strength. Test Unit B4, loaded monotonically, was the only unit to reach its expected flexural strength. Every other test unit failed prematurely by degradation of the boundary elements or crushing in the structural wall, confirming that cyclic loading reduces the ultimate flexural capacity of such walls. Ten of the test units failed in web crushing (see Figures 1.9 and 1.10). The results from these tests are used in Chapter 8 to evaluate several analytical models for web crushing strength of structural walls with boundary elements. Some observations from these test units' behavior are given below.

Transverse reinforcement was increased to roughly twice as much as the baseline in Test Unit B8. Results from this test confirmed that added transverse reinforcement did not significantly influence the cyclic behavior of the wall. No tests were performed, however, with less transverse reinforcement.

Test Unit B4 was loaded monotonically and showed more than twice the deformation capacity (δ_u 0.069) than the rest of the units that were loaded cyclically ($\delta_u \simeq 0.029$). This test unit failed in flexure, by fracture of the longitudinal reinforcing

Test Unit	Shape	$P/f'_c A_g$	f'_c		Reinforcement (%)			
			psi	MPa	ρ_l	ρ_n	ρ_s	ρ_h
R1	rectangular	0.000	6490	44.7	1.47	0.25	0.0	0.31
R2	rectangular	0.000	6735	46.4	4.00	0.25	2.07	0.31
B1	barbell	0.000	7685	53.0	1.11	0.29	0.0	0.31
B3	barbell	0.000	6860	47.3	1.11	0.29	1.28	0.31
B4	barbell	0.000	6530	45.0	1.11	0.29	1.28	0.31
B2	barbell	0.000	7775	53.6	3.67	0.29	0.0	0.63
B5	barbell	0.000	6570	45.3	3.67	0.29	1.35	0.63
B5R	barbell	0.000	6205	42.8	3.67	0.29	1.35	0.63
B6	barbell	0.130	3165	21.8	3.67	0.29	0.81	0.63
B7	barbell	0.080	7155	49.3	3.67	0.29	1.35	0.63
B8	barbell	0.090	6085	42.0	3.67	0.29	1.35	1.38
B9	barbell	0.090	6395	44.1	3.67	0.29	1.35	0.63
B9R	barbell	0.060	7510	51.8	3.67	0.20	1.35	0.42
B10	barbell	0.080	6615	45.6	1.97	0.29	1.35	0.63
F1	flanged	0.000	5575	38.4	3.89	0.30	0.0	0.71
F2	flanged	0.070	6610	45.6	4.35	0.31	1.43	0.63

Table 1.4: Test Unit geometry and reinforcement, Oesterle et al. (1976-1979)

Test Unit	Loading	V_{utest}/V_{ucalc}	v_u/f'_c	δ_u $_u/L$	Failure Mode
R1	cyclic	0.91	0.014	0.023	bar buckling
R2	cyclic	0.85	0.024	0.029	comp. zone unstable
B1	cyclic	0.85	0.026	0.029	bar buckling
B3	cyclic	0.84	0.030	0.039	bar buckling
B4	monotonic	1.01	0.038	0.069	bar fracture
B2	cyclic	0.89	0.066	0.023	web crushing
B5	cyclic	0.80	0.087	0.028	web crushing
B5R	cyclic	0.79	0.090	0.027	web crushing
B6	cyclic	0.97	0.195	0.017	web crushing
B7	cyclic	0.86	0.103	0.029	web crushing
B8	cyclic	0.91	0.120	0.029	web crushing
B9	cyclic	0.91	0.114	0.030	web crushing
B9R	cyclic	0.91	0.097	0.038	web crushing
B10	cyclic	0.95	0.080	0.028	web crushing
F1	cyclic	0.77	0.112	0.011	web crushing
F2	cyclic	0.82	0.101	0.022	web crushing

Table 1.5: Test Unit force and displacement capacities, Oesterle et al. (1976-1979)

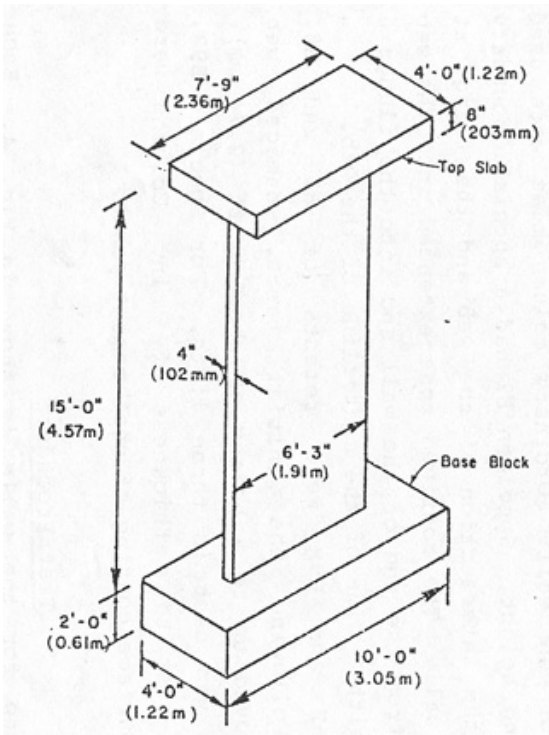

Figure 1.7: Oesterle et al. test unit overall geometry [6].

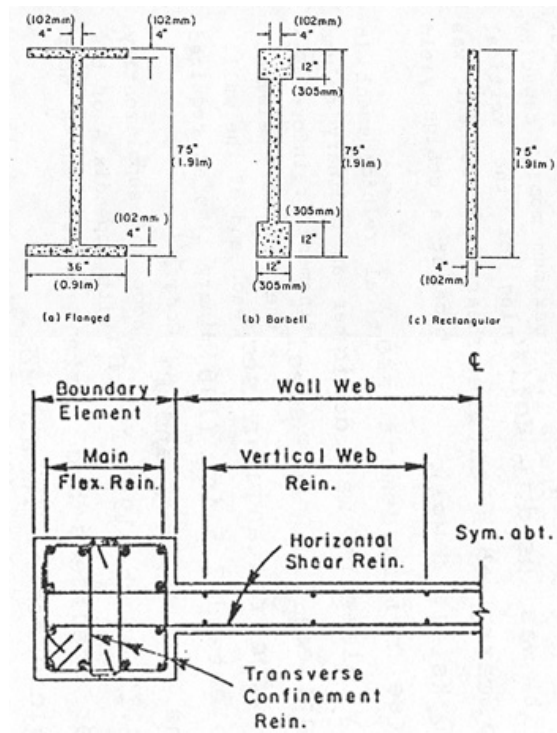

Figure 1.8: Oesterle et al. test unit section geometry and reinforcement [6].

bars.

Web crushing was influenced by the cyclic nature of the loading, the level of deformation and the level of shear stress. Increasing the axial load tended to increase the web crushing strength of the test units by reducing the width of shear cracks at similar load levels. Many of the test units under axial load developed vertical failure surfaces (see Figure 1.9) whereas the units without axial load developed more horizontal failure surfaces related to sliding.

Test Unit B6, with a concrete strength of f'_c 3165 psi [21.8 MPa], failed by web crushing at a drift ratio of δ_u 0.017 and an ultimate load of F_u 185.5 kips [825.5 kN] whereas Test Unit B7, with a concrete strength of f'_c 7155 psi [49.3 MPa], failed by web crushing at a drift ratio of δ_u 0.029 and an ultimate load of F_u 220.4 kips [980.8 kN]. This great difference between two test units with similar reinforcement demonstrated the extent to which concrete strength affected the capacity of the compression struts in the structural wall and the overall deformation capacity. Comparing Test Units B6 and B7 by the non-dimensional ratio v_u/f'_c (B6

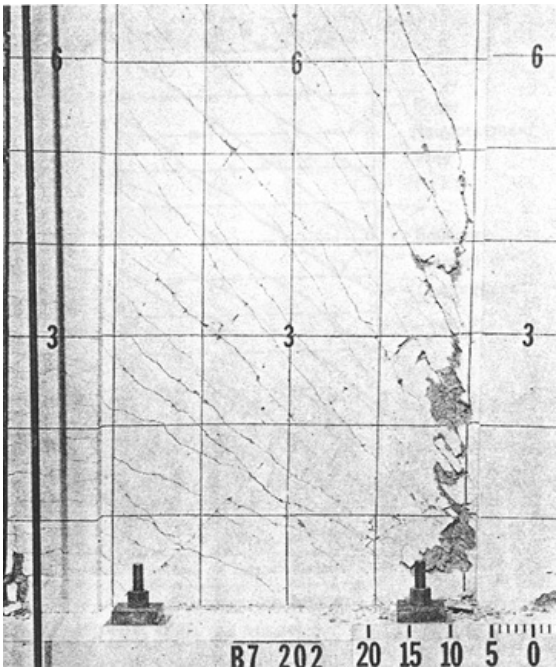

Figure 1.9: Web crushing in Test Unit B7 (μ_Δ .8) [7].

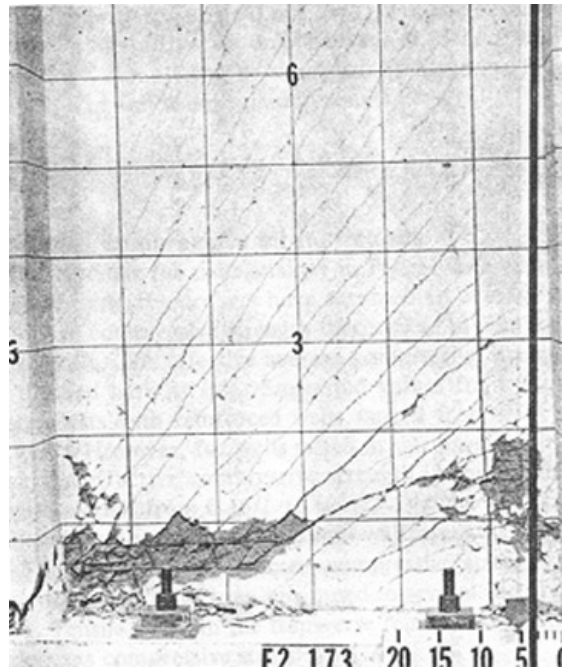

Figure 1.10: Web crushing in Test Unit F2 (μ_Δ .5) [7]. =3

0.195, B7 0.103) shows that B7 carried a lower ultimate stress, and hence its capacity did not increase in proportion to the dramatic increase in concrete strength. Whereas the ratio of concrete strengths between the two test units was $\frac{f'_{cB7}}{f'_{cB6}}$ .26, the ratio of ultimate shear demands was $\frac{V_{uB7}}{V_{uB6}}$ .19.

1.3.3 Sittipunt et al. 1993

Sittipunt et al. at the University of Illinois produced results from three dimensional non-linear finite element models that matched reasonably well results from the cyclic behavior of selected walls tested by Oesterle et al.[14]. Further parametric studies conducted with the calibrated finite element model implied that increasing the level of transverse reinforcement did not significantly affect the load-deflection behavior of such structural walls–as had been proven by Oesterle et al.'s Test B8. Added diagonal reinforcement in the plastic hinge region, however, reduced both shear deformations under cyclic loading and pinching in the hysteresis loops. These results emphasized the inability of added transverse reinforcement to control shear deformations in the plastic hinge region. There was no attempt, however, to find a lower bound on the transverse reinforcement.

1.4 Issues to be Resolved by Further Testing

The test units introduced in Section 1.3 provide a substantial database for web crushing failures in walls with varying axial load ratio and concrete strength. One test was conducted with an increased amount of transverse reinforcement. There were, however, no test results for walls with a minimal amount of transverse reinforcement. Decreasing the amount of transverse reinforcement would have required the boundary element confining steel to carry a greater portion of the shear demand. Existing test data also did not provide substantial information on the relationship between total column length and the spread of plasticity or the equivalent plastic hinge length, because the walls previously tested included little variation in aspect ratio. Existing test data provided little insight therefore into possible differences in flexural performance between tall and short bridge piers. Furthermore, existing test data did not represent a wide enough range of wall and boundary element geometries to provide insight into the nature of the relationship between the relative depth ratio D_w/D_b, and the web crushing strength.

The test units proposed for phases I and II were designed therefore to address these four issues.

1. How do aspect ratio and the level of transverse reinforcement in the wall affect the equivalent plastic hinge length L_p, and how do these parameters influence the spread of plasticity in the plastic hinge region? (see Chapters 5 and 7).

2. What effect does a minimal amount of transverse reinforcement have on wall behavior under various flexure/shear demand ratios?

3. To what degree do the boundary element spirals contribute to the total shear capacity of the bridge pier?

4. How does the web crushing strength of a wall with boundary elements change with changes in the relative depth ratio, D_w/D_b?

The test results presented in this report provide new information for estimating the equivalent plastic hinge length so that pier deflections can be predicted more accurately with section analysis techniques. The test results also provide checks for existing shear assessment and design equations applied to piers with variations in geometry and transverse reinforcement.

1.5 Report Outline

The following report details the design, construction, test setup, test observations and experimental results from the five test units introduced earlier. A description of each chapter follows.

Chapter 1: Introduction

The state of the art in design of reinforced concrete piers for long span bridges is introduced. Critical design issues are discussed. Previous research is discussed and the needs for future research are outlined.

Chapter 2: Test Unit Design and Details

Design criteria and simple hand calculations for the geometry and reinforcement of the Phase I test units are presented. Since the Phase II test units are nearly exact replicas of the Phase I units, no separate calculations are given.

Chapter 3: Construction

This chapter describes the construction process for the Phase I test units and then briefly mentions the construction of the Phase II units, which were built in a similar manner. Material properties for all of the concrete and reinforcing steel are tabulated. Measured stress strain curves are shown with theoretical curves for all reinforcing bars.

Chapter 4: Test Protocol and Instrumentation

Instrumentation and testing procedure are described. The test setup is shown in detail. Loading history and the calculation of the unitary displacement ductility are described.

Chapter 5: Test Predictions

Existing methods for predicting test unit response are described. The procedure for calculating force-deflection relationships based on moment-curvature analysis results is described. Existing models for shear capacity are discussed and prospective modifications to these models are given. Existing models for web crushing are also discussed. The shear envelopes for all available web crushing and shear capacity models are shown on the same plots as the force-deflection predictions from moment-curvature and finite element analyses.

Chapter 6: Test Observations

The tests are described in detail with reference to Appendix A.

Chapter 7: Discussion of Test Results

Test results are discussed comparatively in terms of general performance issues. Test unit hysteretic behavior is evaluated in terms of overall load-deflection response and equivalent viscous damping. Experimentally calculated curvatures, longitudinal bar strains and shear deformations are used to investigate the experimental plastic hinge length. Shear performance is discussed based on crack patterns, transverse bar strains and spiral strains.

Chapter 8: Development of a New Model for Web Crushing

A flexure-shear model for web crushing capacity is developed based on the critical compression struts inside the plastic hinge region. This model is calibrated to the test results of Oesterle et al. and is compared to existing models.

Chapter 9: Conclusions

Design and analysis issues are discussed on the basis of the test results. Design recommendations are given where possible and key issues for future research are highlighted.

Appendix A

Twelve photos from each of the five tests are presented, for a total of 60 photos. The photos correspond to standard performance levels, such as first yield, incipient spalling, and failure.

Appendix B

Data from Test Unit 1A are presented.

Appendix C

Data from Test Unit 1B are presented.

Appendix D

Data from Test Unit 2A are presented.

Appendix E

Data from Test Unit 2B are presented.

Appendix F

Data from Test Unit 2C are presented.

Chapter 2

Test Unit Designs and Details

2.1 Overview

Design criteria and hand calculations for the geometry and reinforcement of the Phase I test units are presented. Since the Phase II test unit section properties almost exactly replicate those of the Phase I units, no separate calculations are given.

2.2 Design Criteria

The test units' geometry and reinforcement were generalized from the Benicia Martinez bridge piers and did not, therefore, represent the bridge to scale. Based on the longitudinal reinforcement ratio of the proposed Benicia Martinez Bridge piers and the hybrid section geometry introduced in Chapter 1, the test units were designed in round English units to facilitate construction. They represented a 17% scale model of the hybrid geometry shown in Figure 1.3. Typically it is not advisable to test reinforced concrete structures below 1/3 scale because deformed bars smaller than No. 3 [D10] do not have reliable stress strain properties and very small aggregates are required. Due to the large scale of the prototypes in question, however, it was necessary to go to a smaller scale in order to accomodate the lab schedule and equipment capacity. This introduced conflicts in design such as the fact that at 17% scale it was not possible to use deformed bars and maintain the bar spacing to scale. Even with wider than average spacing, Test Units 1B and 2B required No. 2 [D6] transverse bars which had stress strain properties that inaccurately modeled those of the prototype transverse reinforcement (see Chapter 3). Furthermore, since the Phase I units had to be designed with an aspect ratio of M/VD 4 that would ensure their flexural behvior as slender members, the columns had to be very tall given even a 48 in. [1219 mm] section depth and a relative depth ratio of D_w/D_b . The test units were not

designed to model a particular bridge pier, but rather intended to reflect the general characteristics of the Bay Area bridge piers.

It was decided that the structural wall between the boundary elements should be at least twice the depth of a single boundary element so as to ensure its significance as a shear element. This resulted in a wall similar to the dimensions of the Benecia Martinez pier in the longitudinal direction. The relative depth ratio for all five test units was 2.00 whereas this ratio was 4.25 in Oesterle's tests and 7.40 in Wang et al.'s and Vallenas et al.'s tests. Octagonal boundary elements were set at 12 in. [305 mm] inscribed diameter and spaced 24 in. [610 mm] apart, connected by a 6 in. [152 mm] thick structural wall. The longitudinal reinforcement ratio was chosen to be ρ_l 0.014 both in the structural wall and in the boundary elements, differing from previous tests where ρ_n, the reinforcement ratio of the wall alone, was on the order of 0.004. The axial load ratio was set at $P/f'_c A_g$ .10.

Figure 2.1 shows the test unit cross section and is followed by calculations for test unit confinement and shear. Note that the transverse reinforcement was headed only on one end in order to monitor possible differences in the shear capacity between the push and pull directions due to slippage of the non-headed ends. The Phase II test units were designed with an alternative symmetric anchorage detail.

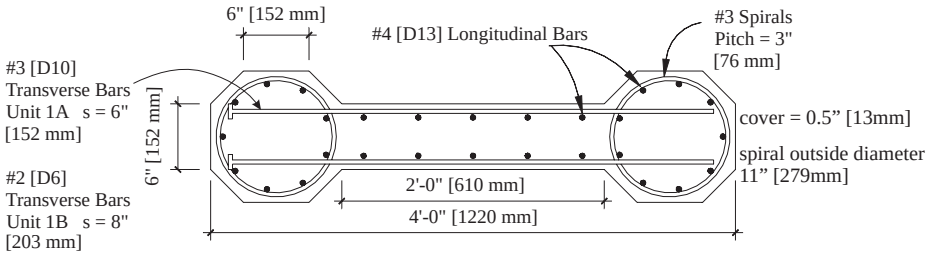

Figure 2.1: Cross section of Test Phase I Units 1A and 1B with reinforcement.

2.3 Phase I Test Units

The calculations below were used to design the Phase I test units. In their simplicity, these calculations demonstrated a first attempt to approach the design of such columns in as direct and transparent a manner as possible.

2.3.1 Confinement

1. Proposed Benicia Martinez boundary element confinement

   $\rho_s \quad \frac{4A_s}{D's}$

   No. 8 [D25] spirals spaced at 4in. [100mm]

   $\rho_s \quad \frac{4(510mm^2)}{(1638mm)(100mm)} \quad .012$ 0

2. Maximum longitudinal bar size was No. 4 [D13]. Spacing was designed to satisfy anti-buckling requirements.

   $s \leq [3 + 6(\frac{f_u}{f_y} - 1)]d_{bl}$

   $s \leq [3 + 6(0.5)]0.5in$

   $s \leq 3in.[76mm]$

   No. 3 [D10] spirals were used to ensure accurate stress strain properties. It was acceptable to increase ρ_s slightly beyond the Benicia Martinez value, however, the spacing could also be kept at a maximum in order to stay close to the desired value of ρ_s.

   The spiral pitch was set at 3in. [76mm].

   $\rho_s \quad \frac{(4)(0.11in^2)}{(10.6in)(3in)} \quad .0138$ 0

2.3.2 Load Capacity

The nominal moment capacity was estimated by assuming that the tension boundary element steel and the structural wall steel have reached yield. The section compression and tension forces were assumed to act at centroids positioned in the center of the wall and the boundary elements (see Figure 2.2).

1. Benicia Martinez longitudinal reinforcement ratios

   boundary element reinforcement ratio

   24 No. 14 [D43] bars $\Rightarrow A_s \quad 24(1451mm^2) = 34,824mm^2$

   $A_{be} \quad (1800mm)^2 - 2(500mm)^2 \quad ,740,000mm^2$

   $\rho_l \quad \frac{34,824mm^2}{2,740,000mm^2} \quad .0127$ 0

   wall reinforcement ratio

   14 No. 11 [D36] bars $\Rightarrow A_s \quad 14(1006mm^2) = 14,084mm^2$

   $A_w \quad (800mm)(1400mm) \quad 1,120,000mm^2$

   $\rho_n \quad \frac{14,084mm^2}{1,120,000mm^2} \quad .0126$ 0

2. Test unit longitudinal reinforcement

   boundary element reinforcement

   $A_{be} \quad (12in.)^2 - 2(3in.)^2 \quad 26in.^2$ =1

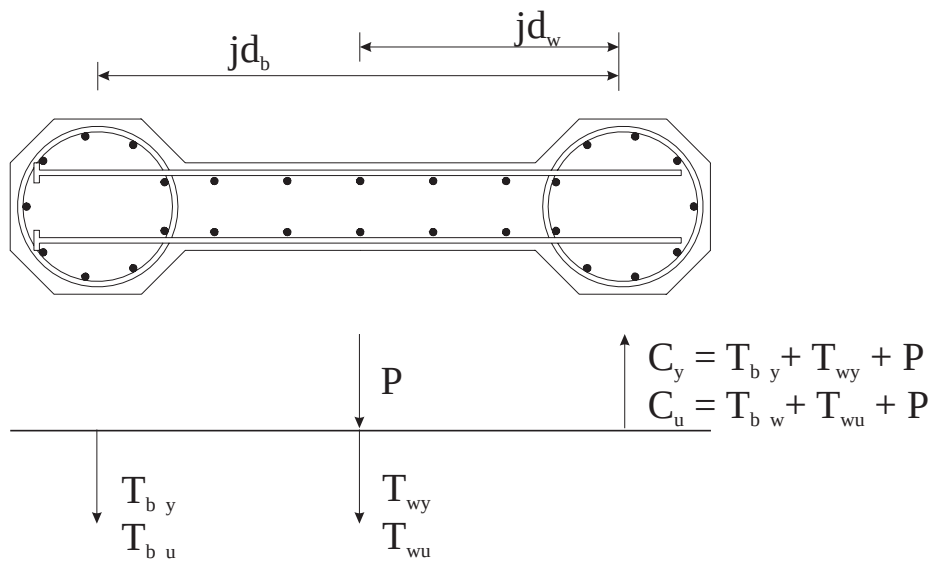

Figure 2.2: Force couples in the Phase I test units.

A_s $.0127(126in.^2)=$ $1.6in.^2$ A_s increased slightly to get ρ_l closer to $=0.0015$.

9 No. 4 [D13] bars

ρ_l $\frac{9(0.2in.^2)}{126in.^2}$ $.0143$ 0

wall reinforcement

No. 4 [D13] bars kept and ρ_n ρ_l

10 No. 4 [D13] bars

ρ_n $\frac{(10bars)(0.2in.^2)}{(24in.)(6in.)}$ $.0139$ 0

3. Boundary element tensile yield capacity

   T_{by} $0.2in.^2)(9bars)(66ksi)$ $119kips[530kN]$ =(

4. Boundary element tensile ultimate capacity

   T_{bu} $0.2in.^2)(9bars)(99ksi)=$ $178kips[793kN]$ =(

5. Structural wall tensile yield capacity

   T_{by} $0.2in.^2)(10bars)(66ksi)=$ $132kips[587kN]$ =(

6. Structural wall tensile ultimate capacity

   T_{bu} $0.2in.^2)(10bars)(99ksi)$ $198kips[881kN]$ =(

7. Axial Load

   P/f'_cA_g $.10$ $\Rightarrow P$ $0.10)(396in.^2)(5ksi)$ $198kips[881kN]$ =0 =(

8. Nominal moment and corresponding shear

$M_n \quad T_{by} j d_b + (T_{wy} + P) j d_w$

$M_n \quad 119kips)(3.0ft) + (132kips + 198kips)(1.5ft) \quad 852kft[1154kNm]$

$F_n \quad \frac{852kft}{16ft} \quad 3kips[234kN]$

9. Ultimate moment and corresponding shear

$M_u \quad T_{bu} j d_b + (T_{wu} + P) j d_w$

$M_u \quad 178kips)(3.0ft) + ((198kips) + (198kips))(1.5ft) \quad 1128kft[1528kNm]$

$F_u \quad \frac{1128kft}{16ft} \quad 1kips[316kN]$

2.3.3 Displacement Capacity

1. Nominal yield curvature

$\phi_n \quad \frac{2.5\varepsilon_y}{D}$

$\phi_n \quad \frac{2.5(0.0023)}{48in.} \quad 0.00012$ 1/in. [0.00473 1/m]

2. Nominal yield displacement

$\Delta_n \quad \frac{\phi_n L^2}{3} \quad \frac{(0.00012)(192in.)^2}{3} \quad .47in.[37.3mm]$

3. Ultimate curvature

strain limit set at

$\varepsilon_{cu} \quad .02$, or $\varepsilon_{su} \quad .06$

c 9in. [229mm] (from section analysis)

$\phi_u \quad min \left\{ \begin{array}{c} \frac{\varepsilon_{cu}}{c} \\ \frac{\varepsilon_{su}}{D-c} \end{array} \right\}$

$\phi_u \quad \frac{0.06}{39in.} \quad .00154$ 1/in. [0.0607 1/m]

4. Ultimate displacement

$L_p \quad .08L + 0.15 f_y d_b$

$L_p \quad .08(192in.) + 0.15(66ksi)(0.5in.) = 20.3in.[515.6mm]$

$\Delta_u \quad n\frac{M_u}{M_n} + (\phi_u - \phi_n \frac{M_u}{M_n}) L_p L$

$\Delta_u \quad .47in. \frac{1128kft}{852kft} + (0.00154 - 0.00012 \frac{1128kft}{852kft})(20.3in.)(192in.) \quad 7.33in.[186.2mm]$

2.3.4 Shear

No. 3 [D10] bars were the smallest available with headed reinforcement and were chosen as the transverse bars for the test units in order to reflect the choice of headed transverse bars in the Benicia Martinez proposal.

1. Assumed (conservatively) that the transverse steel was activated only inside the structural wall.

   Transverse Steel $\Rightarrow$ 2 No. 3 [D10] bars spaced at 6 in. [152 mm]

   $V_c \quad \left(1 + \frac{P}{2000(A_g)}\right) \sqrt{f'_c} A_e$ where $A_e \quad .8Dt_w \quad =2$

   $V_c \quad \left(1 + \frac{198{,}000lbs}{2000(396in.^2)}\right) \frac{\sqrt{5000psi}}{1000} 230in.^2 \quad 1kips[182kN] \quad =2$

   $V_s \quad \frac{A_{str} f_{ytr} D_w}{s_{tr}}$

   $V_s \quad \frac{(0.22in^2)(60ksi)(24in.)}{(6in.)} \quad 3kips[236kN]$ 5

   $V \quad \phi(V_c + V_s) \quad 0.85(41kips + 53kips) = \ 80kips \geq F_u \quad 1kips[316kN]$

2. Checked that the transverse steel did not exceed the limit ratio specified in the Caltrans BDS [2].

   $V_s \quad \frac{(0.22in.^2)(24in.)(66ksi)}{(6in.)} \quad 8kips[258kN]$ 5

   $8\sqrt{f'_c} b_w D \quad \sqrt{5000psi}(6in.)(24in.)/1000lbs \quad 1kips[360kN] \quad =8$

   $81kips[360kN] \geq 58kips[258kN]$ BDS Satisfied.

2.3.5 Other Design Considerations

1. Designed the structural wall steel in Test Unit 1B to control shrinkage.

   Transverse Steel $\Rightarrow$ 2 No. 2 [D6] bars spaced at 8in.

   $V_s \quad \frac{(0.10in.^2)(60ksi)(24in.)}{(8in.)} \quad 8kips[80kN]$ 1

   $V \quad \phi(V_c + V_s) \quad 0.85(41kips + 18kips) = \ 50kips \leq F_u \quad 1kips[316kN]$

Figure 2.3 shows elevations of Test Units 1A (a) and 1B (b), making clear the difference in transverse reinforcement size and spacing.

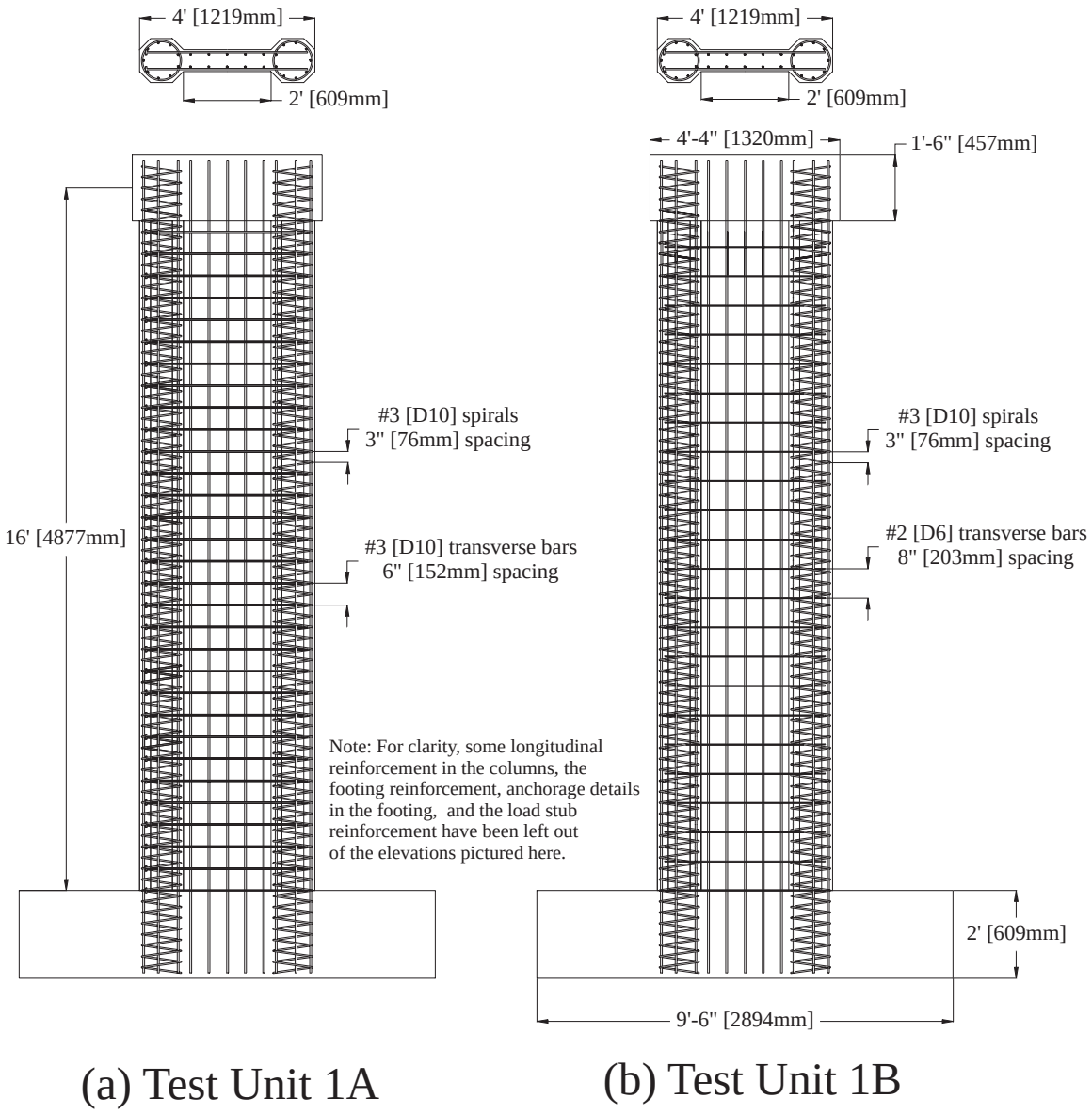

(a) Test Unit 1A (b) Test Unit 1B

Figure 2.3: Test Units 1A (a) and 1B (b) with column reinforcement.

Figure 2.4 shows the theoretical force deflection curve derived from a moment curvature analysis on the section along with the bilinear curve calculated earlier by hand. The shear capacity assessment envelopes according to the UCSD shear model are also give in this figure.

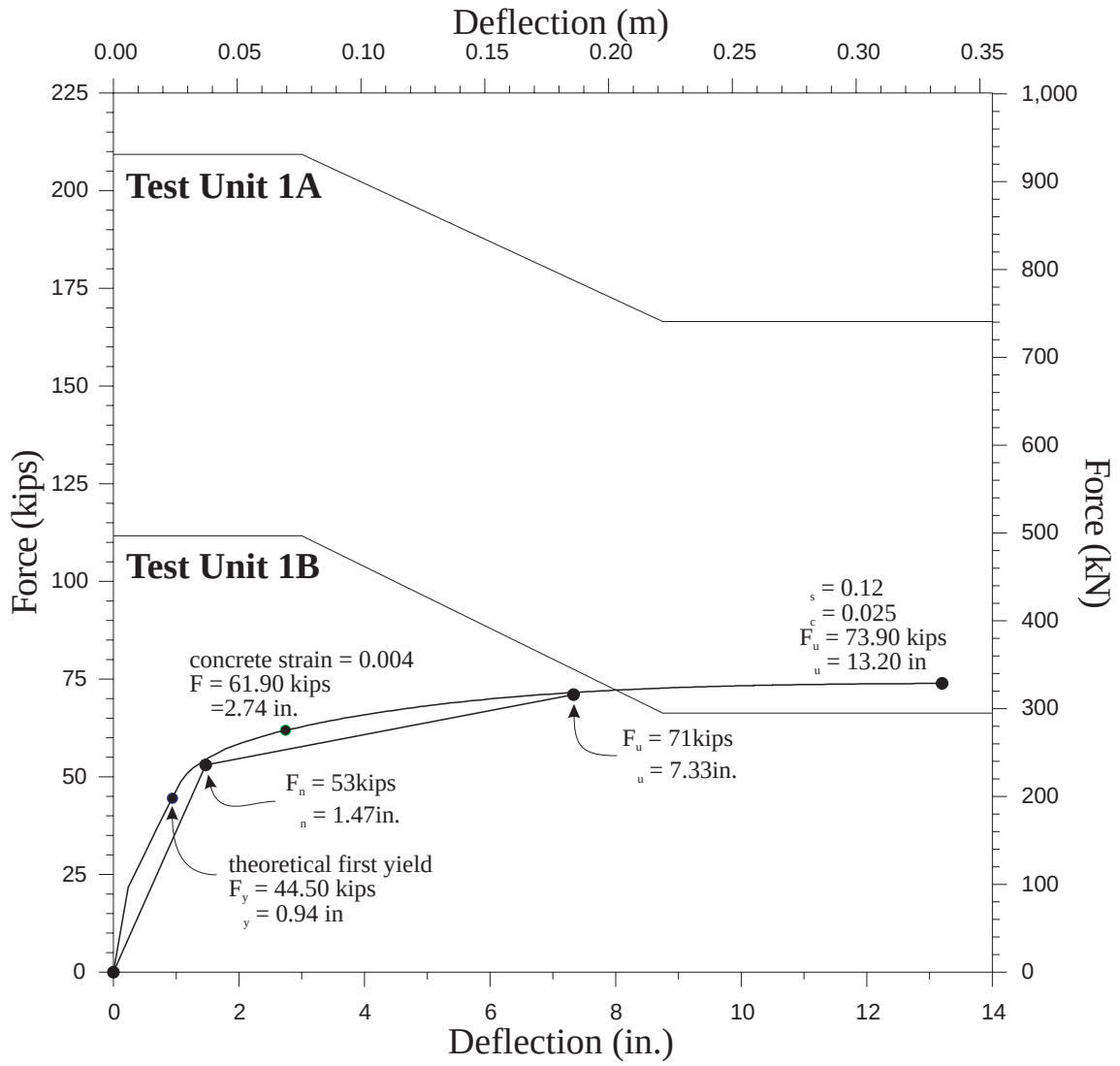

Figure 2.4: Theoretical force-deflection curves with shear capacity envelopes for Test Units 1A and 1B.

2.4 Phase II Test Units

The Phase II Test Units A and B were designed with the same reinforcement as the Phase I Test Units A and B but had an aspect ratio of M/VD 2 instead of M/VD 4. Furthermore, the transverse reinforcement in the Phase II units had a different anchorage detail, with 180° hooks at one end of each bar as pictured in Figures 2.5 and 2.6. The hooked ends were then arranged in an alternating pattern up the column height. In Test Unit 2C, the wall thickness was reduced from 6 in. [152 mm] to 4 in. [102 mm]. The Phase II test units are shown with column reinforcement in Figure 2.7.

Figure 2.8 shows the theoretical force deflection curves with the relevant shear capacity assessment and design curves for the Phase II test units [10]. Chapter 5 presents the calculations for these curves in detail.

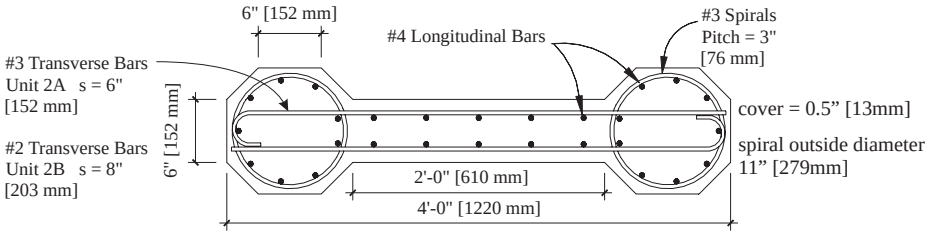

Figure 2.5: Cross section of Test Phase II Units 2A and 2B with reinforcement.

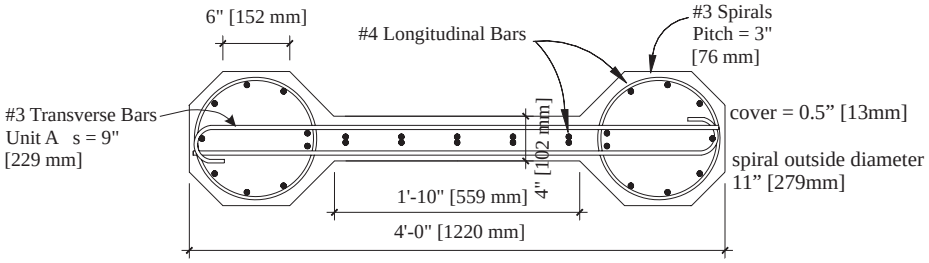

Figure 2.6: Cross section of Test Phase II Unit 2C with reinforcement.

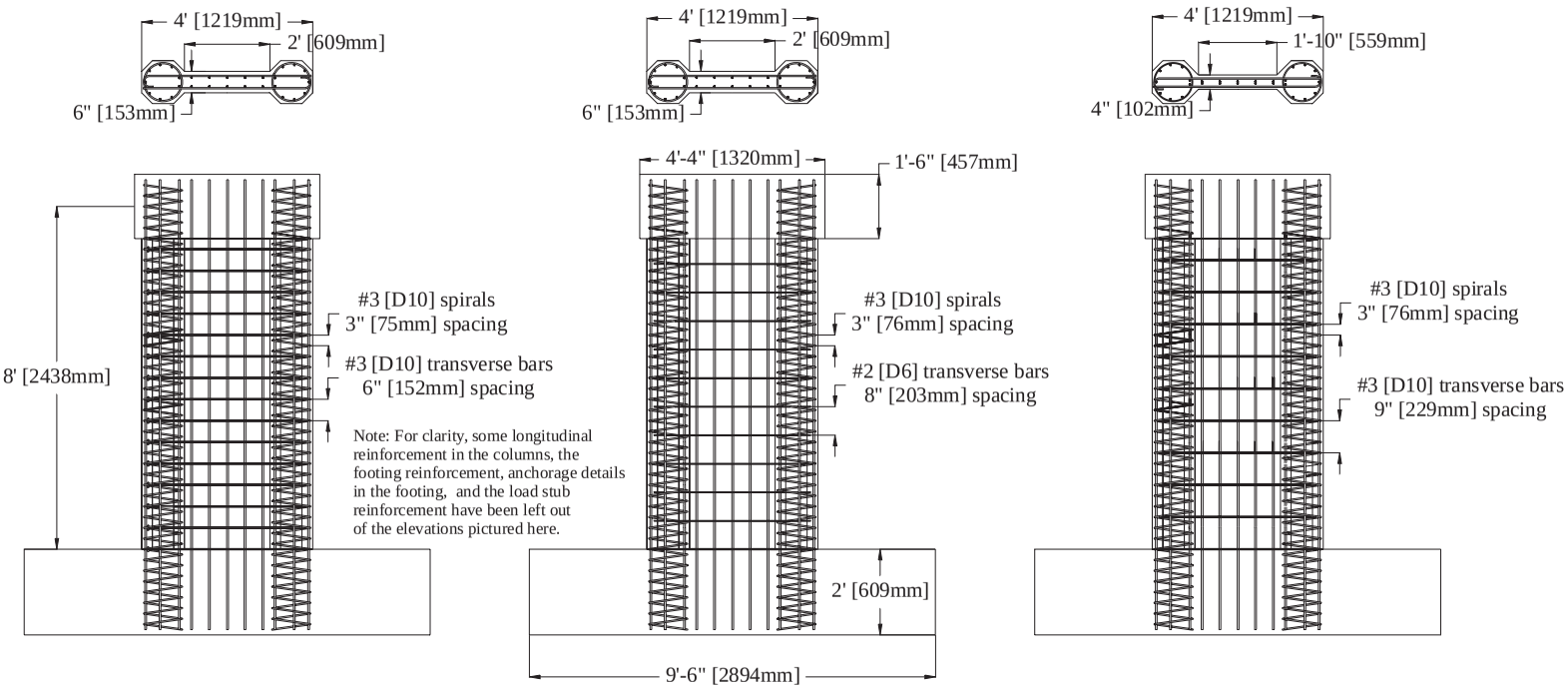

(a) Test Unit 2A (b) Test Unit 2B (c) Test Unit 2C

Figure 2.7: Phase II sections and elevations with column reinforcement. (a) Test Unit 2A, (b) Test Unit 2B, (c) Test Unit 2C.

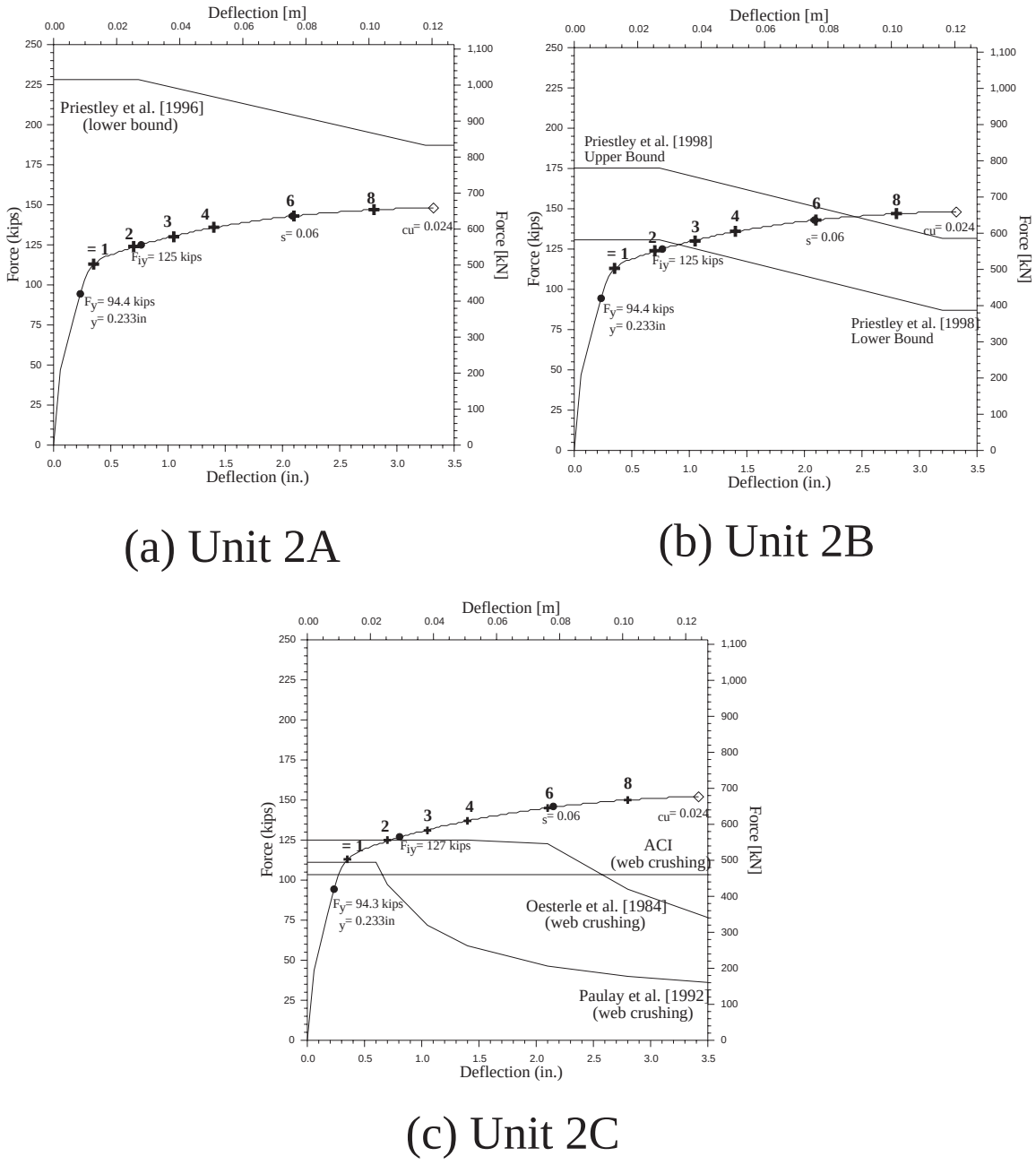

(a) Unit 2A

(b) Unit 2B

(c) Unit 2C

Figure 2.8: Force-Deflection characterizations with shear capacity envelopes for (a)Unit 2A, (b) Unit 2B, (c) Unit 2C.

Chapter 3

Construction and Material Properties

3.1 Overview

The test units were constructed in the Charles Lee Powell Laboratories at the University of California San Diego. The following chapter describes the construction process for the Phase I test units and then briefly mentions the construction of the Phase II units, which were built in a similar manner.

Material properties for all of the concrete and reinforcing steel are tabulated. Measured stress strain curves are shown with theoretical curves for all reinforcing bars.

3.2 Construction of the Phase I Test Units

The Phase I test units were cast in three lifts, consisting of the footing, the column and the load stub. Figure 3.1 shows the longitudinal footing steel laid out on a lab yard casting bed. The boundary elements had been tied previously as individual circular columns and were lifted into place via forklift (see Figures 3.2 and 3.3). Once the boundary elements had been placed in the footing and secured to an external bracing system, the rest of the footing was tied, including the top mat of transverse steel and the seismic hooks (see Figures 3.4 and 3.5). The footings were cast with vertical, longitudinal and transverse ∅ 2 in. [51 mm] PVC pipe ducts (see Figure 3.6). The vertical ducts provided space for the tiedowns and axial load rods. The longitudinal ducts were used to post tension the footing with two ∅ 1 3/8 in. [35 mm] DYWIDAG bars at 150 kips [667.5 kN] each for increased shear capacity. The transverse ducts provided space for inserting DYWIDAG bars to serve as pickpoints

for lifting the test units (see Figure 3.7).

Once inside the laboratory, the transverse steel was tied completely for each of the columns. Before assembling the column forms, mechanical couplers were inserted at points where curvature rods were to be attached to the column. Figure 3.8 shows a detail of these couplers which were mounted on the either end of thread rod and secured to the boundary element steel. After the columns were cast, the cover concrete was chipped away at each coupler location and the foam heads were extracted, leaving the coupler open for connection with an externally mounted curvature rod. This detail was abandoned for the Phase II test units in favor of drilling through the forms and mounting only a single curvature rod in the middle of each boundary element. Figures 3.9 and 3.10 show the column reinforcement just before the column formwork was fully assembled. These two Figures show clearly the difference in transverse reinforcement between Test Unit 1A and Test Unit 1B.

The 184.5 in. [4686 mm] high columns were cast in a single lift by placing the concrete with a boom pump (see Figure 3.11). The load stub was cast (see Figure 3.12) in one lift with 2 in. [51 mm] longitudinal PVC pipe ducts for attaching the actuator and 3/4 in. [19 mm] lateral ducts for attaching the channel used for the lateral restraint system.

Figure 3.13 shows Test Units 1A and 1B as the column formwork was being removed. Figure 3.14 shows Test Unit 1A partially instrumented and in place.

3.3 Construction of the Phase II Test Units

The Phase II Test Units were constructed in a manner similar to the Phase I units. Since these units were simply half the height of the Phase I units, they were much easier to construct and their construction is not documented in detail. The boundary elements were lifted into place by hand prior to casting the load stub. Figure 3.15 shows Units 2A and 2B with footings cast on the casting beds. Figure 3.16 shows the anchorage detail of the transverse reinforcement in the boundary element. This detail can also be seen as a drawing in Figure 2.5. The columns were cast outdoors and columns and load stubs were cast together in a single lift. The casting of the 2C column proceeded without problems even though the wall thickness had been reduced to 4 in. [102 mm]. The Phase II columns were then left to cure outside.

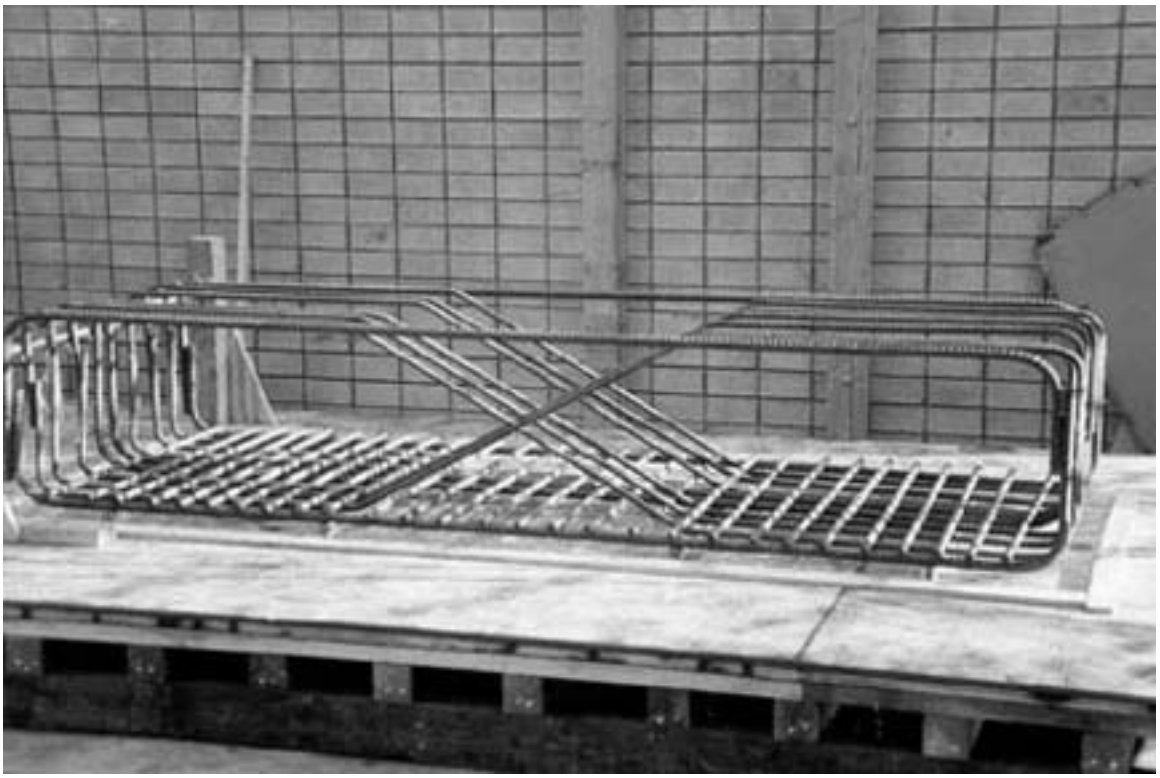

Figure 3.1: Footing longitudinal bars: No. 8 [D25] U-bars and No. 6 [D19] Z-bars.

Figure 3.2: Boundary element cages are tied separately.

Figure 3.3: Boundary element cages are lifted into place via forklift.

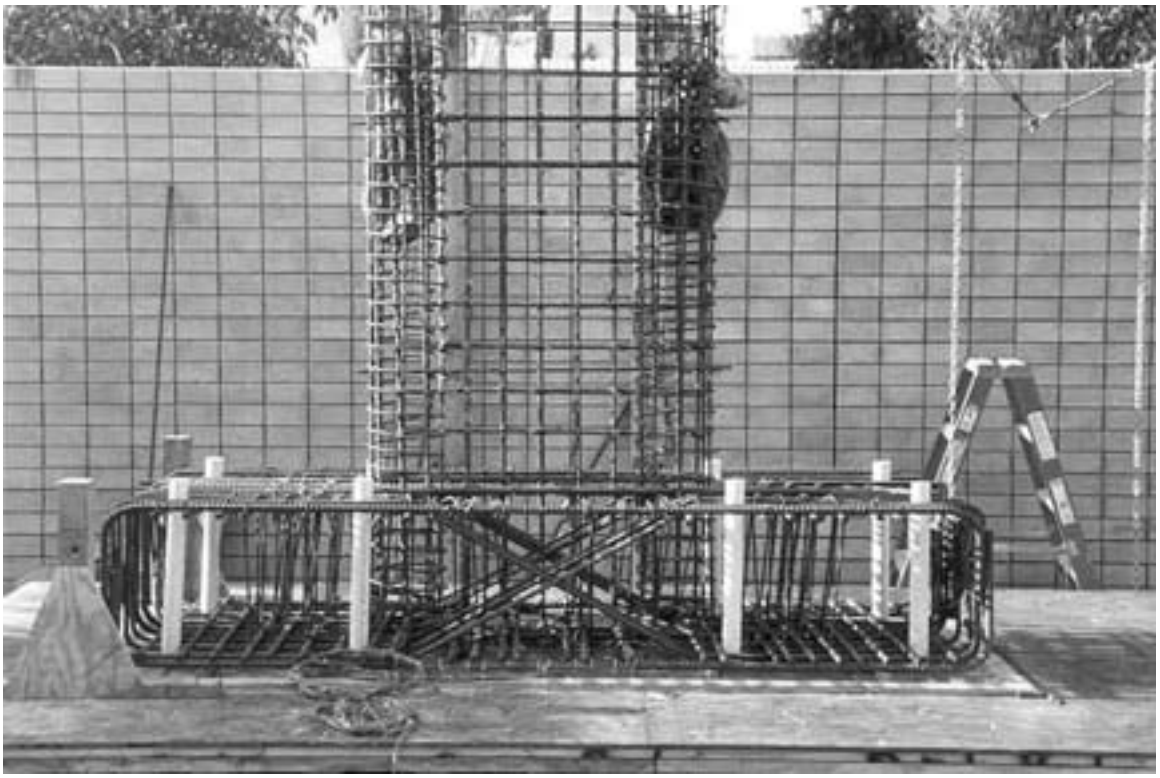

Figure 3.4: Test Unit 1A: footing and column cage.

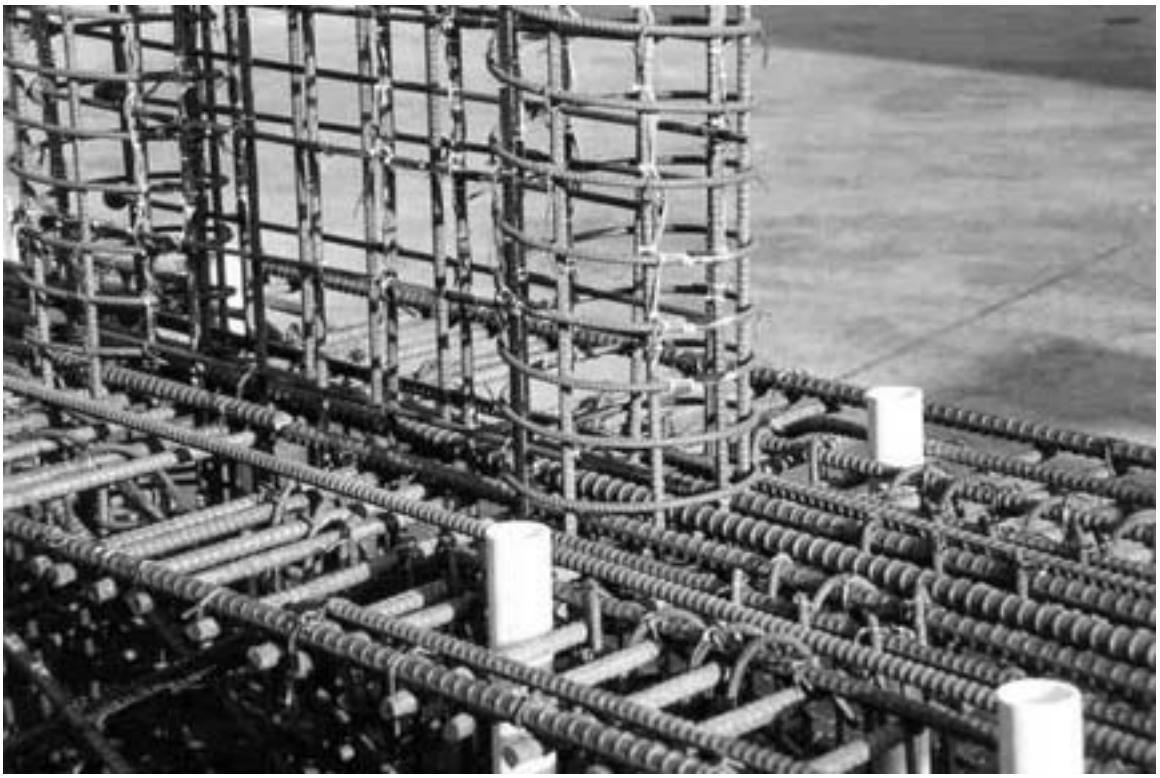

Figure 3.5: Test Unit 1A: detail of footing and column reinforcement.

Figure 3.6: Test Units 1A and 1B in lab yard with footings cast.

Figure 3.7: Moving Test Unit 1A into the laboratory before casting the column and load stub.

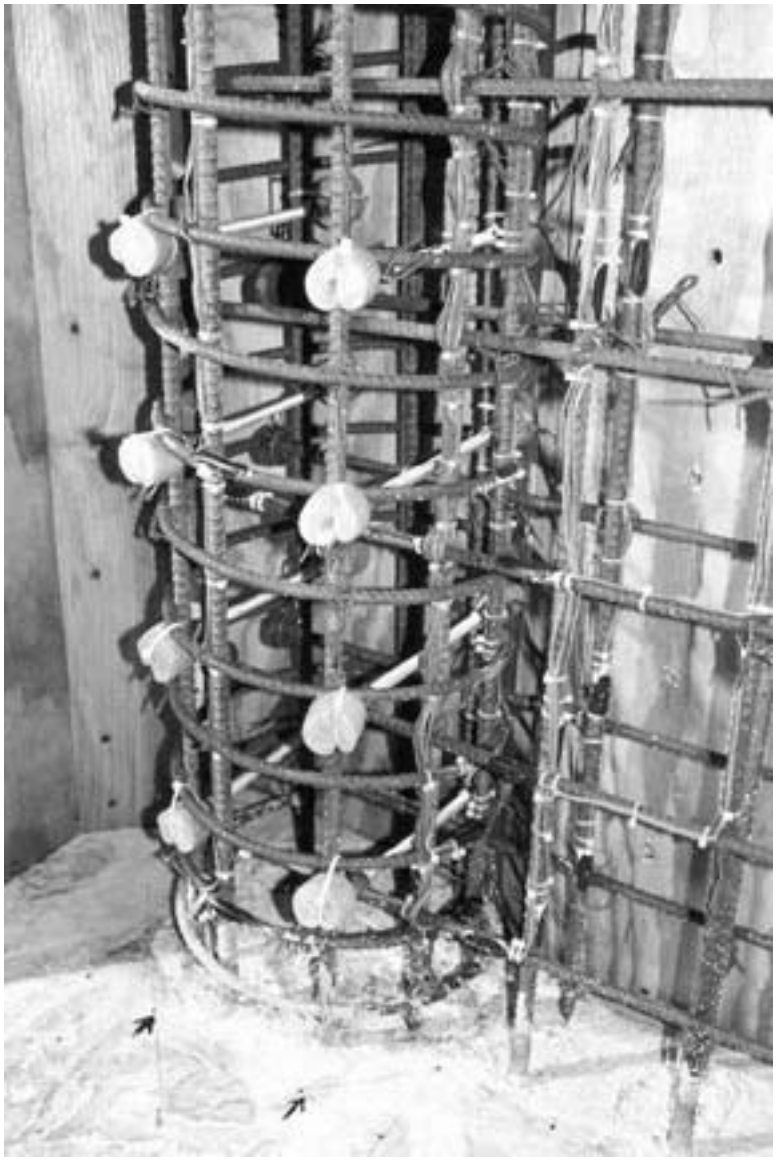

Figure 3.8: Test Unit 1A: detail of boundary element curvature rod attachments.

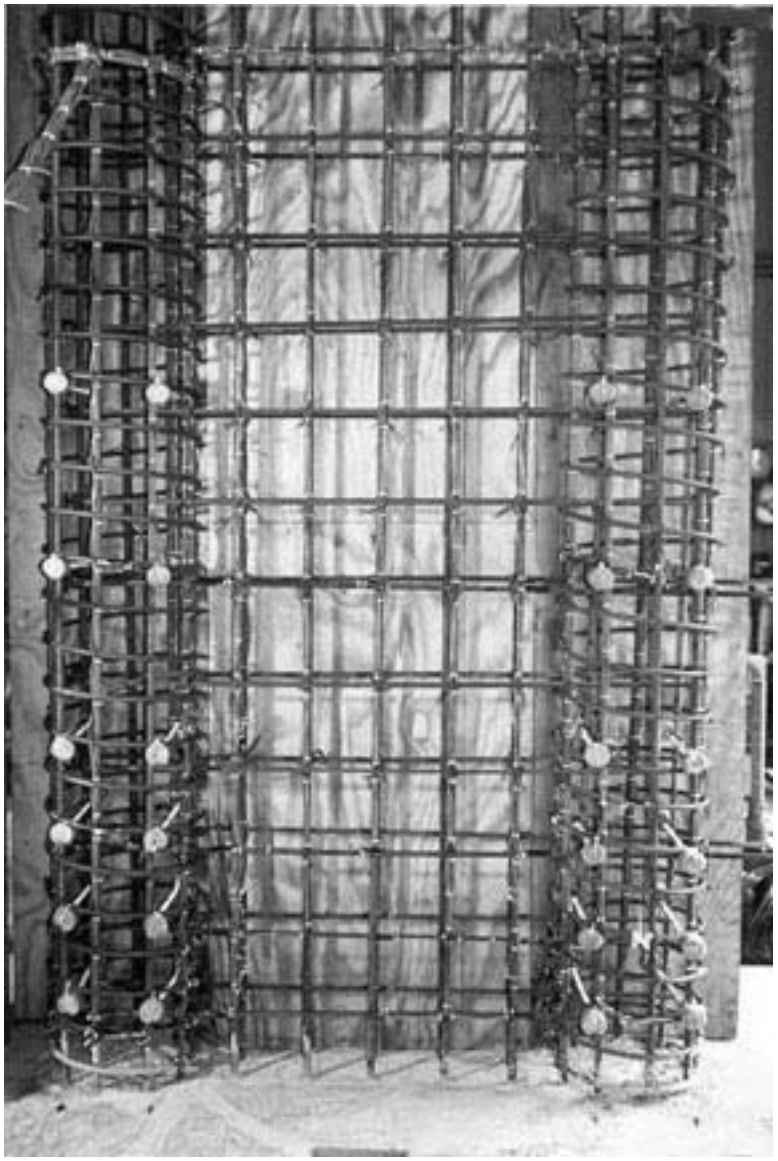

Figure 3.9: Test Unit 1A: Reinforcement detail. Transvserse bars are spaced vertically at s = 6 in. [152 mm].

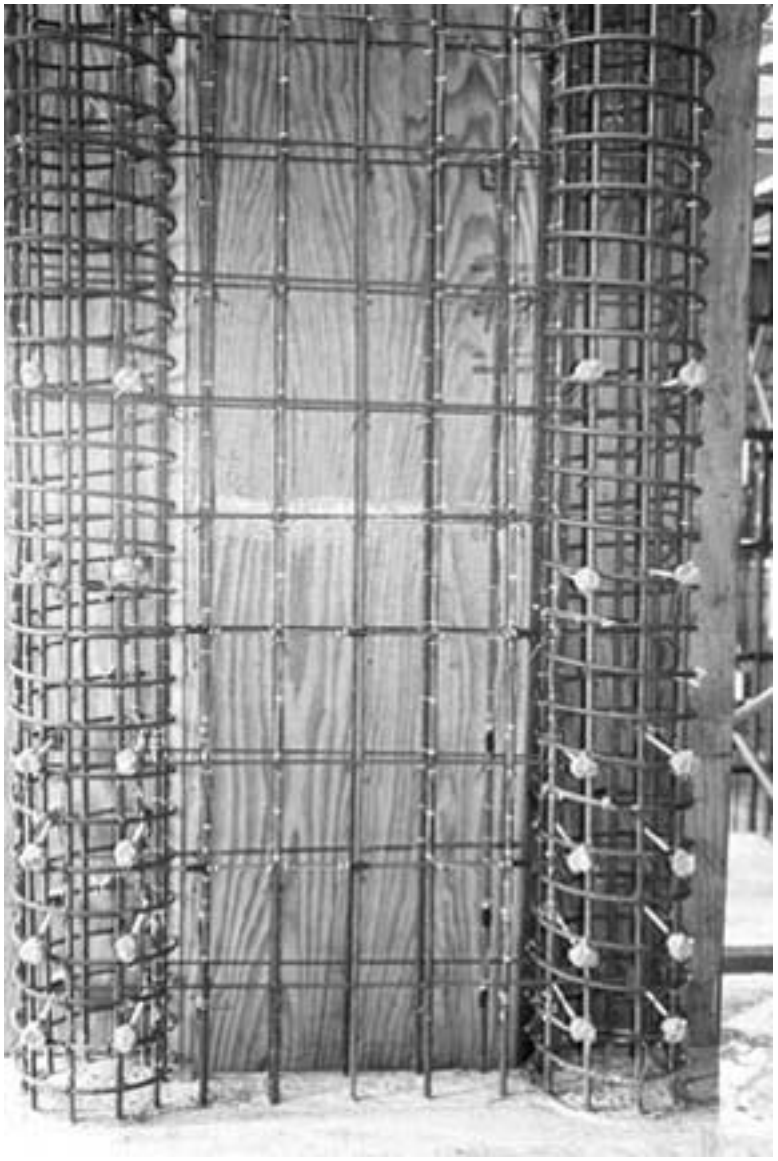

Figure 3.10: Test Unit 1B: Reinforcement detail. Transvserse bars are spaced vertically at s = 8 in. [203 mm].

Figure 3.11: Test Units 1A and 1B: casting the columns.

Figure 3.12: Test Units 1A and 1B: casting the load stubs.

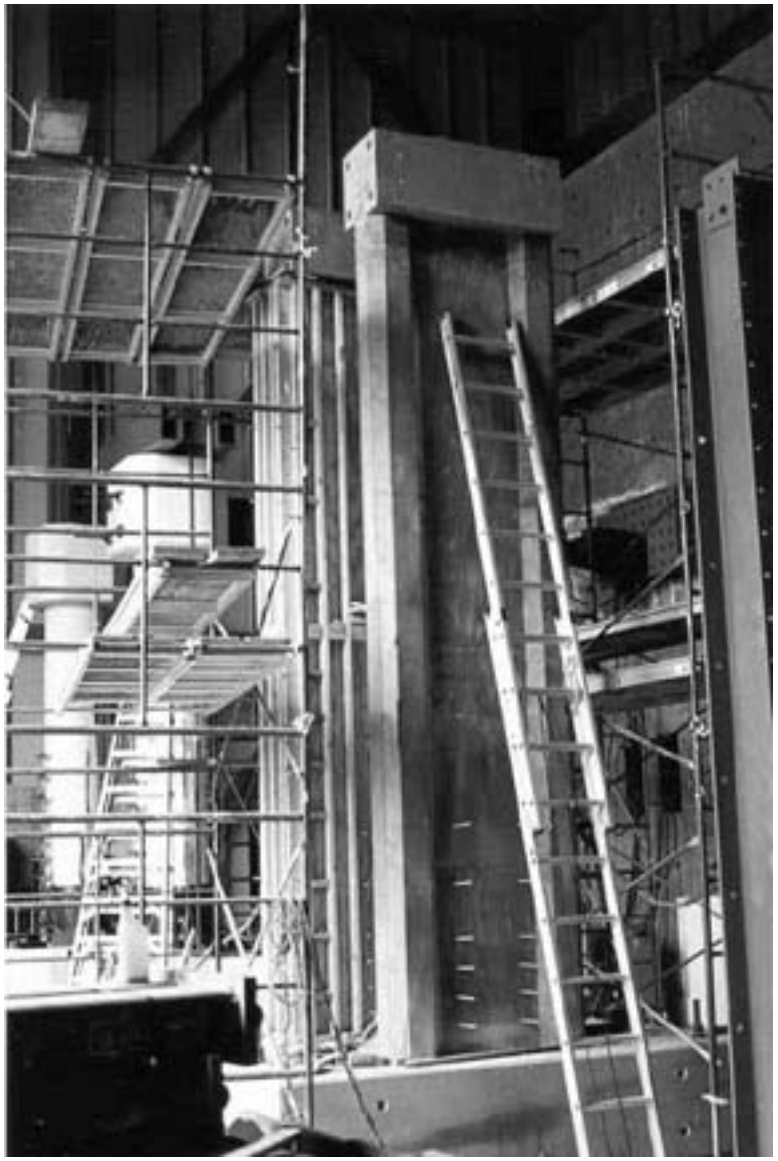

Figure 3.13: Test Units 1A and 1B: removing column and load stub formwork.

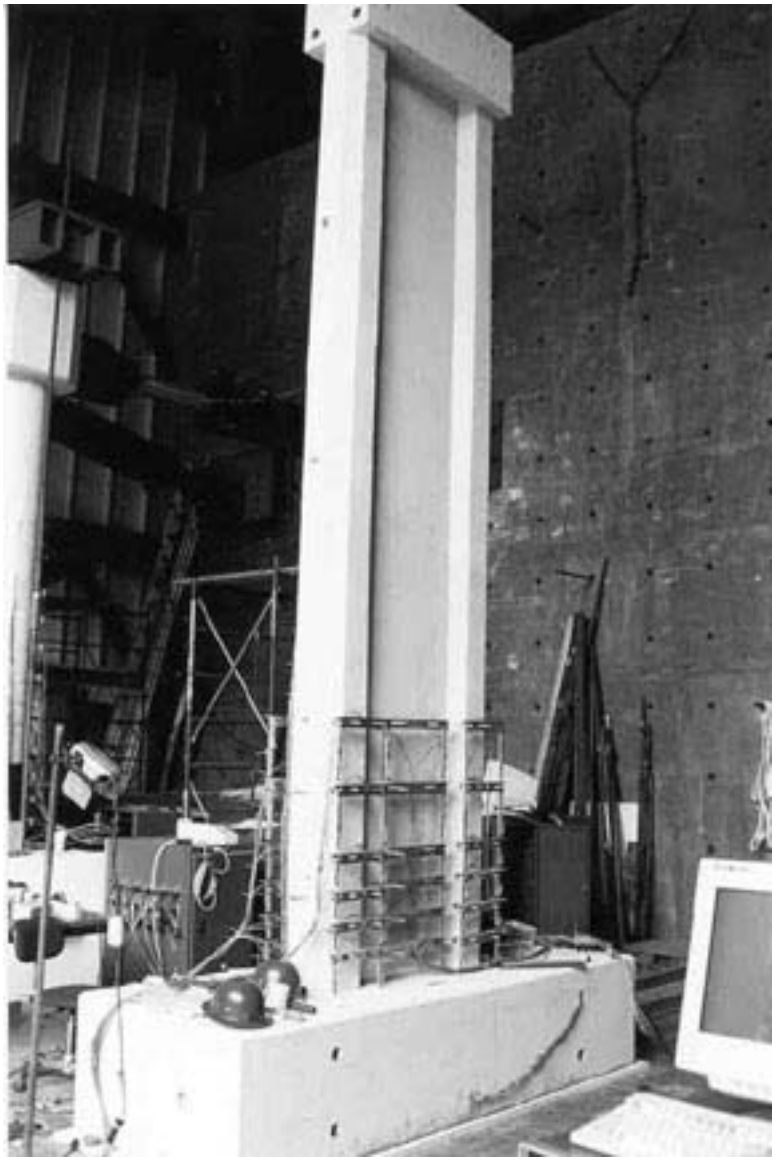

Figure 3.14: Test Unit 1A: partial instrumentation and setup.

Figure 3.15: Test Units 2A & 2B on the casting beds, with footings cast.

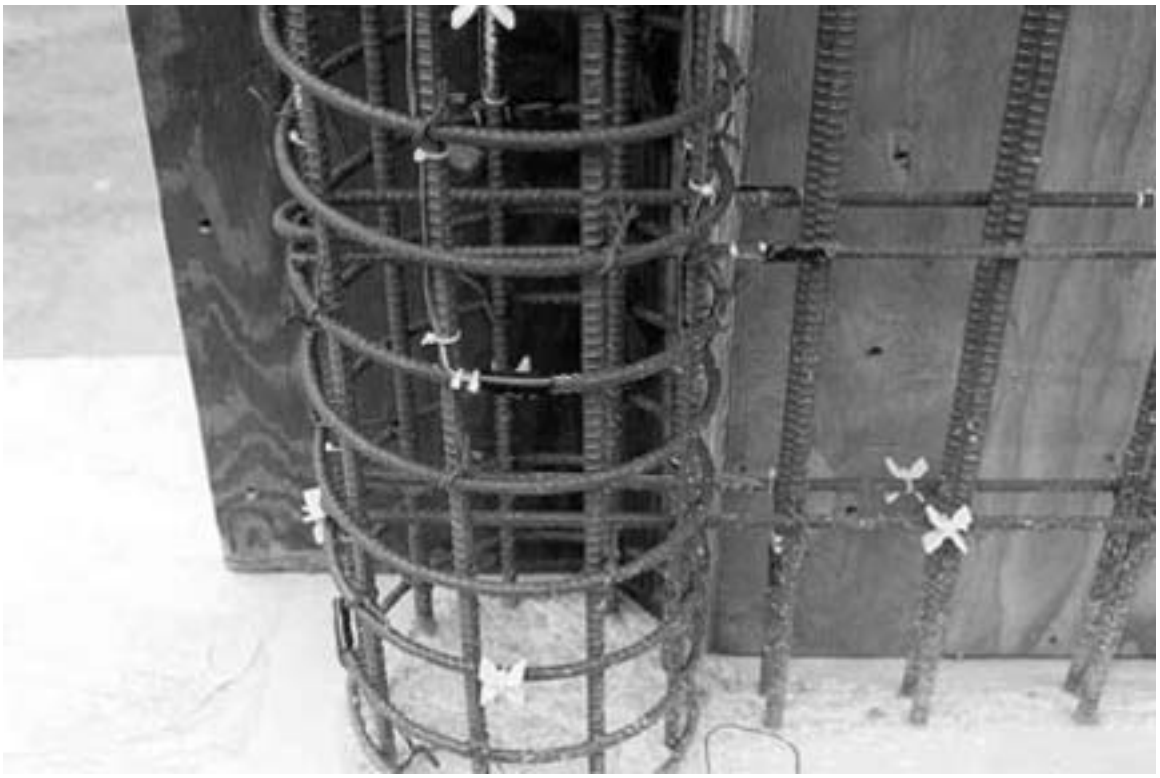

Figure 3.16: Phase II test unit reinforcement detail.

3.4 Material Properties

The following section presents the material properties for concrete and steel used for the Phase I and Phase II test units. Design concrete strength for all five test units was f'_c 5 ksi [35 MPa]. Day of test column concrete strengths ranged from 4.509 ksi [31.1 MPa] (Unit 2C) to 6.210 ksi [42.8 MPa] (Unit 1B).

The day of test concrete strengths are used in Chapter 5 for evaluating the shear strength of the test units. In Chapter 5, section analysis concrete properties are based on Mander's model for confined and unconfined concrete [5].

Steel is modeled in Chapter 5 analytically by assuming that E 29,000 ksi [200 GPa] up to the yield stress. The plastic region is assumed to have zero stress up to ε_{sh}, the strain at which hardening is assumed to begin. The strain hardening region is then assumed to follow a power curve based on the modulus at first hardening that is calibrated to best fit the data and is given by the equation

$$f_{sh} \quad f_u - (f_u - f_y)\left(\frac{\varepsilon_{su} - \varepsilon_s}{\varepsilon_{su} - \varepsilon_{sh}}\right)^P \tag{3.1}$$

where f_{sh} is the stress in the strain hardening region, f_u is the ultimate stress of the steel, f_y is the steel yield stress, ε_{su} is the ultimate steel strain, ε_s is the strain in the hardening region, and P is calculated as

$$P \quad E_{sh}\frac{\varepsilon_{su} - \varepsilon_{sh}}{f_u - f_y} \tag{3.2}$$

where E_{sh} is the elastic modulus of the steel at first strain hardening.

All of the steel specified was grade A-706, however grade A-706 was available only for bars of size No. 4 [D13] and larger, meaning that only the longitudinal steel was of this grade. As Figures 3.17 - 3.25 show, the perfectly plastic region for this steel is assumed very small and the yield stress is assumed somewhat arbitrarily to aid in matching the strain hardening portion of the curve. The No. 2 [M6] deformed transverse bars for Test Units 1B and 2B came from existing stock in the Charles Lee Powell Laboratories and exhibited comparatively lower yield and ultimate stress thresholds (see Table 3.5).

Item	Weight per Cubic Yard		Yield	
	lb	kg	yd^3	m^3
Cement	726.0	330.0	0.137	0.104
Fly Ash	144.0	65.5	0.039	0.030
Washed Concrete Sand – 42.01%	1122.0	510.0	0.249	0.190
Mission Valley 1/2" – 44.01%	1149.0	522.3	0.261	0.199
Mission Valley 3/8" – 13.98%	363.0	165.0	0.083	0.063
Water	354.9	161.3	0.211	0.161
DARATARD 12	30.0	13.6	–	–
DAREX II	1.5	0.7	–	–
Air %	2.0	–	0.02	0.015
Water/(Cement + Fly Ash) Ratio	0.41			
Slump, inches 1A & 1B Footing 1A & 1B Column 2A & 2B Footing 2C Footing	 4 1/4 [108 mm] 3 1/2 [89 mm] – –			
Concrete unit weight, pcf	144.2 [2315 kg/m^3]			

Table 3.1: Concrete mix design for Phase I & II units 1/2" aggregate.

Item	Weight per Cubic Yard		Yield	
	lb	kg	yd^3	m^3
Cement	672.0	305.5	0.127	0.097
Fly Ash	118.0	53.6	0.034	0.026
Washed Concrete Sand – 49.9%	1363.0	619.5	0.304	0.232
Mission Valley 3/8" – 50.1%	1330.0	604.5	0.303	0.231
Water	358.2	162.8	0.213	0.163
WRDA-64	23.2	10.5	–	–
DARAVAIR 1000	1.5	0.7	–	–
DARACEM 19	77.0	35	–	–
Air %	2.0	–	0.02	0.015
Water/(Cement + Fly Ash) Ratio	0.45			
Slump, inches 1A & 1B Loadstub 2A & 2B Column 2C Column	 2 [50.8mm] – 4 1/4" [108mm]			
Concrete unit weight, pcf	146 [2344 kg/m^3]			

Table 3.2: Concrete mix design for Phase I & II units 3/8" aggregate.

Unit	Design Strength	7 Day	28 Day	D.O.T.	Age (days)
1A	5000 [34.5]	4550 [31.4]	5490 [37.9]	5530 [38.1]	27
1B	5000 [34.5]	4550 [31.4]	5490 [37.9]	6210 [42.8]	53
2A	5000 [34.5]	3910 [27.0]	5310 [36.6]	5310 [36.6]	29
2B	5000 [34.5]	3910 [27.0]	5310 [36.6]	6017 [41.5]	40
2C	5000 [34.5]	3480 [24.0]	4509 [31.1]	4509 [31.1]	28

Table 3.3: Test unit concrete compressive strengths psi [MPa].

Footing	Design Strength	7 Day	28 Day	D.O.T.	Age (days)
1A	5000 [34.5]	4400 [30.3]	5619 [38.7]	5820 [40.1]	43
1B	5000 [34.5]	4400 [30.3]	5619 [38.7]	6480 [44.7]	70
2A	5000 [34.5]	–	5210 [35.9]	5440 [37.5]	49
2B	5000 [34.5]	–	5210 [35.9]	5520 [38.1]	65
2C	5000 [34.5]	4430 [30.5]	5240 [36.1]	5593 [38.6]	58

Table 3.4: Test unit footing concrete compressive strengths psi [MPa]

Unit	Bar	f_y ksi [MPa]	f_u ksi [MPa]	ε_y	ε_{sh}	ε_{su}	E_s ksi	E_{sh} ksi [MPa]
1A	#4 long.	67.0 [462.0]	100.0 [689.5]	0.0023	0.005	0.118	29,000	1150 [7929]
	#3 spiral	67.0 [462.0]	107.0 [737.8]	0.0023	0.006	0.101	29,000	1600 [11032]
	#3 trans.	67.0 [462.0]	107.5 [741.2]	0.0023	0.003	0.115	29,000	1500 [10343]
1B	#4 long.	67.0 [462.0]	100.0 [689.5]	0.0023	0.005	0.118	29,000	1150 [7929]
	#3 spiral	67.0 [462.0]	107.0 [737.8]	0.0023	0.006	0.101	29,000	1600 [11032]
	#2 trans.	59.0 [406.8]	77.0 [530.9]	0.0020	0.004	0.101	29,000	650 [4482]
2A	#4 long.	66.0 [455.0]	96.0 [662.0]	0.0023	0.010	0.100	29,000	850 [5861]
	#3 spiral	73.0 [503.3]	108.0 [744.7]	0.0025	0.003	0.110	29,000	1400 [9653]
	#3 trans.	70.0 [482.7]	105.0 [724.0]	0.0024	0.003	0.100	29,000	1350 [9308]
2B	#4 long.	66.0 [455.0]	96.0 [662.0]	0.0023	0.010	0.100	29,000	850 [5861]
	#3 spiral	73.0 [503.3]	108.0 [744.7]	0.0025	0.003	0.110	29,000	1400 [9653]
	#2 trans.	59.0 [406.8]	77.0 [530.9]	0.0020	0.004	0.101	29,000	650 [4482]
2C	#4 long.	72.0 [496.4]	105.0 [724.0]	0.0025	0.008	0.100	29,000	1100 [7585]
	#3 spiral	72.0 [496.4]	102.0 [703.3]	0.0025	0.005	0.100	29,000	1100 [7585]
	#3 trans.	70.0 [482.7]	105.0 [724.0]	0.0024	0.003	0.100	29,000	1350 [9308]

Table 3.5: Test unit steel reinforcement properties

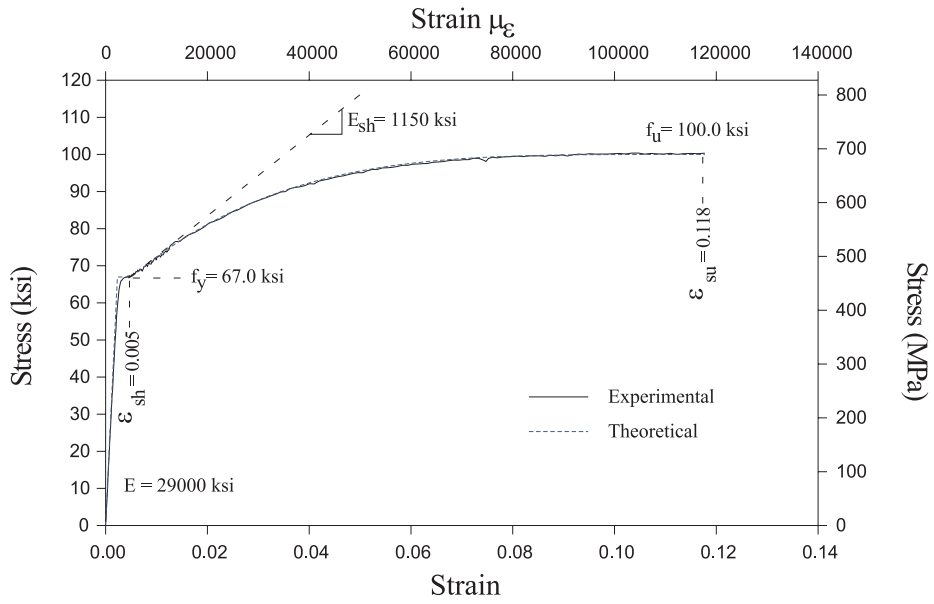

Figure 3.17: Stress strain curves for Units 1A and 1B #4 [D13] longitudinal bars.

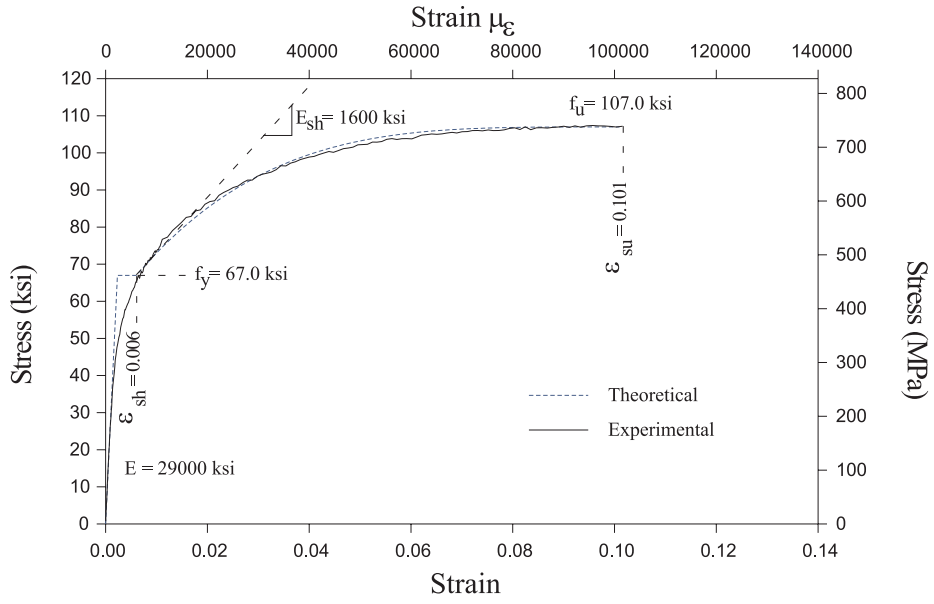

Figure 3.18: Stress strain curves for Units 1A and 1B #3 [D10] spirals.

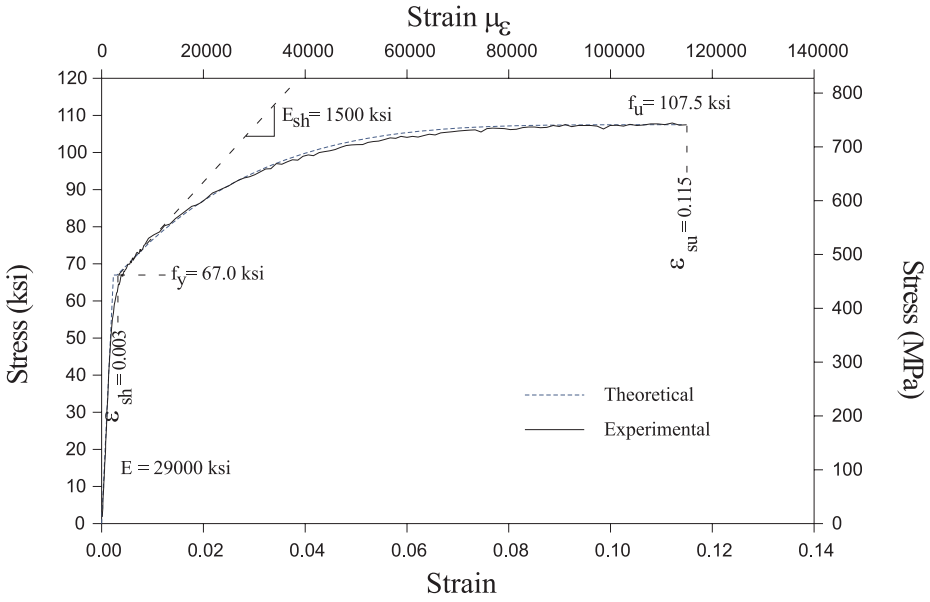

Figure 3.19: Stress strain curve for Unit 1A #3 [D10] transverse bars.

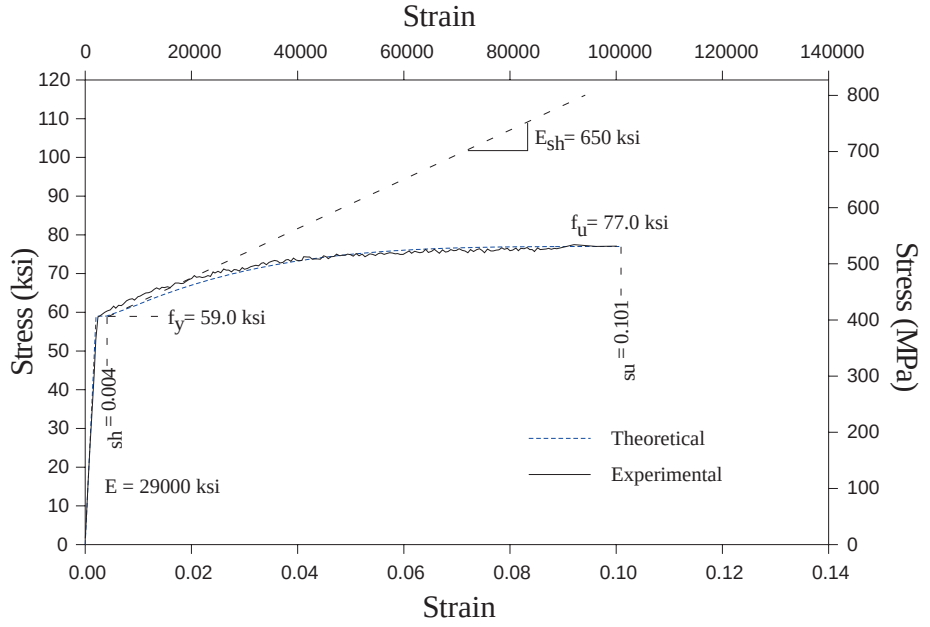

Figure 3.20: Stress strain curves for Units 1B and 2B #2 [D6] transverse bars.

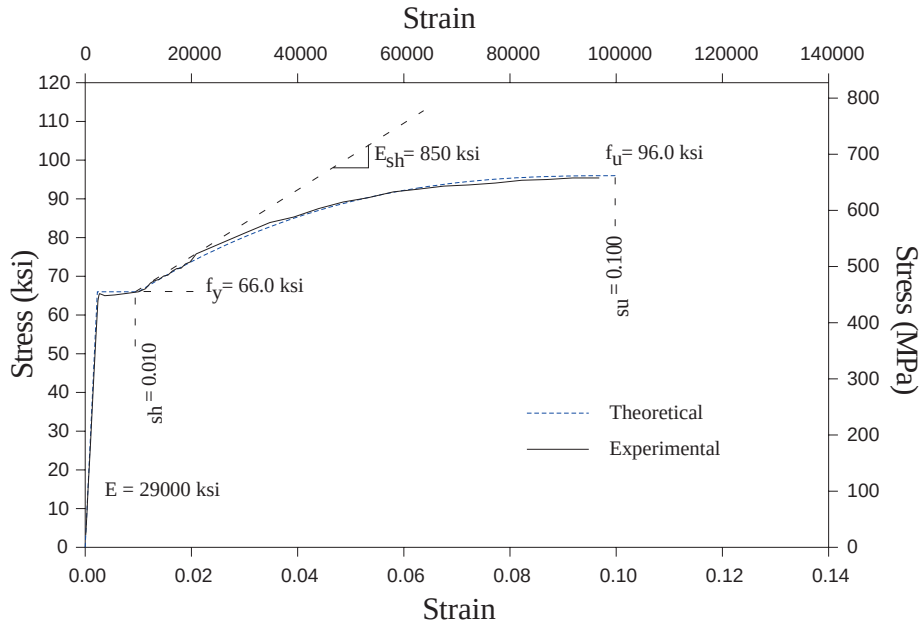

Figure 3.21: Stress strain curves for Units 2A and 2B #4 [D13] longitudinal bars.

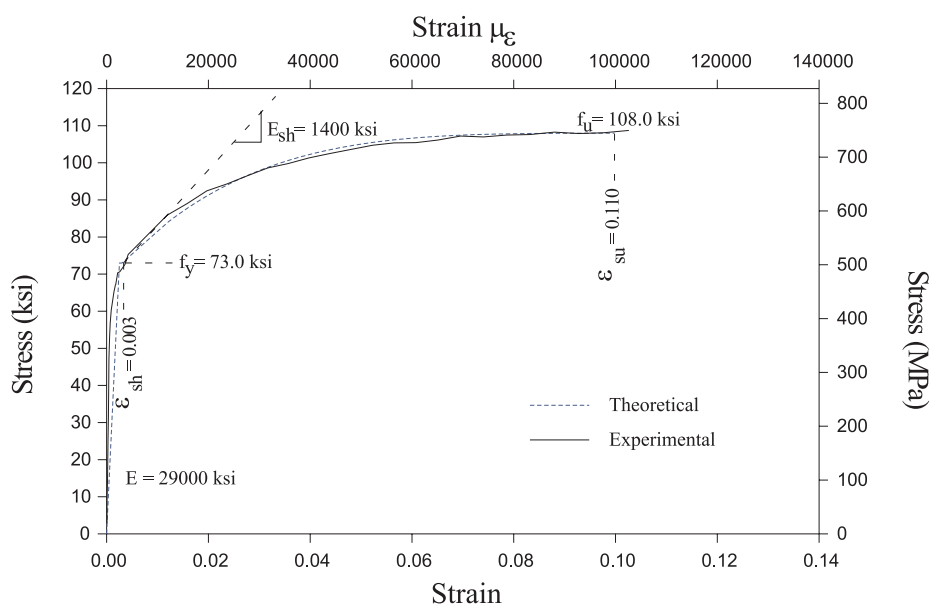

Figure 3.22: Stress strain curves for Units 2A and 2B #3 [D10] spirals.

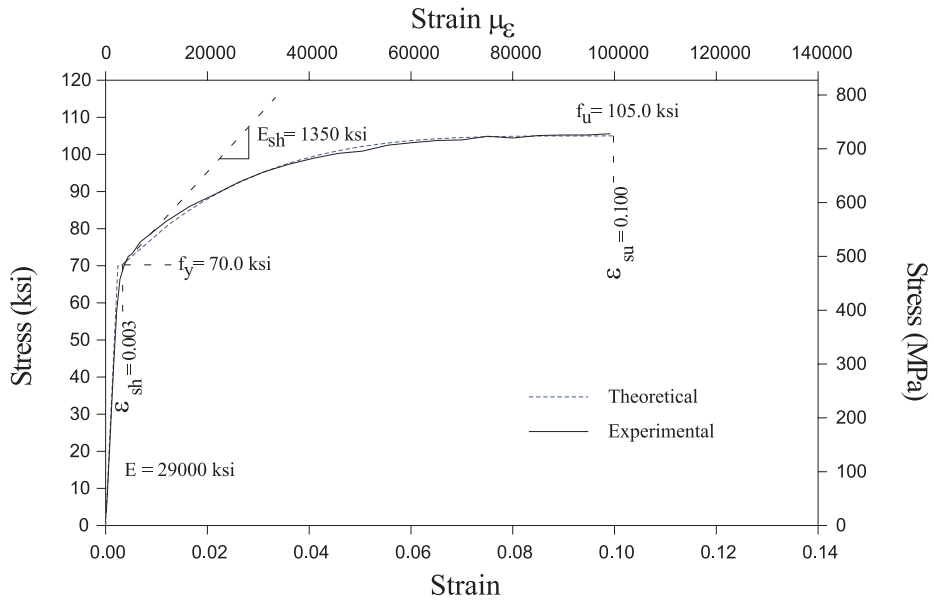

Figure 3.23: Stress strain curves for Units 2A and 2C #3 [D10] transverse bars.

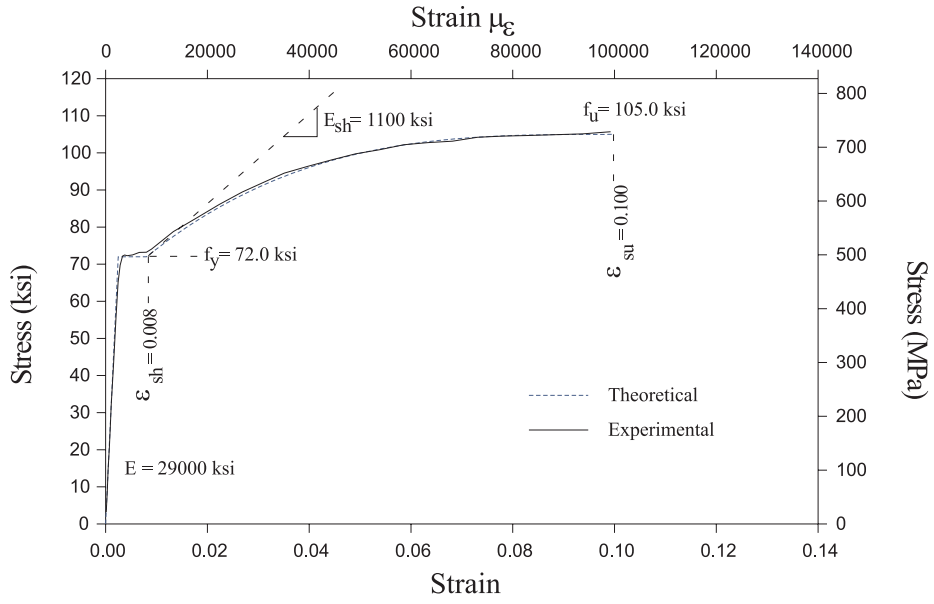

Figure 3.24: Stress strain curve for Unit 2C #4 [D13] longitudinal bars.

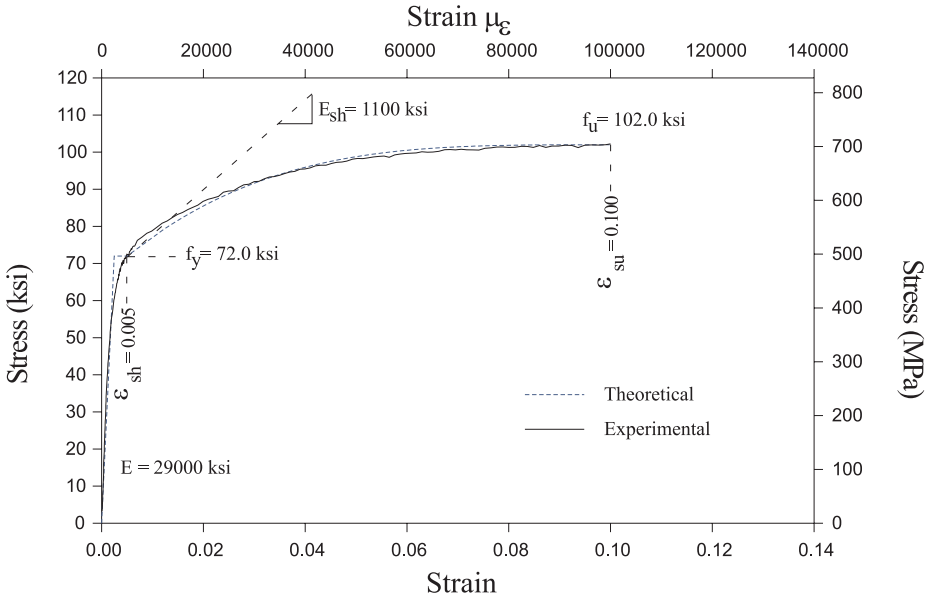

Figure 3.25: Stress strain curve for Unit 2C #3 [D10] spirals.

Chapter 4

Test Protocol and Instrumentation

4.1 Overview

This chapter describes the test setup and instrumentation for the five test units. The test setup was designed to load the columns cyclically in single bending. Instrumentation was typically concentrated on the lower portion of the columns to monitor behavior in the plastic hinge region. As mentioned previously, these tests were conducted in two phases, however the test setups for both phases were similar in every respect except column height.

Lateral restraint was provided in each test to prevent the test units from bending out of plane. None of the test units showed any tendency to bend out of plane during testing. Test Unit 1A was instrumented for curvature readings on both the east and west faces. After the first test a decision was made to instrument only the east faces of the remaining test units for curvature and for shear deformations, leaving the west face open for the marking of cracks. Hence, the photos in Appendix A are all of the west face.

4.2 Test Setup

All test units were loaded both laterally and vertically by two independent loading systems (see Figures 4.2, 4.3 and 4.4), each of whose loads were measured with calibrated load cells. The lateral load was applied with a 220 kip [979 kN] MTS long-stroke, servo-controlled, hydraulic actuator with a displacement capacity of ± 24 in. [610 mm].

The 200 kip [890 kN] vertical load was applied via two ∅ 1 3/8 in. [35 mm] DYWIDAG bars set up on the east and west sides of the test unit and anchored at the top into a cross beam and at the bottom under the strong floor. Tension was applied to these bars via two 200 kip [890 kN] hydraulic jacks that were situated under the strong floor in the first test phase and above the axial load application frame in the second test phase. The vertical load jacks were slow to respond to changes in load and therefore could not keep a constant axial load on the test units under lateral excursions. Figure 4.1 gives a sample of the fluctuation in axial load for Test Units 1A and 2A.

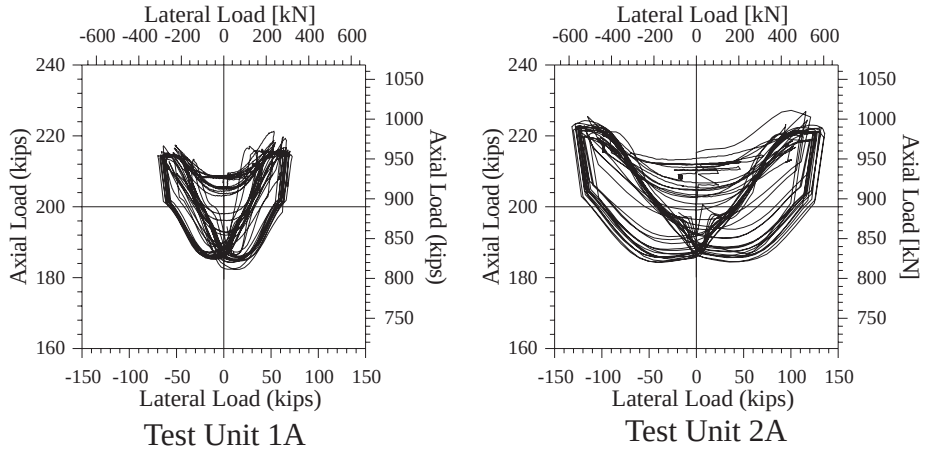

Figure 4.1: Fluctuation in axial load as a function of displacement. Left: Unit 1A; Right: Unit 2A.

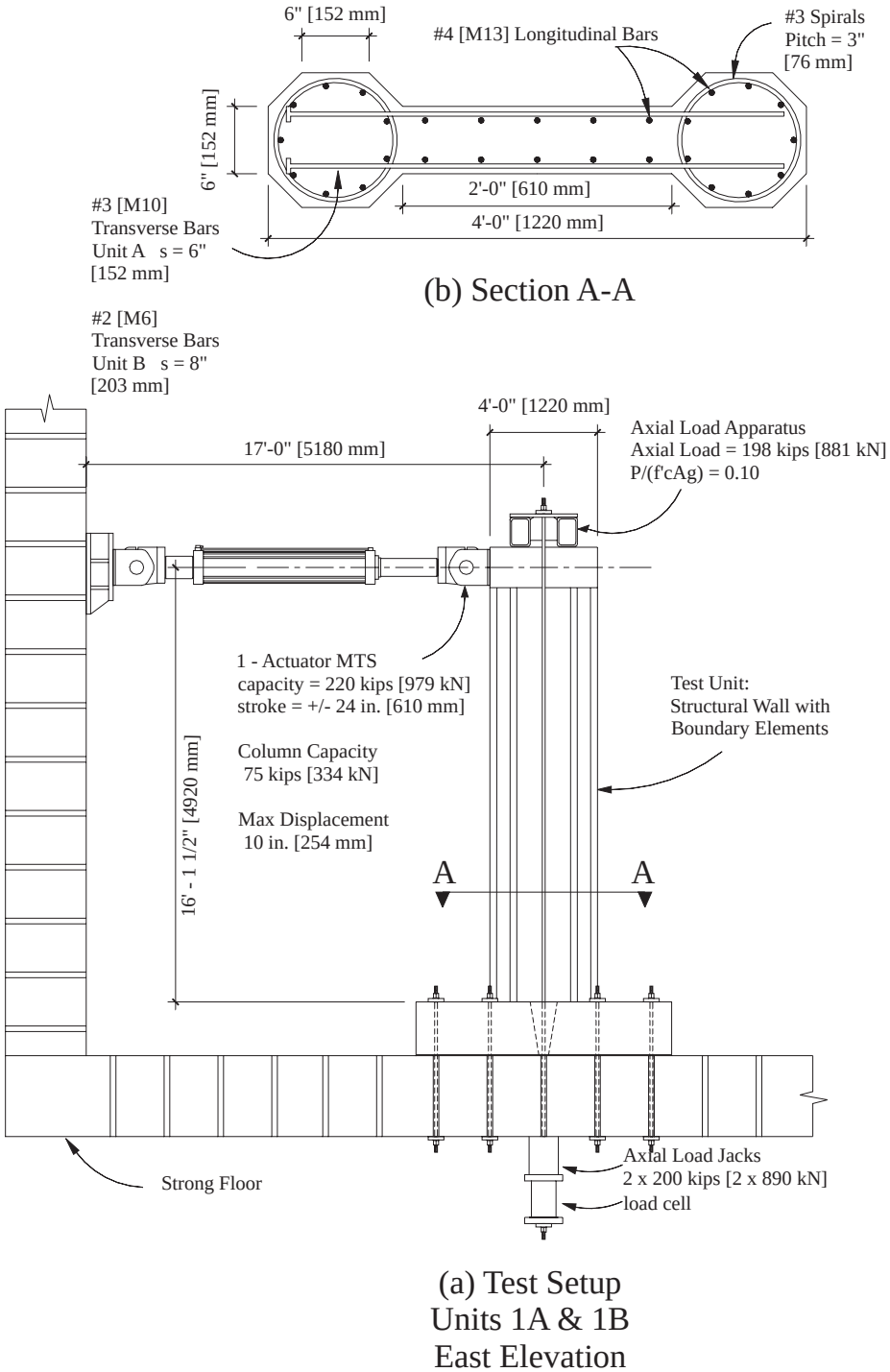

Figure 4.2: Test setup for Units 1A and 1B.

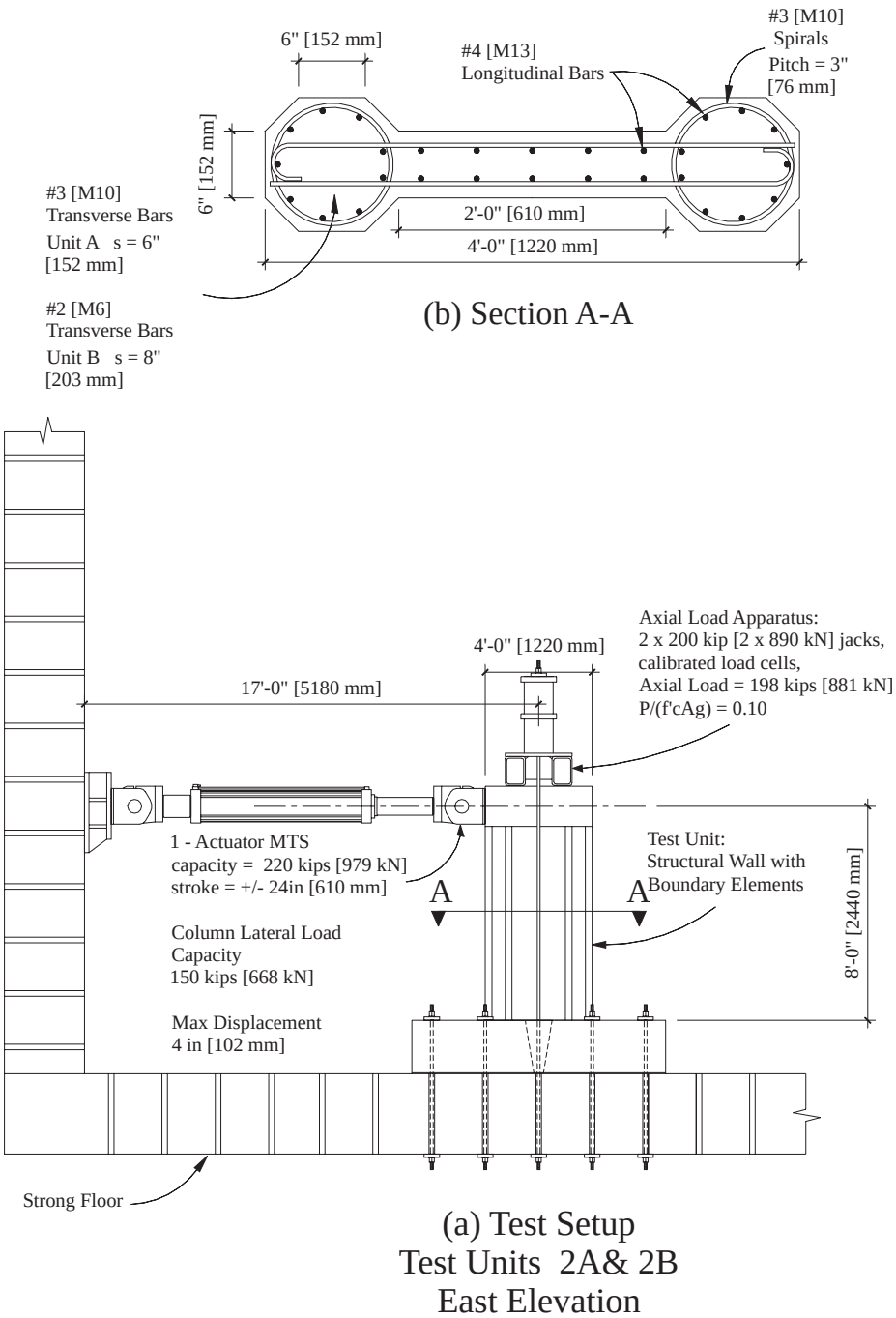

Figure 4.3: Test setup for Units 2A and 2B.

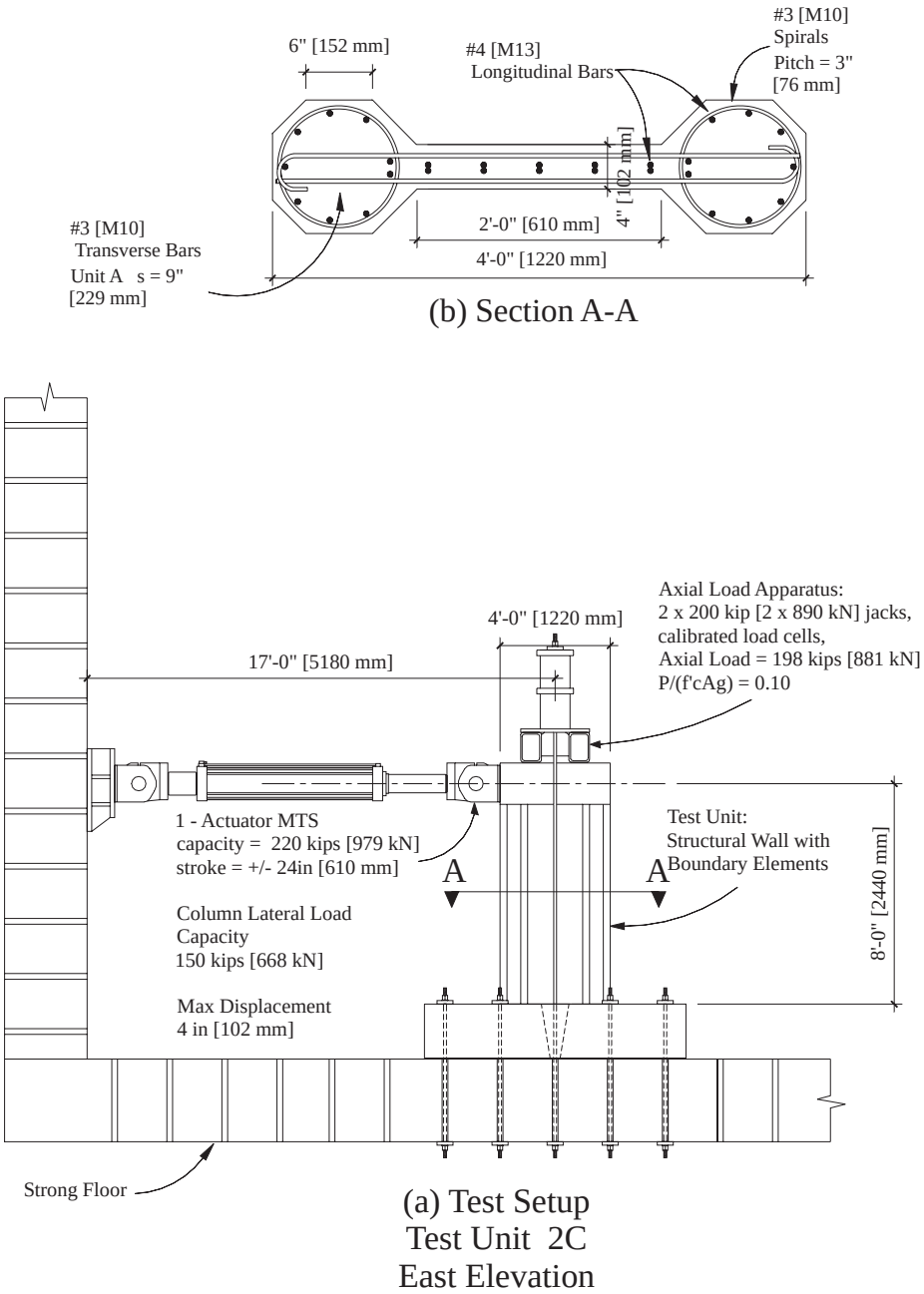

Figure 4.4: Test setup for Unit 2C.

4.3 Instrumentation

4.3.1 Strain Gages

Strains in the reinforcing bars were measured with electrical resistance strain gages. The gages used had a 120Ω resistance and a 0.2 in. [5 mm] gage length. The reinforcing bar surface was prepared by sanding smooth a section of bar, roughing the sanded surface with plummer's mesh, and cleaning it with methyl ethyl-keytone. The gages were applied to the prepared surface with a super-adhesive (alpha cyanoacrylate monomer), coated with an acrylic based water-proofing agent and then protected with a vinyl mastic membrane.

Strain gage locations for each of the test units are displayed in Figures 4.5 - 4.8. Figure 4.5 shows the longitudinal strain gage locations for Test Units 1A, 1B, 2A, 2B and 2C. Figure 4.6 shows the transverse bar and spiral strain gage locations for Test Units 1A and 1B. Figure 4.7 shows the transverse bar strain gage locations for Test Units 2A, 2B and 2C. Figure 4.8 shows the spiral strain gage locations for Test Units 2A, 2B and 2C.

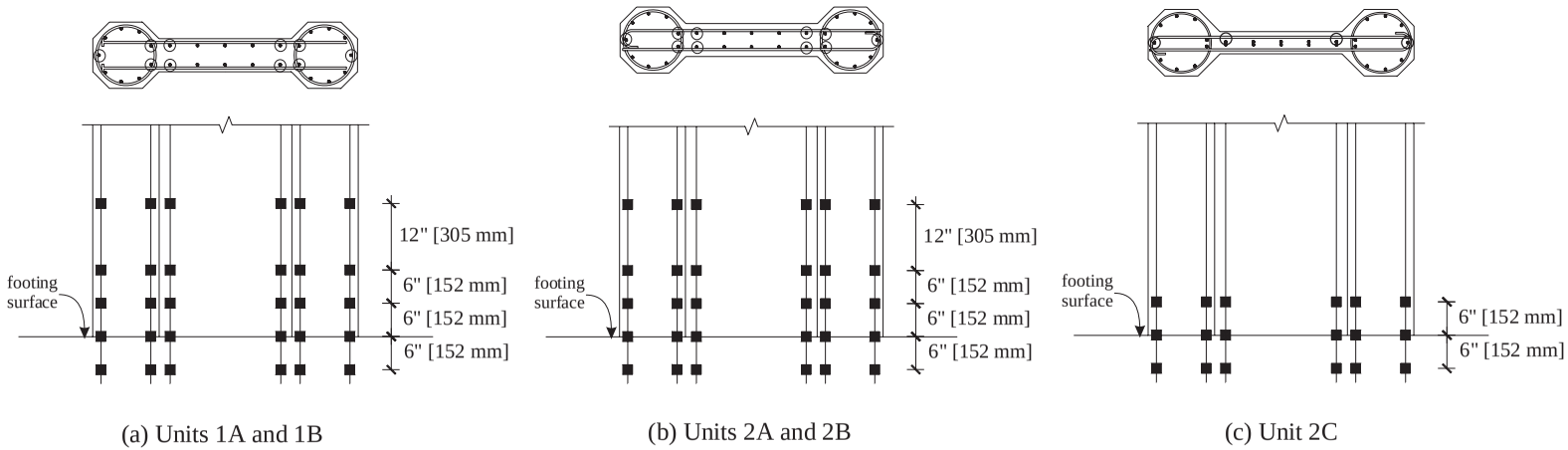

Figure 4.5: Phase I longitudinal strain gage locations: (a) Test Units 1A and 1B, (b) Test Units 2A and 2B, (c) Test Unit 2C.

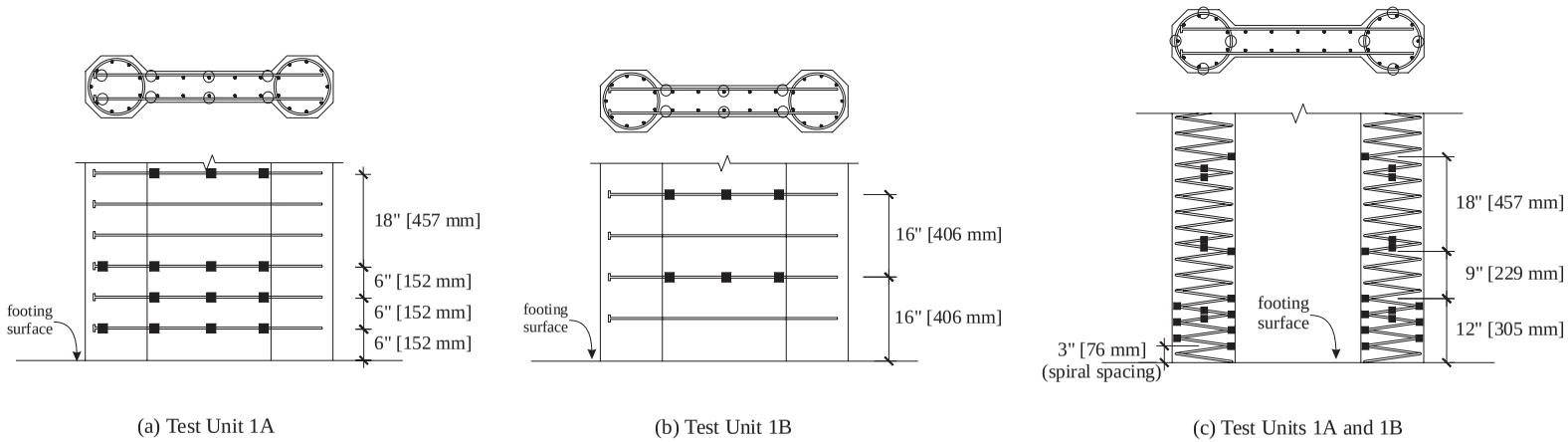

Figure 4.6: Phase I transverse strain gage locations: (a) Test Unit 1A, (b) Test Unit 1B; Spiral strain gage locations: (c) Test Units 1A and 1B.

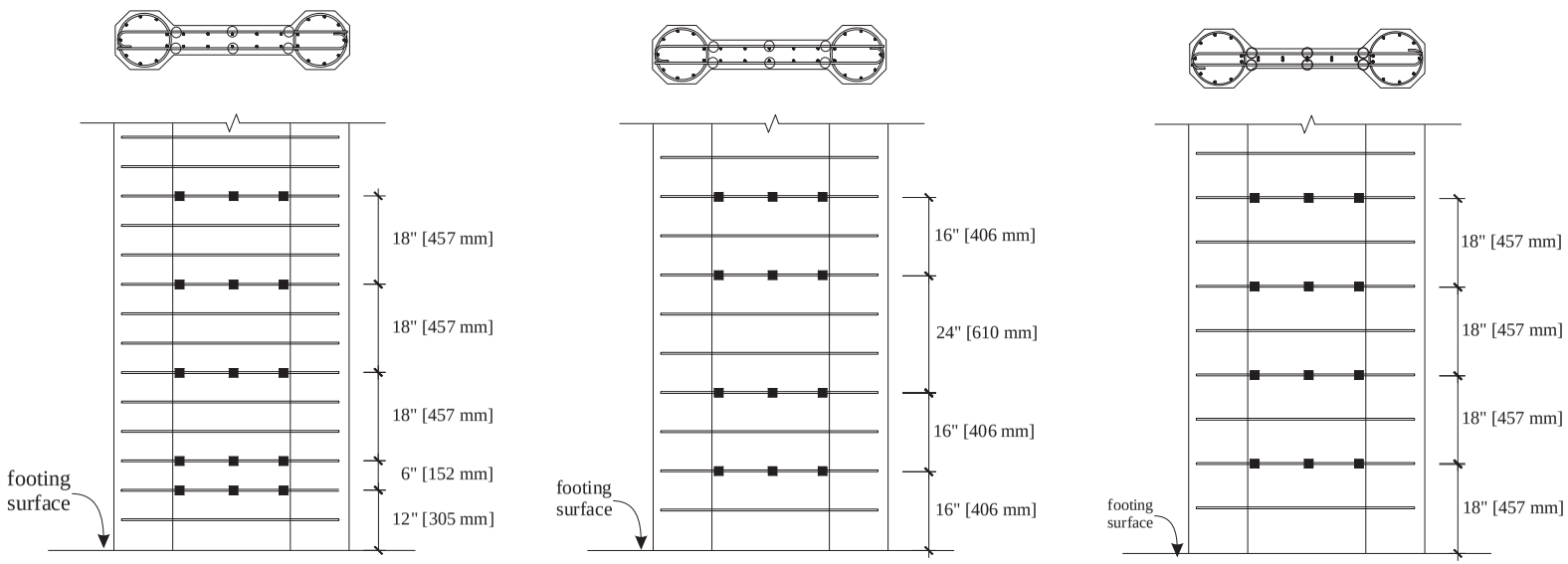

(a) Test Unit 2A (b) Test Unit 2B (c) Test Unit 2C

Figure 4.7: Phase II transverse strain gage locations: (a) Test Unit 2A, (b) Test Unit 2B, (c) Test Unit 2C.

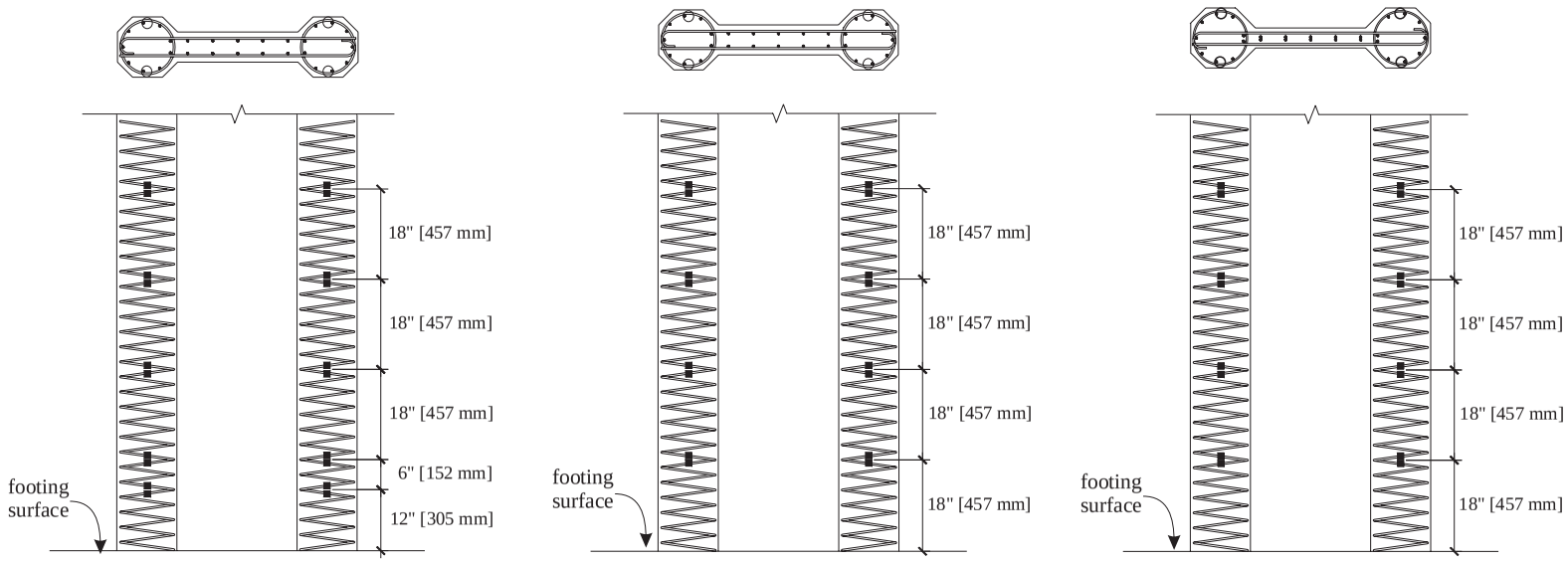

(a) Test Unit 2A (b) Test Unit 2B (c) Test Unit 2C

Figure 4.8: Phase II spiral strain gage locations: (a) Test Unit 2A, (b) Test Unit 2B, (c) Test Unit 2C.

4.3.2 Slip of Transverse Bars

Test Unit 1A was instrumented to measure the slippage of the transverse bars at 18 in. [457 mm] and 36 in. [914 mm] height above the footing. Only the south ends of the transverse bars were headed while the north ends were straight. The north ends of the bars were expected to slip when the test unit was loaded in the negative direction, with the north boundary element in tension. At higher displacement levels, this slippage was expected to become significant because of the increasing flexural crack width. Pictured in Figure 4.9 is the instrumentation set up for measuring slippage in the transverse bars. Figure 4.10 shows the actual instrumentation mounted at 18 in. [457 mm] height. If slippage occurred, the bars were expected to slip into the column on negative (pull) excursions, thereby compressing the displacement potentiometer mounted on an aluminum angle bracket and giving a negative reading.

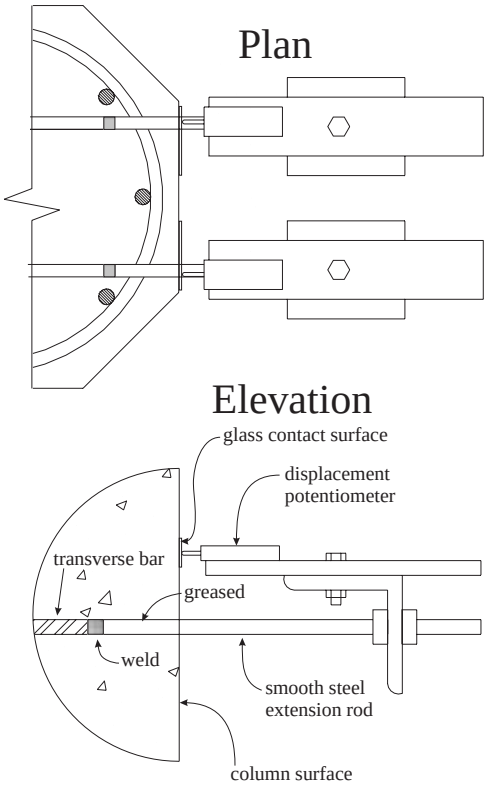

Figure 4.9: Plan and elevation of transverse bars slippage instrumetation.

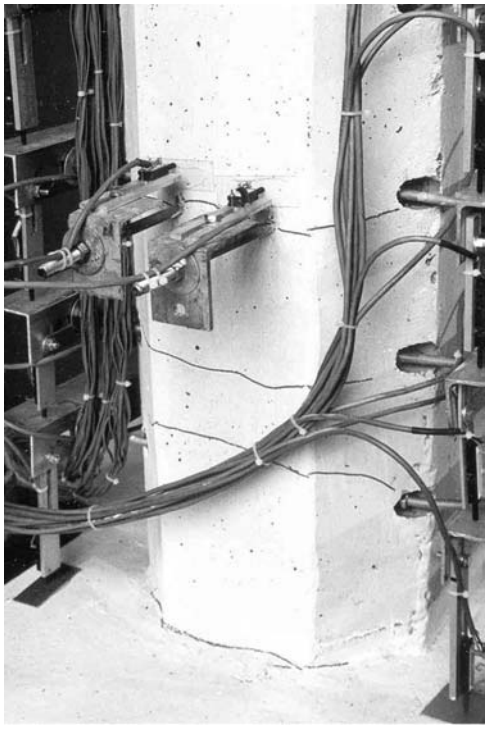

Figure 4.10: Bar slippage instrumentation mounted at 18 in. [457 mm] height.

4.3.3 Curvature Instrumentation

Displacement transducers were mounted on the east face of each test unit in order to record data for calculating experimental curvature values. Only on Test Unit 1A was this instrumentation mounted also on the west face. Test Units 1A and 1B were fitted at each level with six 1 1/2 in. [38 mm] displacement potentiometers mounted on aluminum angle brackets (see Figure 4.11).

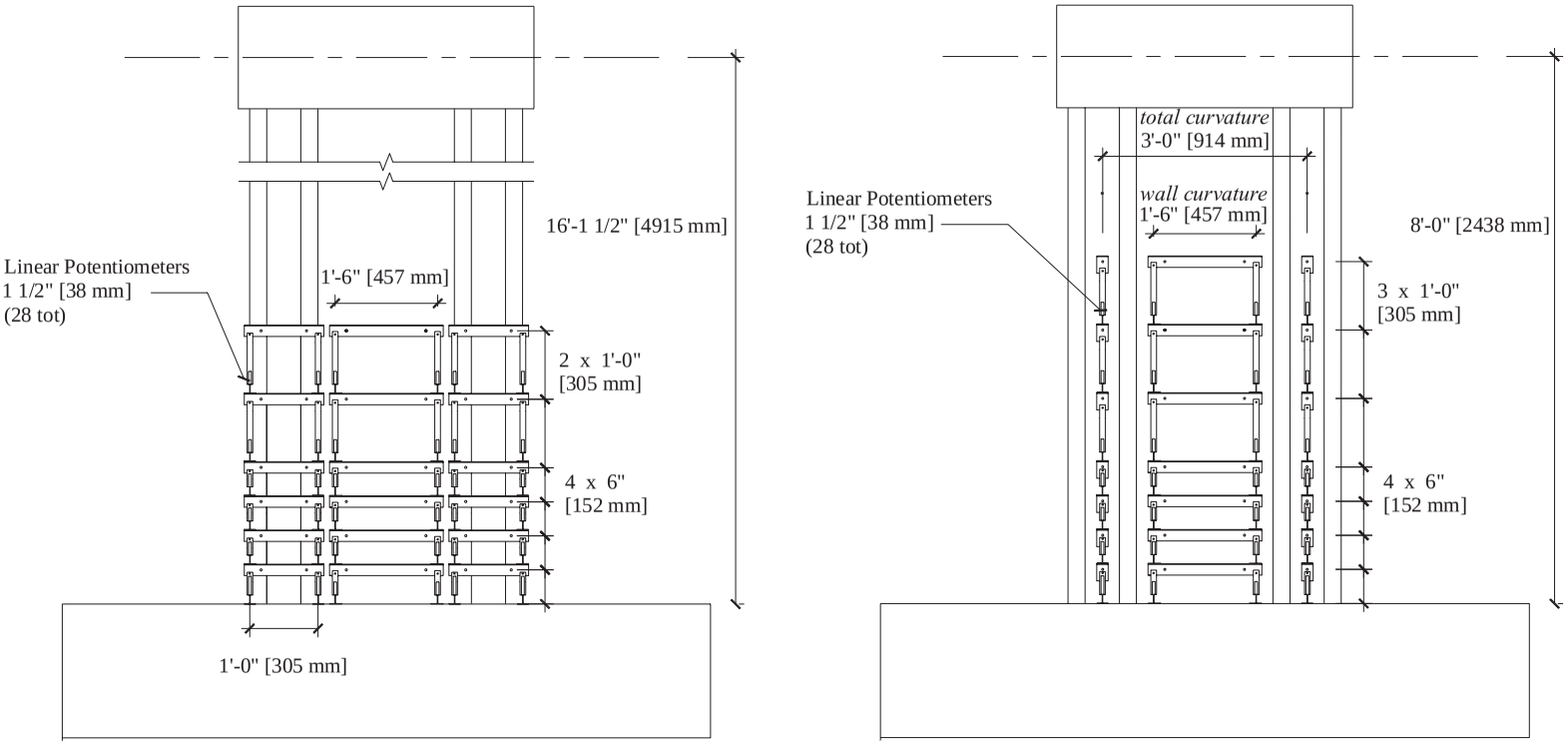

Figure 4.11: Phase I curvature instrumentation (left). Phase II curvature instrumentation (right).

The levels were set at 6 in. [152 mm] intervals up to 24 in. [610 mm] above the footing and 12 in. [305 mm] intervals up to 48 in. [1220 mm] above the footing. Test Units 2A, 2B and 2C were instrumented at height increments identical to those of the Phase I test units, with one additional level added at 60 in. [1524 mm] above the footing. The Phase II test units were, however, fitted with only four linear potentiometers per level (see Figure 4.11). Figures 4.12 and 4.13 show details of the instrumentation for Test Unit 2A. By instrumenting the side of the test units

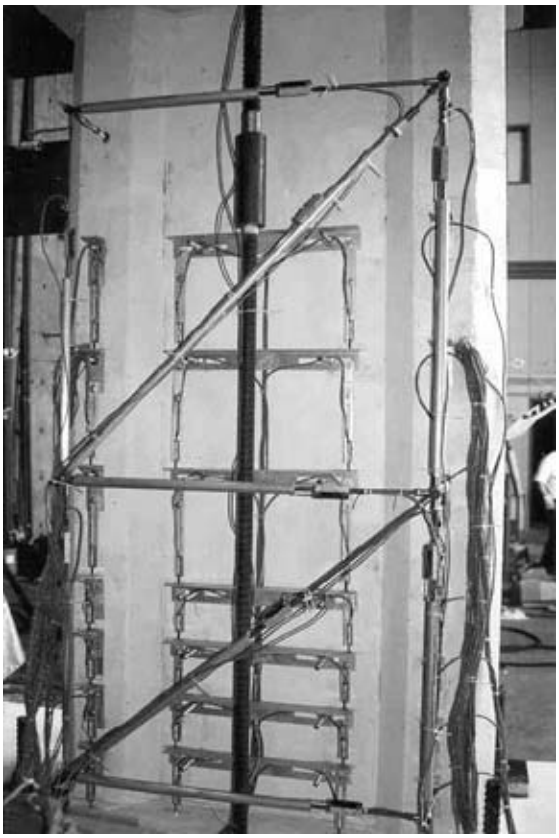

Figure 4.12: Curvature and shear panel instrumentation on Unit 2A: East Face.

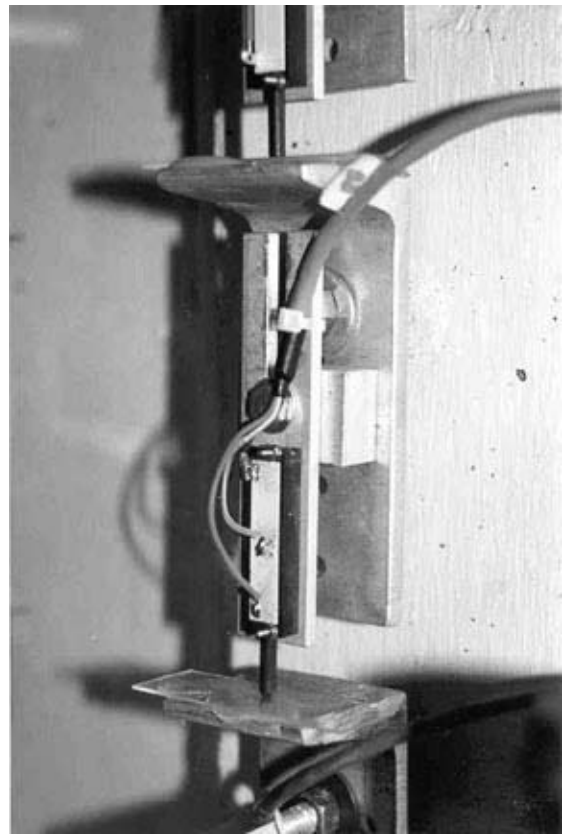

Figure 4.13: Curvature instrumentation detail – linear potentiometer.

for displacement as shown, it was possible to compare curvatures in the structural wall with curvatures for the entire section (see Figures B.2, C.2, D.2, E.2, F.2 in the appendices). These curvatures were calculated from the displacement readings as

$$\phi_w \quad \frac{\Delta_{wn} - \Delta_{ws}}{l_w h_i} \tag{4.1}$$

for the wall curvature, and

$$\phi_{tI} \quad \frac{\Delta_{nbn} - \Delta_{sbs}}{l_D h_i} \tag{4.2}$$

for the total curvature of the Phase I test units as shown in Figure 4.14, where h_i is the gage height between transducer brackets. The total curvature at a given height for the Phase II test units was calculated according to the diagram in Figure 4.15 as

$$\phi_{tII} \quad \frac{\Delta_{nb} - \Delta_{sb}}{l_t h_i} \tag{4.3}$$

At the base, h_i was taken for all test units at displacement levels of $\mu_\Delta \geq 1$ to be

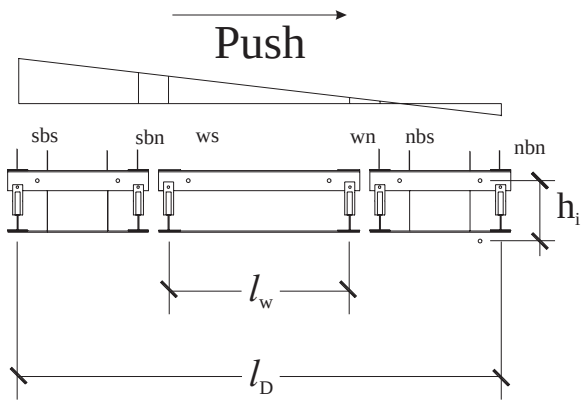

Figure 4.14: Detail of curvature instrumentation for Test Units 1A and 1B.

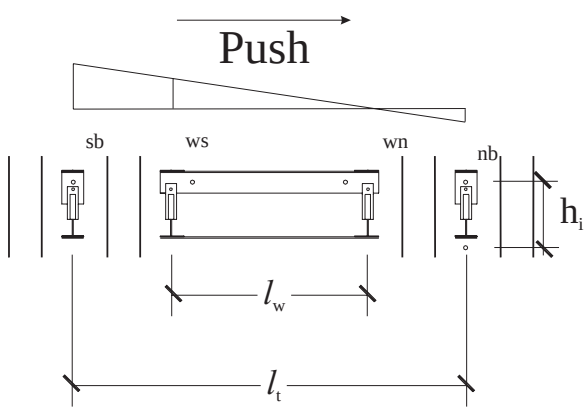

Figure 4.15: Detail of curvature instrumentation for Test Units 2A, 2B and 2C.

the gage height (6 in. [152 mm]) plus a strain penetration term calculated as

$$L_{sp} \quad .15 d_b f_y \quad .15(0.5in.)(66ksi) = \ 4.95in.[126mm] \tag{4.4}$$

where d_b is the longitudinal bar diameter and f_y is the assumed longitudinal bar yield stress. The average curvature at the base was therefore plotted in Figures B.2, C.2, D.2, E.2 and F.2 at the footing level, which was close to the center of the

modified gauge length. For initial displacement levels of $\mu_\Delta \leq 1$, the effects of strain penetration were not considered significant. Therefore the base curvature values from the initial stages of loading were plotted at 3in. [76mm] above the base, which was the center of the nominal gauge length.

Multiplying the curvatures by the gauge height produced a rotation assumed to act at the center of the gauge height.

$$_i \quad \phi_{i,av} h_i \tag{4.5}$$

For instance, $_i$ at the base was assumed to act at the footing level for all displacement levels of $\mu_\Delta \geq 1$, while $_i$ measured from the instrumentation mounted at 12 in. [305 mm] above the footing was assumed to act at 9 in. [229 mm] above the footing–half way in between the curvature rods mounted at 6 in. [152 mm] and 12 in. [305 mm].

Column displacement due to flexural deformations was then calculated by multiplying rotations $_i$ by their distances from the top of the column and taking their sum.

$$\Delta_{flex} \quad \sum_i \; _i \left[L - \left(\sum_{j=1}^{i-1} h_j + h_i/2 \right) \right] \tag{4.6}$$

Chapter 7 presents these experimentally calculated deflections in comparison with the measured displacements at the tops of the columns.

4.3.4 Shear Deformation

Shear deformation was measured by panels consisting of five independent linear potentiometers attached to the east or west column face via the same rods that were used for mounting the curvature instrumentation. For the Phase II test units, this instrumentation can be seen in Figure 4.12. Figure 4.16 show the panel configurations for the Phase I and Phase II test setups.

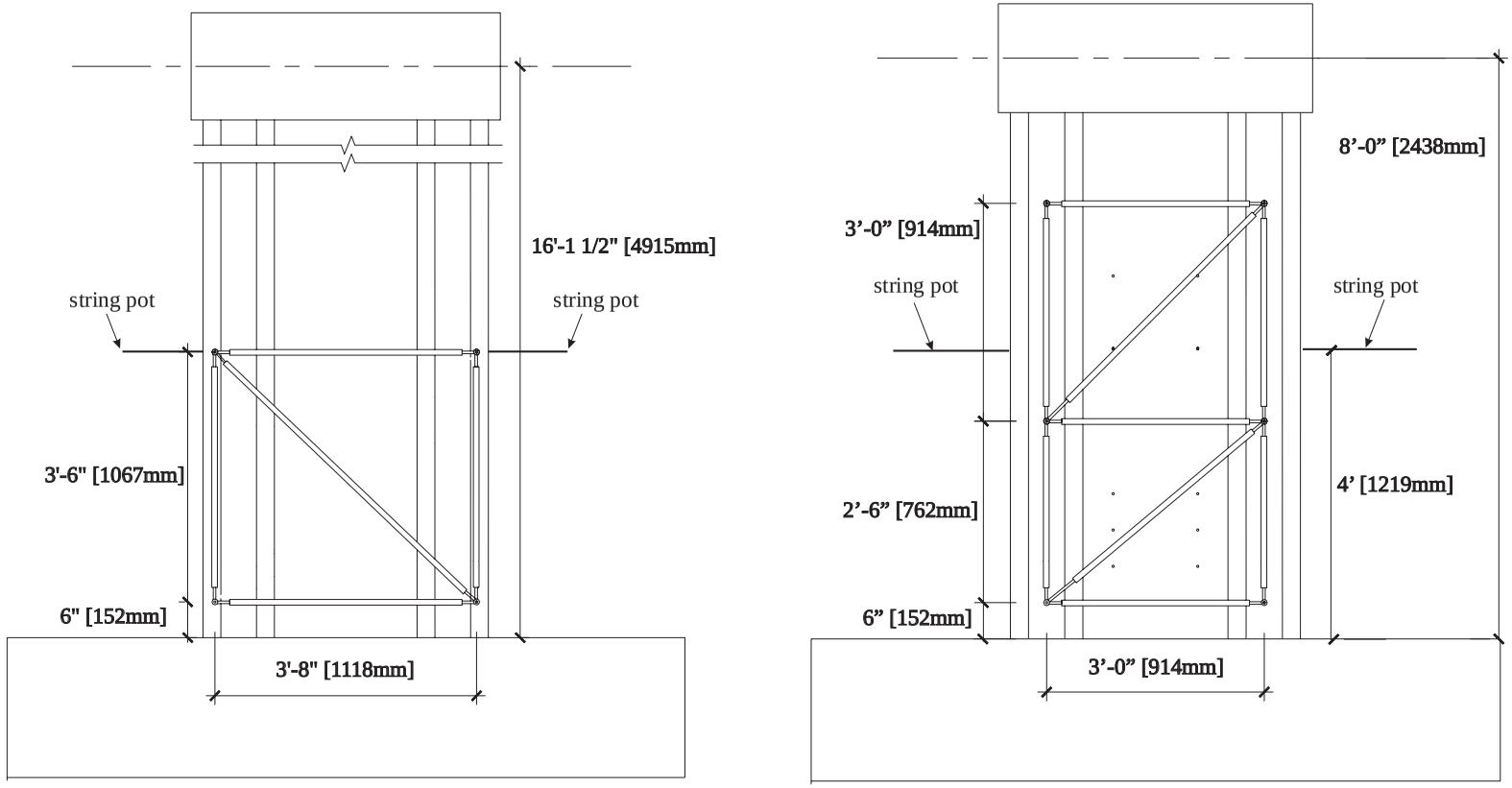

Figure 4.16: Phase I shear instrumentation (left). Phase II shear instrumentation (right).

The deformation due to shear could be broken down into five independent deformation modes (see Figure 4.17). The formula for calculating each deformation mode from the nodal displacements is given in Equation 4.7

$$\begin{Bmatrix} \gamma \\ \Delta_{\ x} \\ \Delta_{\ y} \\ \Delta_x \\ \Delta_y \end{Bmatrix} \begin{bmatrix} \frac{1}{2h} & \frac{1}{2d} & \frac{1}{2h} & -\frac{1}{2d} & -\frac{1}{2h} & -\frac{1}{2d} & -\frac{1}{2h} & \frac{1}{2d} \\ -\frac{1}{h} & 0 & \frac{1}{h} & 0 & -\frac{1}{h} & 0 & \frac{1}{h} & 0 \\ 0 & \frac{1}{d} & 0 & -\frac{1}{d} & 0 & \frac{1}{d} & 0 & -\frac{1}{d} \\ \frac{1}{2} & 0 & -\frac{1}{2} & 0 & -\frac{1}{2} & 0 & \frac{1}{2} & 0 \\ 0 & \frac{1}{2} & 0 & \frac{1}{2} & 0 & -\frac{1}{2} & 0 & -\frac{1}{2} \end{bmatrix} \begin{Bmatrix} u1 \\ u2 \\ u3 \\ u4 \\ u5 \\ u6 \\ u7 \\ u8 \end{Bmatrix} \tag{4.7}$$

The nodal displacements were obtained from the panel deformation as follows. For the panel configuration shown in Figure 4.18, let the initial lengths of the potentiometers be B_0 (bottom), T_0 (top), N_0 (north), S_0 (south) and D_0 (diagonal). The instrumentation lengths in the deformed mode are then defined as in Equations 4.8 - 4.12 using the measured changes in length.

$$B \quad B_0 + \Delta B \quad d + \Delta B \tag{4.8}$$

$$T \quad T_0 + \Delta T \quad d + \Delta T \tag{4.9}$$

$$N \quad N_0 + \Delta N \quad h + \Delta N \tag{4.10}$$

$$S \quad S_0 + \Delta S \quad h + \Delta S \tag{4.11}$$

$$D \quad D_0 + \Delta D \quad \sqrt{d^2 + h^2} + \Delta D \tag{4.12}$$

By establishing the geometry of the deformed panel from Equations 4.13 - 4.16 and assuming $u_8 \quad 0$, the remaining nodal displacements were calculated using Equations 4.17 - 4.23 with respect to the reference node 3.

$$_1 \quad \text{os}^{-1} \quad \frac{B^2 + N^2 - D^2}{2BN} \tag{4.13}$$ =c

$$_2 \quad \text{os}^{-1} \quad \frac{B^2 + D^2 - N^2}{2BD} \tag{4.14}$$ =c

$$_3 \quad \text{os}^{-1} \quad \frac{S^2 + D^2 - T^2}{2SD} \tag{4.15}$$ =c

$$_7 \quad \pi - \ _1 \tag{4.16}$$

$$u_1 \quad N \cos \ _7 \tag{4.17}$$

$$u_2 \quad N \sin \ _7 - h \tag{4.18}$$

$$u_3 \quad S \cos(\ _2 + \ _3) \tag{4.19}$$

$$u_4 \quad S \sin(\ _2 + \ _3) - h \tag{4.20}$$

$$u_5 \tag{4.21}$$

$$u_6 \tag{4.22}$$

$$u_7 \quad B - d \qquad B \tag{4.23}$$

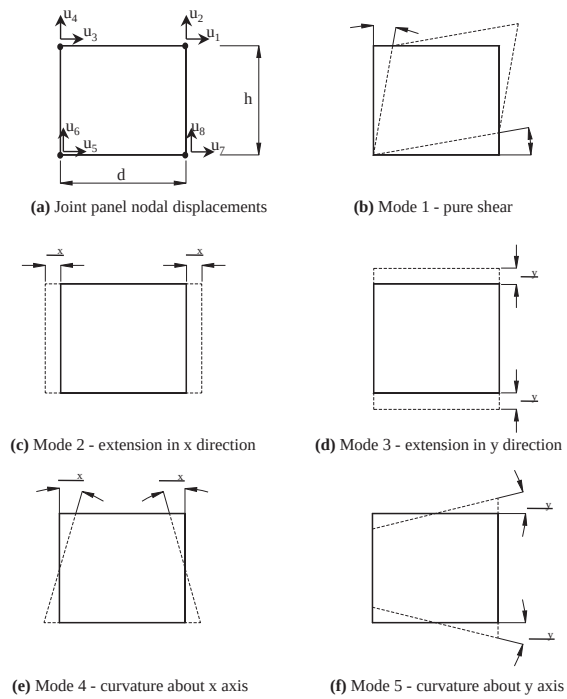

Figure 4.17: Decomposition of panel deformation into five independent modes [15].

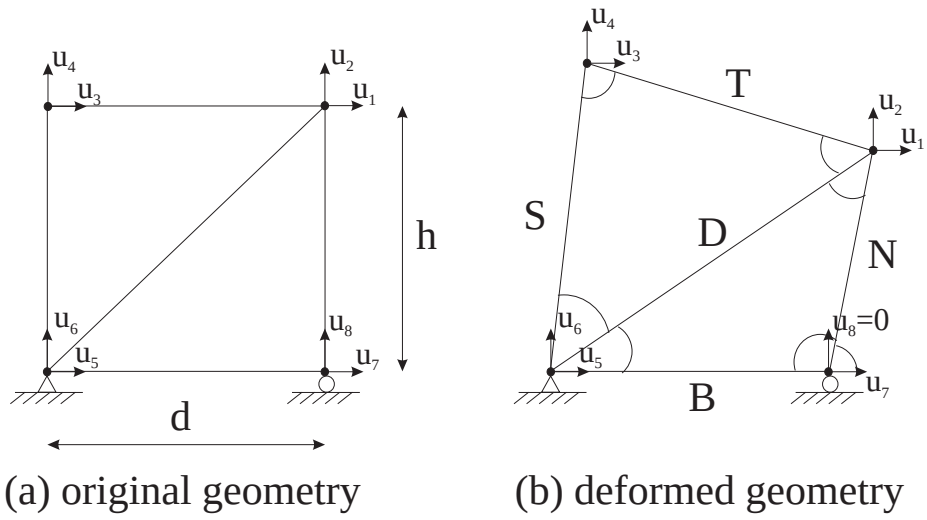

Figure 4.18: Panel deformation [15].

While the diagonal members of the lower shear panels consistently experienced too much friction to measure deformation properly during the tests, and hence rendered the aforementioned method of calculating shear displacements inoperative for the lower panels, an alternative method of calculating the shear displacement in the first 48 in. [1219mm] of column height was employed. For the Phase II test units, the shear strain calculated from the upper panels was then multiplied by 24 in. [610mm] as opposed to 36 in. [914mm] to account for the 24 in. [610mm] directly above the lower 48 in. [1219mm]. This resulted in a total of 72 in. [1829mm] height over which shear displacements were measured in the Phase II tests.

In case the diagonal pots malfunctioned, as they indeed did, string pots were also mounted to independent reference columns and attached to the columns on the north and south sides at 48 in. [1219mm] above the footing (see Figure 4.16). From the horizontal measurements given by these string pots, from the vertical measurements given by the curvature pots and assuming small angles, the experimental shear was calculated for each of the five test units by the alternative method presented below.

Shear deformation can be estimated based on the action of two diagonals crossing the zone of deformation. Figures 4.19 and 4.20 show that the deformed diagonal

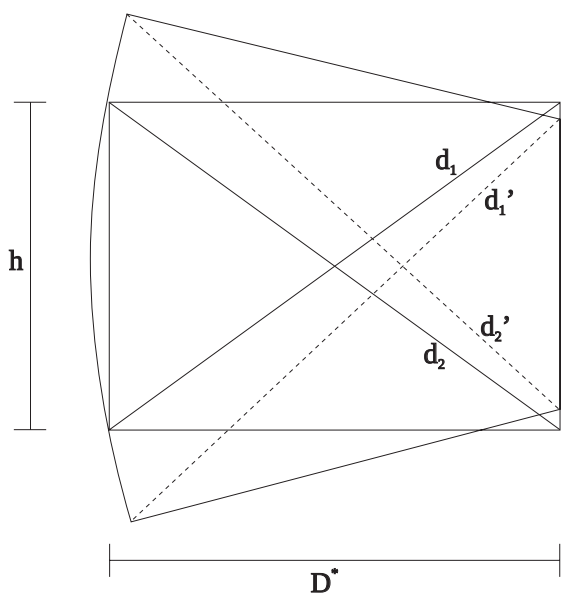

Figure 4.19: Diagonal deformations are equivalent in flexure.

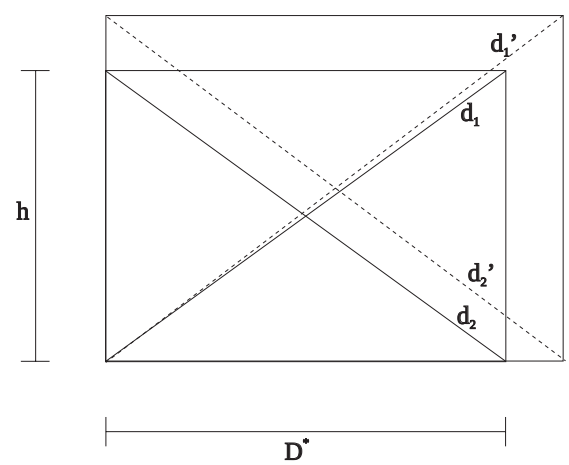

Figure 4.20: Diagonal deformations are equivalent in horizontal and vertical expansion.

lengths δ_1 and δ_2 remain equal to one another under flexure and under expansion of the region with height h and depth D^*. Only in shear do the deformed diagonals

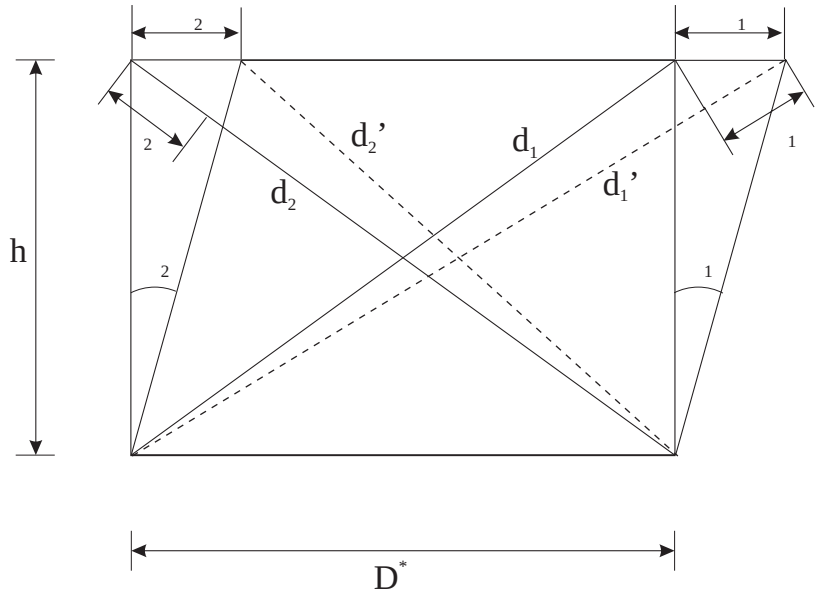

Figure 4.21: Diagonal deformations are used to estimate shear deformation.

have different lengths. Assuming small angles, the average shear deformation in the region γ, was estimated as the average of the shear deformations calculated on either side of the region.

$$\gamma \quad \frac{\gamma_1 + \gamma_2}{2} \quad \frac{\Delta_1 + \Delta_2}{2h} \tag{4.24}$$

Where the lateral deformations Δ_1 and Δ_2 due to shear deformation are calculated from the diagonal deformations according to the ratio

$$\frac{\Delta}{\delta} \quad \frac{d}{D^*} \tag{4.25}$$

where

$$\delta \quad d' - d \tag{4.26}$$

as shown in Figure 4.21. Combining Equations 4.24 and 4.25 yields the equation

$$\gamma \quad \frac{\delta_1 d_1 - \delta_2 d_2}{2hD^*} \tag{4.27}$$

which characterizes the average shear deformation over a given region with height h, and depth D^*. Figure 4.22 shows the parameters involved in creating the artificial diagonals whose deformations $\delta \quad d' - d$ were then used according to Equation 4.27. The deformed diagonals were calculated as

$$d_1' \quad \sqrt{(48 - \Delta_{xn})^2 + (48 + \Delta_{yn})^2} \tag{4.28}$$

$$d_2' \quad \sqrt{(48 - \Delta_{xs})^2 + (48 + \Delta_{ys})^2} \tag{4.29}$$

for the Phase I test units corresponding to the left hand side of Figure 4.22, and as

$$d_1' \quad \sqrt{(36 - \Delta_{xn})^2 + (48 + \Delta_{yn})^2} \tag{4.30}$$

$$d_2' \quad \sqrt{(36 - \Delta_{xs})^2 + (48 + \Delta_{ys})^2} \tag{4.31}$$

for the Phase II test units, corresponding to the right hand side of Figure 4.22.

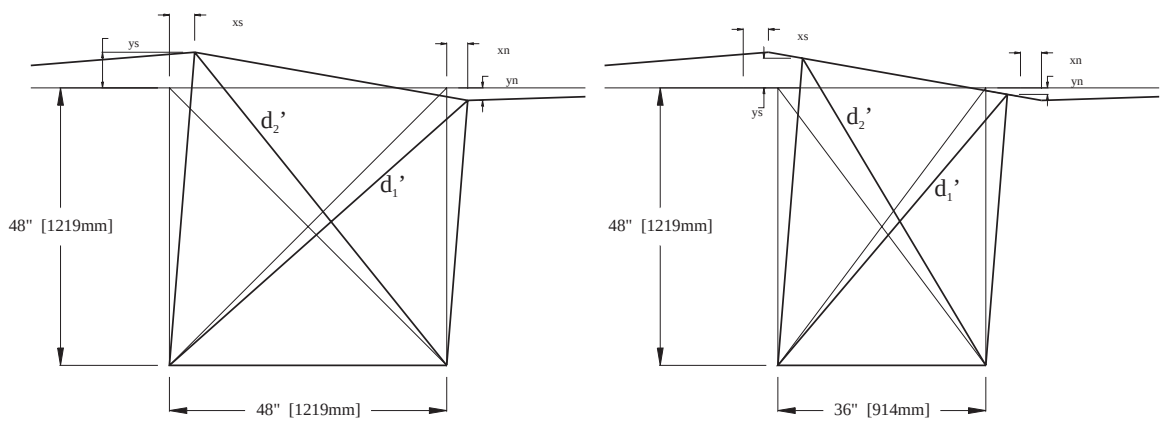

Figure 4.22: Alternative method for calculating shear based on artificial crossing diagonals. Phase I test units (left), Phase II test units (right).

4.4 Loading History

All test units were subjected to the standard cyclic loading history shown in Figure 4.23 with four initial cycles in load control up to theoretical first yield of the extreme longitudinal reinforcing bars and then in displacement control until failure of the test unit. Table 4.1 gives values for the load control portion of the loading history for all five test units. The load values were derived theoretically up through F_y and the displacement values were recorded experimentally. The displacement values for μ_Δ 1 were calculated for Test Units 1A and 2A by equation 4.33, whereas the load values corresponded to experimental values.

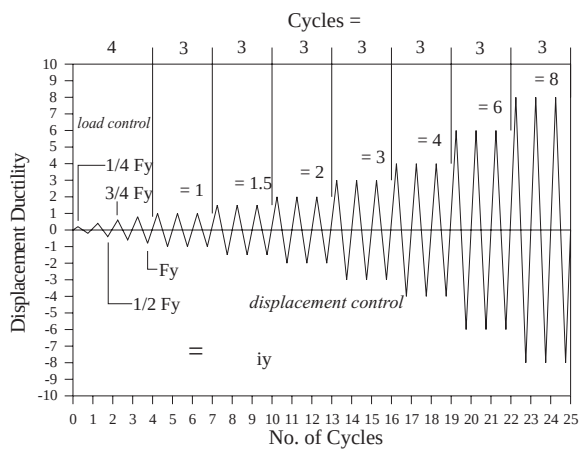

Figure 4.23: Standard loading history for all test units.

The shear force F_y at first yield of the extreme longitudinal reinforcing bars was calculated based on a moment curvature analysis of the given section, based on measured material properties. F_y was then determined by dividing the first yield moment by the column cantilever length. When the column reached first yield in the first loading direction, the actual top displacement was used to calculate the experimental elastic bending stiffness.

$$K_e \quad F_{y,theory}/\Delta_{y,exp} \tag{4.32}$$

This stiffness was then used in conjunction with the theoretical force at which the concrete cover reached ε_c .004 to determine the experimental ideal yield displacement, Δ_{iy}. =0

$$\Delta_{iy} \quad F_{\varepsilon_c=0.004}/K_e \quad \Rightarrow \mu_\Delta \tag{4.33}$$

Level	1A		1B		2A		2B		2C	
	load kips kN	disp. in. mm	load kips kN	disp. in. mm	load kips kN	disp. in. mm	load kips kN	disp. in. mm	load kips kN	disp. in. mm
$1/4F_y$	11.1	0.076	11.1	0.078	23.6	0.024	23.6	0.025	23.6	0.029
	49.4	1.9	49.4	2.0	105.0	0.6	105.0	0.6	105.0	0.7
$1/2F_y$	22.2	0.178	22.2	0.182	47.2	0.068	47.2	0.058	47.2	0.07
	98.8	4.5	98.8	4.6	210.0	1.7	210.0	1.5	210.0	1.8
$3/4F_y$	33.3	0.361	33.3	0.378	70.8	0.135	70.8	0.119	70.8	0.160
	148.2	9.2	148.2	9.6	315.0	3.4	315.0	3.0	315.0	4.1
F_y	44.4	0.716	44.4	0.754	94.4	0.269	94.4	0.245	94.4	0.359
	197.6	18.2	197.6	19.2	420.0	6.8	420.0	6.2	420.0	9.1
F_{y*}	47.3	0.810	47.3	0.924						
	210.5	20.6	210.5	23.5						
μ_Δ	53.0	1.11	54.2	1.11	105.4	0.35	107.1	0.35	91.0	0.35
	235.9	28.2	241.2	28.2	469.0	8.9	476.6	8.9	405.0	8.9

Table 4.1: Load and displacement values for initial loading stages of the five test units.

The ideal yield displacement was then defined as displacement ductility one, which marked the first excursion in displacement control. The ideal yield force, F_{iy} was the experimental load required to bring the column to its ideal yield displacement.

Test Units 1A and 1B were cycled five times in load control instead of four because of an initial mistake in the calculation of F_y. The original theoretical yield force was predicted to be F_y 44.4 kips [196.6 kN], however during the test it was determined that the theoretical yield force should be F_{y*}, which corresponded to the determined theoretical yield of the Unit 1A longitudinal steel. Test Unit 1B was then subjected to the exact same loading history as Unit 1A, without recalculating the displacement value for μ_Δ 1, in order to enable direct comparisons of the results in terms of displacements.

The Phase II test units were also cycled through identical load histories based on F_y and μ_Δ . Unit 2C showed a slightly weaker moment-curvature response than =1 Units 2A and 2B because of its thinner structural wall (4 in. [102 mm] as opposed to 6 in. [152 mm]) and its lower concrete strength (4509 psi [31.1 MPa] as opposed to 5310 psi [36.6 MPa] for Unit 2A, and 6017 psi [41.5 MPa] for Unit 2B).

4.5 Data Acquisition and Control

Lateral load was applied via an MTS 220 kip [979 kN], ± 24 in. [610 mm] long-stroke, servo-controlled hydraulic actuator controlled by an MTS *Flextest* digital controller. Strains and displacements were recorded as voltages and then converted to digital signals by a 16 bit analog to digital converter.

Chapter 5

Analytical Considerations and Test Predictions

5.1 Overview

Existing methods for predicting test unit response are presented. The procedure for deriving force-deflection relationships from moment-curvature analysis results is presented. Existing models for shear capacity are discussed as well as prospective modifications to these models. Existing models for web crushing are also discussed. Predictions for shear, web crushing and flexural capacity of the test units are compared.

5.2 Failure Mechanisms

The design calculations in Chapter 2 were based on traditional, conservative estimates of shear strength. A more advanced, predictive shear capacity assessment model demonstrates that although only Test Unit 1A was designed to withstand the entire section shear, both Phase I test units had sufficient reserve shear capacity from the concrete, axial load and tension boundary element spiral to resist the entire ultimate shear F_u 80 kips [356 kN]. Calculations based on this predictive model show also that sufficient reserve capacity was expected in all three Phase II test units to resist the applied shear force. Although a traditional shear failure with fracture of the transverse bars was not expected in any of the Phase I or Phase II tests, other modes of failure were thought possible and are described below.

1. Flexural Failure: The boundary elements and the structural wall would behave in an integral manner with plane sections remaining plane. A flexural failure

would occur by crushing of the compression boundary element concrete, buckling of the boundary element longitudinal reinforcing bars followed by rupture, or directly by rupture of the longitudinal reinforcing bars. Note that rupture of the longitudinal reinforcing bars due to low-cycle fatigue is primarily a phenomenon of laboratory testing and is not generally recognized as a form of column failure in the field. This mode of failure is typical for circular and rectangular columns.

2. Web Crushing Failure: The compression struts in the wall that transfer shear through the plastic hinge region to the compression toe of the column would become weakened by large flexure-shear cracks opening in both directions under cyclic loading and eventually crush.

3. Vertical Slippage Failure: The test units would lose stiffness as the boundary elements become uncoupled from the structural wall through severe flexure-shear cracking along their interfaces. Failure would occur in the poorly-confined structural wall. Such uncoupling might also occur inside the structural wall, instead of at the interfaces between the walls and the boundary elements.

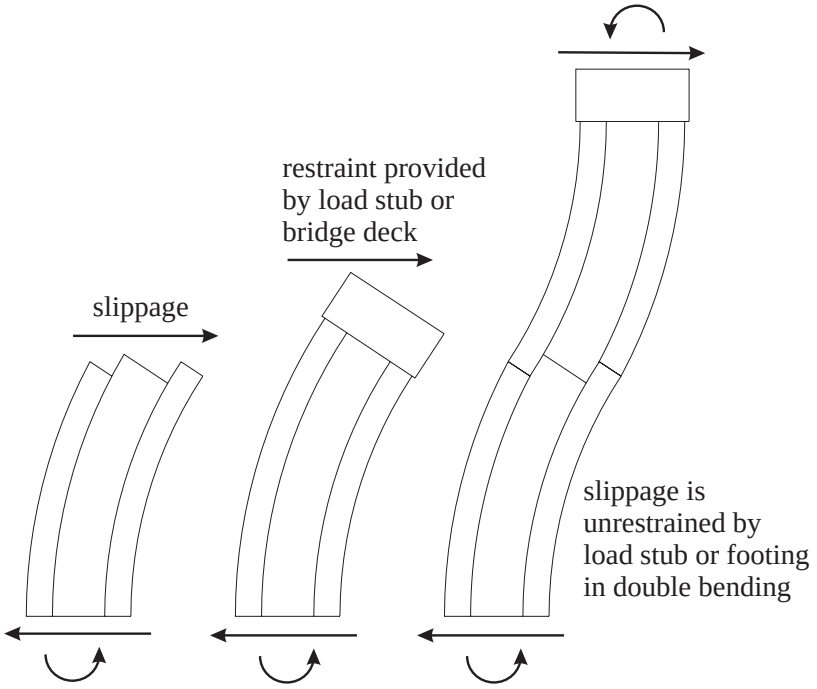

Figure 5.1: Slippage between the boundary elements and the wall caused by shear.

The third failure mechanism might have occured in two different ways. Figure 5.1 shows that the load stub or the bridge deck restrains the boundary elements from slipping vertically against the structural wall in single bending. If, however, differences existed in the longitudinal strain gradients of the tension boundary element and the tension side of the structural wall, slippage might have occured in the plastic hinge region slightly above the footing. In the case of double bending (i.e. longitudinal response of a bridge with moment-resisting connections at top and bottom) such deformations and slippage may occur unrestrained, even if the longitudinal strain gradient is uniform. The case of double bending would have been expected to allow for more dramatic vertical slippage.

With the possibility of such slippage, two criteria for evaluating the effectiveness of transverse reinforcement are important. The reinforcing bars must both resist the horizontal shear force, as in the case of a typical circular or rectangular bridge column, and they must resist forces along the wall-boundary element interface resulting from vertical shear stress. Since the Phase I and Phase II tests were loaded in single bending, the first criterion of resisting horizontal shear force was considered sufficient.

5.3 Moment-Curvature Analysis

Moment-curvature analyses were conducted for each test unit section using non-linear concrete and steel reinforcement material models, with strain-based termination criteria. The stress strain relationships for steel are given in Chapter 3 and are described by a linear elastic branch, followed by a yield plateau and ending in a strain hardening branch, whose exponent is defined by the strain hardening modulus E_{sh}. The concrete model follows Mander's equations for confined and unconfined concrete [5]. For the predictions, steel strains were limited to ε_{su}, the measured ultimate tensile steel strain, while the concrete strains were limited to ε_{cu}, determined by the energy balance approach

$$\varepsilon_{cu} = .004 + \frac{1.4\rho_s f_{ysp}\varepsilon_{su}}{f'_{cc}} \tag{5.1}$$

where ρ_s is the volumetric reinforcement ratio of the spirals to the confined concrete, ε_{su} is the ultimate strain of the spiral steel, f_{ysp} is the spiral yield strength, and f'_{cc} is the compression strength of confined concrete according to Mander's model.

Column deflection was predicted as the sum of elastic and plastic components, given as

$$\Delta = \Delta_e + \Delta_p \tag{5.2}$$

Assuming purely flexural deflection and that plastic rotation occured about the column base, top deflection was calculated as

$$\Delta = \frac{\phi_y L^2}{3}\frac{M}{M_y} + \quad \phi - \phi_y \frac{M}{M_y} \quad L_p L \tag{5.3}$$

where M is the moment at a given level of displacement, ϕ is the curvature at that displacement level, M_y is the theoretical first yield moment, ϕ_y is the curvature at first yield, L is the column cantilever length (i.e. the distance between maximum and zero moment), and L_p is the equivalent plastic hinge length given by Priestley et al. [12] calculated as

$$L_p \qquad .08L + 0.15 f_y d_{bl} \geq 0.3 f_y d_{bl} \qquad (ksi) \qquad (5.4) \qquad =0$$

$$L_p \qquad .08L + 0.022 f_y d_{bl} \geq 0.044 f_y d_{bl} \qquad [MPa] \qquad (5.5) = 0$$

This plastic hinge length expression is made up of a component which is a function of the column length, $0.08L$, and a strain penetration component, $L_{sp} \qquad .15 f_y d_{bl}$ (ksi), for which f_y is the yield stress of the longitudinal steel and d_{bl} is the longitudinal bar diameter.

5.4 Web Crushing Failure

ACI [1] limits the allowable shear stress in a reinforced concrete structural wall to

$$v_{max} \qquad 0\sqrt{f'_c} \tag{5.6}$$

An expression containing $\sqrt{f'_c}$ emphasizes the importance of the tensile strength of concrete, while the physical phenomenon of web crushing is clearly a compression failure that should be related to f'_c directly.

While comparatively high shear forces are required to fail the structural wall concrete in direct diagonal compression, the cyclic nature of the applied loads degrades the structural wall in the plastic hinge region substantially at ductilities higher than $\mu_\Delta \quad 4$. Paulay et al. noted that previous tests conducted by Oesterle et al. [8], [6], Wang et al. [18] and Vallenas et al. [16] showed substantial degradation in the structural wall at ductilities higher than $\mu_\Delta \quad 4$. At ductility levels of $\mu_\Delta \leq 3$ the maximum shear stress was consistently $v \geq 0.16 f'_c$. After web failure, the boundary elements still carried a significant amount of shear by dowel action. It is recommended [9], however, not to rely on this dowel action but rather to preserve the integrity of the shear wall by limiting shear stresses according to the following relationship.

$$v_{max} \leq \quad \frac{0.22\phi_{o,w}}{\mu_\Delta} + 0.03 \quad f'_c < 0.16 f'_c \leq 870psi[6.0MPa] \tag{5.7}$$

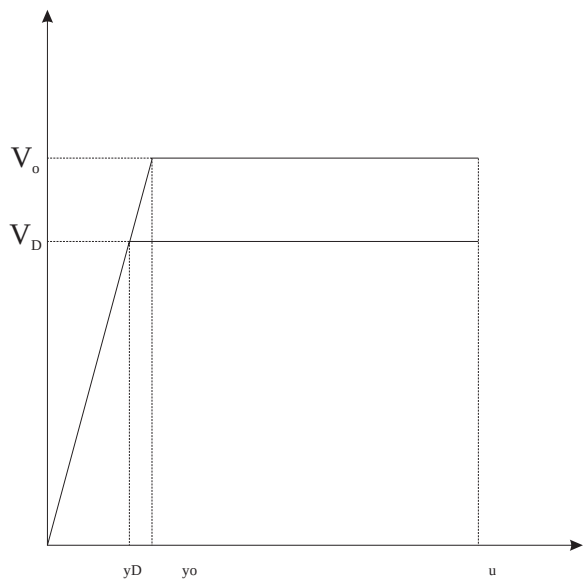

Figure 5.2: Idealized design and overstrength force-deflection curves.

Equation 5.7 is intended to be a conservative design equation, rather than a predictive assessment equation. For the purposes of this report, however, Equation 5.7 is used to assess the web crushing capacity of actual tests. Therefore the overstrength factor $\phi_{o,w}$ has been removed. Although this appears to make the equation even more conservative, it is an adjustment that is consistent with the assumptions behind the design equation.

Figure 5.2 shows that, the actual force level reached in a wall due to overstrength factors is V_o, corresponding to a displacement level of Δ_{yo} and a displacement ductility of $\mu_{\Delta o} \quad \frac{\Delta_u}{\Delta_{yo}}$. Equation 5.8 shows that the displacement ductility $\mu_{\Delta o}$ due to expected overstrength factors is equal to the design displacement ductility $\mu_{\Delta D}$ divided by the overstrength factor $\phi_{o,w}$.

$$\phi_{o,w} \quad \frac{V_o}{V_D} \quad \frac{\Delta_{yo}}{\Delta_{yD}} \quad \frac{\mu_{\Delta_D}}{\mu_{\Delta_o}} \longrightarrow \mu_{\Delta o} \quad \frac{\mu_{\Delta D}}{\phi_{o,w}} \tag{5.8}$$

Since the displacement ductility levels are taken from test results and correspond to $\mu_{\Delta o}$ there is no need to employ the adjustment factor $\phi_{o,w}$.

Oesterle et al. proposed a limitation to the assessment shear for structural walls with boundary elements that was less conservative, and was primarily a function of the axial load and drift ratio [7].

For axial load ratios lower than 9%

$$v_{wc} \quad \frac{1.8 f'_c}{1 + (600 - 2000 \frac{P}{A_g f'_c})\delta} \qquad 0 < \frac{P}{A_g f'_c} \leq 0.09 \tag{5.9}$$

For higher axial load ratios

$$v_{wc} \quad \frac{1.8 f'_c}{1 + 420\delta} \qquad \frac{P}{A_g f'_c} \geq 0.09 \tag{5.10}$$

where $\frac{P}{A_g f'_c}$ is the axial load ratio and $\delta \qquad /L$ is the drift ratio. Oesterle simplified these equations for design, assuming that a reasonable value for the drift ratio was $\delta \qquad .02.$ $=0$

$$v_{wc} \quad .14 f'_c + \frac{P}{2Dt_w} \qquad 0 < \frac{P}{A_g f'_c} \leq 0.09 \tag{5.11}$$ $=0$

$$v_{wc} \leq 0.18 f'_c \qquad \frac{P}{A_g f'_c} \geq 0.09 \tag{5.12}$$

These equations for web crushing are still closely related both to the expressions proposed by ACI and by Paulay et al. in that they assume that the shear is distributed evenly across the section, and the allowable shear stress is limited based on f'_c multiplied by a reduction factor. The assumption that the shear stresses are distributed uniformly across the section implies that only shear acts on the wall with no flexural component (see Figure 5.3).

All of these expressions for web crushing require the designer to determine an effective depth for each wall, however there exists little guidance on how to incorporate the relative size of the boundary elements into the evaluation of an effective depth. For instance, the existing web crushing equations imply that the two sections displayed in Figure 5.4 would have the same web crushing strength because they have the same wall thickness and the same total section depth. For the purpose of this example, imagine that the Carquinez Strait tower has the same web thickness (shown by the dashed line) as the East Bay Bridge Piers. Intuitively it seems that the larger boundary elements of the East Bay Bridge section should give it a greater web crushing capacity.

An alternative expression for web crushing is developed in Chapter 8, based on a model of the critical compression struts in the plastic hinge region instead of compression struts distributed uniformly across the section depth. Since high compressive stresses cannot develop in the struts which terminate at the flexural base crack, the entire shear force is assumed to be transferred into the compression toe via a concentrated region of compression struts. Many of the PCA tests confirm this assumption by demonstrating that web crushing typically initiates just outside of the compression toe.

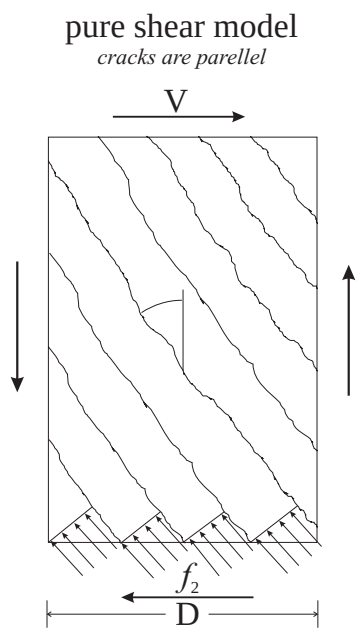

Figure 5.3: Free body diagram on which existing web crushing equations were developed.

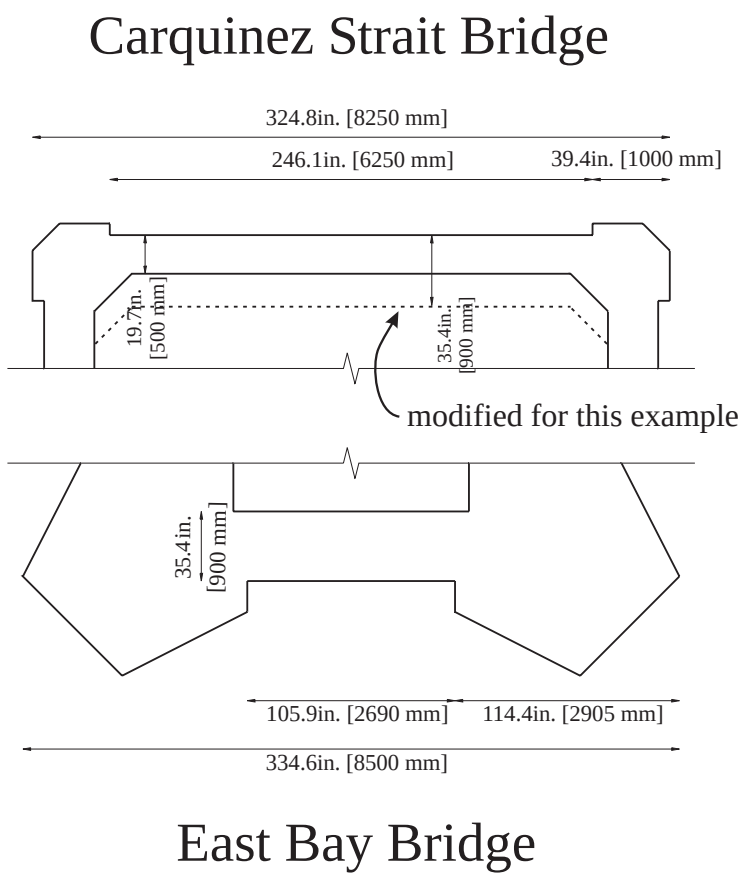

Figure 5.4: Top: Carquinez Strait Bridge Tower, half section. Bottom: San Francisco Oakland Bay Bridge, East Span Skyway Pier, half section.

5.5 Shear Equations

Shear capacity was evaluated based on a three component model (as opposed to the traditional two component model in the ACI Code) that is a function of the concrete, axial load and steel contributions.

$$V_n \quad V_c + V_p + V_s \tag{5.13}$$

The concrete contribution V_c, is a compilation of the shear resistance provided by aggregate interlock, dowel action of the longitudinal reinforcing bars, tension stiffening, and the compression toe. This component degraded according to the value γ with increasing ductility due to reduction in effectiveness of aggregate interlock as the crack width increases with ductility [10]. The concrete component is given as

$$V_c \qquad \gamma\beta\sqrt{f'_c}A_e \tag{5.14}$$

where A_e is the effective concrete area, taken typically as $A_e \quad 0.8A_g$ for circular and rectangular columns. In this report, A_e is taken as $A_e \quad Dt_w$, where D is the total section depth. While the reduction factor of 0.8 has been removed, A_e is still a reduced value of A_g because it does not include area in the boundary elements outside of the structural wall width. The definitions of and β in the V_c component are given below.

$$1 \leq \qquad - M/VD \leq 1.5 \tag{5.15}$$

$$\beta \qquad .5 + 20A_{st}/A_g \leq 1 \tag{5.16}$$

Values for γ as a function of curvature ductility and displacement ductility are given in Figure 5.5. These curves were simplified since [10] to consist of one descending slope instead of two [4].

The axial load contribution V_p, accounts for the fact that the column axial load is transmitted to the compression toe via a diagonal strut whose angle of inclination depends on the column aspect ratio. The expression for a cantilever in single bending is:

$$V_p \quad P\frac{D/2 - c/2}{L'} \tag{5.17}$$

where P is the axial load, D is the total section depth, c is the neutral axis depth and L' is the vertical distance from the point of axial load application to the compression toe of the column.

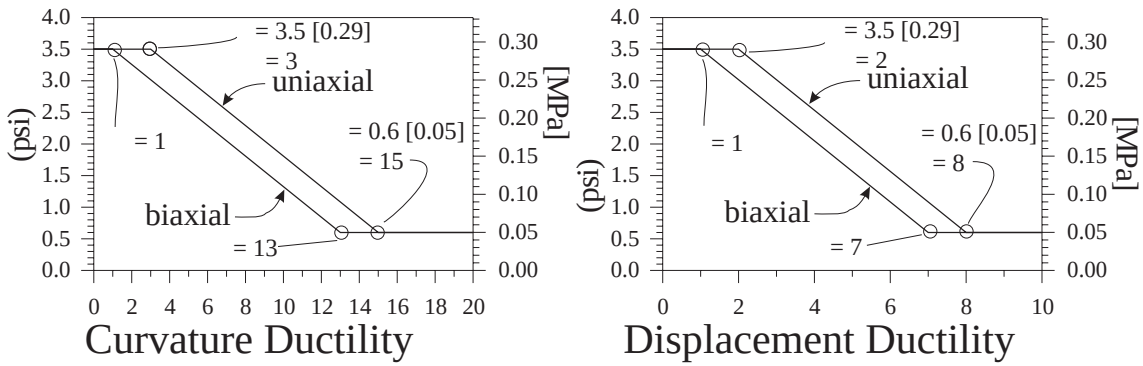

Figure 5.5: V_c parameter γ as a function of μ_ϕ and μ_Δ [4].

The steel contribution, V_s, accounts for the transverse steel that directly resisted lateral shear force across inclined cracks. V_s has separate expressions for rectangular and circular columns.

For rectangular columns

$$V_s \quad \frac{A_{tr} f_{ytr}(D - c - c_o)}{s_{tr}} cot\theta \tag{5.18}$$

and for circular columns

$$V_s \quad \frac{\pi}{2} \frac{A_{sp} f_{ysp}(D - c - c_o)}{s_{sp}} cot\theta \tag{5.19}$$

where A_{tr} is the steel area for a single layer of transverse reinforcement, A_{sp} is the area of a spiral, f_{ytr} is the transverse steel yield stress, f_{ysp} is the spiral steel yield stress, D is the total section depth, c is the compression zone depth, c_o is the depth of cover, s_{tr} is the vertical spacing between transverse bars, s_{sp} is the vertical spacing between the hoops or spirals, and is the average crack angle measured from the vertical, typically taken as 35° for design and 30° for assessment.

For this report, V_s is assumed to have an upper bound and a lower bound for structural walls with confined boundary elements. The lower bound includes only the transverse steel in the wall and in the tension boundary element. The upper bound includes the tension boundary element spiral in addition to the transverse steel.

5.6 Phase II Shear Capacity Envelopes

Figures 5.6-5.8 show the section analysis and finite element analysis predictions for Test Units 2A, 2B and 2C along with five separate shear capacity envelopes for these test units. These shear capacity envelopes represent the values calculated for the

Unit	A_g		A_e		f'_c		$\sqrt{f'_c}$		t_w		D	
	$in.^2$	$[m^2]$	$in.^2$	$[m^2]$	ksi	$[MPa]$	psi	$[kPa]$	$in.$	$[mm]$	$in.$	$[mm]$
2A	396	[0.255]	288	[0.185]	5.310	[36.6]	72.9	[502.4]	6.0	[152]	48.0	[1219]
2B	396	[0.255]	288	[0.185]	6.017	[41.5]	77.6	[535.1]	6.0	[152]	48.0	[1219]
2C	350	[0.225]	192	[0.124]	4.509	[31.1]	67.1	[463.0]	4.0	[102]	48.0	[1219]

Unit	f_{ytr}		A_{tr}		s_{tr}		f_{ysp}		A_{sp}		P	
	ksi	$[MPa]$	$in.^2$	$[mm^2]$	$in.$	$[mm]$	ksi	$[MPa]$	$in.^2$	$[mm^2]$	lbs	$[kN]$
2A	70.0	[482.7]	0.22	[142]	6.0	[152]	73.0	[503.3]	0.11	[71]	198,000	[881]
2B	59.0	[406.8]	0.10	[65]	8.0	[203]	73.0	[503.3]	0.11	[71]	198,000	[881]
2C	70.0	[482.7]	0.22	[142]	9.0	[229]	72.0	[496.4]	0.11	[71]	175,000	[779]

Table 5.1: General properties for the Phase II test units.

models discussed previously in this chapter and are labeled accordingly. Calculations for each test unit were performed for the following section. Table 5.1 gives general properties for the columns. A_g is the gross cross sectional area of the test unit, $A_e \quad Dt_w$ is the effective shear area, f'_c is the unconfined concrete strength measured on the day of the test, t_w is the wall thickness, D is the total depth of the test unit, f_{ytr} is the yield strength of the transverse steel, A_{tr} is the area of the transverse steel, s_{tr} is the vertical spacing of the transverse steel, f_{ysp} is the spiral strength, A_{sp} is the area of spiral steel, and P is the axial load applied to the test unit.

5.6.1 ACI 318-95

$$V_c \qquad 2(1+\frac{P}{2000A_g})\sqrt{f'_c}A_e$$

$$V_s \qquad A_{tr}f_{ytr}\frac{0.8D}{s_{tr}}$$

$$V \qquad V_c + V_s$$

Unit	V_c		V_s		V	
	$kips$	$[kN]$	$kips$	$[kN]$	$kips$	$[kN]$
2A	52.5	[233.5]	98.6	[438.8]	151.0	[672.1]
2B	55.8	[248.5]	28.3	[125.9]	84.2	[374.6]
2C	32.2	[143.4]	65.7	[292.4]	97.9	[435.8]

5.6.2 UCSD Shear Model: Priestley et al. [2000]

V_c $\quad \alpha\beta\gamma\sqrt{f'_c}A_e$

$$1 \leq \quad - M/VD \leq 1.5 \qquad =3$$
$$\beta \quad .5 + 20\frac{\rho_l+\rho_n}{2} \leq 1 \qquad =0$$
$$\gamma \quad f(\mu_\phi) \text{ (see Figure 5.5)}$$

V_p $\quad P\frac{D/2-c/2}{L'}$

V_{sw} $\quad A_{tr}f_{ytr}\frac{D-c-c_o}{s_{tr}}\cot 30°$

V_{tbe} $\quad \frac{\pi}{2}A_{sp}f_{ysp}\frac{D_{sp}}{s_{sp}}\cot 30°$

V_{up} $\quad V_c + V_p + V_{sw} + V_{tbe}$ (upper bound)

V_{low} $\quad V_c + V_p + V_{sw}$ (lower bound)

Unit	α		β		V_p		V_{sw}		V_{stb}	
					$kips$	$[kN]$	$kips$	$[kN]$	$kips$	$[kN]$
2A	1.0		0.78		36.8	[163.6]	171.0	[760.7]	77.1	[343.1]
2B	1.0		0.78		36.8	[163.6]	49.1	[218.6]	77.1	[343.1]
2C	1.0		0.82		32.5	[144.6]	114.0	[507.2]	76.0	[338.4]

Unit			μ_Δ	γ		V_c		V_{up}		V_{low}	
	$in.$	$[mm]$		ksi	$[MPa]$	$kips$	$[kN]$	$kips$	$[kN]$	$kips$	$[kN]$
2A	0.00	0.00	0.0	3.5	0.29	71.9	[319.8]	356.7	[1587.3]	279.6	[1244.2]
	0.74	19	2.1	3.5	0.29	71.9	[319.8]	356.7	[1587.3]	279.6	[1244.2]
	3.25	83	9.3	0.6	0.05	12.3	[54.8]	297.1	[1322.3]	220.0	[979.2]
	3.50	89	10.0	0.6	0.05	12.3	[54.8]	297.1	[1322.3]	220.0	[979.2]
2B	0.00	0.00	0.0	3.5	0.29	76.5	[340.5]	239.5	[1065.8]	162.4	[722.7]
	0.74	19	2.1	3.5	0.29	76.5	[340.5]	239.5	[1065.8]	162.4	[722.7]
	3.25	83	9.3	0.6	0.05	13.1	[58.4]	176.1	[783.7]	99.0	[440.6]
	3.50	89	10.0	0.6	0.05	13.1	[58.4]	176.1	[783.7]	99.0	[440.6]
2C	0.00	0.00	0.0	3.5	0.29	46.3	[205.8]	269.8	[1200.7]	192.7	[857.6]
	0.76	19	2.2	3.5	0.29	46.3	[205.8]	269.8	[1200.7]	192.7	[857.6]
	3.38	86	9.7	0.6	0.05	7.9	[35.3]	231.5	[1030.2]	154.4	[687.1]
	3.50	89	10.0	0.6	0.05	7.9	[35.3]	231.5	[1030.2]	154.4	[687.1]

5.6.3 ACI 318-95 – Web Crushing

v_{wc} $\quad 10\sqrt{f'_c}$

V_{wc} $\quad v_{wc}0.8Dt_w$

Unit	v_{wc}		V_{wc}	
	ksi	$[MPa]$	$kips$	$[kN]$
2A	0.73	[5.0]	167.6	[745.5]
2B	0.78	[5.4]	178.4	[793.6]
2C	0.67	[4.6]	103.4	[459.9]

5.6.4 Oesterle et al. [1984] – Web Crushing

$$v_{wc} \quad \frac{1.8 f'_c}{1+420\delta} \quad \leq \quad 0.18 f'_c$$

$$V_{wc} \quad v_{wc} 0.8 D t_w$$

Unit	Δ		δ	μ_Δ	v_{wc}		V_{wc}	
	$in.$	$[mm]$			ksi	$[MPa]$	$kips$	$[kN]$
2A	0.00	0.00	0.000	0.0	0.96	[6.6]	219.8	[978.1]
	2.10	53	0.022	6.0	0.94	[6.5]	215.8	[960.3]
	2.80	71	0.029	8.0	0.72	[5.0]	165.9	[738.3]
	3.50	89	0.036	10.0	0.59	[4.1]	134.8	[600.0]
2B	0.00	0.00	0.000	0.0	1.08	[7.5]	249.1	[1108.5]
	2.10	53	0.022	6.0	1.06	[7.3]	244.5	[1088.0]
	2.80	71	0.029	8.0	0.82	[5.7]	188.0	[836.6]
	3.50	89	0.036	10.0	0.66	[4.6]	152.7	[679.5]
2C	0.00	0.00	0.000	0.0	0.81	[5.6]	125.0	[556.3]
	2.10	53	0.022	6.0	0.80	[5.5]	122.7	[546.0]
	2.80	71	0.029	8.0	0.61	[4.2]	94.3	[419.6]
	3.50	89	0.036	10.0	0.50	[3.4]	76.6	[340.9]

5.6.5 Paulay et al. [1992] – Web Crushing

$$v_{wc} \quad \frac{0.22}{\mu_\Delta} + 0.03 \quad f'_c \quad \leq \quad 0.16 f'_c \quad \leq \quad 870psi[5.98MPa]$$

$$V_{wc} \quad v_{wc} 0.8 D t_w$$

Unit	Δ		μ_Δ	v_{wc}		V_{wc}	
	$in.$	$[mm]$		ksi	$[MPa]$	$kips$	$[kN]$
2A	0.00	0	0.0	0.85	[5.9]	195.4	[869.5]
	0.35	9	1.0	0.85	[5.9]	195.4	[869.5]
	0.70	18	2.0	0.74	[5.1]	171.0	[761.0]
	1.05	27	3.0	0.55	[3.8]	126.2	[561.6]
	1.40	36	4.0	0.45	[3.1]	103.8	[461.9]
	2.10	53	6.0	0.35	[2.4]	81.4	[362.2]
	2.80	71	8.0	0.31	[2.1]	70.2	[312.4]
	3.50	89	10.0	0.28	[1.9]	63.5	[282.6]
2B	0.00	0	0.0	0.96	[6.6]	221.8	[987.1]
	0.35	9	1.0	0.96	[6.6]	221.8	[987.1]
	0.70	18	2.0	0.84	[5.8]	193.7	[862.0]
	1.05	27	3.0	0.62	[4.3]	143.0	[636.4]
	1.40	36	4.0	0.51	[3.5]	117.6	[523.3]
	2.10	53	6.0	0.40	[2.8]	92.3	[410.7]
	2.80	71	8.0	0.35	[2.4]	79.6	[354.2]
	3.50	89	10.0	0.31	[2.1]	72.0	[320.4]
2C	0.00	0	0.0	0.72	[5.0]	111.1	[494.4]
	0.35	9	1.0	0.72	[5.0]	111.1	[494.4]
	0.70	18	2.0	0.63	[4.3]	97.2	[432.5]
	1.05	27	3.0	0.47	[3.2]	71.8	[319.5]
	1.40	36	4.0	0.38	[2.6]	59.0	[262.6]
	2.10	53	6.0	0.30	[2.1]	46.3	[206.0]
	2.80	71	8.0	0.26	[1.8]	39.9	[177.6]
	3.50	89	10.0	0.23	[1.6]	36.1	[160.6]

5.6.6 Force-Deflection Curves and Shear Envelopes

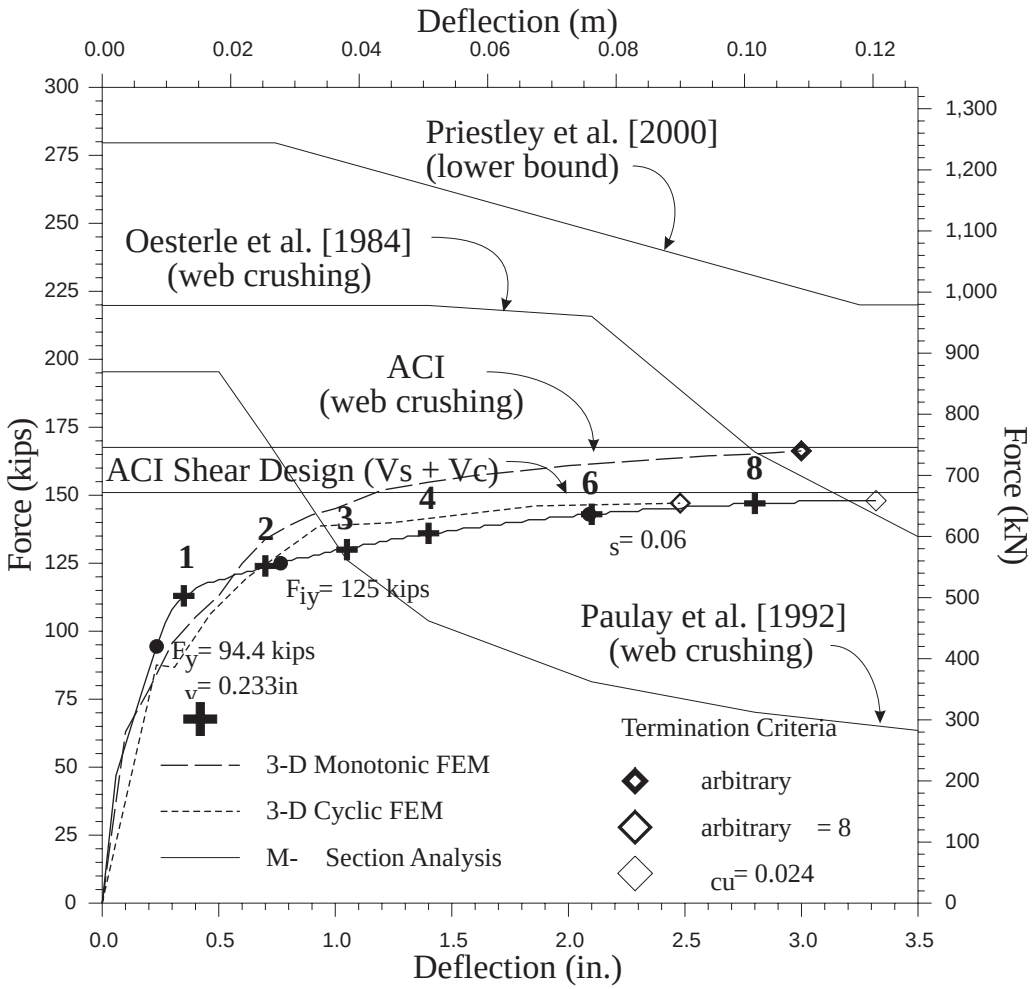

Figure 5.6: Unit 2A: predicted force-deflection curves and shear envelopes.

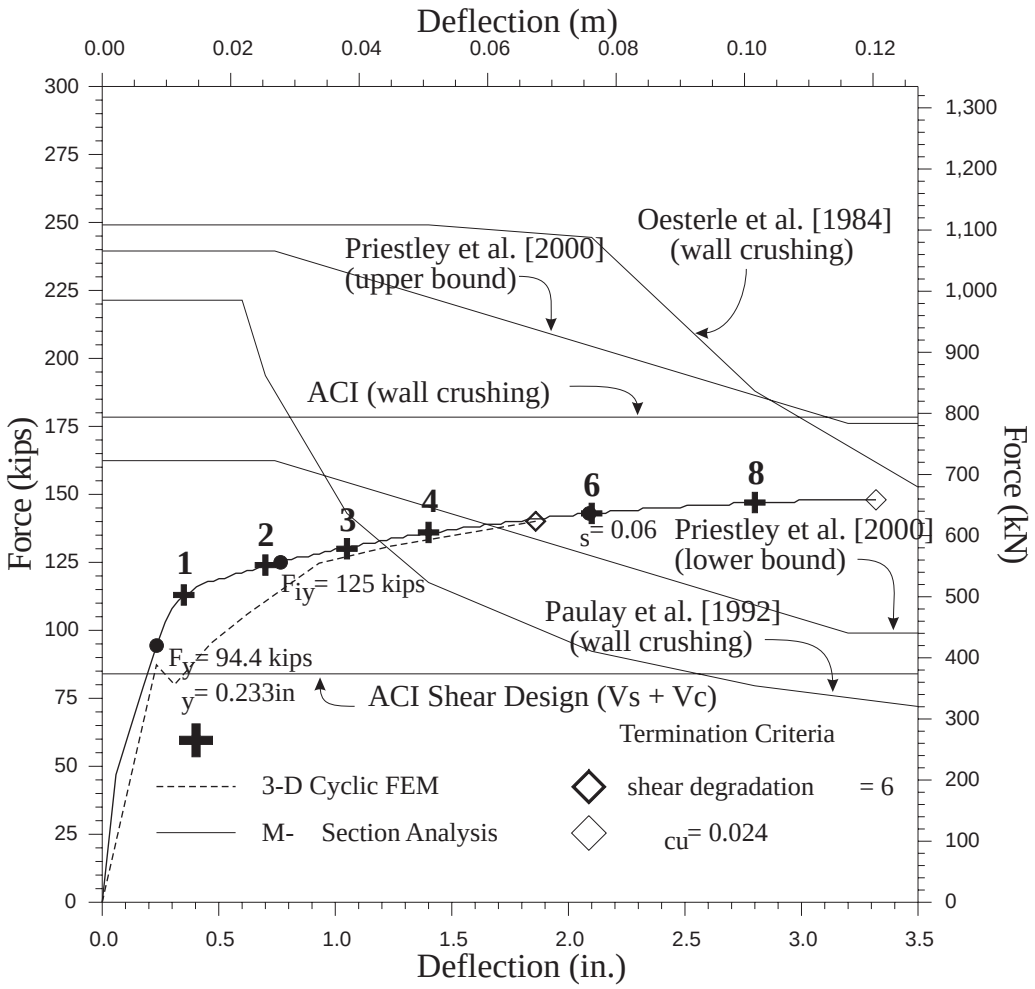

Figure 5.7: Unit 2B: predicted force-deflection curves and shear envelopes.

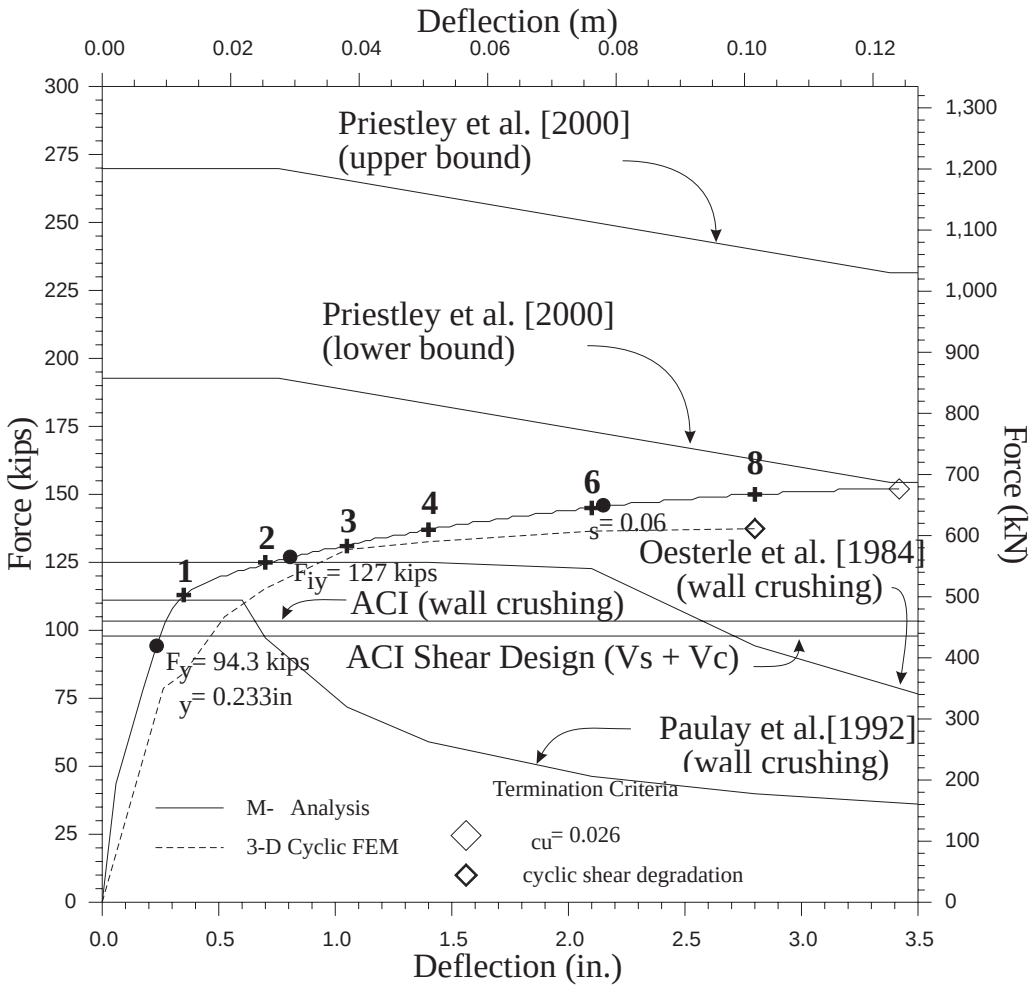

Figure 5.8: Unit 2C: predicted force-deflection curves and shear envelopes.

Chapter 6

Test Observations

6.1 Overview

Test observations are presented for each of the five tests. These observations refer to the photos in Appendix A.

6.2 Unit 1A

6.2.1 Summary

Test Unit 1A performance was dominated by flexure, with flexural cracks extending just over half way up the column height. Cracks tended to originate as horizontal cracks in the tension boundary element and then arc gradually downward once inside the wall. Cracks propagated into the compression boundary element by $\mu_\Delta = 3.0$, reaching the neutral axis position of 9 in. [229 mm] into the compression boundary element from the extreme compression fiber predicted by the moment-curvature analysis. Spalling at the column base due to high compressive strains began to occur at $\mu_\Delta = 3.0$. Before spalling off, the concrete cracked vertically at the base of the compression boundary elements, causing the cover concrete to fall off in chunks roughly 3in. x 5in. [76mm x 127mm] in size. Longitudinal bars began to buckle during the first cycle of $\mu_\Delta = 6.0$ and fractured during the third cycle of $\mu_\Delta = 6.0$, causing severe strength degradation.

6.2.2 First Cracking ($3/4F_y$)

The first cracks formed at a load of F=31.9kips [142.0kN]. These cracks formed at roughly 6in. [152mm] intervals and remained within the tension boundary element (see Figure A.2).

6.2.3 Steel Yield (F_y)

Cracks formed up to a height of 60in. [1524mm] in the tension boundary element and propagated up to half way into the wall. These cracks arced into the wall very gradually. They were nearly horizontal on the inside face of the tension boundary element and reached a maximum angle of 45° from the vertical half way into the wall (see Figure A.1).

6.2.4 Propagation of Flexure/Shear Cracks ($\mu = 1.0 - 2.0$)

Figure A.3 shows a flexure-shear crack just reaching the inside face of the compression boundary element at μ_Δ=1.5x1 (F=63.1kips [280.8kN]). Figure A.4 shows the cracking pattern for the lower portion of the column at μ_Δ=1.5x3.

At μ_Δ =2.0x1 (F=63.5kips [282.6kN]) cracks reached a height of roughly 96in. [2438mm] (1/2 of the unit height) on either side of the unit. Flexural cracks at the base of the wall were shared under both positive and negative loading.

6.2.5 Initiation of Spalling ($\mu = 3.0$)

Figure A.5 shows incipient spalling at the compression boundary element base during the first cycle (F=66.0kips [293.7kN]). Vertical cracks can be seen outlining chunks of cover concrete that were about to spall off in single pieces. By the third positive excursion to μ_Δ =3 .0, these chunks had fallen off only the south boundary element. Figure A.6 depicts the extent of spalling in this column reaching up to a height of 13in. [330mm].

6.2.6 Growth of Spalled Region ($\mu = 4.0$)

The spalled region on the north boundary element is shown in Figure A.7 not having developed much further than its state at μ_Δ =3.0x1.

6.2.7 Full Development of Spalled Region ($\mu = 6.0$)

Figure A.9 shows the fully developed spalled region for the compression boundary element (north). The spalled region on the north boundary element reached a height of 18in. [457mm] whereas the spalled region on the south boundary element reached a height of 24in. [610mm]. Figure A.8 shows the deformation and crack pattern for the first cycle (F=72.5kips [322.6kN]). Flexure shear cracks extended just over half way

up the column, reaching the compression boundary element at heights below 48in. [1219mm].

6.2.8 Strength Loss due to Bar Fracture ($\mu = 6.0 - 8.0$)

The first longitudinal bar fractured during the third positive excursion to μ_Δ .0. This bar did not show visible signs of buckling before it fractured, so it was assumed to have experienced very high compressive and tensile strains just as a consequence of deforming axially under high curvatures.

Figure A.11 shows the extent of deformation in the column at μ_Δ =-8.0x1 (F=63.8kips [283.9kN]). Figure A.12 shows the full degradation of the tension boundary element (south) after the third excursion to μ_Δ .0. The concrete core crushed and spilled out, moving the compression zone into the wall.

6.3 Unit 1B

6.3.1 Summary

Test Unit 1B performance was dominated by flexure, with flexural cracks extending almost three quarters of the way up the column height. Cracks tended to originate as horizontal cracks in the tension boundary element and then arc gradually downward once inside the wall. At μ_Δ 1.5, new shear cracks formed to join up pre-existing flexural cracks to create new flexure-shear cracks at steeper angles. Both the wall and the boundary elements cracked to a much greater extent than they did in Unit 1A. Spalling at the column base due to high compressive strains began to occur at μ_Δ .0. The concrete spalled off in large chunks, similar to Unit 1A. Longitudinal bars began to buckle during the first cycle of μ_Δ .0 and fractured during the first cycle of μ_Δ .0, causing severe strength degradation in the unit. =8

6.3.2 First Cracking ($3/4F_y$)

The first cracks formed at a load of F=33.5kips [149.1kN] and are shown in Figure A.13. These cracks formed at roughly 6in. [152mm] intervals up to a height of 24in. [610mm] and then at 12in. [305mm] intervals up to a height of 62in. [1575mm] (see Figure A.2). These cracks penetrated into the wall only in the bottom 36in. [914mm] to a maximum of 4in. [102mm].

6.3.3 Steel Yield (F_y)

Flexural cracks formed at regular 6in. [152mm] intervals up to a height of 72in. [1829mm]. These cracks propagated into the wall inclined at an average angle of 60° from the vertical and a maximum inclination of 45° from the vertical. Such flexure-shear cracks in the wall reached up to 4in. [102mm] from the compression boundary element at a height of 24in. [610mm], but closer to 8in. [203mm] from the compression boundary element at greater and lesser heights (see Figure A.14).

6.3.4 Propagation of Flexure/Shear Cracks ($\mu = 1.0 - 2.0$)

Figure A.15 shows a shear crack that formed from 39in. [991mm] to 44in. [1118mm] height between the wall and the tension boundary element during the first negative excursion to μ_Δ 1.0 (F=-54.2kips [241.2kN]). Also visible are the slight propagations of the existing flexure-shear cracks from the positive cycle. Figure A.16 shows how shear cracks formed consistently from a height of 43in. [1092mm] to a height of 75in. [1905mm] to join existing flexural cracks at μ_Δ=1.5x1. These new shear cracks ranged in inclination from 50° from the vertical at 48in. [1219mm] to 25° from the vertical at 64in. [1626mm].

At μ_Δ=2.0x1 (F=65.5kips [291.5kN]) cracks reached a height of roughly 96in. [2438mm] (1/2 of the column height) on either side of the unit. Flexure/shear cracks arced through the wall and reached the compression boundary element up to 24in. [610mm] high at a maximum inclination of 25° from the vertical.

6.3.5 Initiation of Spalling ($\mu = 3.0$)

Figure A.18 shows initial spalling at the tension boundary element base during the first cycle (F=-66.3kips [-295.0kN]). The spalled region is clear cut, indicating that the concrete came off in large chunks as it did in Unit 1A.

Figure A.17 depicts the crack pattern at μ_Δ=-3.0x1 from 12in. [305mm] to 72in. [1829mm] up the column height. Flexure-shear cracks penetrated 3in. [76mm] into the compression boundary element at less than 24in. [610mm] height.

6.3.6 Growth of Spalled Region ($\mu = 4.0$)

Figure A.19 shows further development of the spalled region, where concrete has spalled off from 0in. to 6in. [152mm] height and from 18in. [457mm] to 42in. [1067mm] height. The concrete between the two spalled regions most likely did not

fall off because it was more strongly attached to the boundary element via wire ties or plastic cable ties, not because it had not experienced high compression strains.

6.3.7 Full Development of Spalled Region ($\mu = 6.0$)

Figure A.20 shows the deformation and crack pattern up to a height of 84in. [2134mm] at μ_Δ=6.0x1. Spalling can be seen to have occurred up to 24in. [610mm] high on the compression boundary element (left) and up to 18in. [457mm] high on the tension boundary element (right). Figure A.21 shows major spalling in the compression boundary element up to a height of 24in. [610mm]. Even though, concrete spalled up to a height of 42in. [1067mm] it is likely that the zone containing high compressive strains extended only up to 24in. [610mm].

6.3.8 Strength Loss due to Bar Fracture ($\mu = 6.0 - 8.0$)

Figure A.22 shows the first signs of bar buckling in the compression boundary element during the third negative excursion to μ_Δ .0. Figure A.23 shows a front view of the deformation and cracked pattern of the column at μ_Δ=8.0x1. Flexure/shear cracks extended nearly three quarters of the way up the column height. Figure A.24 shows three bar fractures that occurred in the tension boundary element while cycling to μ_Δ -2.0 (F=-55.9kips [-248.8kN]) at 1.5in. [38mm], 7.5in. [191mm] and 10.5in. [267mm] height. While completing the third cycle at μ_Δ 8.0, several more bars fractured, leading to significant strength degradation and degradation of the core concrete at the base of each boundary element.

6.4 Unit 2A

6.4.1 Summary

Test Unit 2A performance was dominated by flexure, with shear cracks extending up higher than 3/4 of the column height. Cracks tended to originate as horizontal cracks in the tension boundary element and then angle downward once inside the wall. Shear cracks formed either independently or to connect existing flexural cracks on the interface between the tension boundary element and the wall. Cracks propagated 3 in. [76 mm] from the wall/boundary element interface into the compression boundary element by μ_Δ 3.0, reaching the predicted neutral axis position. Spalling at the column base due to high compression strains began to occur at μ_Δ .0. The spalled region increased in size through μ_Δ 4.0 and developed fully by the last cycle of

μ_Δ .0. Longitudinal bars began to buckle during the third cycle of μ_Δ=6 .0 and fractured during the second cycle of μ_Δ .0, causing severe strength degradation.

6.4.2 First Cracking ($3/4F_y$)

The first cracks formed at a load of F=70.8kips [315.1kN]. These cracks formed at roughly 6in. [152mm] intervals up to a height of 22in. [559mm]. While remaining nearly horizontal in the tension boundary element, the two cracks below 12in. [305mm] angled sharply into the wall at roughly 55° from the vertical, forming an initial compression strut (see Figure A.25). During the excursion to $-3/4F_y$ cracks formed up to a height of 24in. [610mm].

6.4.3 Steel Yield (F_y)

Cracks formed up to a height of 48in. [1219mm] in the tension boundary element at widths of roughly 0.0039in. [0.1mm]. At a height of 35in. [889mm], these cracks began to see some inclination in the tension boundary element. The crack at 48in. [1219mm] inclined to 45° from the vertical in the tension boundary element and 35° from the vertical half way into the wall at a height of 32in. [813mm]. All of the cracks formed at $3/4F_y$ extended at constant angles to the base, pushing the neutral axis close to the inside edge of the compression boundary element (see Figure A.26).

6.4.4 Formation of Shear Cracks ($\mu = 1.0 - 2.0$)

At μ_Δ=1.0x1 (F=105.4kips [469.0kN]), existing cracks propagated further into the wall, however no new cracks formed higher than 48in. [1219mm] above the base. At roughly 42in. [1067mm] above the base, an existing crack in the tension boundary element inclined sharply through the chamfer to join up with the crack that had formed 36in. [914mm] above the base. Likewise, at μ_Δ=-1.0x1 (F=-105.5kips [469.5kN]), existing cracks propagated further into the wall. One new crack formed just higher than 54in. [1372mm] above the base, inclined 65° from the vertical on the inside chamfer (see Figure A.27). A flexural crack at 37in. [940mm] inclined to 40° from the vertical through the inside chamfer to connect with another existing crack at 34in. [864mm]. Such inclination of cracks in the tension boundary element suggested that the spirals were mobilized to enhance the unit's shear capacity. Note that these cracks crossed the transverse bars placed at 36in. [914mm] and 54in. [1372mm] height. By the third cycle of μ_Δ 1.0 (F=102.8kips [457.5kN]), no new cracks had formed and existing

cracks propagated roughly 2in. [51mm] further into the wall. Flexural crack widths reached 0.0039in. [0.1mm] and shear crack widths reached 0.0019in. [0.05mm].

At μ_Δ=1.5x1 (F=121.4kips [540.2kN]) two new flexural cracks formed in the tension boundary element at 55in. [1397mm] and at 60in. [1520mm]. These cracks essentially joined in the wall to form a single crack that propagated further into the wall at 35° from the vertical. In the first negative excursion to μ_Δ=-1.5x1 (F=-119.4kips [531.3kN]), three new shear cracks formed at heights of 60in. [1524mm], 66in. [1676mm] and 71in. [1803mm] above the base in the tension boundary element (see Figure A.28). The lower two of these cracks propagated into the wall at 35° from the vertical. The lowest crack, beginning at 60in. [1524mm] height inside the tension boundary element propagated to within 3in. [76mm] of the compression boundary element. Cracks in the wall propagated 1in. [25mm] to 2in. [51mm] further during the third cycle.

At μ_Δ=2.0x1 (127.0kips [565.2kN]) cracks reached a height of roughly 72in. [1829mm] (3/4 of the unit height) on either side of the unit. Nearly vertical cracks propagated upward from several existing tension boundary element cracks ranging from 24in. [610mm] to 66in. [1676mm] high, indicating that the spirals were mobilized to resist the column shear. Cracks extended up to 3in. [76mm] into the compression boundary element. Flexural crack widths reached from 0.0335in. [0.85mm] to 0.0472in. [1.2mm] and shear crack widths reached 0.0059in. [0.15mm].

6.4.5 Initiation of Spalling ($\mu = 3.0$)

Figure A.29 shows the deformation and crack pattern for the entire unit during the first cycle (F=131.9kips [587.0kN]). Existing cracks propagated further, but no new cracks formed. Figure A.30 shows incipient spalling at the base of the compression boundary element. During the first cycle flexural crack widths reached 0.0709in. [1.8mm] and shear crack widths reached 0.0079in. [0.2mm]. At the third positive cycle (F=124.1kips [552.2kN]), cracks in the wall increased in width as displayed in Table 6.1. At the third negative cycle (F=-123.0kips [547.4kN]) new cracks propagated upward from existing cracks in the tension boundary element.

6.4.6 Growth of Spalled Region ($\mu = 4.0$)

The spalled region increased in size to a height of 7in. [178mm] as shown in Figure A.31. New flexure shear cracks formed in the plastic hinge region. In the third cycle (F=126.2kips [561.6kN]) new shear cracks formed above 72in. [1829mm] high. A

Height, in. [mm]	Angle from Vertical	Crack Width, in. [mm]
7 [178]	45°	0.0315 [0.80]
20 [508]	50°	0.0236 [0.60]
32 [813]	45°	0.0197 [0.50]
42 [1067]	45°	0.0098 [0.25]

Table 6.1: μ_Δ=3.0x3: Crack widths up column height.

Height, in. [mm]	Angle from Vertical	Crack Width, in. [mm]
7 [178]	45°	0.0551 [1.40]
20 [508]	50°	0.0472 [1.20]
32 [813]	45°	0.0236 [0.60]
42 [1067]	45°	0.0118 [0.30]

Table 6.2: μ_Δ=6.0x3: Crack widths up column height.

vertical crack also formed between the tension boundary element and the structural wall at 30in. [762mm], the location of another pair of transverse bars.

6.4.7 Full Development of Spalled Region ($\mu = 6.0$)

Figure A.32 shows the deformation and crack pattern for the first cycle (F=135.9kips [604.8kN]). Flexural cracks grew to widths of 0.1575in. [4mm]. Both spiral and longitudinal reinforcing steel became visible in the fully developed spalled region see Figure A.33. Longitudinal bars showed the first sign of buckling in the compression boundary element during the first negative cycle (F=-131.8kips [586.5kN]). By the third positive cycle (F=128.3kips [570.9kN]) crack widths reached their values displayed in Table 6.2. Figure A.34 shows the extent of bar buckling at the peak of the third negative cycle (F=-125.8kips [559.8kN]).

6.4.8 Strength Loss due to Bar Fracture ($\mu = 8.0$)

Figure A.35 shows the deformation and crack pattern at the peak of the first positive cycle (F=135.0kips [600.8kN]). Existing flexure-shear cracks in the plastic hinge region were fully connected by vertical shear cracks on the tension boundary element/wall interface. Longitudinal bars buckled further in both boundary elements and began to fracture at the second cycle (F=118.0kips [525.1kN]). Figure A.36 shows such a bar after fracture.

6.5 Unit 2B

6.5.1 Summary

Test Unit 2B performance was dominated by flexure up to μ_Δ 8.0, with shear cracks extending up the entire column height. Cracks lower on the column tended to originate as horizontal cracks in the tension boundary element and then angle downward once inside the structural wall. Cracks higher up the column began at roughly 45° from the vertical in the tension boundary element and inclined to as much as 25° from the vertical once inside the wall. Cracks propagated one quarter of the way into the compression boundary element by μ_Δ .0, reaching the predicted neutral axis position. Spalling at the unit base due to high compression strains began to occur at μ_Δ 3.0. The spalled region increased in size through μ_Δ 4.0 and developed fully by the last cycle of μ_Δ 6.0. The wall began to show signs of crushing during the first cycle of μ_Δ .0. Longitudinal bars began to buckle during the first cycle of μ_Δ 8.0, however, by the third cycle of μ_Δ 8.0 the wall had crushed extensively at the midheight and the column strength had begun to degrade. During the last cycle of μ_Δ .0 the column grew significantly wider in the middle due to large transverse strains at the column midheight. This gave the column the appearance of deforming in double bending.

Particular attention is devoted to the development of flexure-shear cracks in the tension boundary element and structural wall. The development of these cracks, particularly in between steel yield and spalling, shows how the transverse reinforcement in the wall and the spiral reinforcement in the tension boundary element were mobilized through cracking to help the column resist shear.

6.5.2 First Cracking ($3/4F_y$)

The first cracks formed at a load of F=71.1kips [316.4kN]. These two cracks formed in the tension boundary element at 7in. [178mm] and 15in. [381mm] height, barely penetrating into the structural wall (see Figure A.37). Three more cracks formed during the negative excursion to F=-71.0kips [-316.0kN] at 8in. [203mm] intervals to a height of 24in. [610mm]. These cracks propagated a maximum of 5in. [127mm] into the wall.

6.5.3 Steel Yield (F_y)

At a load of 94.5kips [420.5kN], cracks formed up to a height of 42in [1067mm] in the tension boundary element and propagated into the wall to within 3in. [76mm] of the compression boundary element. Cracks in the tension boundary element began to incline up to 45° from the vertical from 15in. [381mm] to 19in. [483mm] and from 35in. [889mm] to 40in. [1016mm] reaching a width of 0.0019in. [0.05mm] (see Figure A.38). Cracks reached up to 44in. [1118mm] high in the tension boundary element during the negative excursion, with angles of 45° from the vertical inside the structural wall.

6.5.4 Formation of Shear Cracks ($\mu \quad = 1.0 - 2.0$)

At μ_Δ=1.0x1 (F=107.1kips [476.6kN]), cracking extended up to 48in [1219mm] high in the tension boundary element. Some of these cracks angled steeply to join each other as a single crack in the structural wall. At 16in. [406mm] and 31in. [787mm] cracks propagated upward from existing cracks in order to activate the capacity of the transverse bars found at these locations. (Transverse bars in Unit 2B were spaced on 8in. [203mm] vertical intervals.) Likewise, at μ_Δ=-1.0x1 (F=-104.1kips [463.2kN]), vertical cracks formed between the tension boundary element and structural wall at 24in. [610mm] and 48in. [1219mm] high–also locations of transverse bars (see Figure A.39).

At μ_Δ 1.5x1 (F=118.8kips [528.7kN]) two new flexural cracks formed in the tension boundary element at 60in. [1524mm] and at 72in. [1829mm]. The highest crack reached an angle of 25° from the vertical in the structural wall. Flexure/shear cracks penetrated into the compression boundary element up to a height of 18in. [457mm]. During the first negative excursion (F=-119.9kips [533.6kN]), new flexure-shear cracks formed at 64in. [1626mm] and 72in. [1829mm] high inside the tension boundary element. On the inside chamfer, the crack at 64in. [1626mm] was inclined to 35° from the vertical. At 72in. [1829mm] the crack inclined only to 50° from the vertical. Figure A.40 shows a new shear crack that originated from 56in. [1422mm] to 63in. [1600mm] on the tension boundary element/wall interface during the third positive cycle, μ_Δ=1.5x3 (F=112.4kips [500.2kN]). During the third negative cycle, μ_Δ=-1.5x3 (F=-112.8kips [-502.0kN]), a new shear crack formed on the tension boundary element/wall interface at a height of just above 72in. [1829mm]. The fact that new shear cracks formed at the top of the column during both the positive and negative excursions of the third cycle indicated that the column deformed further in

shear with additional cycles.

At μ_Δ=2.0x1 (F=125.3kips [557.6kN]) a new shear crack formed in the wall at an angle 25° from the vertical, 48in. [1219mm] high near the compression boundary element. Other shear cracks extended further into the wall, reaching a width of 0.0354in [0.9mm]. At μ_Δ=-2.0x1 (F=-123.0kips [-547.4kN]) flexure-shear cracks became almost vertical as they penetrated into the compression boundary element. Shear cracks penetrated further into the top of the tension boundary element. Flexural cracks in the lower tension boundary element reached a width of 0.0551in. [1.4mm] at 7in. [178mm]. During the third cycle, some new shear cracks formed under both positive and negative loading, indicating again that the column deformed further in shear with additional cycles.

6.5.5 Initiation of Spalling ($\mu = 3.0$)

Figure A.41 shows the deformation and crack pattern for the entire column during the first positive excursion (F=130.0kips [578.5kN]). Figure A.42 shows incipient spalling at the base of the compression boundary element up to a height of 3in. [76mm]. Flexure shear cracks penetrated into the compression boundary element to a depth of 3in. [76mm] to 5in. [127mm] up to a height of 10in. [254mm]. Flexure/shear cracks reached a width of 0.0236in. [0.6mm] at 16in. [406mm] up the wall and 0.0472in. [1.2mm] at 42in. [1067mm] up the wall. During the first negative excursion (F=-126.5kips [-562.9kN]), new vertical cracks formed in the wall close to the compression boundary element/wall interface from 54in. [1372mm] to 68in. [1727mm]. A crack also propagated from the compression boundary element/wall interface at 82in. [2083mm] into the load stub. Cracks symmetric to those just described in the negative direction also formed by the third positive excursion (F=121.6kips [541.1kN]).

6.5.6 Growth of Spalled Region ($\mu = 4.0$)

Figure A.43 shows that the spalled region reached a height of 7in. [178mm] in the compression boundary element. During the third positive excursion (F=121.8kips [542kN]) a shear crack formed from the load stub down to the compression boundary element at 48in. [1219mm], forming a steeply angled compression strut in the wall. Flexure/shear crack widths are displayed in Table 6.3.

Height, in. [mm]	Angle from Vertical	Crack Width, in. [mm]
20 [508]	45°	0.0551 [1.40]
32 [813]	40°	0.0315 [0.80]
44 [1118]	40°	0.0551 [1.40]
53 [1346]	35°	0.0551 [1.40]

Table 6.3: μ_Δ=6.0x3: Crack widths up column height.

6.5.7 Full Development of Spalled Region ($\mu \quad = 6.0$)

Figure A.45 shows the full extent of spalling in the compression boundary element. Figure A.44 shows the deformation and crack pattern for the first cycle (F=134.1kips [596.7kN]). With the shear crack that formed at $\mu_\Delta \quad 4.0x3$, it is clear that the compression struts inclined up the unit to an extent that direct load transfer is possible from the load stub to the compression toe. This figure shows how the shear crack formed at μ_Δ=4.0x3 has linked up with the shear cracks formed at μ_Δ=3.0x3 to form the outline of this compression strut. Some incipient crushing occurred in the wall near the tension boundary element at a height of 28in. [711mm]. Similar spalling occurred inside the wall at 49in. [1245mm]. The steepest shear crack inside the wall, reached a width of 0.0709in [1.8mm] at 65in. [1651mm] high and 0.0787in. [2.0mm] at 71in. [1803mm] high.

During further cycles, major shear cracks reached a width of 0.0984in. [2.5mm] and new signs of wall degradation appeared by the end of each excursion. Figure A.46 shows the onset of wall degradation at a height of 44in. [1118mm] in the center of the structural wall.

6.5.8 Strength Loss due to Wall Degradation ($\mu \quad = 8.0$)

Figure A.47 shows the deformation and crack pattern at the peak of the first positive excursion (F=128.8kips [573.2kN]). From the crack pattern it is possible to see a single compression strut connecting the load stub and the compression toe. Almost vertical cracks opened near the interface of the wall and the compression boundary element from 30in. [762mm] to 38in. [965mm], directing the compression strut to a point of convergence in the compression toe. By the peak of the first negative excursion (F=-126.3kips [-562kN]), a bar in the compression boundary element had begun to buckle and a major shear crack had reached a width of 0.2362in. [6mm] near the base.

Figure A.48 shows that by the third positive excursion (F=101.1kips [449.9kN]),

the wall degraded to the point of exposing both the longitudinal and transverse reinforcement. The transverse strains grew to an extent that was visible to the naked eye.

6.6 Unit 2C

6.6.1 Summary

Test Unit 2C performance was dominated by flexure up to μ_Δ 8.0, with shear cracks extending up the entire column height. Cracks lower on the column tended to originate as horizontal cracks in the tension boundary element and then angle downward once inside the structural wall. Cracks higher up the column began at roughly 45° from the vertical in the tension boundary element and inclined to as much as 25° from the vertical once inside the wall. Most shear cracking occurred as early as F_y, but then once the shear cracks formed, they did not dramatically increase in size at higher displacement ductilities. After μ_Δ 1.5 the much wider cracks began to develop in the plastic hinge region and flexure dominated for the rest of the test. Cracks propagated 3 in. [76 mm] from the wall/boundary element interface into the compression boundary element by μ_Δ .0, reaching the predicted neutral axis position. Spalling at the column base due to high compression strains began to occur at μ_Δ 3.0. The spalled region increased in size through μ_Δ 4.0 and developed fully by the last cycle of μ_Δ 6.0. The wall began to show signs of crushing during the first cycle of μ_Δ .0. Longitudinal bars began to buckle during the first cycle of μ_Δ .0 and eventually fractured while cycling at μ_Δ .0. =8

6.6.2 First Cracking ($3/4F_y$)

The first cracks formed at a load of F=71.1kips [316.4kN]. These two cracks formed in the tension boundary element at 6in. [152mm] intervals up to 18in. [457mm] height, angling to 45° from the vertical once inside the structural wall (see Figure A.49). Cracks formed during the negative excursion to F=-71.0kips [-316.0kN] at approximately 8in. [203mm] intervals to a height of 24in. [610mm].

6.6.3 Steel Yield (F_y)

At a load of F 94.5kips [420.5kN], the column deformed to the prescribed μ_Δ displacement of 0.35in. [8.9mm]. Flexural cracking extended 60in. [1524mm] up the tension boundary element. One shear crack, angled at 35° from the vertical,

Height, in. [mm]	Angle from Vertical	Crack Width, in. [mm]
13 [330]	60°	0.0020 [0.05]
19 [483]	40°	0.0118 [0.30]
46 [1168]	35°	0.0098 [0.25]
63 [1600]	35°	0.0020 [0.05]

Table 6.4: μ_Δ=1.5x1: Crack widths up column height.

originated in the tension boundary element inside chamfer at 72in. [1829mm] and extended through the wall to within 6in. [152mm] of the compression boundary element. On the negative excursion to F -94.6kips [-421.0kN], Figure A.50 shows the shear crack that originated at just under 70in. [1778mm] inside the wall, extending through the entire wall depth. A shear crack formed in the load stub, extending down the wall along the wall/compression boundary element interface to a height of 58in. [1473mm] (see the upper right hand corner of Figure A.50). These cracks opened up suddenly, as true shear cracks, during the excursion to F -94.6kips [-421.0kN].

6.6.4 Formation of Shear Cracks ($\mu = 1.0 - 2.0$)

Since the column had been pushed to the μ_Δ 1.0 displacement at F_y, no new cracks formed during the first cycle at μ_Δ 1.0. During the third cycle, however, new shear cracks formed on the tension boundary element/wall interface (see Figure A.51) which made the unit look as if it were uncoupling in this region.

During the first positive excursion to μ_Δ .5 (F=109.8kips [488.6kN]), new shear cracks formed at the top of the tension boundary element. These cracks propagated mostly from existing shear cracks in the wall back into the tension boundary element. Flexure/shear cracks penetrated into the compression boundary element up to a height of 28in. [711mm]. During the negative excursion (F=-110.4kips [-491.3kN]), new shear cracks formed in the wall and tension boundary element from a height of 60in. [1524mm] to the load stub, at angles ranging from 35° to 25° from the vertical (see Figure A.52). Crack widths are shaped in Table 6.4.

While cycling at μ_Δ=2.0 new shear cracks formed and existing shear cracks extended into the upper region of the wall and tension boundary element. Some shear flexure/cracks at unit mid-height formed at very steep angles on the wall/compression boundary element interface.

Height, in. [mm]	Angle from Vertical	Crack Width, in. [mm]
13 [330]	60°	0.0157 [0.4]
19 [483]	40°	0.0157 [0.4]
46 [1168]	35°	0.0157 [0.4]
63 [1600]	35°	0.0118 [0.3]

Table 6.5: μ_Δ=3.0x1: Crack widths up column height.

Height, in. [mm]	Angle from Vertical	Crack Width, in. [mm]
13 [330]	60°	0.0354 [0.90]
19 [483]	40°	0.0197 [0.50]
46 [1168]	35°	0.0157 [0.40]
63 [1600]	35°	0.0118 [0.30]

Table 6.6: μ_Δ=4.0x1: Crack widths up column height.

6.6.5 Initiation of Spalling ($\mu = 3.0$)

Figure A.53 shows the full extent of deformation and cracking at this level under the first positive excursion (F=127.7kips [568.3kN]). Figure A.54 shows incipient spalling at the base of the tension boundary element under the first negative excursion (F=-128.9kips [573.6kN]). At heights of 36in. [914mm] and 48in. [1219mm] the wall and compression boundary element showed signs of uncoupling through splitting on the wall/compression boundary element interface. Crack widths are shown in Table 6.5.

6.6.6 Growth of Spalled Region ($\mu = 4.0$)

Figure A.55 shows that the spalled region reached a height of 3in. [76mm] in the compression boundary element. Crack widths are displayed in Table 6.6.

6.6.7 Full Development of Spalled Region (μ =6.0)

Figure A.57 shows the full extent of spalling in the compression boundary element which reached a height of 12in. [305mm] once the column underwent a negative excursion.

Figure A.56 shows the deformation and crack pattern for the first cycle (F=132.8kips [591.0kN]). By this time, the column appeared to deform fully in flexure, with very little increase in shear crack widths but with substantial increase in flexural crack widths (see Table 6.7).

Height, in. [mm]	Angle from Vertical	Crack Width, in. [mm]
13 [330]	60°	0.0551 [1.40]
19 [483]	40°	0.0354 [0.90]
46 [1168]	35°	0.0197 [0.50]
63 [1600]	35°	0.0177 [0.45]

Table 6.7: μ_Δ=6.0x1: Crack widths up column height.

Height, in. [mm]	Angle from Vertical	Crack Width, in. [mm]
13 [330]	60°	0.0709 [1.80]
19 [483]	40°	0.0472 [1.20]
46 [1168]	35°	0.0276 [0.70]
63 [1600]	35°	0.0197 [0.50]

Table 6.8: μ_Δ=4.0x1: Crack widths up column height.

Figure A.58 shows incipient bar buckling in the compression boundary element at a height of 6in. [152mm] after the third excursion to μ_Δ 6.0 (F=122.0kips [542.9kN]).

6.6.8 Strength Loss due to Longitudinal Bar Fracture (μ =8.0)

Figure A.59 shows the deformation and crack pattern at the peak of the first positive excursion (F=129.3kips [575.4kN]). Crack widths are shown in Table 6.8. This deformation appeared to be primarily flexural. A single bar fractured in the tension boundary element at 6in. [152mm] during the first negative excursion (F=-123.4kips [549.1kN]). Tension boundary element cracks had formed regularly at the 3in. [76mm] spiral spacing intervals. Figure A.60 shows a state of high degradation in the compression boundary element during the third positive excursion at μ_Δ .0 (F=104.5kips [465.0kN]). During the third negative excursion (F=-94.4kips [420.1kN]) spalling began in the wall close to the compression boundary element in a way that suggested the onset of wall crushing. Because the bars fractured, however, the force dropped to a level unable to sustain wall crushing.

Chapter 7

Discussion of Test Results

7.1 Overview

Test results are comparatively discussed in terms of general performance issues. Column hysteretic behavior is evaluated in terms of overall force-deflection behavior and equivalent viscous damping. Experimental curvatures and shear deformations are used to derive experimental plastic hinge lengths. Shear performance is discussed based on crack patterns, transverse bar strains and boundary element spiral strains.

7.2 Hysteretic Behavior

7.2.1 Phase I

Both test units exhibited similar hysteretic behavior with almost no difference in overall force-deflection characteristics as evidenced in Figures 7.1 and 7.2. There was some slight loss of strength in Unit 1B, with lighter transverse reinforcement (see Chapter 2), in comparison with Unit 1A. The only significant difference in behavior between the two units was evident in the transverse bar strains which for Unit 1A remained below yield but climbed to 2% in Unit 1B. Both columns exhibited stable hysteretic behavior up through μ_Δ 6, and degraded gradually in strength as longitudinal bars in the boundary columns ruptured successively over several cycles (see Figures 7.3 and 7.4). These ruptures were precipitated by longitudinal bar buckling between the spirals spaced at 3 in. [76 mm] and indicated that a spiral pitch of less than $6d_b$ would have been more desirable as a means to restrain the longitudinal bars against buckling.

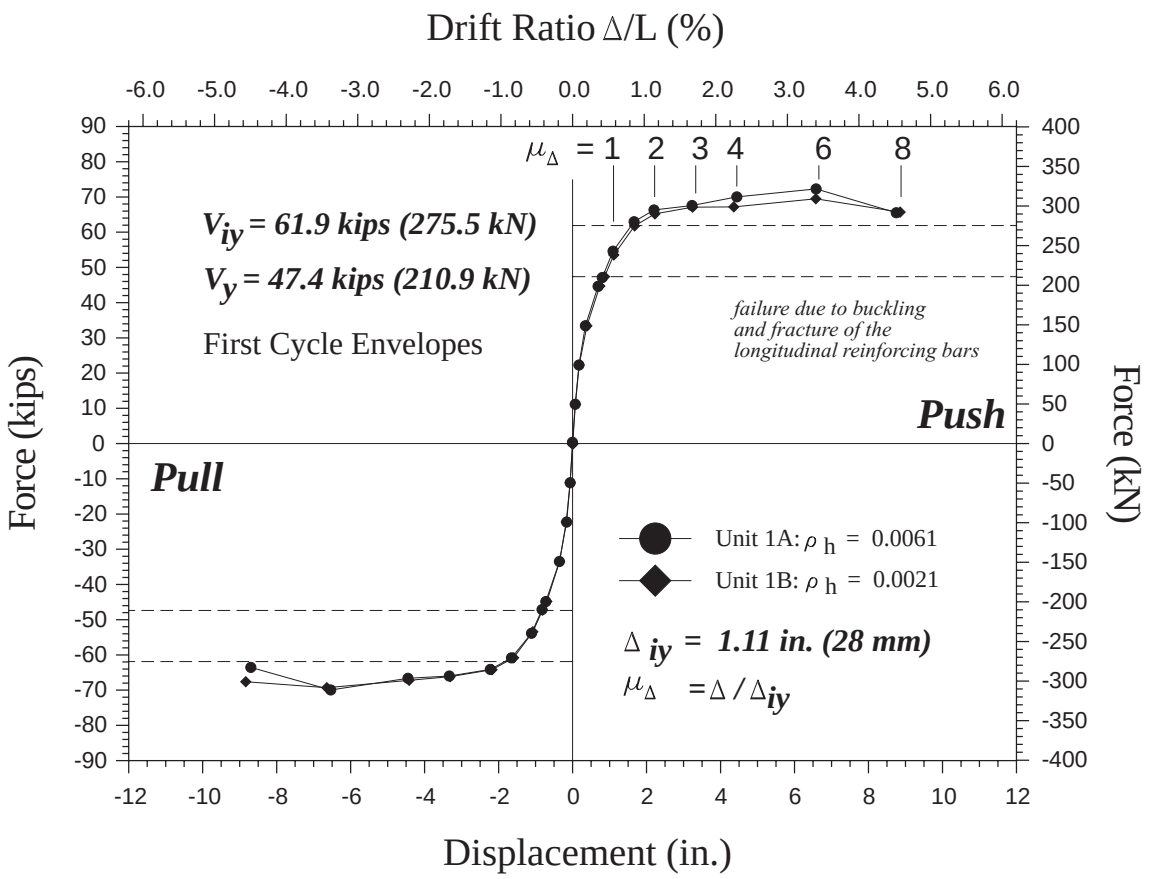

Figure 7.1: First cycle force-displacement envelopes for Units 1A and 1B.

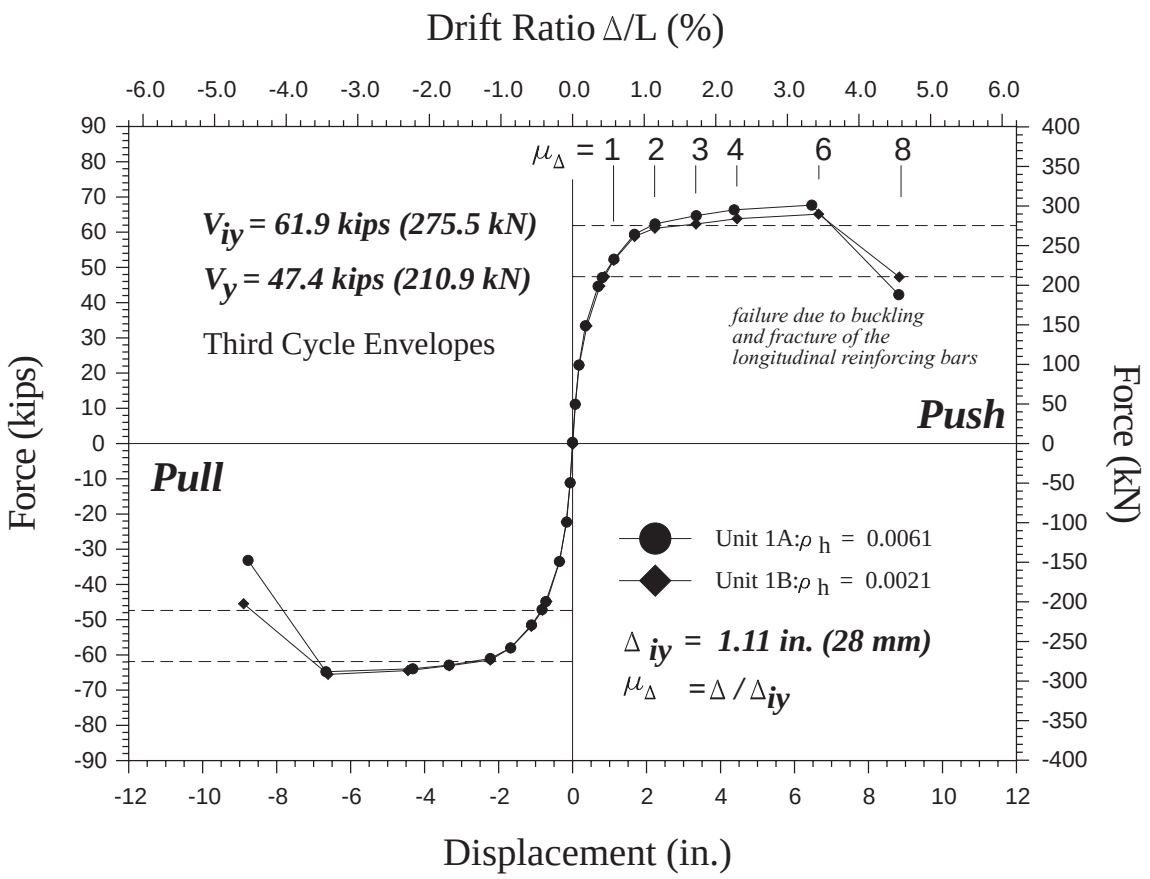

Figure 7.2: Third cycle force-displacement envelopes for Units 1A and 1B.

Figure 7.3: Fractured longitudinal reinforcing bars at end of Test 1A.

Figure 7.4: Fractured longitudinal reinforcing bars during final cycles of Test 1B.

Force-deflection predictions based on a moment-curvature analysis traced the shape of the experimental force-deflection envelope reasonably well. These predictions did not, however, have adequate termination criteria to predict maximum displacements under cyclic loads (see Chapter 5). The termination criteria were based on ultimate confined concrete strains, however the real failure was caused by bars buckling and fracturing at lower ultimate strains. The fracture of individual bars was marked by sharp drops in load capacity in the hysteresis loops for both test units (see Figures 7.5 and 7.6). The hysteresis loops showed that once a bar fractured and the force capacity dropped, the column gradually regained its strength with increased deformation by shifting the tensile demand to bars further inside the column. In the case of Test Unit 1A, all of the bars in the boundary elements had fractured by the last cycle of μ_Δ 8 (see Figure 7.3) and only then was the structural wall mobilized as a compression zone that experienced crushing.

Alternative termination criteria in conjunction with a modified equivalent plastic hinge length are discussed in Section 7.3.

Both test units also experienced spalling that initiated at μ_Δ 3 (see Figure 7.7), where concrete strains were calculated from curvature data to range between between ε_c 0.004 and ε_c 0.008. This spalling developed further by μ_Δ 4 (see Figure 7.8) and developed fully by μ_Δ . =6

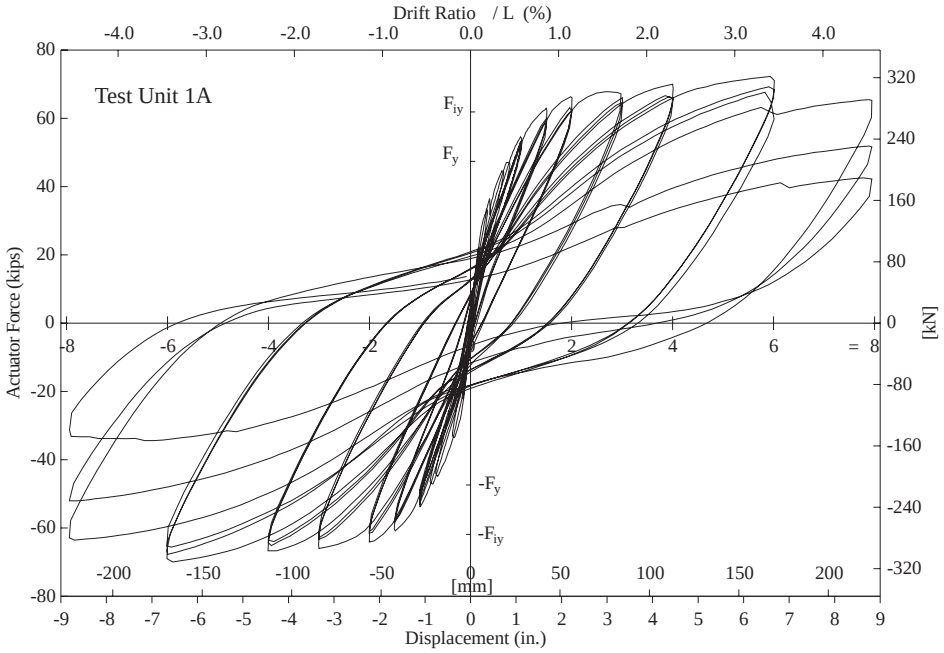

Figure 7.5: Test Unit 1A hysteretic behavior.

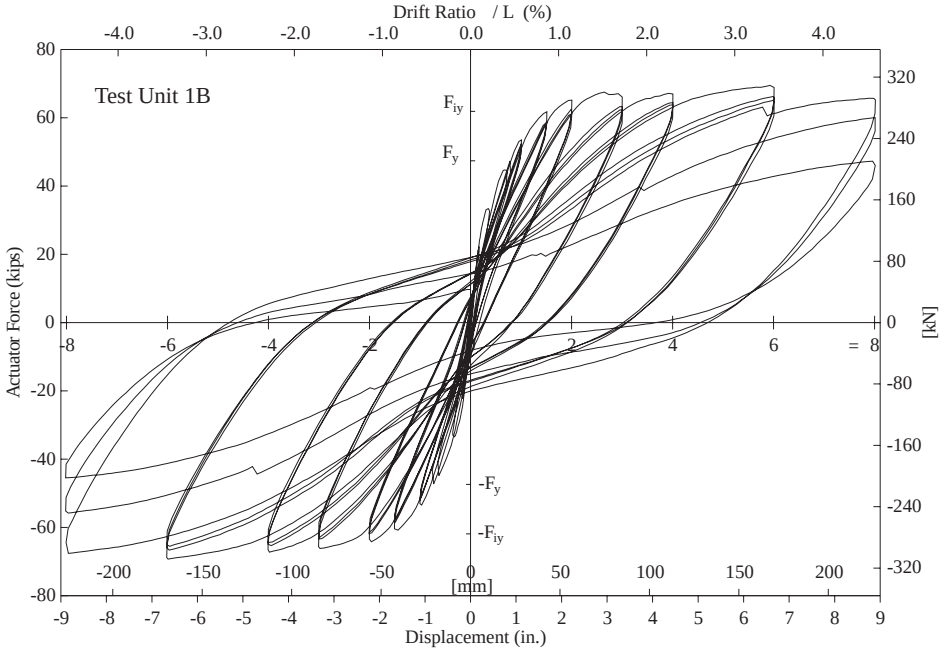

Figure 7.6: Test Unit 1B hysteretic behavior.

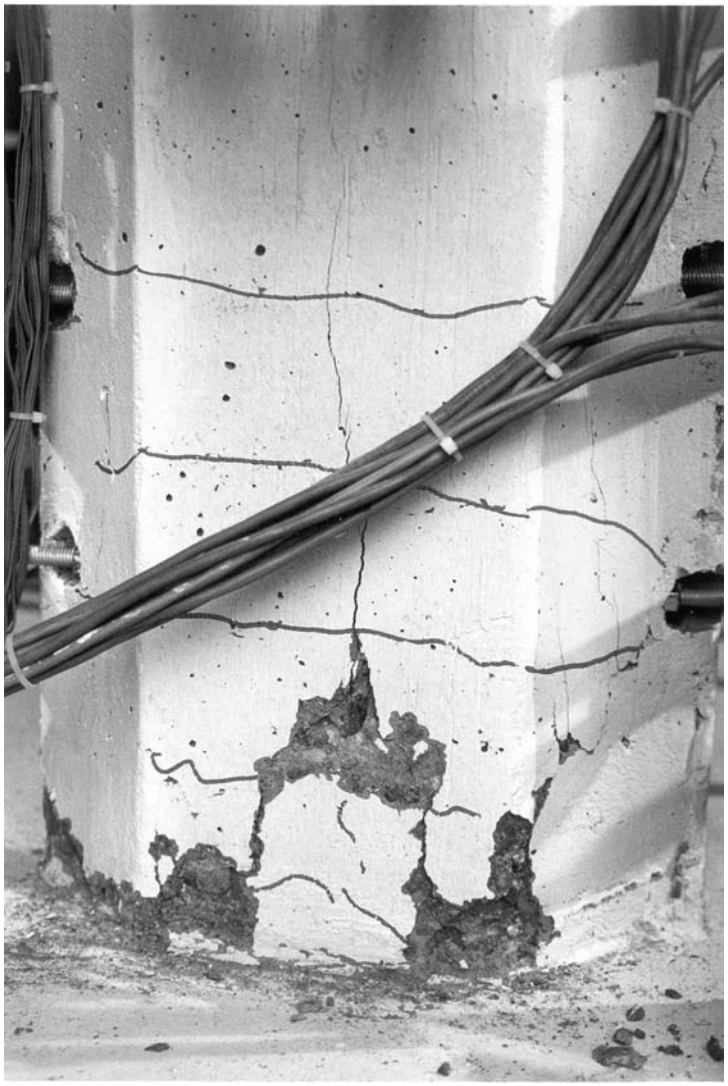

Figure 7.7: Incipient spalling in Test Unit 1A at μ_Δ 3. 4

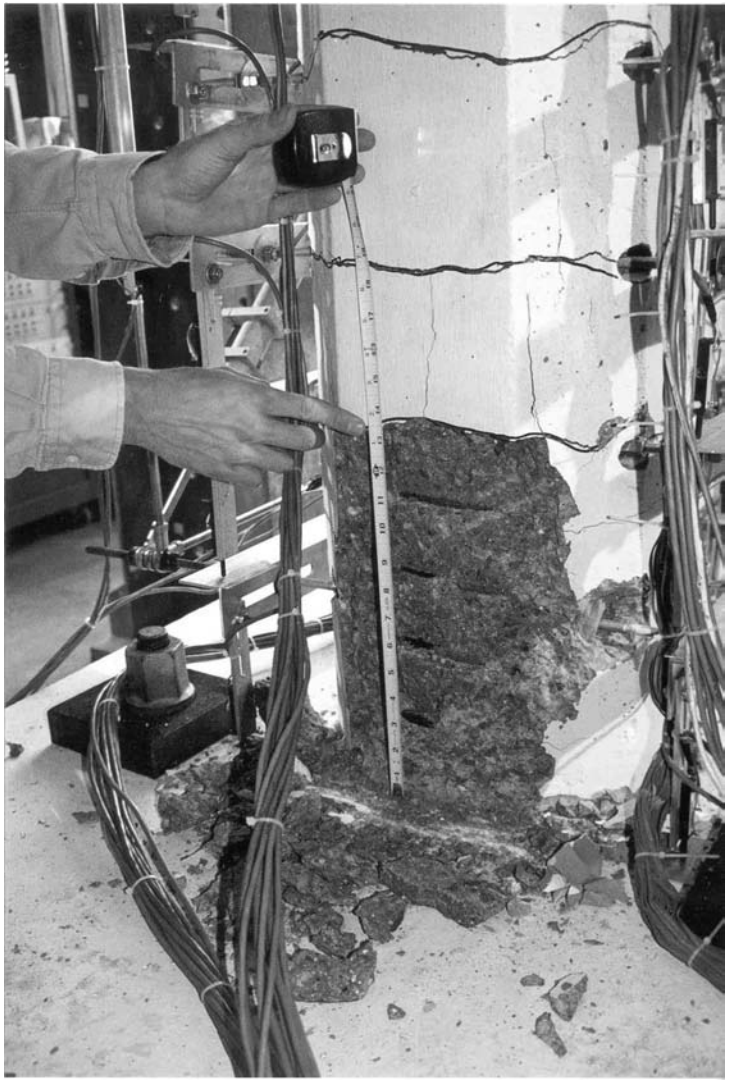

Figure 7.8: Partial development of spalled region in Test Unit 1A at μ_Δ .

7.2.2 Phase II

Figure 7.9 shows the deformation and crack patterns of the Phase II columns at failure. Unit 2A failed in flexure with buckling and fracture of the boundary element longitudinal reinforcing bars similar to the failure observed in Units 1A and 1B. Unit 2A, with the highest level of transverse reinforcement, experienced the least amount of damage to the structural wall, with cracks not reaching the height of the load stub and with no crushing in the wall.

(a) Test Unit 2A

(b) Test Unit 2B

(c) Test Unit 2C

Figure 7.9: Deformation and crack pattern μ_Δ 8 for (a) Test Unit 2A, (b) Test Unit 2B, (c) Test Unit 2C.

Unit 2B failed in shear (see Figure 7.9 (b)). This failure appeared as a gradual loss in strength due to degradation of the structural wall concrete while cycling at μ_Δ . The shear cracks at midheight in Unit 2B reached crack widths upwards of 0.16in. [4mm] while cycling at μ_Δ , allowing transverse strains at the column midheight =6 to reach a level where their effects became visible to the naked eye. Such a shear failure did not imply the collapse of the test unit, as the boundary elements alone retained strength to carry vertical and lateral loads. Although the wall degraded, this could not be considered a web crushing failure because the critical compression struts in the plastic hinge region remained in tact. This forced the wall to degrade at column midheight where it was least confined against transverse strains.

Although the wall in Unit 2C did not have sufficient thickness according to the web crushing design equations introduced in Chapter 5, the test unit ultimately failed in flexure via fracture of the longitudinal reinforcement in the boundary elements while cycling at μ_Δ . At low levels of deformation, up to μ_Δ 1, shear cracks formed up =8 the entire height of the wall, indicating that the test unit was likely to fail in shear. Once these cracks formed, however, the transverse reinforcement held the column together tightly in shear and the column deformed almost exclusively in flexure.

Despite large differences in the amount of transverse reinforcement between the Phase II test units, Figures 7.10 and 7.11 show remarkably similar force-deflection responses for the three test units. Figure 7.9 shows differences in the crack patterns and failure modes of the three test units that demonstrate the effects of transverse reinforcement and wall thickness on shear transfer through the walls.

Comparing the plots in Figure **??**, the hysteresis loops for Unit 2A are noticeably fatter than those for Units 2B and 2C, indicating greater flexural performance. The hysteresis loops for Unit 2B show no sharp decreases in load capacity because no longitudinal bars fractured during the test and all strength losses were a result of degradation in the structural wall. Although subtle differences in hysteretic behavior between the three test units are apparent in Figures 7.12, 7.13 and 7.14, much greater differences appear in the crack patterns in Figure 7.9. Hence, while low levels of transverse reinforcement and thinner walls might be acceptable for maintaining desired force-deflection characteristics, they have undesirable effects on other performance characteristics of the bridge piers, such as excessive shear cracking.

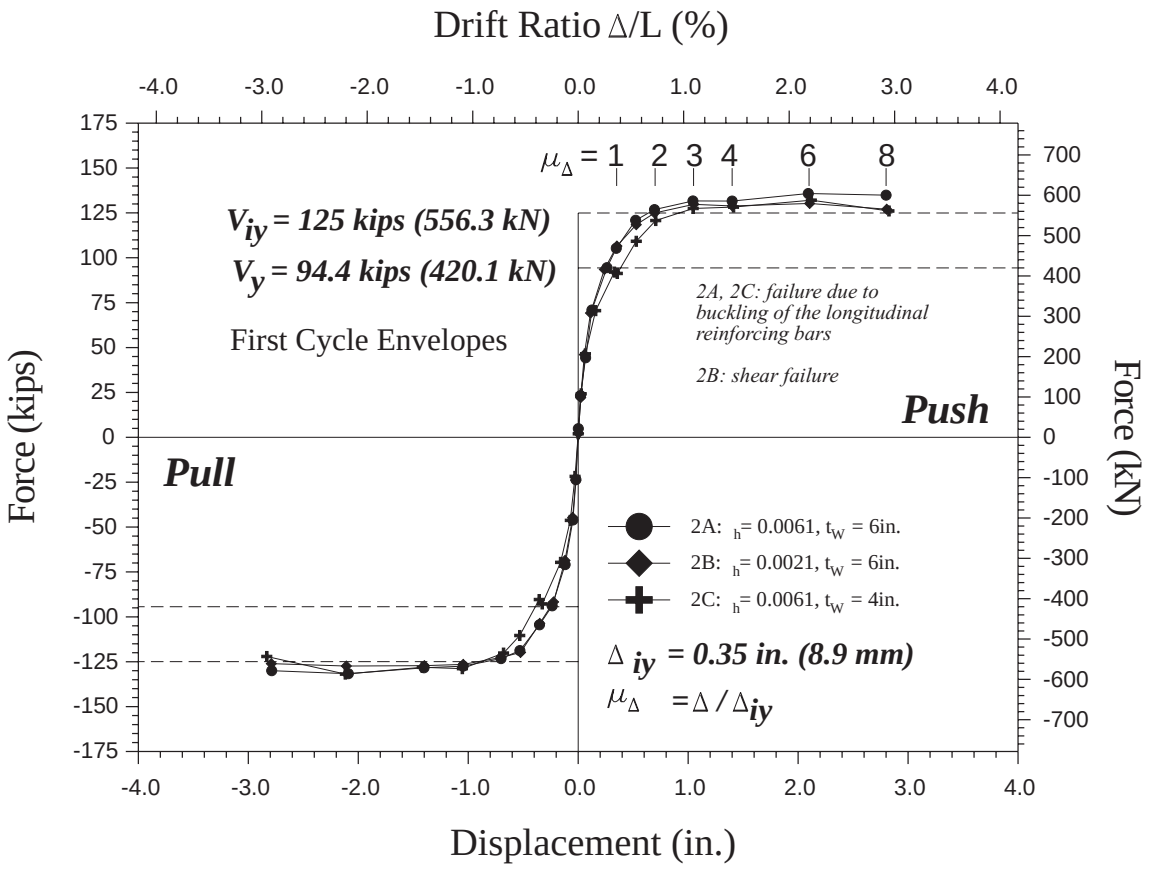

Figure 7.10: Third cycle force-displacement envelopes for Units 2A, 2B and 2C.

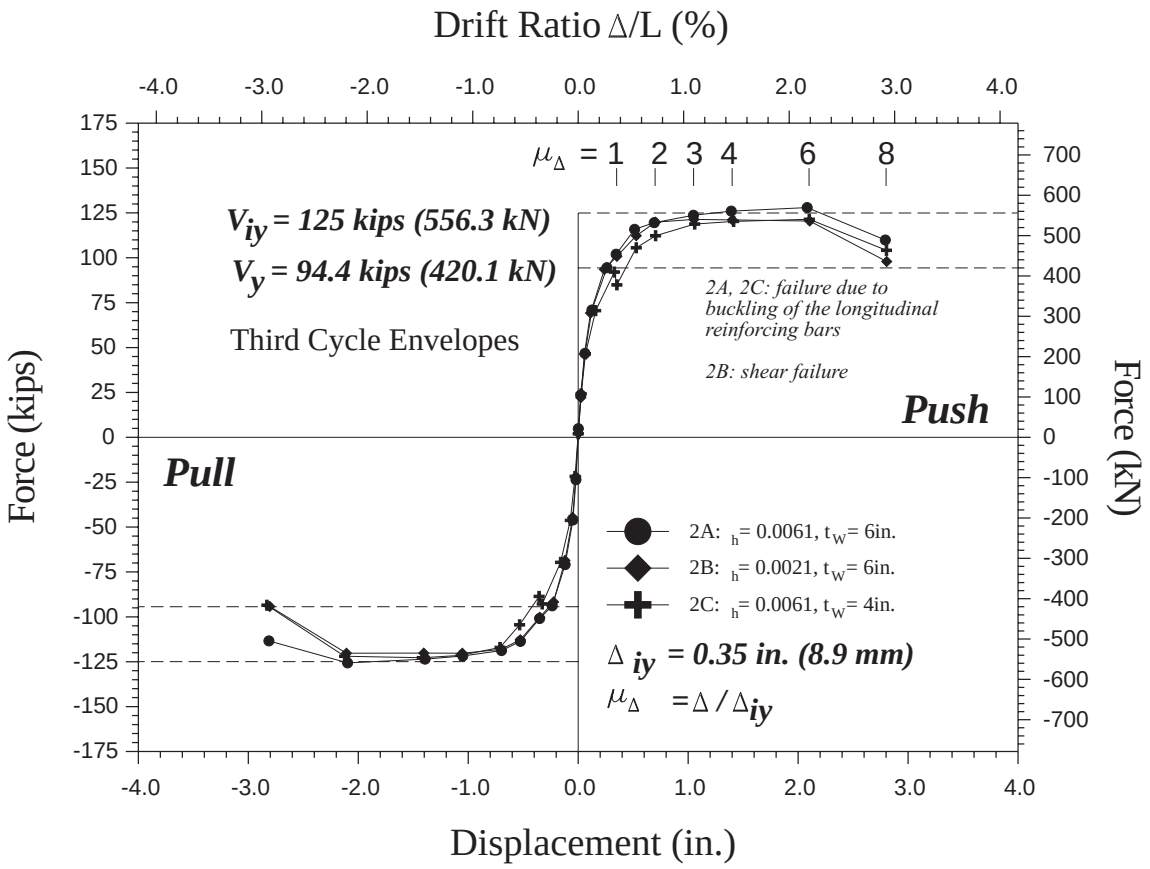

Figure 7.11: Third cycle force-displacement envelopes for Units 2A, 2B and 2C.

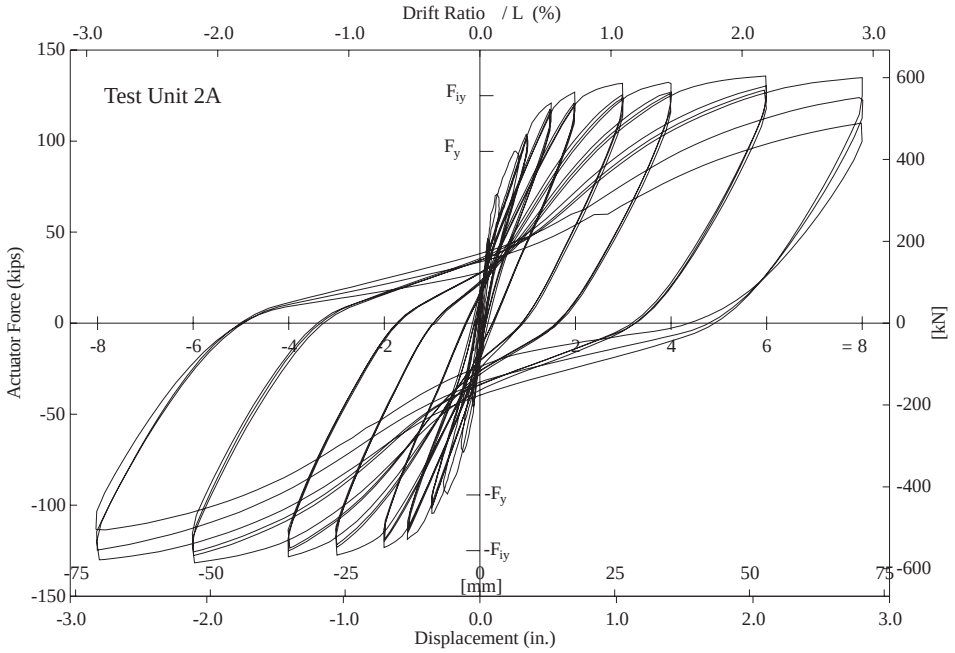

Figure 7.12: Test Unit 2A hysteretic behavior.

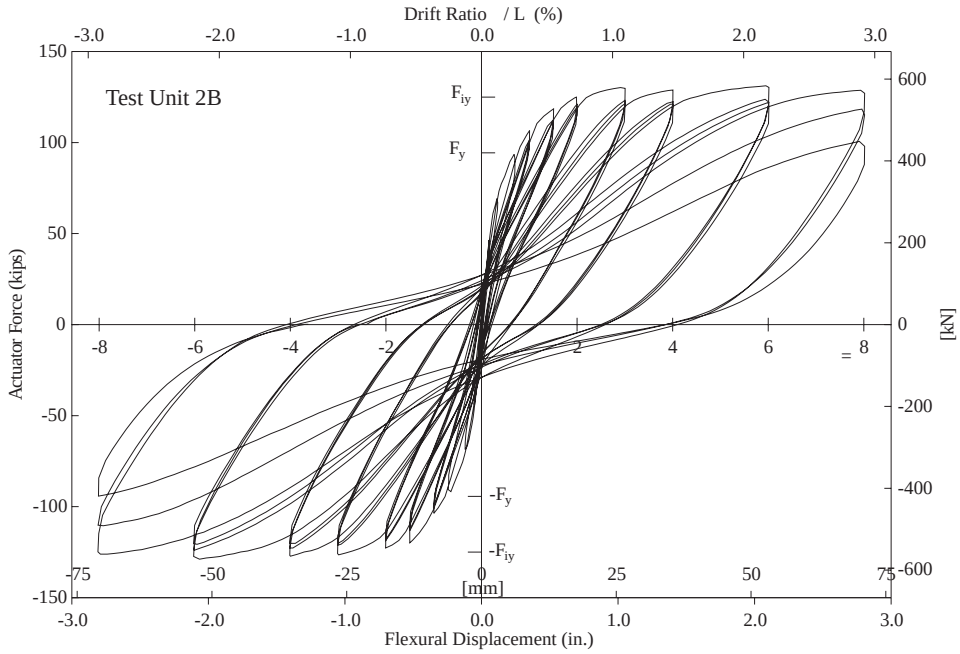

Figure 7.13: Test Unit 2B hysteretic behavior.

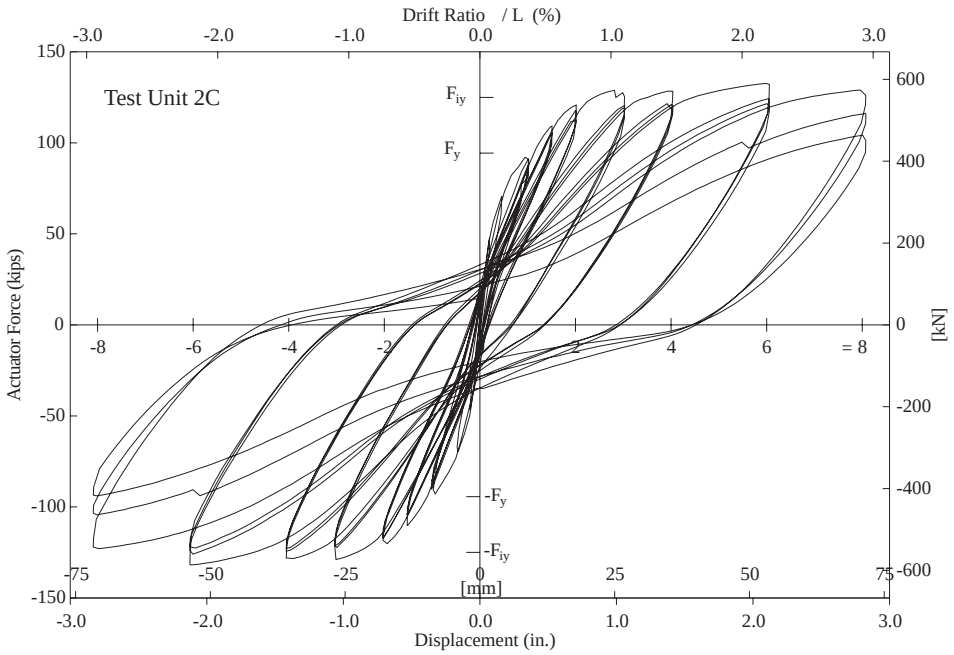

Figure 7.14: Test Unit 2C hysteretic behavior.

7.2.3 Comparison of Finite Element Predictions and Test Results

Fully cyclic, non-linear predictions for each test were developed in cooperation with ANATECH Corp. using three dimensional finite element analysis with the program ABAQUS and ANATECH's constitutive models [13]. Figure 7.15 shows the meshes for the models used to predict the Phase I and Phase II tests. Because of the axis of symmetry parallel to the direction of loading, it was sufficient to model only half the column. This reduced the required number of elements by a factor of 2, allowing for a finer mesh and faster run times.

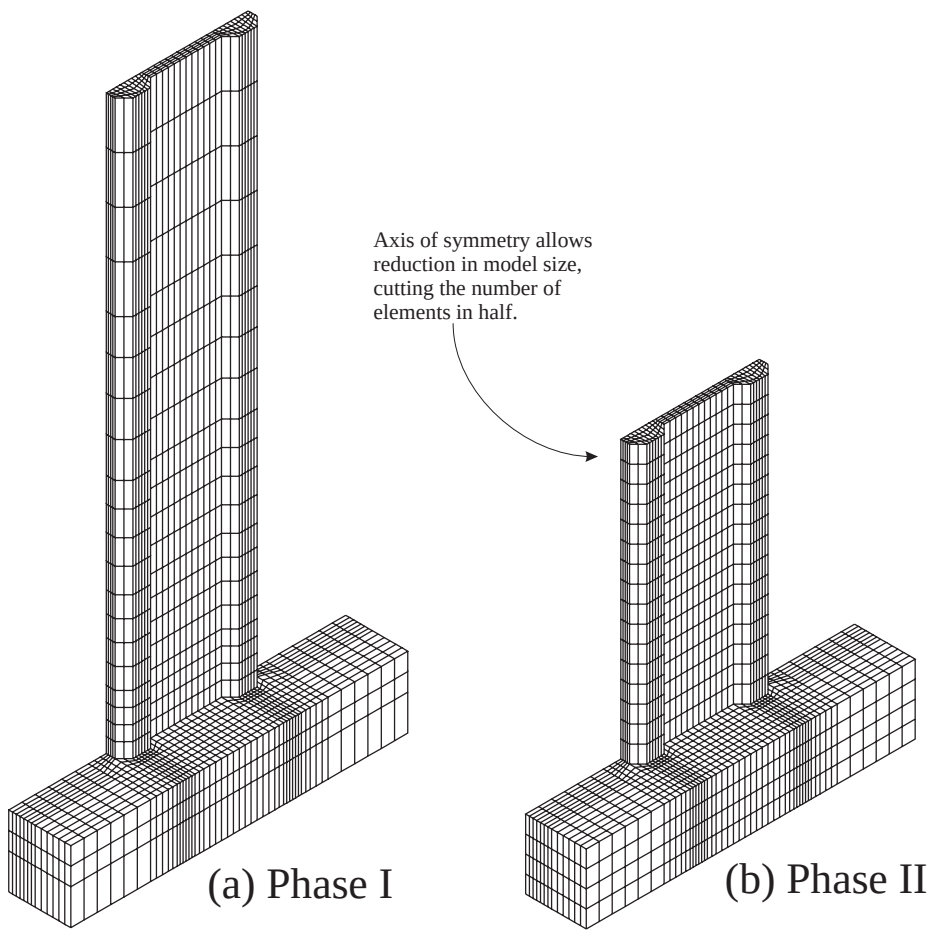

Figure 7.15: (a) Finite element mesh for the Phase I tests. (b) Finite element mesh for the Phase II tests.

Loading History

The hysteretic predictions are presented in Figures 7.16 - 7.20 as dashed lines superimposed on the measured hysteretic behavior of the test units, displayed in solid lines. None of the predictions were altered since the tests, however models for later tests were refined based on previous tests. For this reason, the displacement target values set for the predictions of Tests 1A, 2A and 2B in Figures 7.16, 7.18 and 7.19 do not match the experimental target values shown in these figures. Theoretical values for μ_Δ were determined from section analysis techniques described in Chapter 5 and used as target displacement values for these predictions. Once the experimental displacement target values had been set for each test phase, these values were used as the target values for later predictions. Hence the predictions for Test 1B and 2C in Figures 7.17 and 7.20 match the experimental displacement target levels in these figures. The prediction for Test Unit 2B could also have been calibrated according to the test target levels, however the target values for the 2A prediction were mistakenly used and there was not enough time to produce another prediction before the test.

In spite of the difference in displacement target levels for Test Units 1A, 2A and 2B, meaningful comparisons can be made between the predictions and the test results. The test units and the analytical models were cycled under displacement control after μ_Δ. Therefore differences in displacement at a given ductility do not imply that there were significant differences in the response of a given test unit and its predictive finite element model.

General Observations

Figures 7.16 - 7.20 show that the finite element predictions match the test results fairly well. For each test, the finite element results show greater strength at higher ductility levels. Where the test results show a drop in strength at each target displacement, the predictions show no immediate drops in strength at the target displacements. This difference is a result of the fact that the test units were held at the target displacement for some time in order to observe behavior and to mark cracks, whereas the analytical models were cycled in reverse immediately after reaching the target displacement, not taking relaxation into account. The model results do exhibit degradation in strength after the first cycle to each target displacement, reflecting the test results.

Most difficult to predict for any of the tests was the actual point of failure. This was clearly also the problem for the moment-curvature analyses presented in this report. Computer runs for the finite element prediction of each test unit's behavior

terminated either because they were stopped explicitly at a given displacement ductility level, usually μ_Δ 8x3, or because the analysis failed to converge. Bar buckling could not be predicted because the reinforcing bars were modeled as sub-elements within the concrete elements and not explicitly as separate three dimensional elements. Failure in shear could not be clearly distinguished from excessive distortion of the elements. High steel strains were observed in several of the models and bar fracture due to low-cycle fatigue was observed in model 2C, which was the only model where low-cycle fatigue parameters were included.

Test 1A

Figure 7.16 shows reasonable agreement between the prediction and the results from Test 1A. The predicted hysteretic curve is softer at low displacement levels and then does not plateau to the extent that the experimental curve does beginning at μ_Δ . At displacement ductility levels of μ_Δ 3 and higher, the theoretical curve shows higher strengths for the model than the experimental curve does for the test unit. While some of this increase in strength can be attributed to the fact that the model was pushed to a higher displacement target, it is clear from the predicted strengths at μ_Δ that the model overpredicted the strength of the test unit. =6

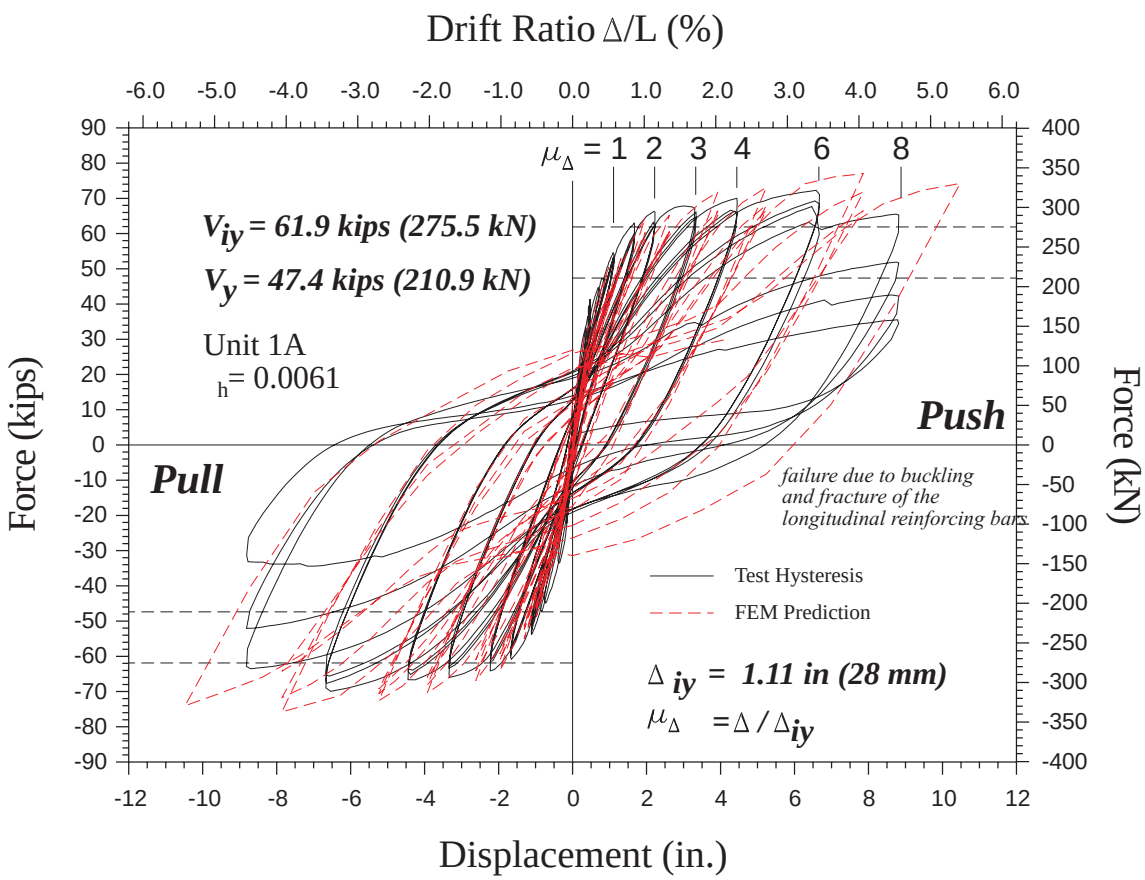

Figure 7.16: Hysteretic behavior for Test Unit 1A with cyclic finite element prediction.

Test 1B

Figure 7.17 shows good agreement between the prediction and the test results up to μ_Δ 4. At higher displacement ductilities, however, the theoretical curve shows higher strength and narrower hysteresis loops than the experimental curve. The thinning of the hysteresis loops can be partially explained by the inability of the finite element model to capture the relaxation in strength of the test unit at the peak of each cycle. If such time-dependent relaxation, resulting from stopping the test to mark cracks, were calculated in the finite element model, the unloading curves in Figure 7.17 would shift downward, matching the test data.

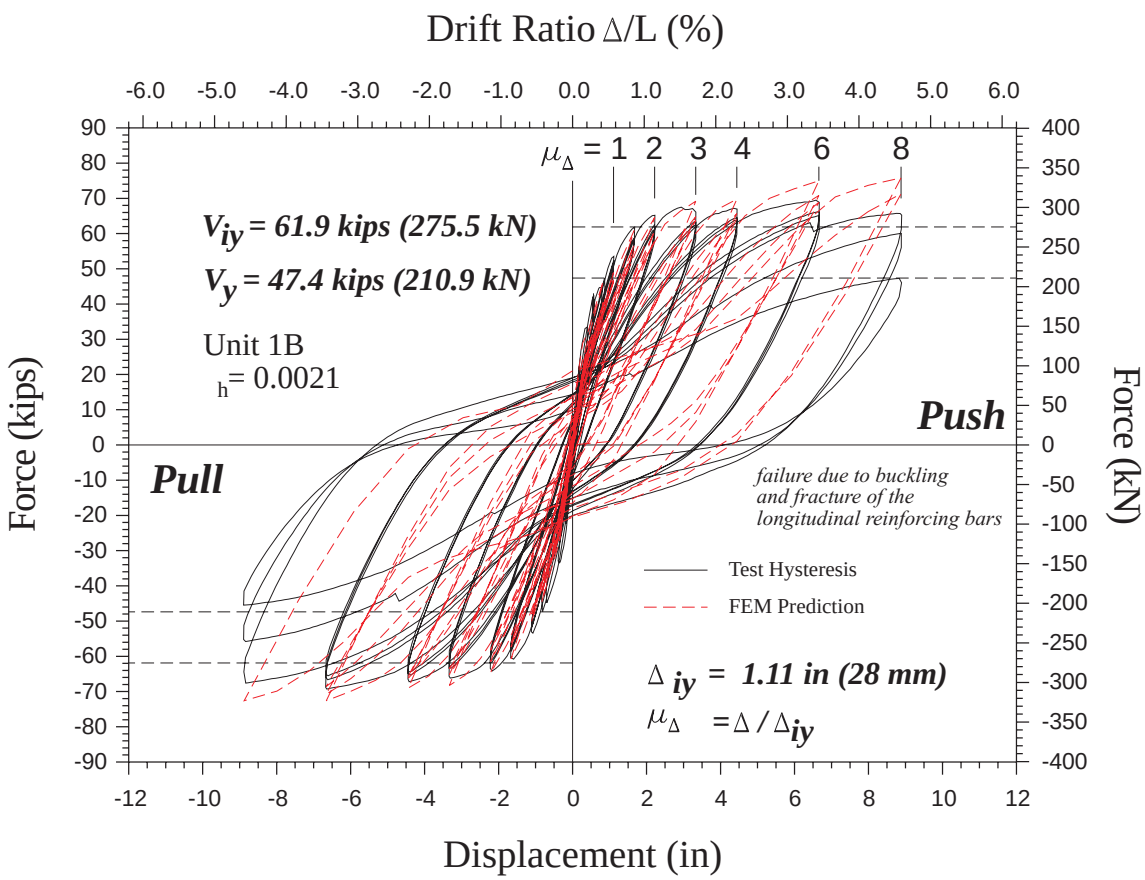

Figure 7.17: Hysteretic behavior for Test Unit 1B with cyclic finite element prediction.

Test 2A

Figure 7.18 shows a higher prediction of the flexural strength in the theoretical curve than is observed in the results of Test 2A. This overprediction of the flexural strength is similar to the predictions for Tests 1A and 1B. The prediction for Test 2A also shows higher stiffnesses when approaching the target displacements and less of a tendency to plateau at a given force level from μ_Δ and higher.

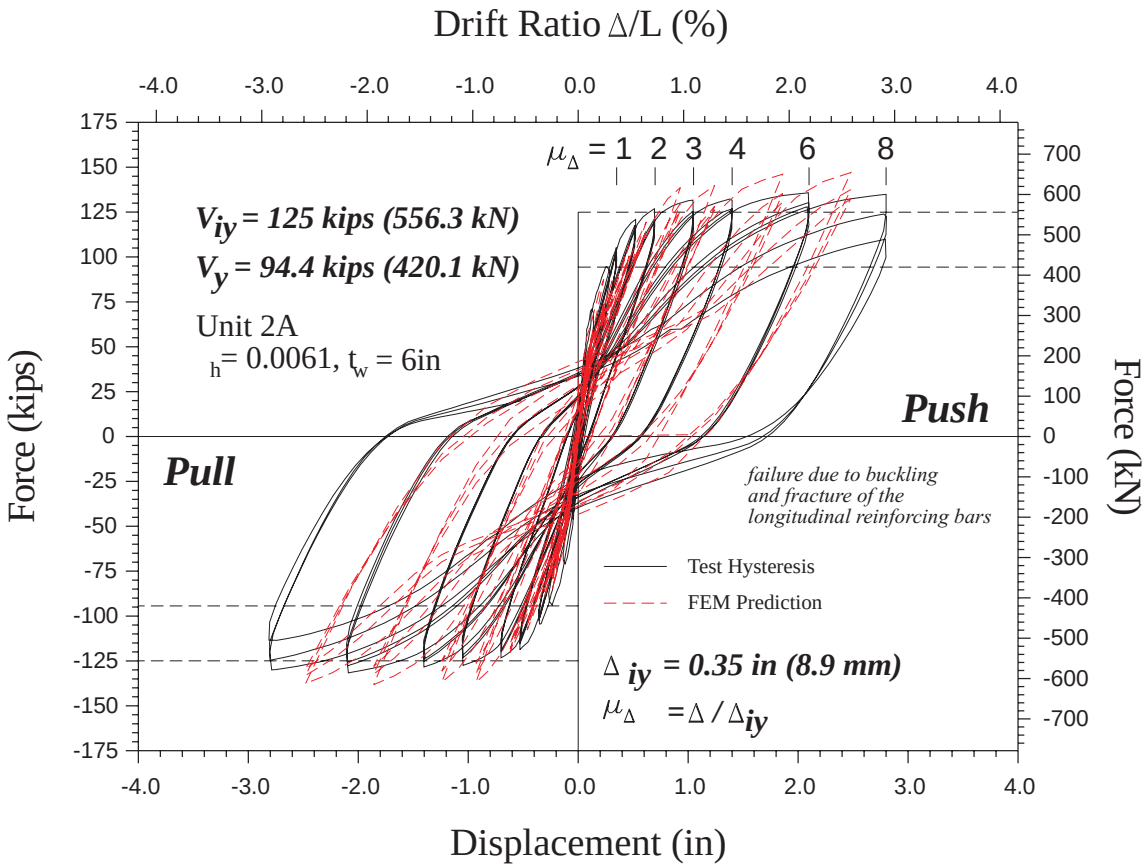

Figure 7.18: Hysteretic behavior for Test Unit 2A with cyclic finite element prediction.

Test 2B

Figure 7.19 shows that the predictions for Test 2B terminate prior to μ_Δ 8, with the run dying on the second cycle of μ_Δ due to severe distortion of some of the elements. This is interpreted as a shear failure and is confirmed by the manner in which the test unit failed. The test unit, however, failed in shear only after cycling at μ_Δ . =8

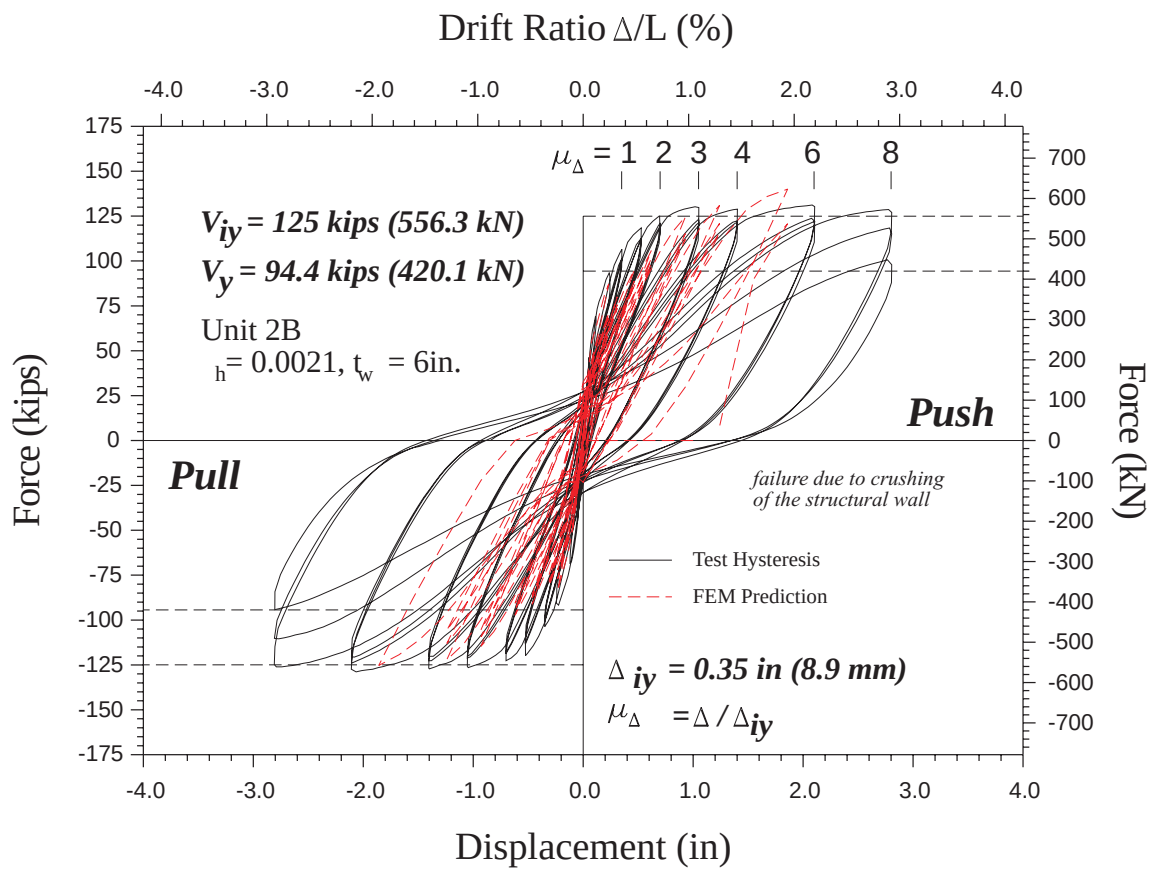

Figure 7.19: Hysteretic behavior for Test Unit 2B with cyclic finite element prediction.

Test 2C

Figure 7.20 shows the closest correlation between predictions and test unit behavior. The predictions match both the initial stiffness and the strength at higher displacement ductilities with reasonable accuracy. The model results also show severe strength degradation at μ_Δ -8x3 where bars were predicted to fracture due to low cycle fatigue. The results from the predictions for Test 2C show that refining the material models for the other tests, such as adding the possibility for low cycle fatigue to the steel, promise better predictions of the failure limit states for such columns.

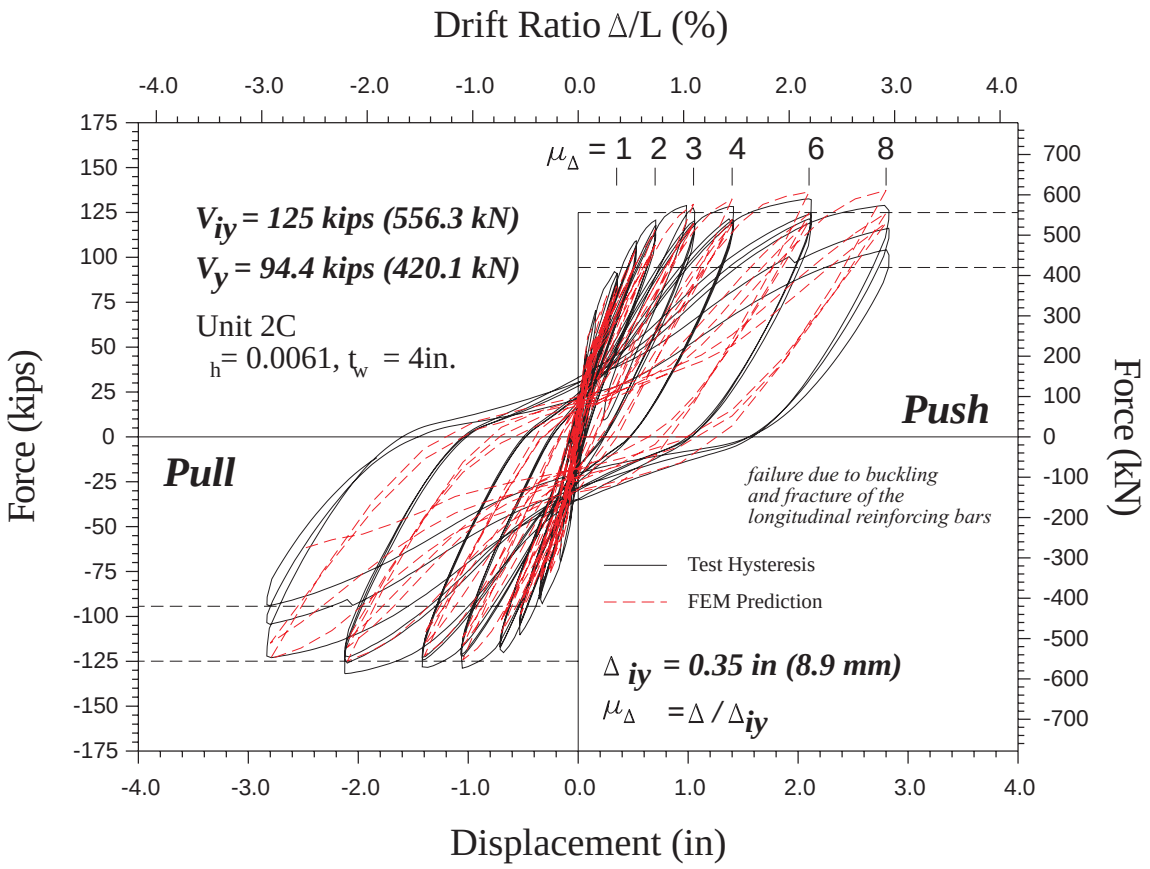

Figure 7.20: Hysteretic behavior for Test Unit 2C with cyclic finite element prediction.

Performance Level	Unit 1A	Unit 1B	Unit 2A	Unit 2B	Unit 2C
First Cracking	6.9%	7.9%	9.1%	6.6%	8.0%
First Yield	4.9%	5.4%	8.6%	8.5%	10.2%
Incipient Spalling	13.4%	13.6%	13.9%	12.4%	13.3%
Fully Developed Spalled Region	19.6%	19.4%	18.3%	17.1%	17.7%
Column Failure	21.6%	19.6%	21.5%	16.2%	16.1%

Table 7.1: Equivalent viscous damping, ξ_{eq} for Phase I and II test units at specified performance levels.

7.2.4 Equivalent Viscous Damping

Table 7.1 gives values for equivalent viscous damping in the test units during the first cycle at each specified performance level. While the damping values remain similar between the various test units, results from Tests 2B and 2C show lower damping levels at higher levels of displacement, consistent with the increased pinching and the larger shear deformations expected and observed in these test units.

7.3 Plastic Hinge Length

The equivalent plastic hinge length has been a matter of much discussion in the design of the new Bay Area bridges. Currently, this value is based on an equation that is primarily a function of the column length [12], given as

$$L_p \quad .08L + 0.15 f_y d_{bl} \geq 0.3 f_y d_{bl} \qquad (ksi) \qquad (7.1) \qquad =0$$

$$L_p \quad .08L + 0.022 f_y d_{bl} \geq 0.044 f_y d_{bl} \qquad [MPa] \qquad (7.2) =0$$

and introduced in Chapter 5. This section discusses curvature data and longitudinal bar strain data measured from the tests, with the aim of calibrating the plastic hinge length to reflect the properties of the test units.

Experimental plastic hinge lengths are calculated based on deformations measured from the tests. Based on these values as well as values calculated from ten of Oesterle et al.'s tests [8, 6], a new expression for the plastic hinge length is developed to include as a parameter the total column depth, D in addition to the column length, L and the strain penetration term L_{sp}. The total column depth D is known as the tension shift parameter in the modified equation for equivalent plastic hinge length.

7.3.1 Curvature Profiles

Curvature data calculated from all five tests, calculated according to the method described in Chapter 4, show relatively linear curvature profiles in the plastic hinge regions of the columns. These linear profiles contrast with the expected increases in curvature near the column bases observed in circular and rectangular columns.

Phase I

Figures 7.21 and 7.22 indicate that no significant discrepancy exists between curvature results from the two test units. The figures show plastic curvature distributions for both columns to be relatively linear and to extend beyond the measured region. The large curvature value calculated at the base for Unit 1A at μ_Δ 8 x -1 can be explained by the fact that longitudinal bars in the compression boundary element fractured in the previous half cycle, allowing for losses in the boundary element core concrete. See Figure 7.3 for the full extent of core concrete losses after cycling at μ_Δ . =8

The curvatures in Figures 7.21 and 7.22 were integrated up the column height according to the method outlined in Chapter 4 to obtain the experimental flexural component of the column total deflection. Figures 7.23 and 7.24 show these flexural displacements in comparison with measured shear displacements and the total displacement measured at the top of the column. In both cases, the calculated displacements underestimate the measured displacements. Additional curvature and shear instrumentation should have been placed higher up the columns in order to capture the total deformations due to shear and flexure more accurately. This was done for the Phase II test units (see Chapter 4).

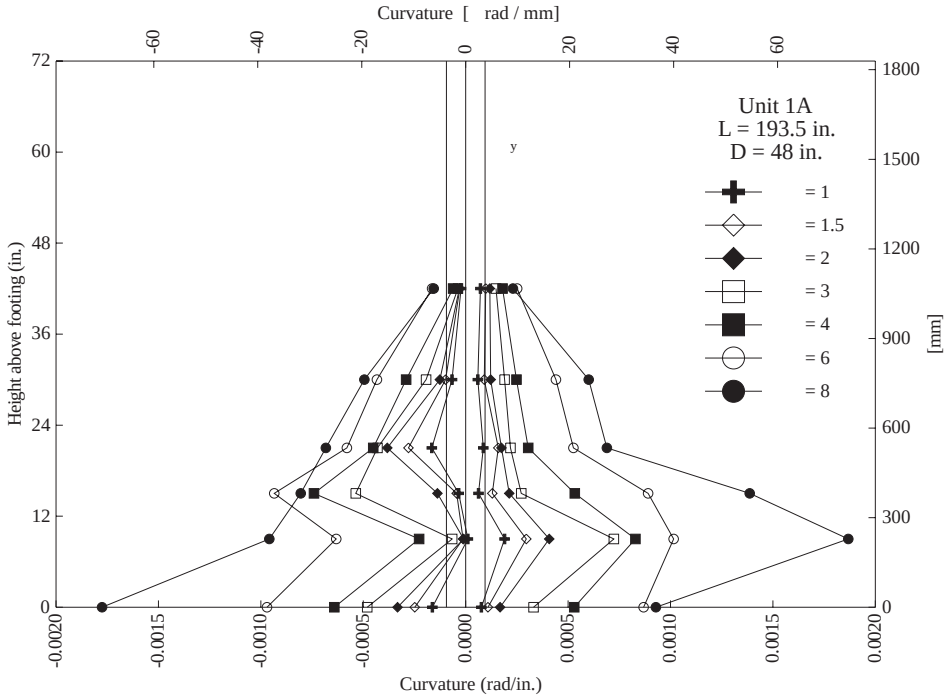

Figure 7.21: Test Unit 1A curvature profiles.

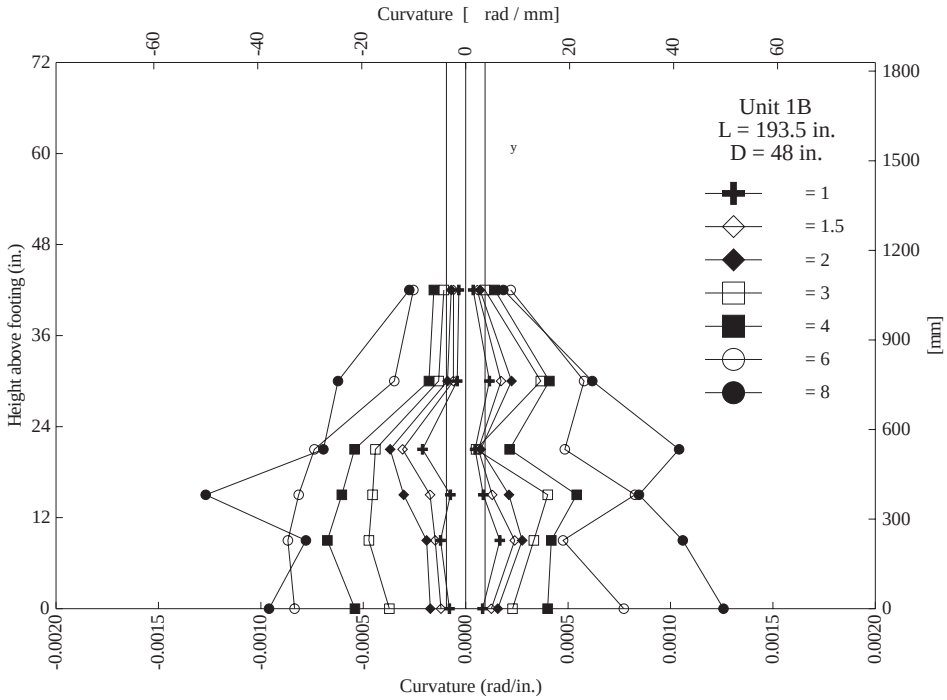

Figure 7.22: Test Unit 1B curvature profiles.

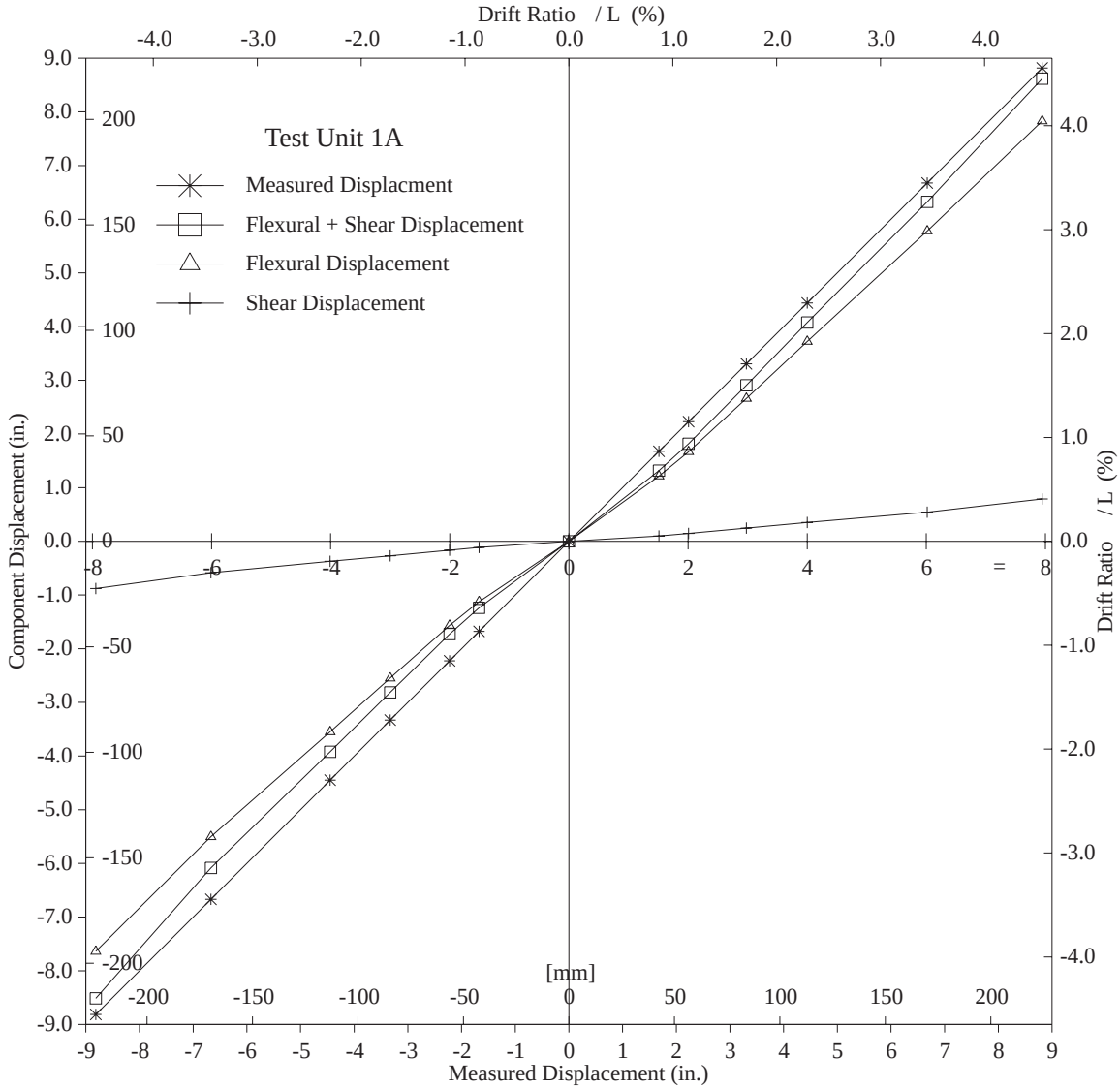

Figure 7.23: Test Unit 1A experimental displacement values.

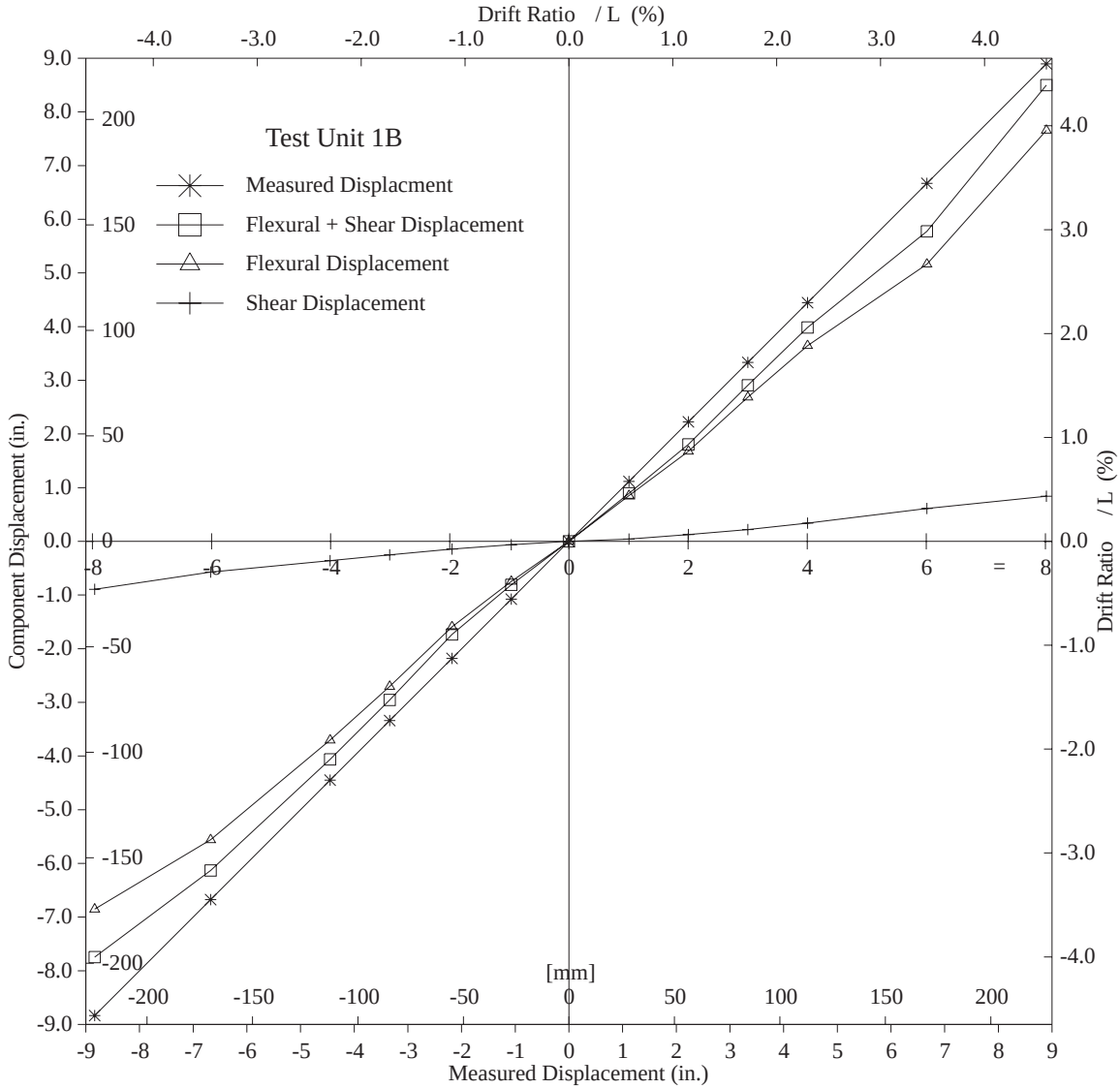

Figure 7.24: Test Unit 1B experimental displacement values.

Phase II

The curvatures calculated from the test results of the Phase II units have roughly linear distributions through the plastic hinge region (see Figures 7.25, 7.26 and 7.27). Test results show maximum curvatures of 0.001 1/in. [0.039 1/m] at the column base, slightly less than the values reported for Tests 1A and 1B. Large changes in the curvature from one height to the next, such as in Unit 2B, are probably the result of curvature rods being intercepted by diagonal cracks bounding different compression struts in the wall. For instance, it is difficult to asses the curvature on a single so-called plane section when the two rods used to measure that curvature deformed with two different compression struts during the tests.

Figures 7.28, 7.29 and 7.30 compare the total displacements measured at the top of the Phase II columns with both the flexural displacements integrated from experimental curvature values and with the experimental shear displacements. Results from all three test units show good correlation between the flexural plus the shear displacements and the total top displacement. Figure 7.29 shows Test Unit 2B to have experienced the largest percentage of shear displacements, corresponding to the low amount of transverse reinforcement. Figures 7.28 and 7.30 show Test Units 2A and 2C to have experienced relatively comparable shear displacements, which is interesting in light of the fact that 2C had 2/3 the wall thickness and also 2/3 the transverse reinforcement of 2A. 2C was observed to have higher shear deformations and more extensive shear cracking at earlier levels than 2A. For instance, 2C had fully developed shear cracks at the first yield force level, F_y, which had been defined based on the properties of 2A, and was applied to 2C in order to maintain a consistent loading history for all of the test units.

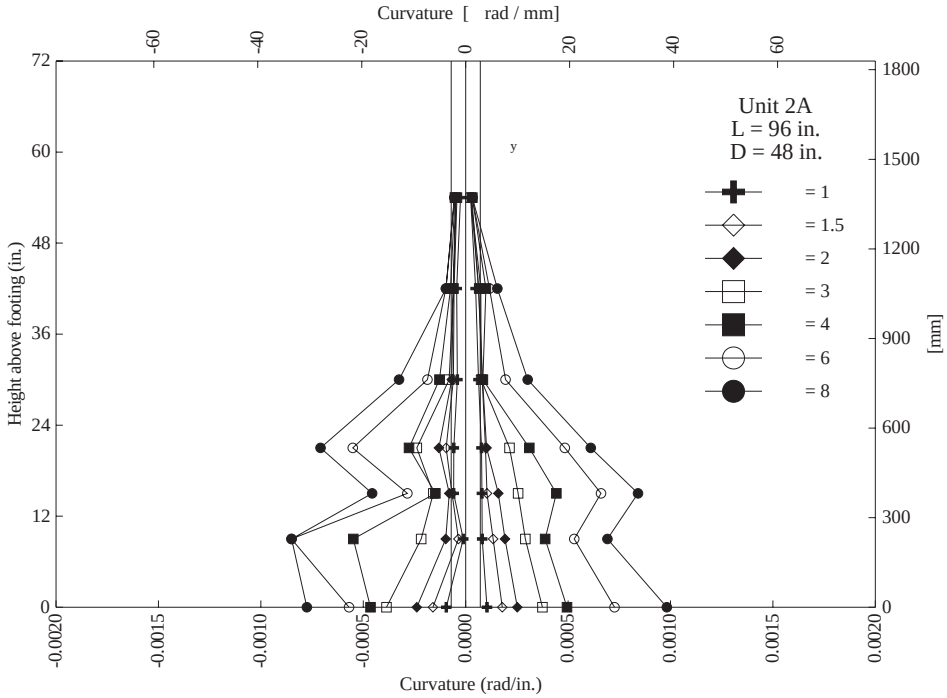

Figure 7.25: Test Unit 2A curvature profiles.

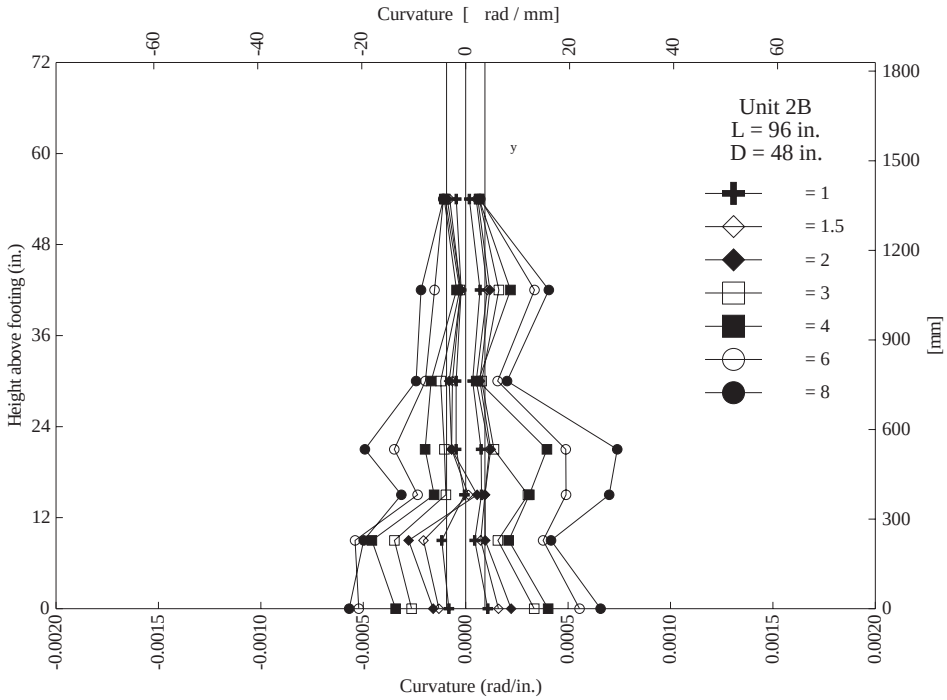

Figure 7.26: Test Unit 2B curvature profiles.

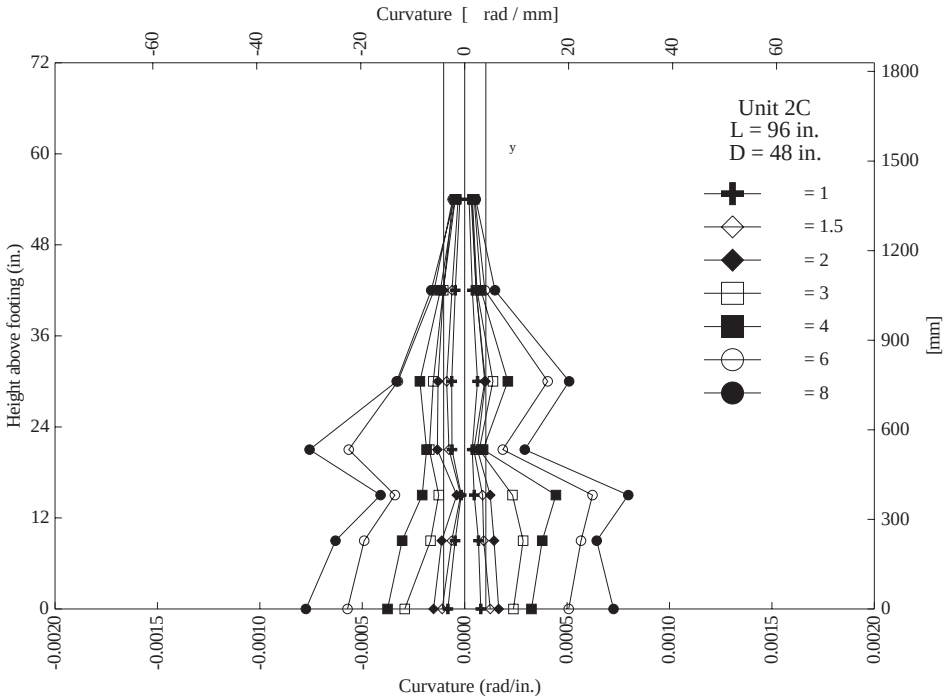

Figure 7.27: Test Unit 2C curvature profiles.

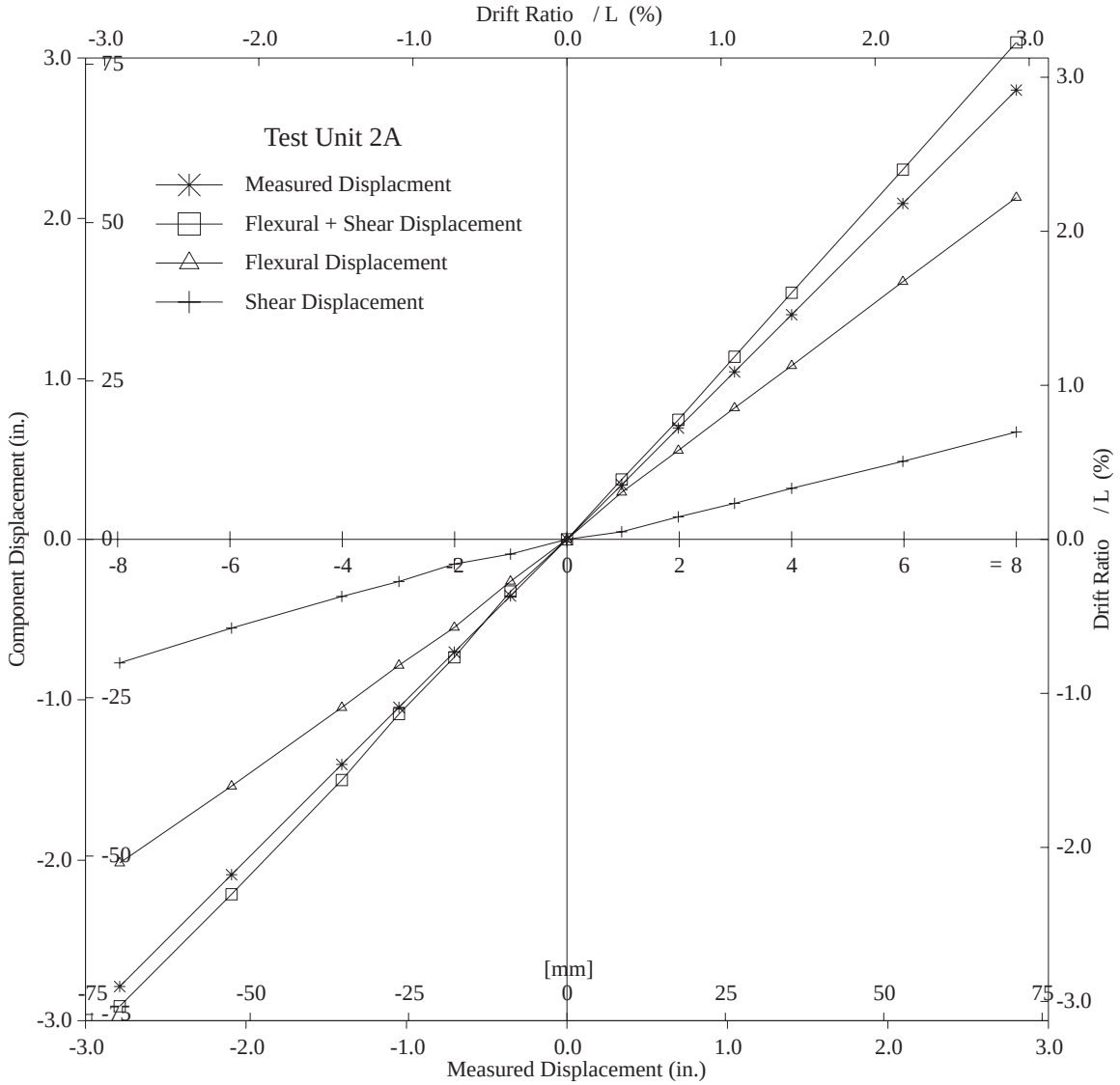

Figure 7.28: Test Unit 2A experimental displacement values.

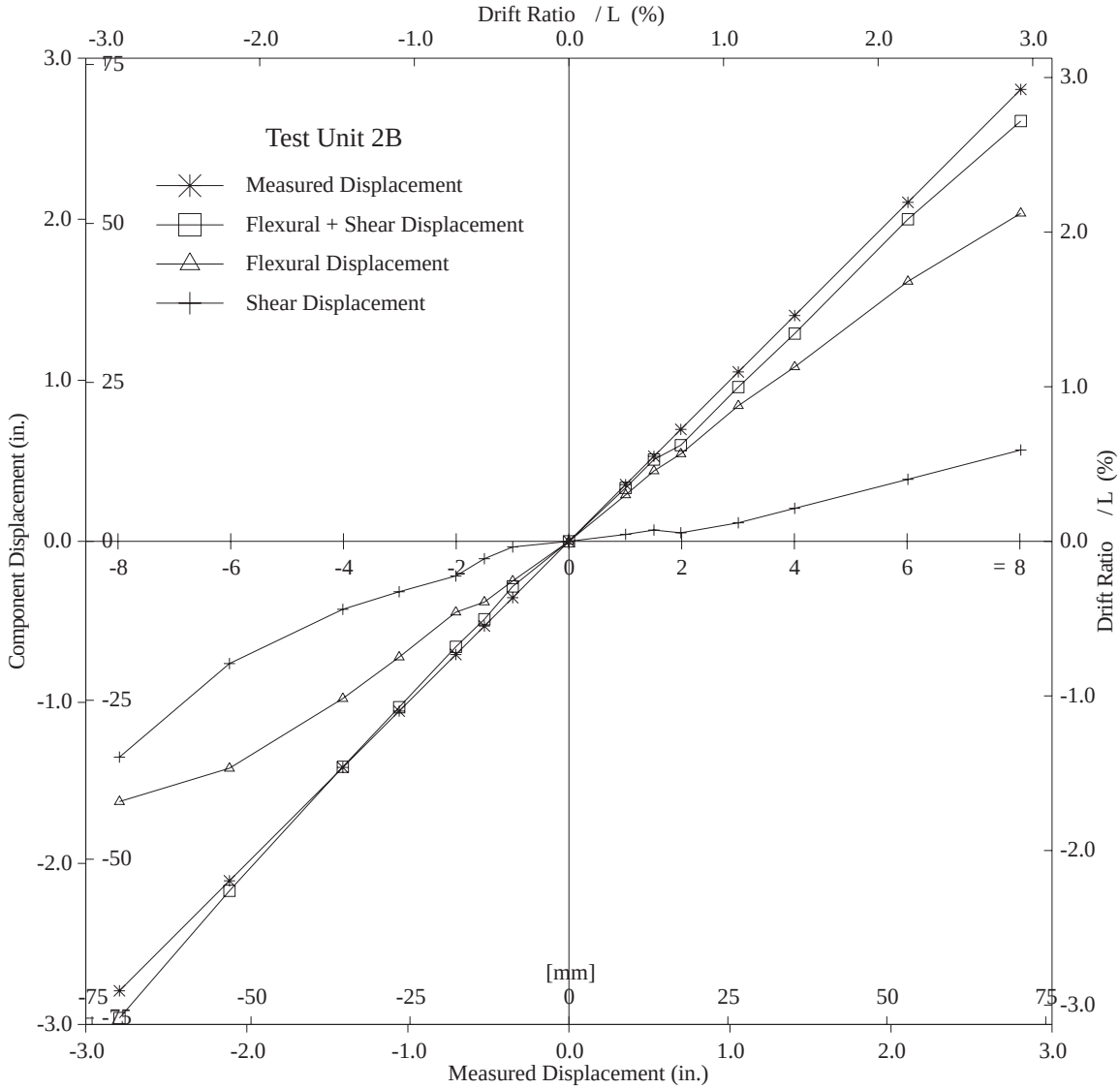

Figure 7.29: Test Unit 2B experimental displacement values.

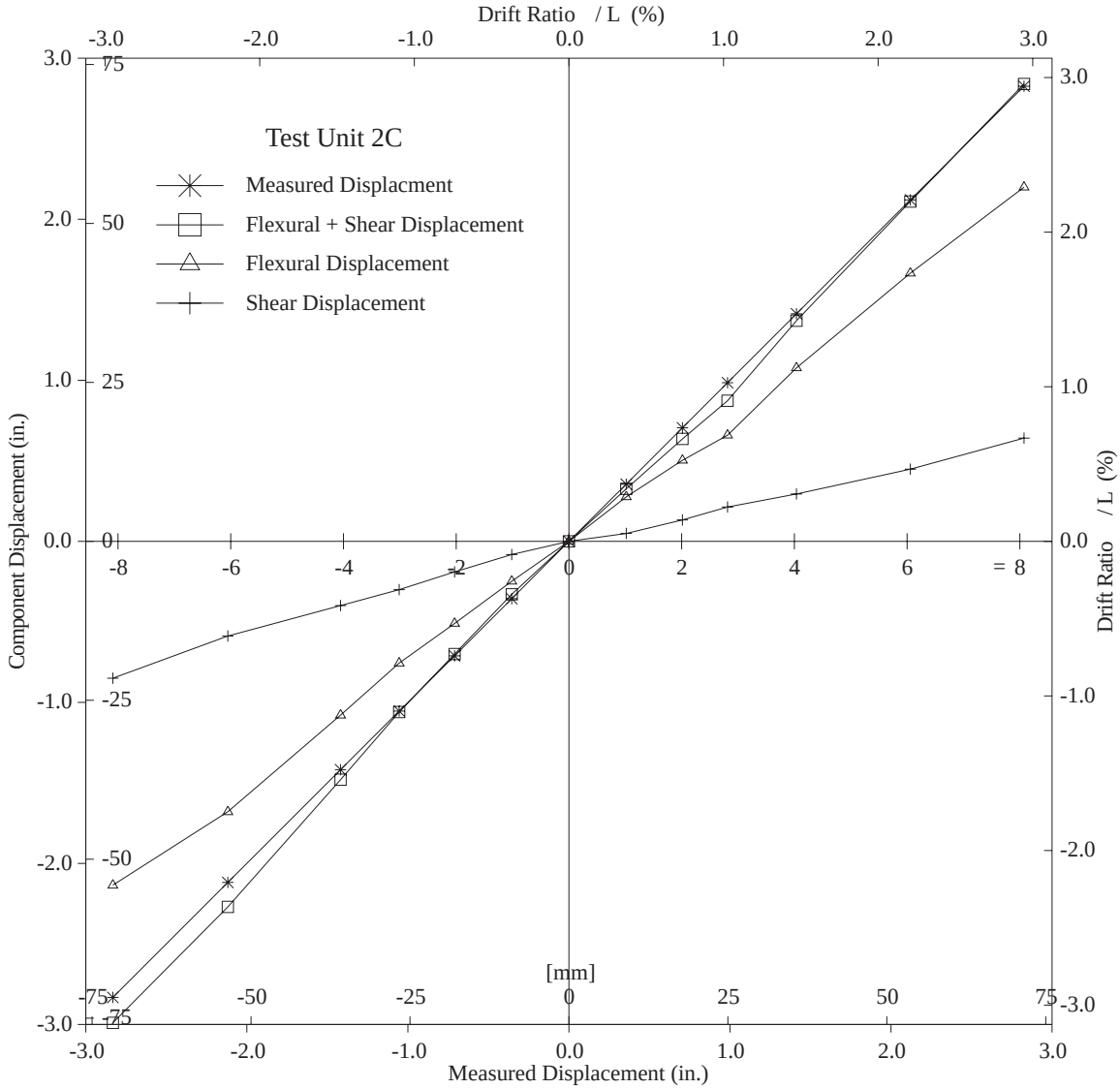

Figure 7.30: Test Unit 2C experimental displacement values.

7.3.2 Longitudinal Bar Strains

Phase I

The longitudinal strain profiles displayed in Figures B.4-B.8 and Figures C.4-C.8 show that the assumption of plane sections remaining plane appears to be valid up to μ_Δ 1 regardless of the level of transverse reinforcement. As discussed in Chapter 5, however, while integral action between the wall and boundary elements was relatively certain to occur in single bending, because of the rigid boundary condition provided by the load stub or bridge deck, in double bending there would have been no restraining boundary condition. In this case the wall and boundary element sections would have been more free to slip vertically against one another.

Phase II

Longitudinal bar strain profiles in Figures D.3 and E.3 show that several longitudinal bars reached yield 6 in. [152 mm] into the footing, with plane sections remaining plane. The strain profiles at footing level (see Figures D.4 and E.4) show large increases in the strains of the extreme steel bars up to $\varepsilon_s \simeq 0.012$ by μ_Δ . Figures D.5 and E.5 at 6 in. [152 mm] above the footing show much greater discrepancies between the boundary element bars which appear to have experienced extreme tensile strain conditions beginning at μ_Δ 2. This is more evident in Unit 2A which had more gages in tact at this level than Unit 2B. The profiles at 12 in. [305 mm] and 24 in. [610 mm] tend to show similar trends with plane sections remaining plane during the initial stages, but exhibit large jumps between gages at higher levels of displacement due to the opening of flexure-shear cracks.

7.3.3 Back Calculation of L_p

To ensure that shear deformations were not included in the calculation of the experimental plastic hinge length, column flexural deformation was calculated directly from the column top displacement minus the displacement calculated from measured shear deformations.

$$\Delta_f \qquad - \Delta_s \tag{7.3}$$

The equivalent plastic hinge length is defined as the length by which the curvature at the column base must be multiplied in order to produce a plastic deformation consistent with the plastic component of the flexural deflection. With the value for the equivalent plastic hinge length, L_p, column deflection can be calculated as the sum of an elastic component and a plastic component

$$\Delta_f \qquad {}_y + \Delta_p \tag{7.4}$$

$$\Delta_y \quad \frac{\phi_y L^2}{3} \frac{M}{M_y} \tag{7.5}$$

$$\Delta_p \qquad \phi_b - \phi_y \frac{M}{M_y} \quad L_p \quad L - \frac{L_p}{2} \qquad \phi_p L_p \quad L - \frac{L_p}{2} \tag{7.6}$$

where ϕ_y is the theoretical first yield curvature of the column section, L is the column length, M is the moment corresponding to the present curvature level, M_y is the moment at first yield, ϕ_b is the present curvature at the base of the column, ϕ_p is the present plastic curvature at the base of the column and the center of rotation is assumed to act at the plastic hinge midheight. Assuming Δ_p to be the plastic flexural deformation calculated in Equation 7.6, the experimental plastic hinge length, L_{pe} is back-calculated by the equation

$$L_{pe} \quad L \quad 1 - \sqrt{1 - \frac{2\Delta_p}{\phi_p L^2}} \Bigg) \tag{7.7}$$

L_{pe} was calculated for test units at every cycle from μ_Δ to μ_Δ 6 and for the first cycle of μ_Δ , which was the last cycle in which strain data was assumed not to be corrupted by longitudinal bar fracture. For each cycle, the base curvatures were averaged between the positive and negative excursions. Thus, 10 data points were collected for each test unit. Figures 7.31 - 7.35 show the experimental plastic hinge length values both for the case where the base curvature was calculated according to

the potentiometer gage length at the column base, assuming no strain penetration effects, and for the case where the gage length at the column base was artificially increased by the strain penetration length before calculating the base curvature (see Chpater 4). It is important to note that the actual value of strain penetration for the tests reported herein is probably somewhere between the two values given, since the footing was post tensioned both vertically and in the plane of the wall. Additionally, included in the figures are the average experimental values and the values determined by the two equations

$$L_p \qquad .08L + 0.15d_{bl}f_{yl} \leq 0.30d_{bl}f_{yl} \qquad (ksi) \qquad (7.8) \qquad =0$$

given in [12] and

$$L_p \qquad .5D + 0.15d_{bl}f_{yl} \leq 0.30d_{bl}f_{yl} \qquad (ksi) \qquad (7.9) \qquad =0$$

as inferred from [11].

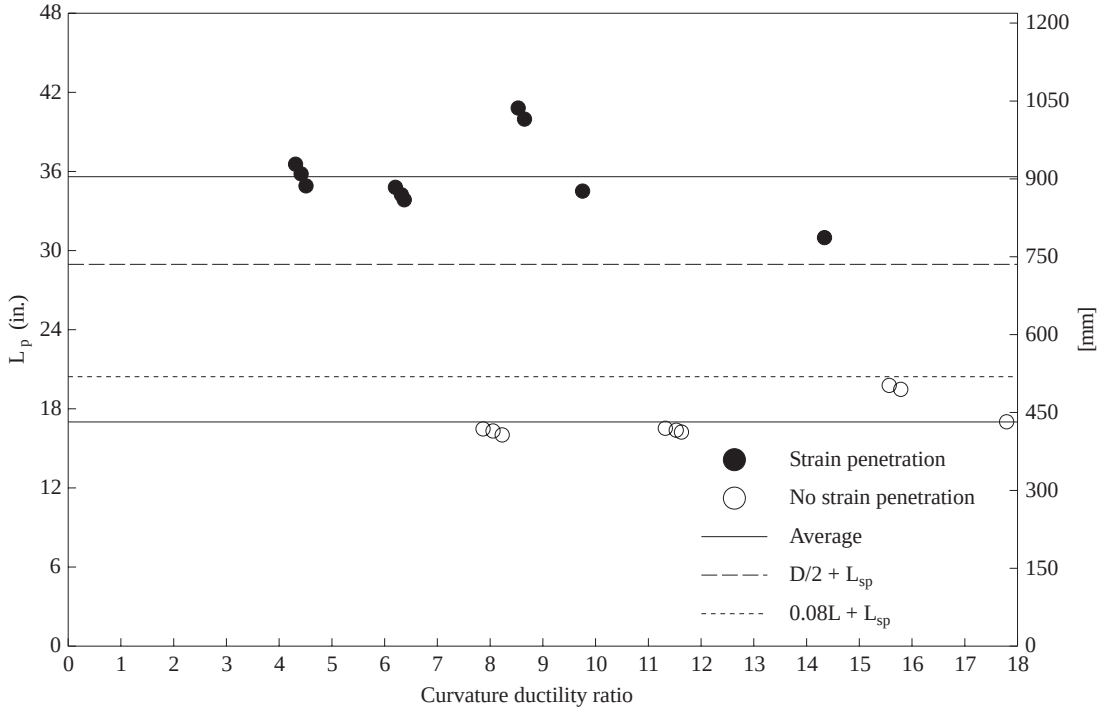

Figure 7.31: Test Unit 1A experimental plastic hinge length values.

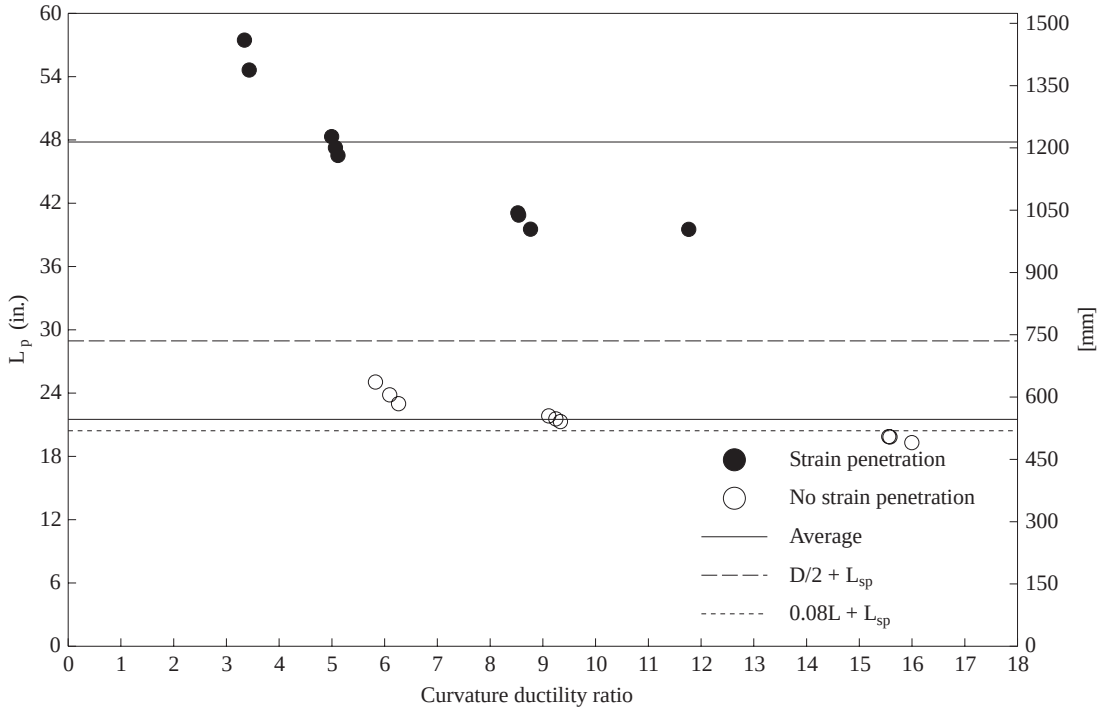

Figure 7.32: Test Unit 1B experimental plastic hinge length values.

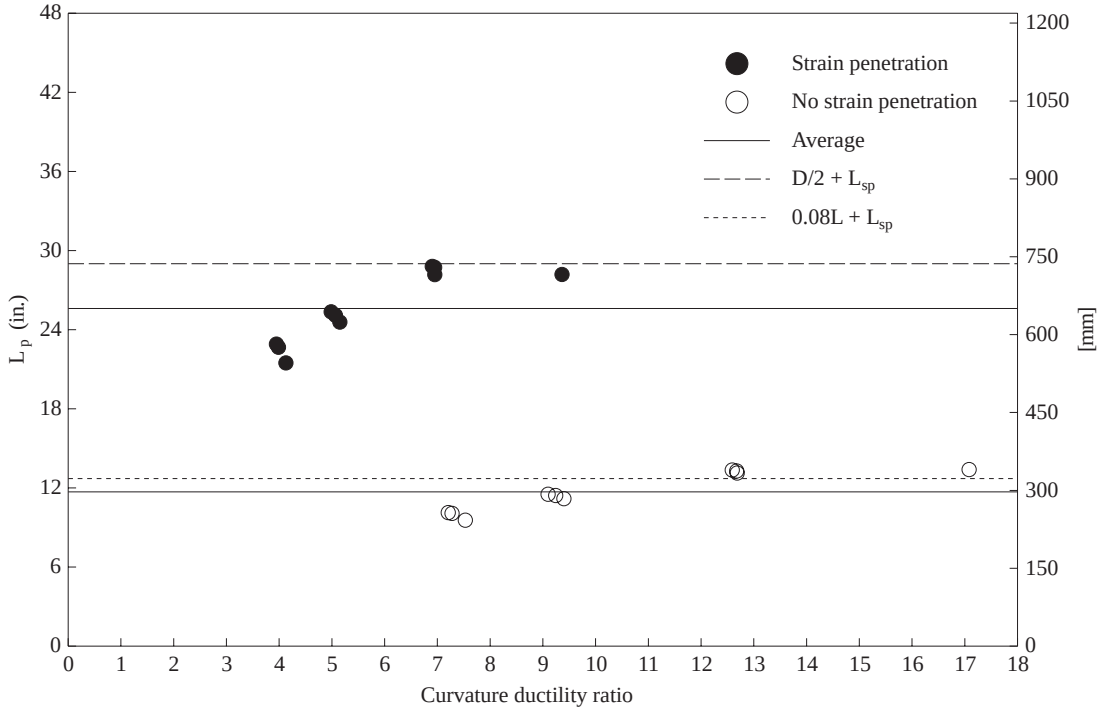

Figure 7.33: Test Unit 2A experimental plastic hinge length values.

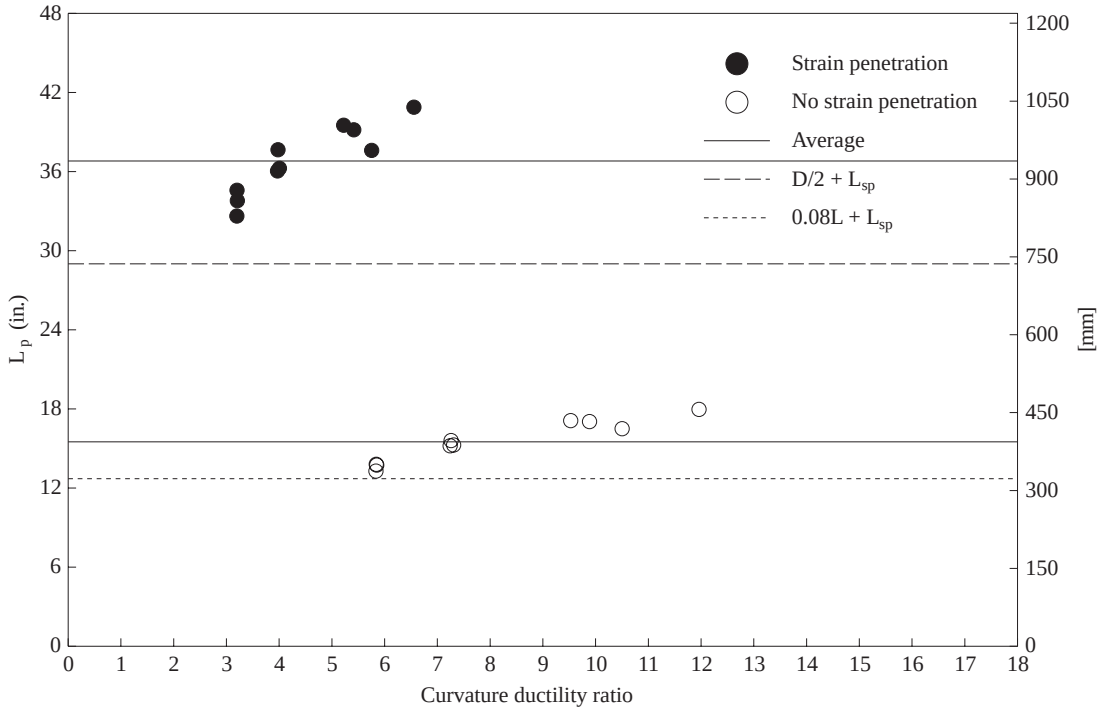

Figure 7.34: Test Unit 2B experimental plastic hinge length values.

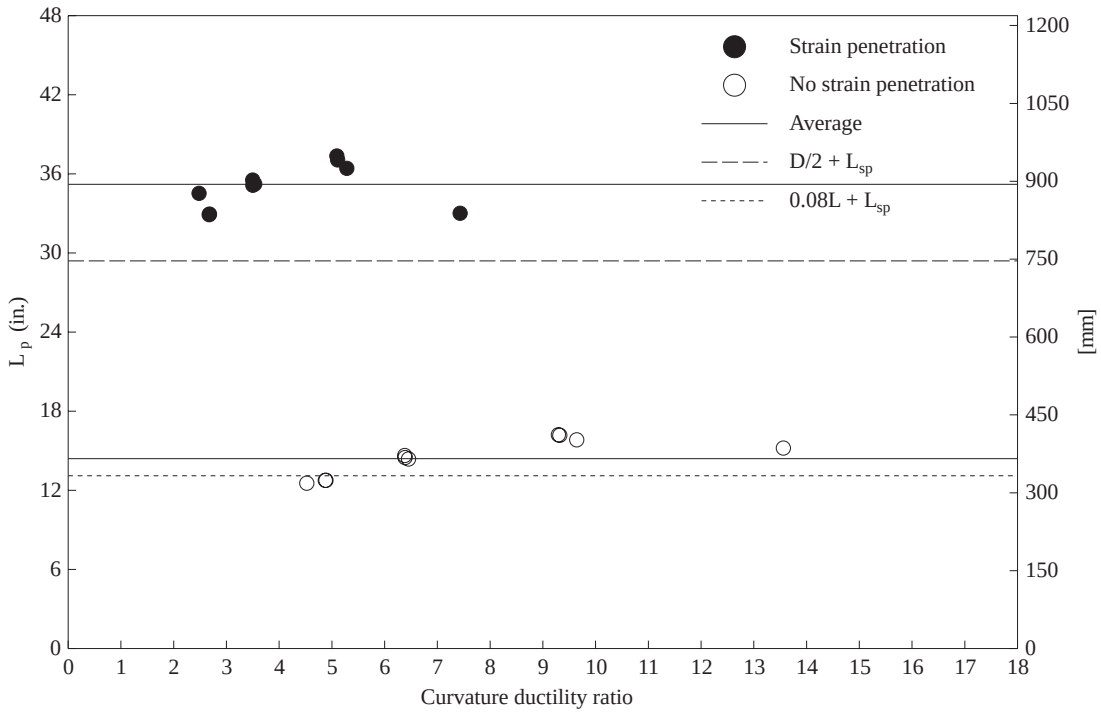

Figure 7.35: Test Unit 2C experimental plastic hinge length values.

Assuming that the strain penetration term, L_{sp} from Equation 7.1 is correct, it should be possible to subtract it from L_{pe} as calculated by Equation 7.7 in order to produce the portion of the plastic hinge length that is a function of the column geometry. Previous authors have defined this portion of the plastic hinge length as a function of either L, D or both L and D. It is logically consistent to include a strain penetration term in an equation for plastic hinge length only if that equation has been calibrated based on the assumption of strain penetration to begin with. Although both the base curvature accounting for strain penetration and the base curvature accounting for no strain penentration were evaluated in the calculation of L_{pe} for the sake of comparison in Figures 7.31 - 7.35, the values assuming strain penetration were considered more consistent with the current approach to estimating plastic hinge length and were therefore taken as the basis for further discussion.

The values for L_{pe} presented in Tables 7.2 and 7.3 are consistently higher than the values for $0.08L + L_{sp}$ and suggest that it may be useful to add another term to the equation that is proportional to the column depth D and accounts for tension shift effects in deeper columns.

Test Unit	Avg. L_{pe}		Std. Dev.	L_{sp}		0.08L		$L_{pD} = L_{pe}-L_{sp}-0.08L$		L_{pD}/D
	in.	mm	%	in.	mm	in.	mm	in.	mm	
1A	35.6	904	8.17	4.95	126	15.5	393	15.2	385	0.316
1B	47.7	1212	16.9	4.95	126	15.5	393	27.3	693	0.568
2A	25.6	650	10.7	5.03	128	7.68	195	12.9	328	0.269
2B	36.8	935	7.23	5.03	128	7.68	195	24.1	612	0.502
2C	35.2	894	4.55	5.40	137	7.68	195	22.1	562	0.461

Table 7.2: Experimental calibration of L_p from UCSD test results.

Test Unit	L_{pe}		L_{sp}		0.08L		$L_{pD} = L_p-L_{sp}-0.08L$		L_{pD}/D
	in.	mm	in.	mm	in.	mm	in.	mm	
B1	55.45	1408.4	6.75	171.5	14.40	365.8	34.30	871.2	0.457
B3	51.67	1312.3	6.75	171.5	14.40	365.8	30.52	775.1	0.407
B4	59.71	1516.6	6.75	171.5	14.40	365.8	38.56	979.4	0.514
B2	73.21	1859.5	6.75	171.5	14.40	365.8	52.06	1322.3	0.694
B5	60.60	1539.2	6.75	171.5	14.40	365.8	39.45	1002.0	0.526
B6	77.46	1967.5	6.75	171.5	14.40	365.8	56.31	1430.3	0.751
B7	68.87	1749.2	6.75	171.5	14.40	365.8	47.72	1212.0	0.636
B8	76.16	1934.5	6.75	171.5	14.40	365.8	55.01	1397.3	0.734
B9	80.54	2045.8	6.75	171.5	14.40	365.8	59.39	1508.6	0.792
B10	90.33	2294.5	6.75	171.5	14.40	365.8	69.18	1757.3	0.922
							Average:		0.643

Table 7.3: Experimental calibration of L_p from Oesterle et al.'s test results.

With regard to the correctness of adding D to the equivalent plastic hinge length equation, two comments are relevant.

1. In favor of maintaining the equivalent plastic hinge length primarily as a function of L: The higher moment gradient in the shorter columns supports the notion that during testing the plastic strains were concentrated over a shorter region, thus implying a shorter plastic hinge length. This is supported by the differences in height of the spalled regions between the Phase I and the Phase II test units as shown in Figures 7.36 and 7.37. The fully spalled region grew to a maximum height of 24 in. [610 mm] in the Phase I test units, whereas it grew to between 7in. [178 mm] and 12 in. [305 mm] in the Phase II test units.

2. In favor of adding D as a parameter to the equation for L_p: Crack patterns in the plastic hinge region suggest, however, that tension shift effects forced plastic strains in the reinforcing bars of the Phase II columns to at least the same height of the Phase I columns (see Figures 7.38 and 7.39). This and the smaller ultimate curvatures measured near the base of the Phase II columns imply that equivalent plastic hinge lengths might be more similar for tall and short columns than is implied by Equation 7.1. It is possible that the higher shear forces in the shorter columns initiated buckling of the longitudinal reinforcing bars at lower levels of strain by pushing outward on them with a higher lateral force. Unfortunately the longitudinal bars were gaged only to a height of 24 in. [610 mm] above the footing, making it impossible to determine the height at which the longitudinal bars no longer yielded in the Phase I and Phase II columns.

The numbers presented in Tables 7.2 and 7.3 support the notion that tension shift in deep columns has a significant effect on the equivalent plastic hinge length. Therefore, the second argument is presumed to be more relevant than the first to the experimental calibration of the equivalent plastic hinge length.

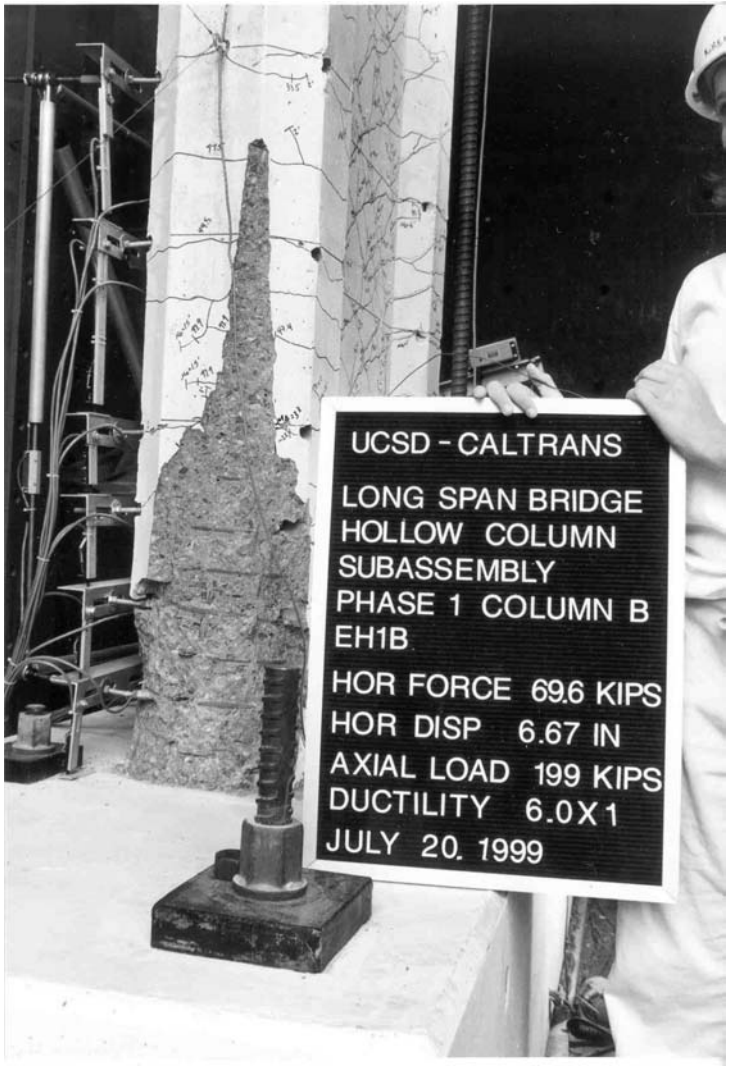

Figure 7.36: Test Unit 1B: fully developed spalled region at μ_Δ

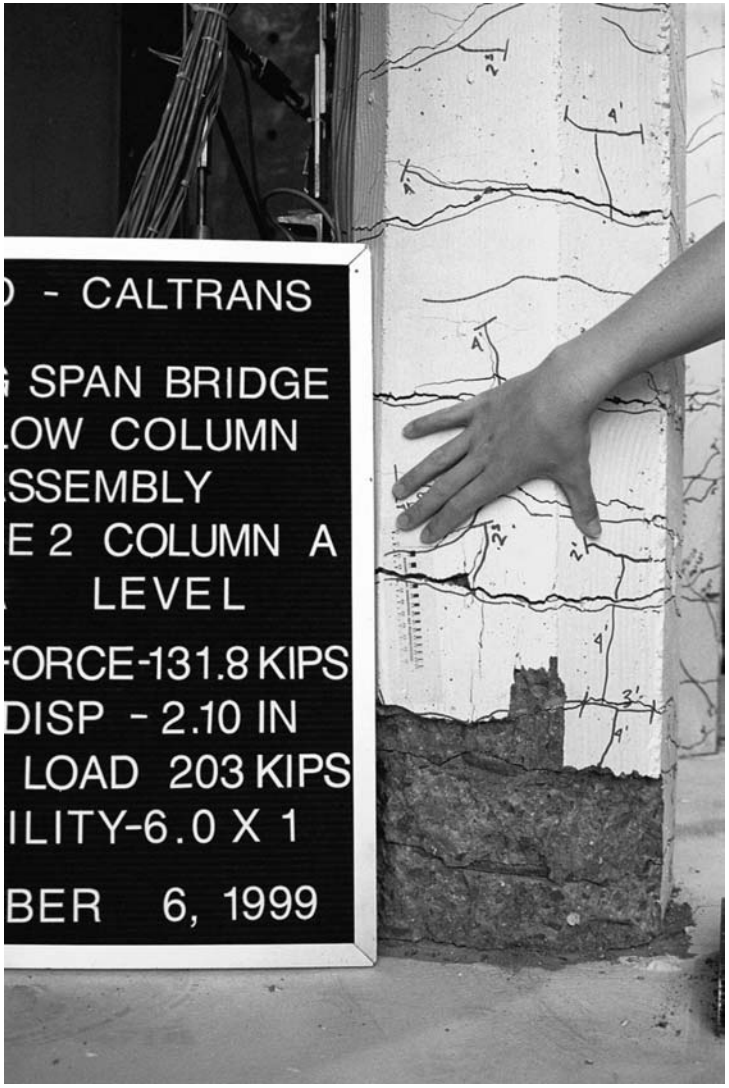

Figure 7.37: Test Unit 2A: fully developed spalled region at μ_Δ .

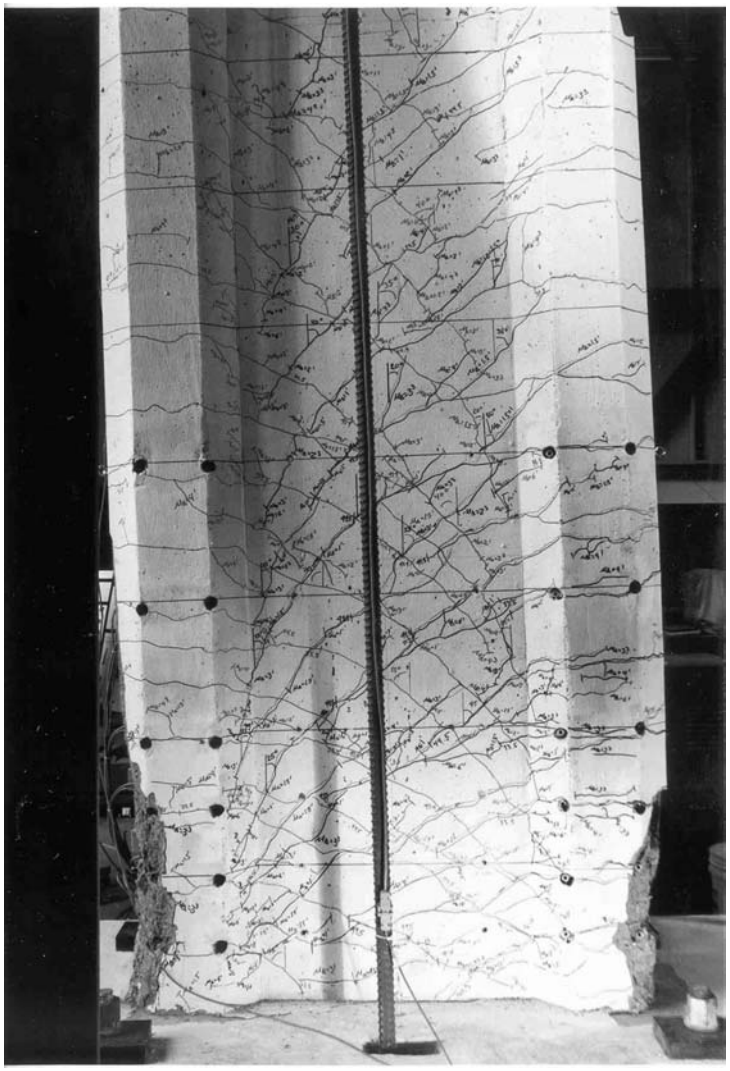

Figure 7.38: Flexure-shear cracks in the hinge region of Test Unit 1B.

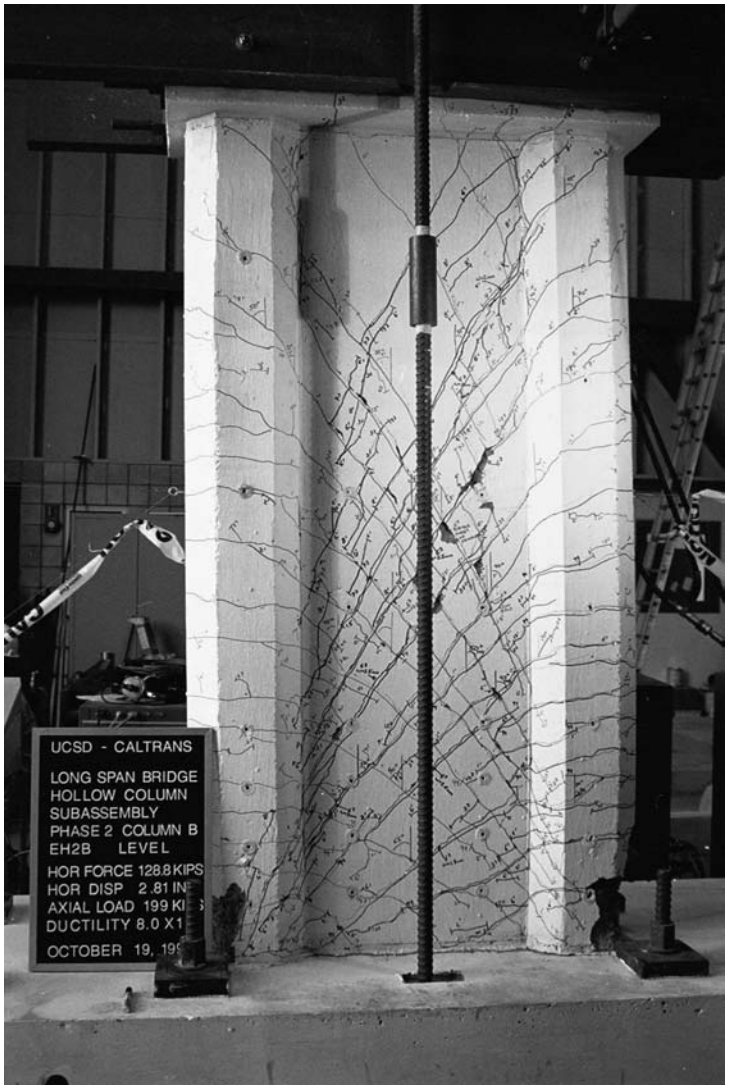

Figure 7.39: Flexure-shear cracks in Test Unit 2B.

Table 7.4 gives the maximum steel and concrete strains at the column base for the Phase I and II tests, derived from the experimental curvature values at the column base shown in Figures 7.21, 7.22, 7.25, 7.26, and 7.27 and used for the calculation of L_{pe}. The values in Table 7.4 are based on the values for μ_{Δ} x 1. For comparison, the strains derived from the base curvatures that neglected strain penetration are also listed in Table 7.4. Based on moment-curvature analysis results, the corresponding extreme fiber steel and concrete strains are also given. The average ultimate base

Unit	$_u$ Avg. (strain pen.) 1/in.	1/m	$_c$ Avg.	$_s$ Avg.	$_u$ Avg. (no strain pen.) 1/in.	1/m	$_c$ Avg.	$_s$ Avg.
Theoretical	0.00228	0.0900	-0.0166	0.0885	0.00228	0.0900	-0.0166	0.0885
1A	0.00135	0.0532	-0.00977	0.0524	0.00247	0.0973	-0.0179	0.0959
1B	0.00111	0.0437	-0.00757	0.0435	0.00203	0.0798	-0.0138	0.0794
Phase I Avg.	0.00123	0.0485	-0.00867	0.0480	0.00225	0.0886	-0.0158	0.0876
2A	0.000877	0.0346	-0.00628	0.0341	0.00160	0.0630	-0.0115	0.0622
2B	0.000614	0.0242	-0.00431	0.0240	0.00112	0.0441	-0.0079	0.0438
2C	0.000765	0.0301	-0.00583	0.0294	0.00140	0.0552	-0.0107	0.0538
Phase II Avg.	0.000752	0.0296	-0.00547	0.0292	0.00137	0.0541	-0.0100	0.0533

Table 7.4: Theoretical and experimental values for ultimate curvature, steel strain and confined concrete strain at the column base.

curvature assuming strain penetration for the Phase I test units was 64% higher than the same average ultimate base curvature for the Phase II test units. In both cases, the extreme concrete and steel strains were well below the theoretical limit states, demonstrating the effect that cyclic loading has on ultimate strain capacity. For these test units, where the spirals were spaced at their maximum allowable of 3 in. [76 mm] $6d_b$, bar buckling occurred within a single 3in. [76 mm] interval and further reduced the ultimate strain capacity of the columns. The Phase II values in Table 7.4 suggest that the presence of higher shear forces in the column reduced the ultimate strain capacity of the boundary elements during testing. Table 7.4 clearly indicates that safe ultimate strain values should be considered to be well below the theoretical values introduced in Chapter 5. Only for the case where zero strain penetration was assumed did the ultimate experimental base curvatures correspond reasonably well to the theoretically calculated ultimate curvatures based on the widely accepted strain limit states of $0.75\varepsilon_{su}$ for steel and ε_{cu} according to Equation 5.1 for confined concrete [12]. In this case, only the Phase I Flexural Test Units reached the assumed strain limits. The Phase II Shear Test Unit strains were consistently lower.

Test data from Phases I and II showed theoretical allowable strains based on

monotonic ultimate strains for steel and confined concrete to be unconservative. They also showed the theoretical equivalent plastic hinge length to be underestimated as a function only of the column length. The fact that the strain capacities in Chapter 5 overestimated the experimental ultimate strains more than the theoretical equivalent plastic hinge length (Equation 7.1) underestimated the experimentally derived values for L_{pe} explains why the theoretical predictions overestimated the displacement capacity of the columns. The experimental strain limits would be higher if the boundary element spirals were spaced more closely to restrain longitudinal bar buckling. Regardless of the exact failure mode, however, a trend in lower allowable strains and longer equivalent plastic hinge lengths due to a relatively linear curvature distribution in the plastic hinge region, can be seen in the Phase I and Phase II test results.

The equivalent plastic hinge lengths calibrated in Table 7.3 give a larger component of the total column depth, D than do the UCSD tests. This can be partially explained by the fact that Oesterle et al. did not report curvatures [8, 6]. Instead they reported rotations measured over roughly the first 36 in. [914 mm] above the footing. For the purposes of calculating values for Table 7.3, this roughly 36 in. [914 mm] gauge height is called L_2. In calibrating L_{pe} from Oesterle et al.'s tests, the base curvature is calculated as the reported rotation $_2$ divided by L_2. L^* is taken as the distance from the top of the column to the assumed center of rotation.

$$L^* \quad L - (L_2 + L_{sp})/2 \tag{7.10}$$

The curvature derived from $_2$ over the gauge height L_2 is certain to be smaller than the curvature taken from rotations measured within the first 12 in. [305 mm] above the column base. In addition, the lever arm L^* is also smaller relative to L for Oesterle et al.'s tests because the center of rotation is taken to act higher above the column base than it is for the UCSD tests. Therefore, the contribution of the total column depth, D can be assumed to be lower than the 0.643 presented in Table 7.3.

Based on these findings it is recommended to calculate the theoretical equivalent plastic hinge length as

$$L_p \quad .08L + \quad \alpha D \quad L_{sp} \tag{7.11}$$

where αD accounts for the effect that the column depth has on the tension shift and hence the spread of plasticity. For columns with properties similar to the UCSD test units or Oesterle's test units, it is suggested to assume 0.3. This value is conservative and corresponds primarily to the two Test Units 1A and 2A that

were well-reinforced in the transverse direction. Although plasticity appeared to spread further in columns with lower transverse reinforcement, such as Test Units 1B and 2B, the phenomenon of actual plasticity spread must be studied more in depth before developing an equation that relates spreading plasticity to the level of transverse reinforcement. The trend of greater plasticity spread in columns with less transverse reinforcement suggests that lowering the transverse reinforcement may help achieve greater plastic rotation capacity. In the application of such logic to column design, however, one must be very careful not to compromise the shear capacity of the column. On the other hand, this logic also implies that over-reinforcing a column in the transverse direction to protect against shear may actually bring other costs in lowering the available plastic rotation capacity.

Although the proposed L_p is larger than before, it does not imply that these columns can safely reach greater displacement ductility levels than circular or rectangular columns. The concrete and steel strains should be limited for design of cyclically loaded members to levels well below their theoretical monotonic limits. The wide spiral spacing in the boundary elements of the test units reported here prevents drawing any hard conclusions about the validity of the strain limit states given in Table 7.4 because it allowed the longitudinal bars to buckle too early. These values could, however, be seen at least as conservative limiting values. It is suggested, based on existing test results, that conservative limits for allowable strains may be set at 40% of the calculated theoretical values for members performing primarily in flexure and at 25% for shear dominated members.

7.4 Performance in Shear

7.4.1 Transverse Strains

The transverse strain data from Test Unit 1A in Figures B.9 and B.10 barely exceeds yield at a height of 36 in. [914 mm] above the footing, whereas lower in the plastic hinge region the transverse strains are reported to be significantly lower. This confirms the notion that the lower part of the plastic hinge region was confined laterally by the base, inhibiting large transverse strains up to a height of roughly $0.5D$. Transverse bar strain data from Unit 1B (see Figures C.9 and C.10) well exceed yield at 18 in. [457 mm] above the footing and thereby show that such columns mobilized more available shear reinforcement to transfer forces when the capacity of the most direct path was reduced.

Similar to results from Tests 1A and 1B, results from Tests 2A and 2B exhibit

large differences in the transverse bar strains, especially in the final stages of testing (see Figures D.8, D.9, E.8 and E.9). Results from the transverse bars in Test 2B show strains in excess of ε_{tr} .01 all the way up the column height, whereas results =0 from the Unit 2A transverse bars show fewer strains above the yield level in the final stages of testing.

7.4.2 Transverse Bar Anchorage and Slip

The transverse bars in Test Unit 1A were designed with heads on the south ends and with no anchorage detail on the north ends. This made it possible to monitor differences in response between the positive and negative loading directions resulting from transverse bar anchorage. The test units exhibited no noticeable differences in force-deflection behavior between the two loading directions due to the difference in anchorage. Strains close to yield were developed inside the structural wall in both directions, implying sufficient anchorage on both sides.

While the lateral load capacity reported for Test Unit 1A is consistently lower in the pull direction than the push direction, this difference amounts to a maximum of 4.8% at μ_Δ 4 and an average of 3.1% over all ductility levels μ_Δ $1-8$. Results from the Phase II test units also show drops in the lateral load capacity in the pull direction. Since the Phase II test units had symmetric transverse reinforcement, this phenomenon of asymmetric load capacity cannot be interpreted strictly as a phenomenon related to asymmetry in the transverse reinforcement. Such drops in capacity are also consistent with previous experience in fully-reversed cyclic laboratory column tests. The results from Test 2A show a maximum drop in capacity of 3.6% after the first reversal at μ_Δ 8 and an average drop of 2.5%.

Table 7.5 shows the percentage drop in capacity from the push to the pull direction for each of the test units. The title "Asymmetric Reinforcement" means that the transverse bars were headed only on one end whereas the title "Symmetric Reinforcement" means that the transverse bars were hooked on one end, but then arranged so that the hooks alternated sides within the column cross section and up the column height. A negative value represents an increase in capacity from the postive to the negative direction. Results from Test 1A show the highest drops in capacity, but these drops are not considered large enough to support any conclusions on the effect of anchorage on column capacity for an amply reinforced column.

Slip of the straight ends was monitored via the instrumentation introduced in Chapter 4. Loading in the pull direction, the north boundary element became the tension boundary element with large flexural cracks in the plastic hinge region. Flex-

μ_Δ	Asymmetric Reinforcement		Symmetric Reinforcement		
	Unit 1A	Unit 1B	Unit 2A	Unit 2B	Unit 2C
1.0	1.4	0.2	0.8	2.7	1.0
1.5	3.4	1.5	1.7	-1.1	-1.1
2.0	3.3	1.5	2.8	1.8	0.5
3.0	2.3	1.4	3.2	2.5	-1.1
4.0	4.8	-0.1	2.4	1.3	0.2
6.0	3.2	0.3	3.0	2.2	0.2
8.0	3.0	-2.9	3.6	0.8	3.2
Avg.	3.1	0.3	2.5	1.5	0.4

Table 7.5: Percent difference in load capacity. Positive: load capacity decreases in the negative (pull) direction. Negative: load capacity increases in the negative (pull) direction.

ural cracks were observed directly at the levels where the transverse bars were monitored for slip (18 in. [457 mm] and 36 in. [914 mm]). These cracks are visible in Figure A.2.

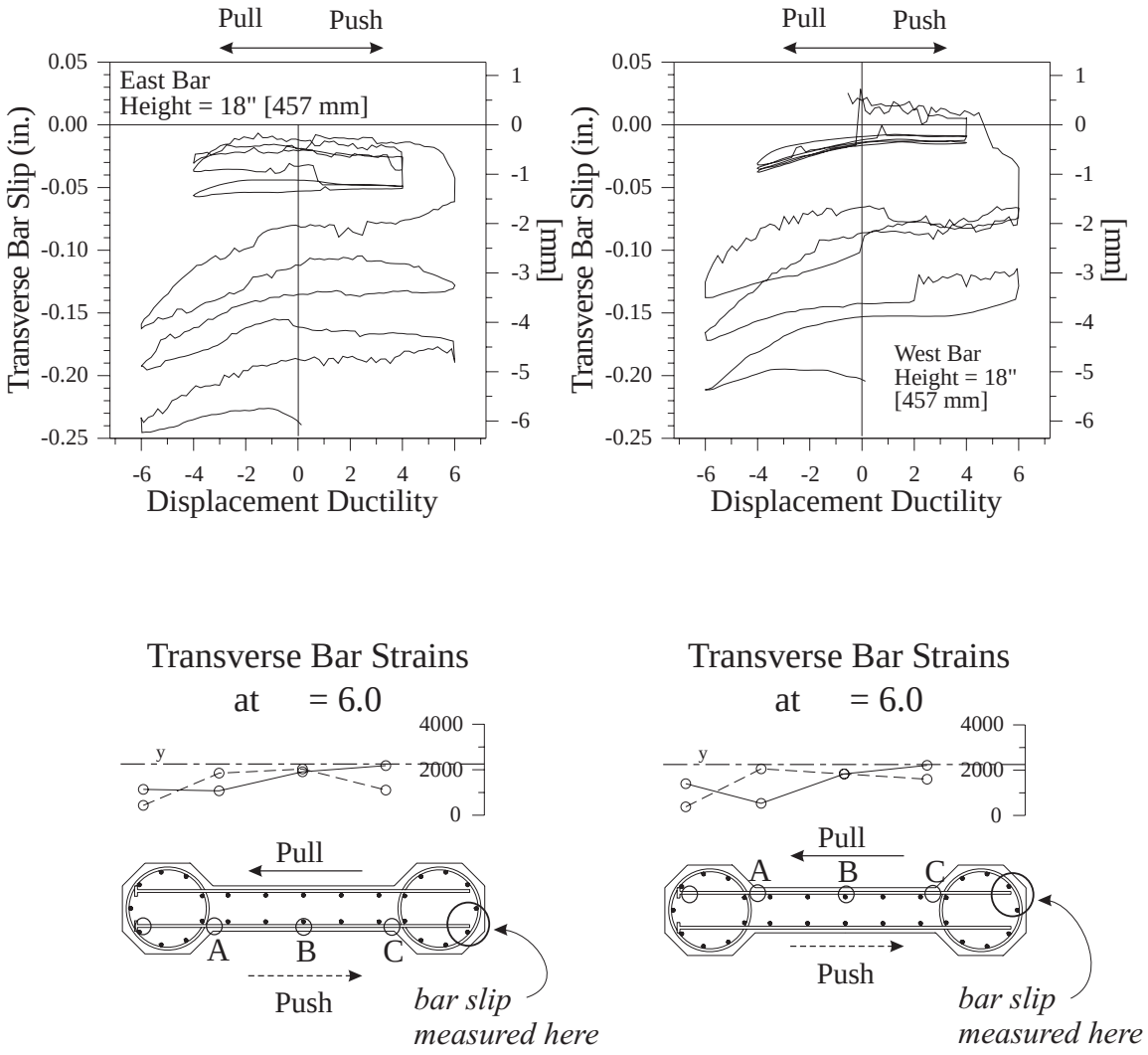

Figure 7.40: Slippage of and strains in the transverse bars at 18 in. [457 mm] above the footing (Test Unit 1A).

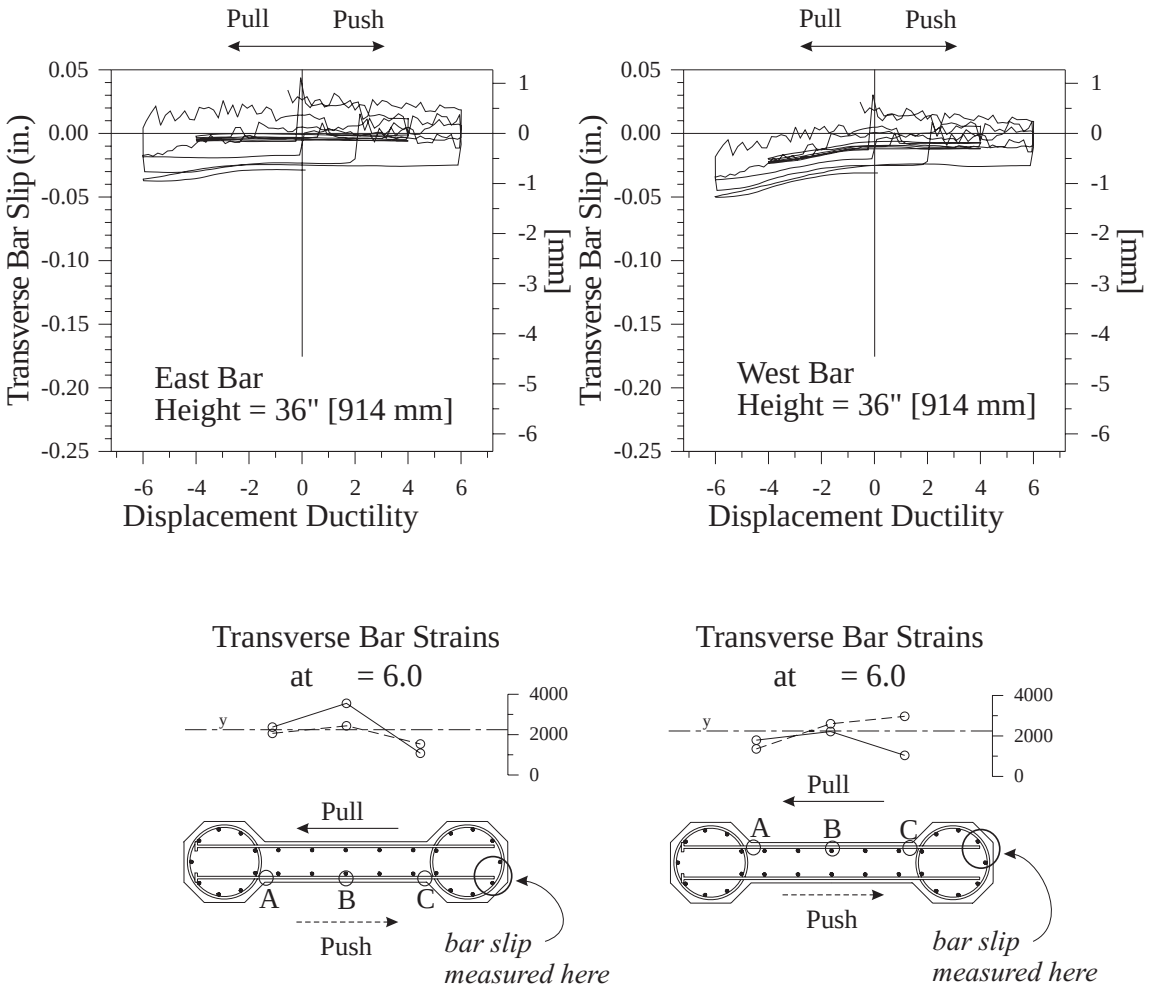

Figure 7.41: Slippage of and strains in the transverse bars at 36 in. [914 mm] above the footing (Test Unit 1A).

Figure 7.40 shows the slippage measured for the bars at 18 in. [457 mm] above the footing. Test results show that noticeable slippage began to occur at μ_Δ 4 and increased in the east bar to -0.25 in. [-6.35 mm] while cycling at μ_Δ 6. Measurements for the west bar in Figure 7.40 exhibit a trend similar to the east bar, however they contain significantly greater noise levels than the measurements for the east bar. The noise in the west bar data is attributed to the power source for the channels in the conditioner cabinet serving the west bar device. This device as well as the two slip devices at 36 in. [914 mm] recorded identical noise during the test, resulting from their connection to a common power supply, independent of the power supply for the east bar device at 18 in. [457 mm]. The measurements that are shown positive for the west bar in Figure 7.40 and for both bars in Figure 7.41 are therefore attributed to noise in the recording and not to actual positive slippage of the transverse bar. Figure 7.41 shows that bar slippage at 36 in. [914 mm] height reached a maximum level of -0.05 in. [-1.27 mm] after cycling at μ_Δ 6, one fifth the level reached by the bars at 18 in. [457 mm].

The greater slippage of the transverse bars at 18 in. [457 mm] above the footing than the bars at 36 in. [914 mm] above the footing could be attributed to the larger flexural cracks that occurred closer to the column base. The slippage of both bars in Figure 7.40 can be seen to be cumulative while cycling at μ_Δ 6, implying that degradation occured in the bond between the bars and the concrete under sustained cyclic loading. The curves for μ_Δ 6 can be seen to dip downward under loading in the pull direction, reflecting the tendency of the straight bar ends to slip in the direction of load when they were unanchored in the tension boundary element. The large dip at the first cycle peak for μ_Δ 6 is attributed to spalling of the cover concrete at the slip device. Figure A.9 shows the spalled region and the slip devices during the first cycle of μ_Δ . The concrete tended to spall off in large chunks and =6 did not always fall off the column right away. It is expected that a chunk of concrete above the slip device became loose under high compression strains at μ_Δ 6, but was held in place by tie wire and plastic cable ties. This loosening would have the effect of compressing the slip device and showing such a reading as is visible in Figure 7.40.

Figure 7.40 also shows strain gage readings for the transverse bars at μ_Δ 6. These readings show little difference in the ability of the bar to reach its yield strength in either the positive or negative loading direction. If slip were to have some effect on the capacity of the bars at the strain gage locations, results from the gage at location C would be expected to show lower readings in the pull direction than would results

from the gage at location A in the push direction.

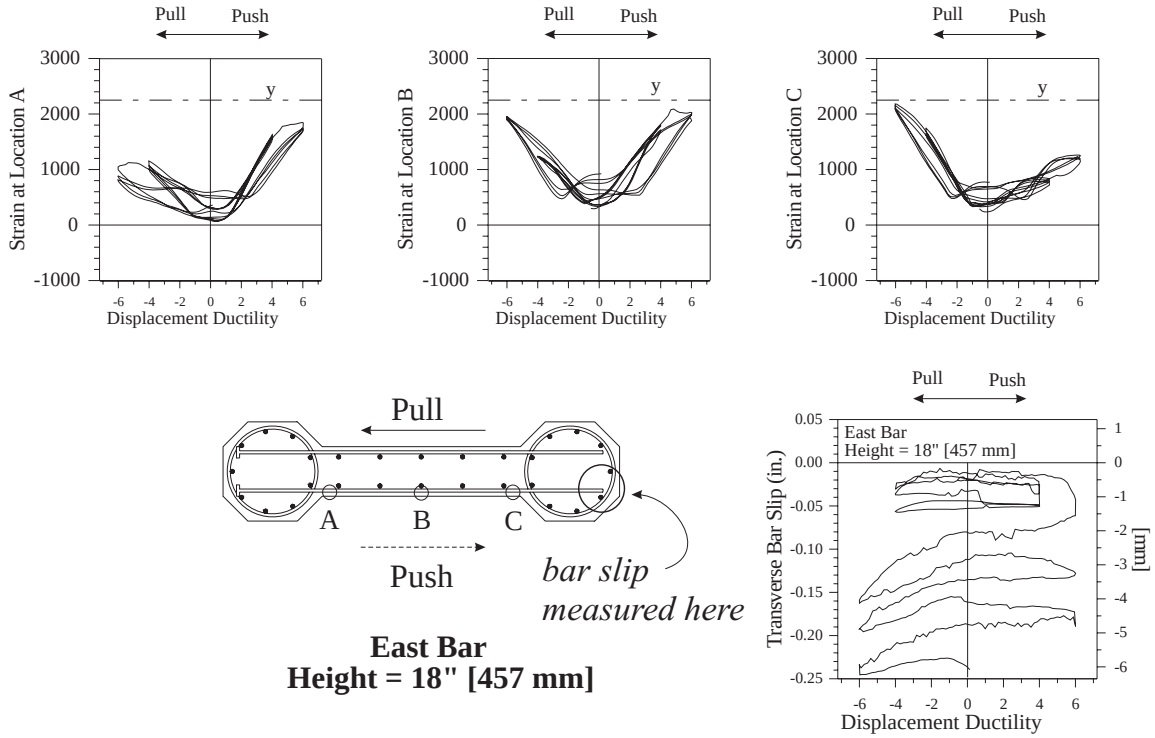

Figure 7.42: Slippage of and strains in the east transverse bar at 18 in. [457 mm]. (Test Unit 1A)

The strain gage readings shown in Figure 7.40 were recorded at the peaks of the first cycle of μ_Δ 6 and might be expected not to represent the effective development of transverse bar yield strength after cycling at μ_Δ . Figure 7.42 shows, however, that the bar strains reached consistently the same level through every cycle of μ_Δ .

While slippage was measured in the transverse bars of Unit 1A during testing, this slippage became significant only in the bars at 18 in. [457 mm] height and was on the order of five times less at 36 in. [914 mm] height. Despite slippage, the transverse bars were still able to develop nearly their full yield strength within the structural wall, implying a necessary development length that at most is equivalent to the 11 in. [279 mm] length of transverse bar inside of the tension boundary element. The ACI code [1] requires a development length of

$$l_d \quad .5\frac{f_y d_{bl}}{65\sqrt{f'_c}} \tag{7.12}$$

for straight end bars, where f_y is the steel yield stress, f'_c is the concrete strength in psi, and d_{bl} is the bar diameter in inches. With f_y 67,000 psi [461.9 MPa] and f'_c

5530 psi [38.1 MPa] for Test Unit 1A, Equation 7.12 gives a development length of 18.2 in. [462 mm]. Test results show, however, that the transverse bars developed their yield strength within at most 11 in. [279 mm] inside of a highly tensile region with large cracks parallel to the bar. The confinement in this region is expected to aid the bar in developing its strength. Furthermore, results from the bars at 36 in. [914 mm] above the footing show little slippage compared to results from the bars at 18 in. [457 mm]. This confirms the idea that there is little reason to expect significant bar slippage to occur within a tensile region when the flexural cracks in this region are not the same order of magnitude as they are in the most highly deformed section of the plastic hinge. Transverse bar strain data for Unit 1A (see Figure B.9) show that bars in the most highly-strained region of the plastic hinge at 6 in. [152 mm], 12 in. [305 mm] and 18 in. [457 mm] did not see demands as high as bars further up the column. This is attributed to the transverse confining effect that the footing had on the column at the base, where the footing carried the shear directly placing less demand on the transverse steel.

Therefore, results from Test 1A show slippage to become significant only at high ductility levels and in bars that were not critical to the shear capacity of the column. Furthermore, even when these bars showed some tendency to slip, they still exhibited a capacity to develop their yield strength anywhere within the structural wall.

7.4.3 Spiral Strains

Crack patterns for Test Unit 1B pictured in Figure A.16 indicate that spiral reinforcement in the tension boundary element was also activated to carry the shear force. The spiral strain data shown in Figures B.11 and C.11 does not clearly support this however, since the recorded spiral strains reach similar levels on Test Units 1A and 1B. These spiral strains are likely as much related to confinement demand as to shear demand. For instance, strain data at locations A and B in Figure C.11 show lower strain values when the left-hand boundary element was in tension (push) rather than when it was in compression (pull). Unit 1A, however, did show that spiral strain data collected at locations A and D (36 in. [915 mm] above the footing), when those locations were in tension, has maximum values of almost half the yield strain (see Figure B.11).

Results from Test 2B show larger transverse strains in the spirals at a height of 72 in. [1829 mm] than results from Test 2A (see Figures D.10 and E.10). This corresponds to the great extent of cracking visible in Unit 2B in Figure 7.9 at this height compared to the lack of cracks in Test Unit 2A at the same height above the

footing.

Figure 7.43 indicates the extent of diagonal cracking in the tension boundary elements of the Phase II test units by μ_{Δ} 1.5. This diagonal cracking suggests that the tension boundary element spirals were engaged to some extent to carry the shear across the section. During the tests such diagonal cracks formed typically out of existing flexural cracks. These cracks would propagated upward along the wall/tension boundary element interface, or diagonally into the tension boundary element. Diagonal cracks reached a maximum inclination of 45° from the vertical inside the tension boundary element. Spiral strain data in Figure 7.44 show that the spirals further up Column 2B, especially at location D, were more engaged in resisting shear than the spirals in the plastic hinge region.

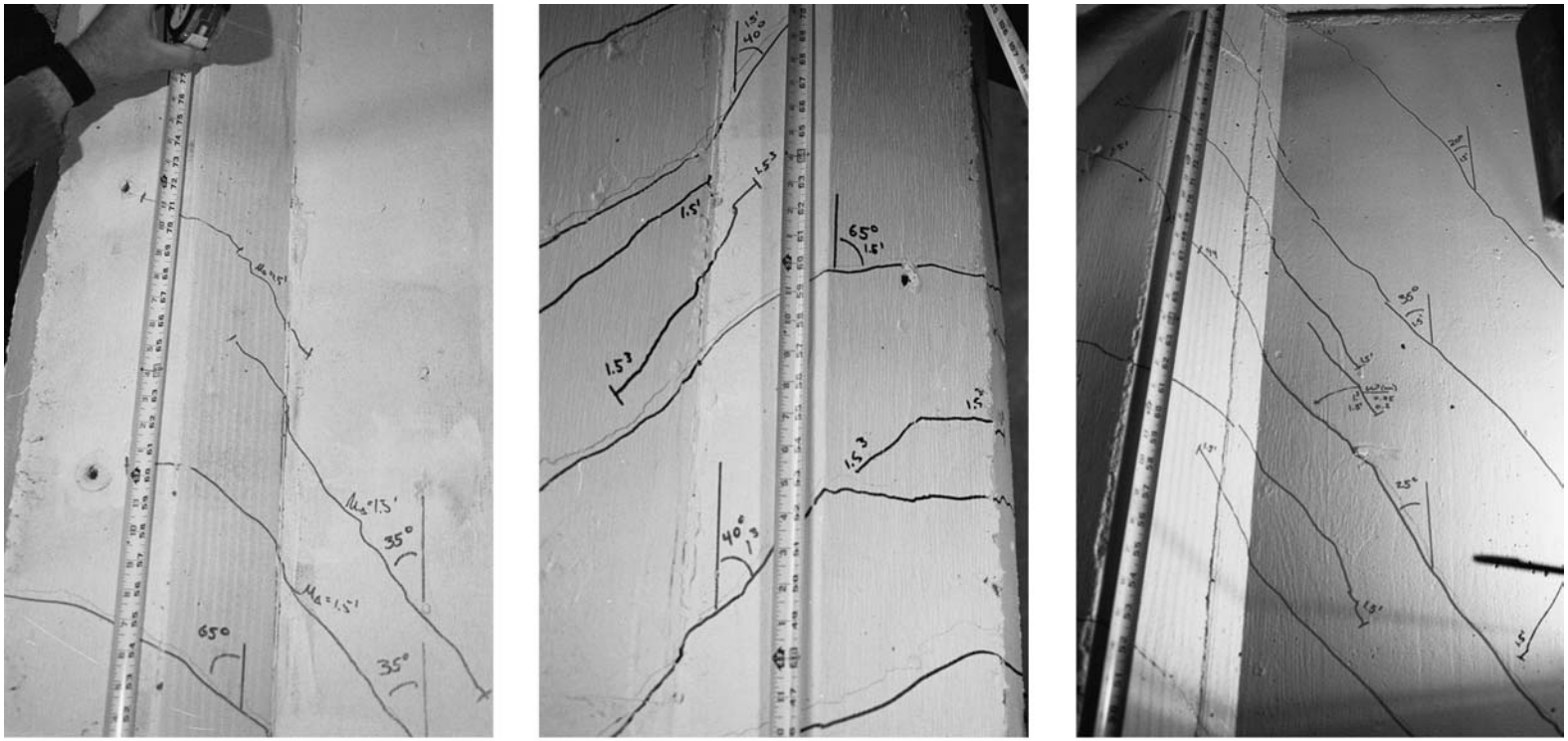

(a) Test Unit 2A (b) Test Unit 2B (c) Test Unit 2C

Figure 7.43: Inclined cracks in the tension boundary element. (a) Test Unit 2A, (b) Test Unit 2B, (c) Test Unit 2C.

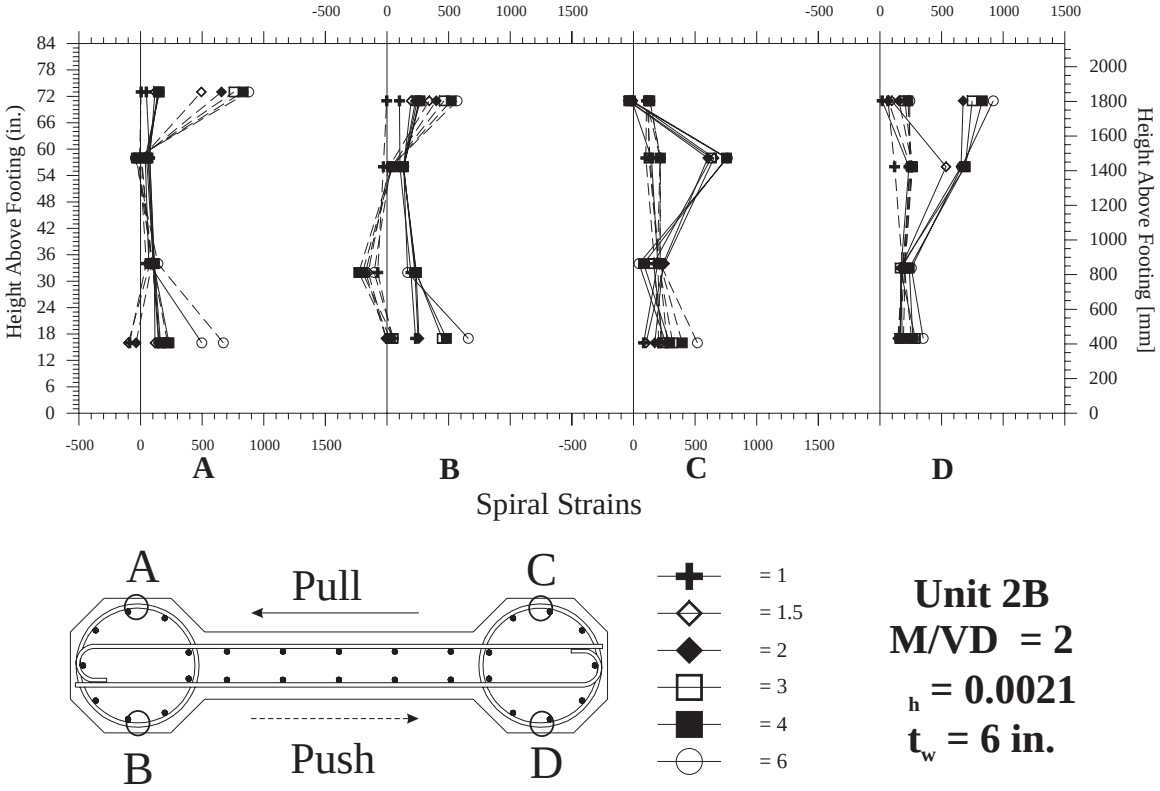

Figure 7.44: Spiral strains in Test Unit 2B.

Chapter 8

Development of a Flexure-Shear Model for Web Crushing

8.1 Overview

A flexure-shear model for web crushing is proposed based on the behavior of the large scale cyclic tests featured in this report and based on the tests performed by Oesterle et al., introduced in Chapter 1. Classical models for web crushing developed for structural walls with boundary elements in buildings are based on the truss analogy and inaccurately characterize the transfer of shear in the plastic hinge region. The classical approach results in expressions that are insensitive to the size of the boundary elements. New pier designs for long span bridges present a variety of new section geometries (see Figure 1.1) that raise the question of whether boundary element size affects web crushing capacity. Whereas the truss analogy, or pure shear model, assumes the principal compression stresses to be distributed relatively evenly across the section depth, the flexure-shear model assumes these stresses to be concentrated along a critical vertical region on the interface between the structural wall and the compression boundary element. The concrete strength of the critical compression struts is calibrated as a function of shear deformation in the plastic hinge region according to test data.

8.2 Classical Models for Web Crushing

The three variations on a classical model for web crushing presented in Chapter 5 are based on the truss analogy. They limit the allowable shear stress on the cross section, implying that this maximum shear stress is uniformly distributed across the section. The classical model is based on the free body diagram in Figure 5.3 The

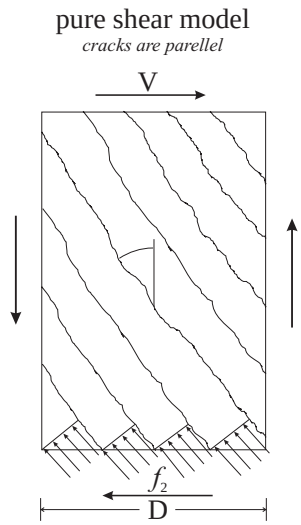

Figure 8.1: Free body diagram for classical web crushing equations.

struts are assumed to be uniformly inclined at an angle from the vertical, implying that the total area available for axial compression in the struts is $Dt_w cos\theta$. The stresses resisting this axial compression have a horizontal component equivalent to $f_2 sin\theta$, where f_2 is the principal compression stress acting along the axis of the struts. The shear force applied to the section is therefore counteracted by the horizontal components of the normal stresses summed over the available area.

$$V \quad f_2 D t_w cos\theta sin\theta \tag{8.1}$$

Defining f_2 as the maximum concrete compressive stress after compression softening due to expanding shear cracks in the wall and expressing the equation in terms of shear stress, the web crushing stress becomes

$$v_{wc} \quad k f'_c cos\theta sin\theta \tag{8.2}$$

where k is a concrete strength reduction factor which reduces with increasing shear deformations.

8.3 Concerns Raised from Test Observations

Contrary to the assumption of pure shear behavior, upon which classical web crushing models are based, the actual phenomenon of web crushing occurs in a concentrated region of the wall where the struts converge at the compression toe of the column [8, 6] as shown in Figure 8.2. This suggests that the web crushing behavior in a plastic

hinge zone does not follow the pure shear model in Figure 8.1 but rather follows a flexure-shear model (see Figure 8.3).

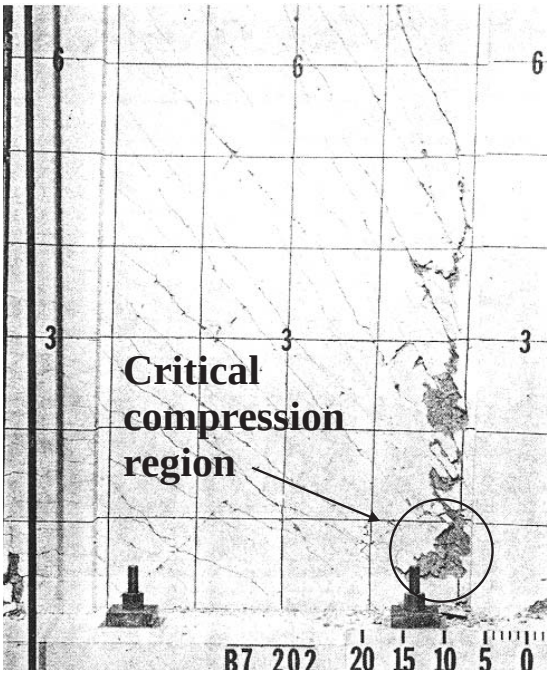

Figure 8.2: Detail of web crushing in a structural wall with confined boundary elements [7].

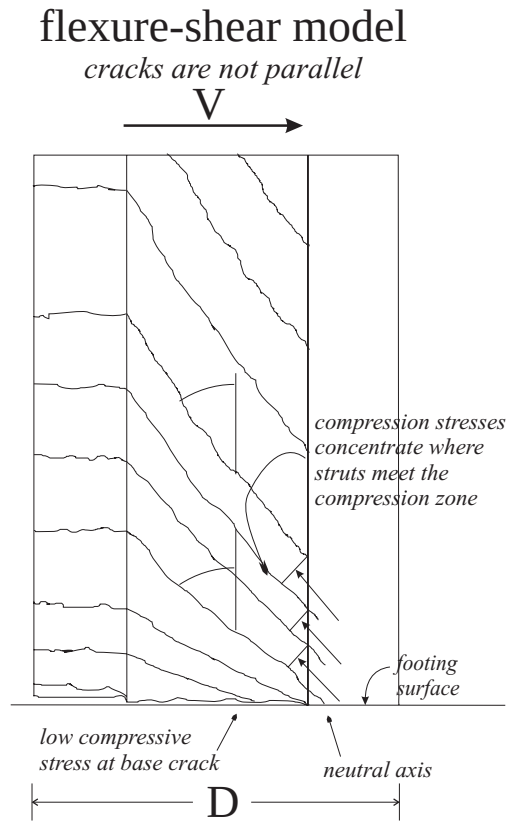

Figure 8.3: Critical compression struts take shear directly into the compression toe.

Typically the critical region crushes just outside of the compression toe and then neighboring struts crush successively either above or to the side of the initial failed struts. Crack patterns for such walls confirm that the diagonal compression stresses are concentrated in this region where the individual struts become thinner and converge in the compression toe (see Figure 8.4).

8.4 Flexure-Shear Approach to Web Crushing Demand and Capacity

An alternative expression for web crushing strength can be derived based on the free body diagram pictured in Figure 8.5. Cracks are assumed to be horizontal in the tension boundary element and the longitudinal steel is assumed to behave elastically

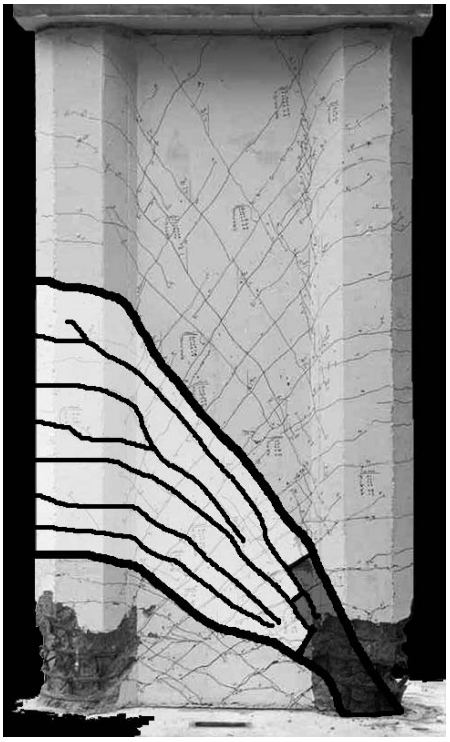

Figure 8.4: Crack pattern and compression struts in the plastic hinge region of UCSD Test Unit 2C.

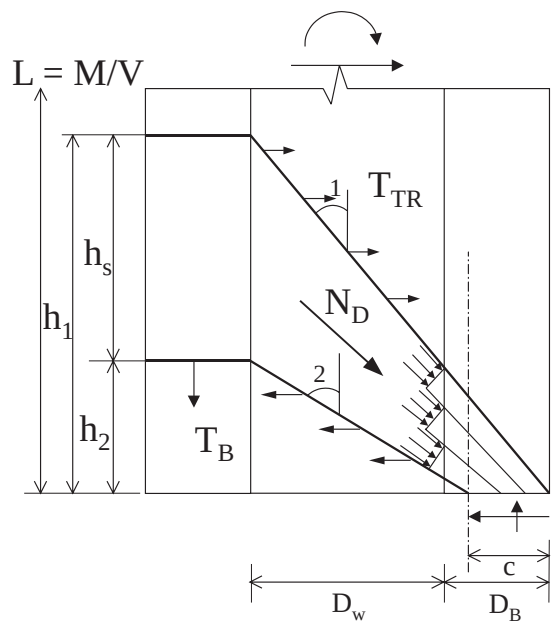

Figure 8.5: Free body diagram for critical compression strut region.

above a height of h_2.

Based on this free body diagram, the web crushing strength is primarily a function of the parameters in Table 8.1. Although the axial load ratio is not directly included in this list, it is implicitly included via the neutral axis depth, c, which increases with increasing axial load. A deeper neutral axis implies an increase in the area of the critical compression struts, and thus an increase in the web crushing capacity, a phenomenon central to Oesterle et al.'s derivation of web crushing strength in 1984.

The demand on the critical compression struts is calculated by summing contributions from the longitudinal and transverse steel. Assuming the longitudinal steel to reach yield at the lower edge of the free body diagram pictured in Figure 8.5, and assuming the stress in the steel to vary linearly from f_{ly} at this lower edge to zero at the point of contraflexure, a net vertical force pulling downward on the bottom of the critical region is produced. This force can be characterized as

$$\Delta T_l \quad A_{sl} f_{yl} \frac{h_s}{L - h_2} \tag{8.3}$$

where A_{sl} is the total area of longitudinal steel contributing to compression in the strut. A_{sl} should include at least the steel in a single boundary element and may also include all of the steel in the in-plane structural wall as well as half of the steel in the out-of-plane structural wall which is in tension. Figure 8.6 shows highlighted the entire region over which the longitudinal steel is expected to contribute to demand on the critical compression struts. f_{yl} is the yield stress for the boundary element

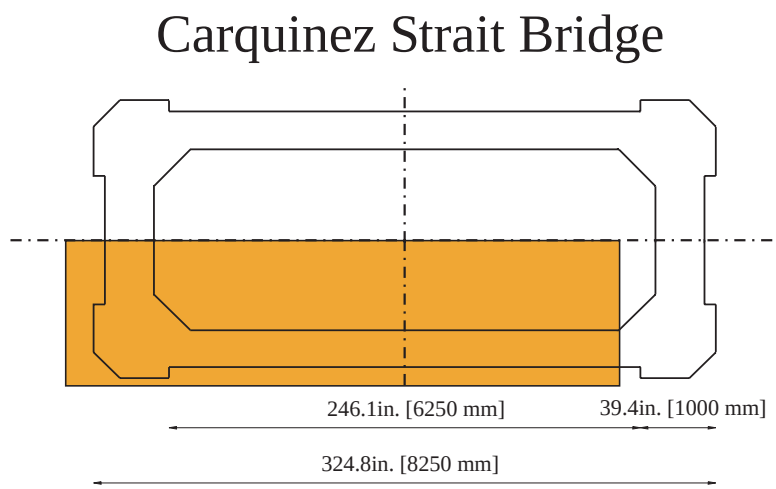

Figure 8.6: Effective region in which longitudinal steel acts on the critical compression strut.

longitudinal steel, h_s is the height of the region in the tension column over which the difference in longitudinal stress is evaluated,

$$h_s \quad D_w + D_b)cot\theta_1 - (D_w + D_b - c)cot\theta_2 \tag{8.4}$$ =(

and $L - h_2$ is the length over which the longitudinal steel stress varies linearly from zero to yield. Hence, without evaluating the actual shear demand on the column, this expression accounts directly for the effects of aspect ratio and longitudinal steel ratio on strut demand.

The horizontal component of the demand on the strut is provided by the net action of transverse steel on the critical compression struts inside the wall, expressed as

$$T_{tr} \quad A_{str} f_{ytr} \frac{D_w(\cot\ _1 - \cot\ _2)}{s_{tr}} \leq \Delta T_l tan\theta_{av} \tag{8.5}$$

The transverse steel is assumed to have yielded, and therefore may produce a greater demand than the longitudinal steel. When this is the case, the transverse steel is limited to providing the same demand as the longitudinal steel. Hence, for low amounts

Demand on the critical compression struts	L	column length M/V
	D	column depth
	ρ_l	longitudinal reinforcement ratio
	ρ_h	transverse reinforcement ratio
	f_y	steel yield stres
Capacity of the critical compression struts	t_w	wall thickness
	D_b	boundary element depth
	c	neutral axis depth
	γ	shear deformation in the plastic hinge region
	f'_c	concrete strength

Table 8.1: Parameters affecting the web crushing strength of bridge piers.

of transverse reinforcement the demand on the compression strut lessens, whereas for high amounts of transverse reinforcement the demand plateaus according the the level of longitudinal steel. Clearly this assumption is an approximation that does not correspond to a rigorous calculation of moment equilibrium on the compression strut, and may be refined in future versions of the model.

The total demand on the strut is then calculated as

$$N_D \qquad T_l cos\theta_{av} + T_{tr} sin\theta_{av} \tag{8.6}$$

The strut capacity is calculated based on the wall thickness t_w, strut depth d_s, concrete strength f'_c, and a concrete compressive strength reduction factor k, to account for weakening of compression struts under large tensile strains. This results in the expression

$$N_C \qquad k f'_c t_w d_s \tag{8.7}$$

where d_s is a function of both the neutral axis depth and the depth of the boundary elements.

$$d_s \qquad c' cos\theta_{av} \tag{8.8}$$

$$c' \qquad D_b cot\theta_1 - (D_b - c) cot\theta_2 \tag{8.9}$$

For design is is recommended that

$$N_C \geq 1.5 N_D \tag{8.10}$$

8.5 Calibration of Concrete Strength

The concrete strength reduction factor, k, decreases as a function of shear distortion in the plastic hinge region [3]. Oesterle et al. calculated experimental values for k based on the truss analogy with the equation

$$k \quad \frac{V_{wc}}{0.8Dt_w 0.5f'_c} \tag{8.11}$$

in which they assumed the value of 0.5 to approximate sin cos . These values matched reasonably well the corresponding theoretical values from the equation proposed by Collins in 1978 [3]

$$k \quad \frac{3.6}{1 + \frac{2\gamma_m}{\varepsilon_0}} \tag{8.12}$$

where

γ_m	the maximum average shear distortion in the plastic hinge region prior to web crushing.
ε_0	concrete strain at maximum compressive stress

Although the model presented by Collins in 1978 was updated in 1986 [17] as a function of the principal tensile strain rather than the shear distortion, the model proposed here uses Collins's 1978 model in order to compare results directly with Oesterle's tests and conclusions. Oesterle et al. published their model in 1984, prior to the 1986 modification. For the flexure-shear web crushing model proposed here, k must be scaled up by a factor of 2 in order to accomodate changes in geometry and compression strut demand from the truss analogy to the flexure/shear model. N_D replaces the actual ultimate load V_{wc} on the column and $d_s t_w$ replaces $0.8Dt_w$ as the area available to resist the critical compression stresses.

Table 8.2 presents properties for Oesterle et al.'s test units and the corresponding N_C/N_D ratios calculated based on the flexure-shear web crushing model. An N_C/N_D ratio of 1.00 would indicate a perfect prediction of web crushing. The flexure-shear model gave low values of N_D for Test Units B7, B8 and B9 whose shear strength and hence compression strut demand was increased by the presence of axial load. While the flexure-shear model accounts for an increase in capacity due to the presence of axial load by accounting for the neutral axis depth, the effect of axial load on compression strut demand is neglected in the initial model presented here. The calculated values of N_D were therefore scaled according to 55% of the measured ultimate loads on all of the units tested by Oesterle et al.

Test Unit	P/f'_cA_g %	f'_c ksi [MPa]	γ	k	f_y ksi [MPa]	c in. [mm]	t_w in. [mm]	N_C/N_D
B2	0.0	7.78 [53.6]	0.028	0.367	59.5 [410]	7 [178]	4.0 [102]	1.18
B5	0.0	6.57 [45.3]	0.022	0.402	64.4 [444]	5 [127]	4.0 [102]	0.98
B5R	0.0	6.21 [42.8]	0.025	0.356	64.4 [444]	5 [127]	4.0 [102]	0.84
B6	13.4	3.17 [21.9]	0.007	0.85	63.9 [441]	10 [254]	4.0 [102]	1.16
B7	7.6	7.16 [49.4]	0.019	0.478	66.4 [458]	7 [178]	4.0 [102]	1.19
B8	9.0	6.09 [42.0]	0.015	0.595	64.9 [447]	8 [203]	4.0 [102]	1.21
B9	8.5	6.40 [44.1]	0.013	0.655	62.3 [430]	8 [203]	4.0 [102]	1.40
F1	0.0	6.58 [45.4]	0.016	0.560	62.4 [430]	7 [178]	4.0 [102]	0.71
F2	7.3	6.61 [45.6]	0.015	0.595	62.3 [430]	9 [229]	4.0 [102]	1.09

Table 8.2: Capacity/Demand ratios and minimum wall thicknesses for PCA tests on isolated structural walls.

Table 8.3 compares the capacity/demand ratios calculated by the four web crushing equations presented in this report both for the tests of Oesterle et al. and for the Phase II tests presented in this report. While the flexure-shear model does not show better correlation for Oesterle et al.'s tests, it does not show significantly worse correlation and may therefore be expected to perform more accurately than the other models for bridge piers with boundary elements of significant size.

For instance, the flexure-shear model predicts more than adequate web crushing strength for the Phase II test units, whereas the other three models predict web crushing in Test Unit 2C. The flexure-shear model is sensitive to the fact that the boundary elements are closer together in the Phase II test units than they are in those tested by Oesterle et al. The height d_s over which the compression strut capacity is calculated is therefore larger in proportion to the distance h_s over which the the primary demand on the compression struts is calculated.

To the authors' knowledge, there exists no substantial experimental evidence to confirm that the web crushing strength is highly dependent on the relative depth ratio D_w/D_b. Section 8.6 outlines a proposal for future research investigating variations in the relative depth ratio parameter.

8.6 Web Crushing Parameter Study

The flexure-shear model for webcrushing introduced in this chapter increases in the ratio of web crushing capacity to column ultimate flexural capacity V_{wc}/V_u, as the relative depth ratio between the wall and the boundary elements D_w/D_b is decreased below 2. This contradicts the philosophy implicit in existing web crushing models that the web crushing capacity is always directly proportional to the total depth

Test Unit	N_C/N_D flexure-shear	Oesterle et al. pure shear	Paulay et al. pure shear	ACI pure shear
Oesterle et al. 1976-1979				
B2	1.18	1.24	0.90	1.38
B5	0.98	0.94	0.72	1.14
B5R	0.84	0.76	1.08	1.13
B6	1.16	0.92	0.52	0.73
B7	1.19	1.04	0.71	0.92
B8	1.21	0.80	0.50	0.85
B9	1.40	0.92	0.60	0.87
F1	0.71	0.89	0.60	0.94
F2	1.09	1.05	0.63	0.98
Avg.	1.08	0.98	0.77	1.03
Std. Dev.	0.21	0.17	0.29	0.23
Hines et al. 1999				
2A	3.92	1.23	0.52	1.24
2B	3.76	1.40	0.59	1.32
2C	1.60	0.70	0.29	0.76

Table 8.3: Capacity/Demand ratios and minimum wall thicknesses for PCA tests on isolated structural walls.

D, of the structural wall. Results of a numerical parametric study conducted on seven columns with identical boundary element longitudinal reinforcement, boundary element confinement, boundary element depth, and material properties, but varying wall depth are presented herein in order to point out this difference between the UCSD model and classical web crushing models.

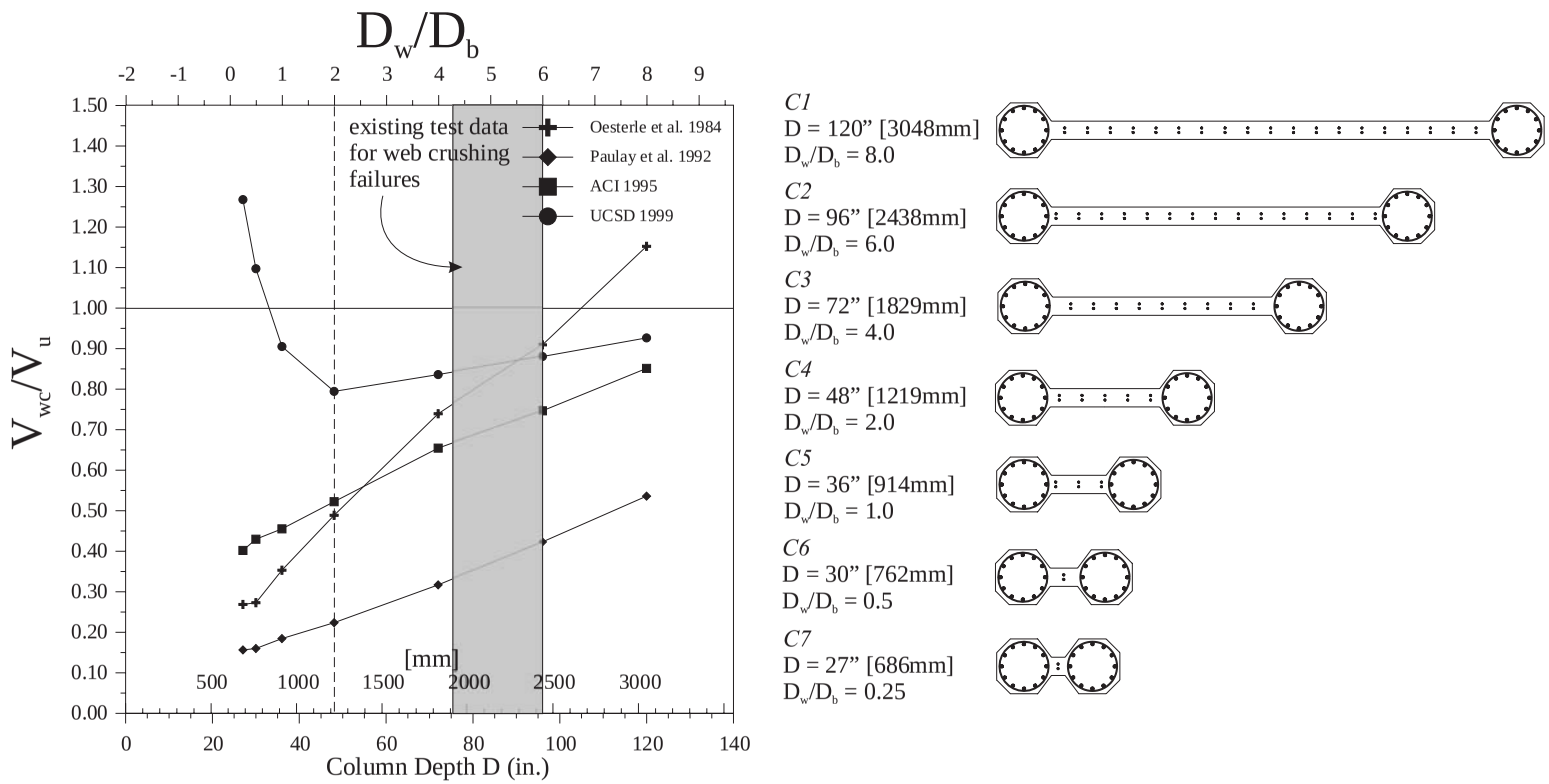

Figure 8.7: Variation in the ratio of web crushing strength to ultimate flexural strength V_{wc}/V_u, as a function of the relative depth ratio D_w/D_b.

Column	M/VD	L		D		D_w		D_b		D_w/D_b	t_w	
		in.	[mm]	in.	[mm]	in.	[mm]	in.	[mm]		in.	[mm]
C1	2.5	300	[7620]	120	[3048]	96	[2438]	12	[305]	8.00	4	[102]
C2	2.5	240	[6096]	96	[2438]	72	[1829]	12	[305]	6.00	4	[102]
C3	2.5	180	[4572]	72	[1829]	48	[1219]	12	[305]	4.00	4	[102]
C4	2.5	120	[3048]	48	[1219]	24	[610]	12	[305]	2.00	4	[102]
C5	2.5	90	[2286]	36	[914]	12	[305]	12	[305]	1.00	4	[102]
C6	2.5	75	[1905]	30	[762]	6	[152]	12	[305]	0.50	4	[102]
C7	2.5	67.5	[1715]	27	[686]	3	[76]	12	[305]	0.25	4	[102]

Table 8.4: Relative Depth Ratio parametric study: geometric properties for columns C1-C7.

Figure 8.7 shows this increase in web crushing capacity predicted by the UCSD model as compared to predictions made based on the classical web crushing models. Table 8.4 details the geometric properties of columns C1-C7. Table 8.5 gives numerical values for the V_{wc}/V_u ratios. Note that the assessment equations given by the UCSD model do not directly depend on the value of V_u. Instead, the demand on the critical compression struts is calculated directly from the free body diagram of these struts (see Figure 8.5) as a function of the column dimensions and longitudinal reinforcement. Hence the ratio calculated via the UCSD model is N_C/N_D and not V_{wc}/V_u.

Figure 8.8 shows the theoretical force-displacement curves produced via moment-curvature analyses and assumed equivalent plastic hinge lengths. The values of F_y and Δ_y are taken from these curves at first yield of the extreme longitudinal reinforcing bar. F_u and Δ_u are taken from these curves at either the point where ε_s 0.06 in the extreme tensile longitudinal bar, or at the point where ε_c 0.02 for the extreme concrete fiber in compression. Δ_{iy} is calculated from the theoretical curves as

$$\Delta_{iy} \quad {}_y\frac{F_{iy}}{F_y} \tag{8.13}$$

where F_{iy} is the theoretical force on the column at which the extreme concrete compression fiber reaches as strain of ε_c 0.004. Shear deformation in the plastic hinge region at ultimate displacement is assumed to be γ 0.02 for all seven columns. Table 8.6 gives the numerical force-deflection properties for the seven columns.

The longitudinal steel in all seven columns consists of 12 No. 6 [D19] bars in each boundary element and pairs of No. 4 [D13] bars spaced at 5in. [127mm] intervals inside the wall. The spiral confinement is deformed No. 3 [D10] bars spaced at 1in. [25mm] inside the lower plastic hinge region. The steel yield stress is assumed to be f_y 66ksi [455MPa], and ultimate stress is assume to be f_u 99ksi [683MPa].

Column	Oesterle et al. V_{wc}/V_u	Paulay et al. V_{wc}/V_u	ACI V_{wc}/V_u	Hines et al. N_C/N_D
C1	1.15	0.54	0.85	0.93
C2	0.91	0.42	0.75	0.88
C3	0.74	0.32	0.65	0.84
C4	0.49	0.22	0.52	0.79
C5	0.35	0.18	0.46	0.91
C6	0.27	0.16	0.43	1.10
C7	0.27	0.16	0.40	1.27

Table 8.5: Column web crushing properties at ultimate displacement Δ_u.

Column	F_y		Δ_y		F_{iy}		Δ_{iy}		F_u		Δ_u		$\mu_{\Delta u}$
	kips	[kN]	in.	[mm]	kips	[kN]	in.	[mm]	kips	[kN]	in.	[mm]	
C1	207	[921]	1.09	[27.7]	305	[1357]	1.61	[40.9]	319	[1420]	6.0	[152]	3.7
C2	185	[823]	0.85	[21.6]	268	[1193]	1.23	[31.2]	291	[1295]	5.4	[137]	4.4
C3	151	[672]	0.52	[13.2]	223	[992]	0.77	[19.6]	249	[1108]	4.4	[112]	5.7
C4	124	[552]	0.37	[9.4]	169	[752]	0.50	[12.7]	208	[926]	3.6	[91]	7.1
C5	116	[516]	0.34	[8.6]	141	[627]	0.41	[10.4]	179	[797]	3.3	[84]	8.0
C6	99	[441]	0.28	[7.1]	124	[552]	0.35	[8.9]	158	[703]	3.4	[86]	9.7
C7	97	[432]	0.26	[1.2]	123	[547]	0.33	[8.4]	152	[676]	2.9	[74]	8.8

Table 8.6: Column force-deflection properties.

Unconfined concrete strength is assumed to be f'_c 5ksi [35MPa]. The axial load ratio P/f'_cA_g on each column was assumed to be 0.10, implying slightly larger axial loads for the deeper columns.

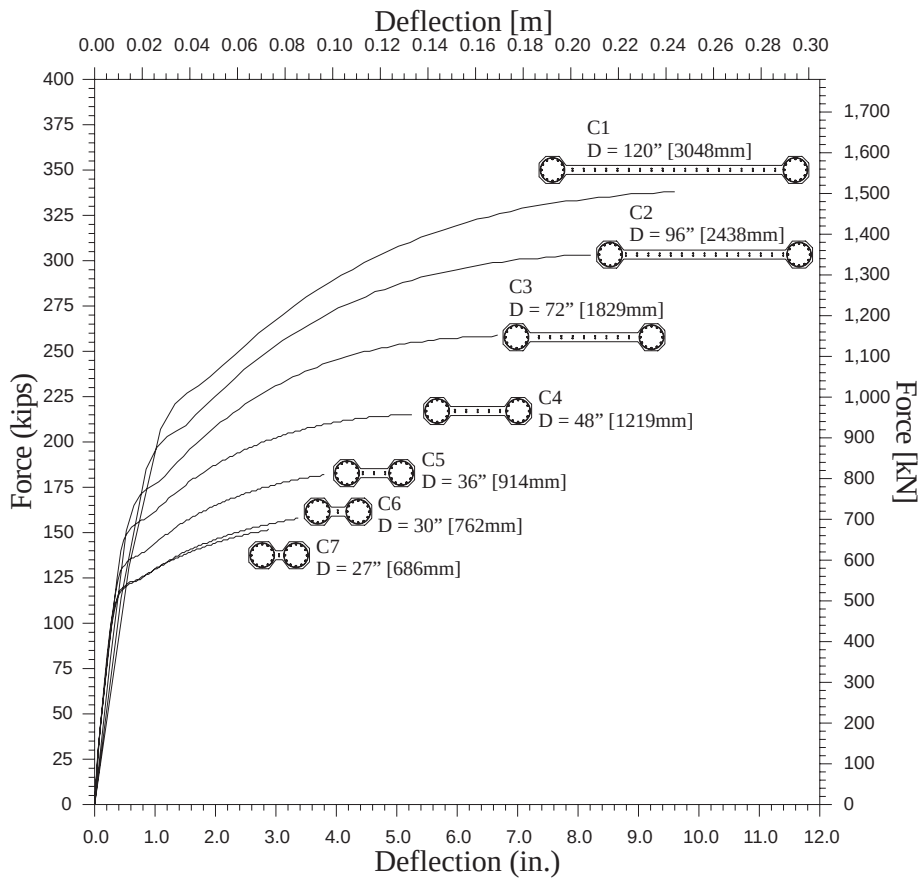

Figure 8.8: Theoretical force-deflection curves for columns C1-C7 of decreasing relative depth ratio D_w/D_b.

Columns C4, C5, and C6 are proposed as test units for Phase III of the UCSD/Caltrans research task CA-08. To ensure web crushing failure in at least one of the test units, it is recommended to increase the level of longitudinal reinforcement in the boundary elements to 12 No. 7 [D22] bars.

Chapter 9

Conclusions

9.1 Overview

The four issues introduced in Section 1.4 of Chapter 1 are discussed in light of test results. Design recommendations are given where possible and key issues for future research are highlighted.

9.2 Flexure

9.2.1 Plastic Hinge Length

- How do aspect ratio and the level of transverse reinforcement in the wall affect the equivalent plastic hinge length L_p, and how do these parameters influence the spread of plasticity in the plastic hinge region?

Test results from the five UCSD tests as well as from ten tests conducted by Oesterle et al. were used to calibrate the plastic hinge length for structural walls with confined boundary elements as a function of column length L, total column depth D, and strain penetration L_{sp} such that

$$L_p \quad .08L + \quad \alpha D \quad 0.15 f_y d_{bl} \geq 0.3 f_y d_{bl} \qquad (ksi) \qquad (9.1) \quad =0$$

$$L_p \quad .08L + \quad \alpha D \quad 0.022 f_y d_{bl} \geq 0.044 f_y d_{bl} \qquad [MPa] \qquad (9.2) \quad =0$$

The αD was added to the equation to capture the effect of column depth on tension shift and hence the distribution of plastic curvature. Currently, it is suggested to make 0.3 for columns with properties similar to the UCSD Phase I and Phase II test units, and for typical circular and rectangular columns. This equation =0

should be used in conjunction with conservative estimates of strain limit states, and must be refined further according to existing and future test data. For instance, existing test results indicate that there is reason to allow the value of L_p to change with variations in the transverse reinforcement.

9.2.2 Material Strain and Limit States

The plastic rotation of columns is commonly calculated by integrating curvatures determined by section analysis over an assumed equivalent plastic hinge length. Both the plastic hinge length and plastic curvature have a linear effect on column plastic rotation through the simplified expression

$$_{p} \quad \phi_p L_p \tag{9.3}$$

The assumed plastic hinge length discussed in Chapter 5 has been calibrated empirically, and has therefore caused concern for the design of bridge piers whose sections are much more complicated than the circular and rectangular sections tested here to date. The plastic curvature, however, has an equally large effect on plastic rotation is also a parameter on which it is rational to impose limits.

With the increase in plastic hinge length, it is recommended to decrease the allowable strain limit states used as termination criteria for a moment-curvature analysis on a given section. For flexural columns, it is recommmended to keep the limit states for longitudinal strains in a flexural member subject to cyclic loading below 40% of the theoretical ultimate strains. For members subject to high shear forces, such as the Phase II columns, it is recommended to set the limit at 25% of the theoretical ultimate strains. These values are based only on results from the five tests reported here and require a larger database of tests to prove their general validity. It is expected, however, that these proposed limit states are sufficiently conservative and can be used to estimate column deflection in conjunction with the revised equivalent plastic hinge length based on a moment curvature analysis of the member section.

9.3 Shear

Two key parameters affected the shear capacity of the columns in question: the transverse reinforcement and the wall thickness. The level of transverse reinforcement had the greatest influence on the shear capacity of a pier evaluated according to the UCSD shear model as discussed in Chapter 5. This model did not provide a

rational check on the wall thickness. Hence, web crushing capacity had to be checked separately.

9.3.1 Transverse Reinforcement

- What effect does a minimal amount of transverse reinforcement have on wall behavior under various flexure/shear demand ratios?
- To what degree do the boundary element spirals contribute to the total shear capacity of the bridge pier?

Both flexural and shear tests have shown that the tension boundary element spirals helped carry shear across the section if necessary. The longitudinal reinforcement in the wall is also expected to have helped the wall resist shear by reducing the width of shear cracks in the wall. Even Test Unit 2B, with the lowest V_s/V_u ratio, exhibited a high amount of toughness, failing in shear only after several cycles at μ_Δ . It is clear, therefore that while the level of transverse reinforcement does have a significant influence on the performance of such piers at higher displacement ductility levels, it is almost immaterial for protecting these columns against catastrophic shear failure.

For design it is recommended to calculate the steel contribution, V_s to the shear capacity based on the transverse bars and not the spirals. This corresponds to the lower bound of the UCSD shear model presented in Chapter 5. Because the spirals provide reliable protection against catastrophic failure, the transverse bars can be assumed to be effective over their entire length in tension, spanning from their end in the tension boundary element to the neutral axis, as stated in equation 5.5. The assumption that the transverse bars carry their yield force along their entire length is admittedly a simple approximation of real behavior. In light of current design practice for the Bay Area bridges, however, it is considered to be both practical and safe.

Anchorage Details

Since the spirals account for a large reserve capacity not accounted for in the recommended version of the UCSD shear model and since they provide confinement to the tension boundary element concrete, anchorage details for the transverse bars can be designed with partial or without anchorage details to facilitate construction and still be considered safe. This means that the bars can be assumed to develop their yield strength very close to each end. Anchorage details, such as seismic hooks or headed

ends should be employed where possible, but may also be staggered as was done for the Phase II test units.

Results from bar slippage measurements discussed in Chapter 7 show that the bars tended to slip only inside the plastic hinge region where the flexural cracks were widest. This region was so close to the footing that it was restrained against significant transverse strains. Thus, it can be concluded that the transverse bars were most likely to slip in a region where they were not essential to resisting the shear demand on the column.

9.3.2 Axial Load Contribution to Shear Capacity, V_p

The shear strength of bridge piers experiencing high axial loads such as the East Bay Bridge or the Benicia Martinez Bridge is greatly enhanced by the horizontal component of the axial load as it is transferred to the footing via the compression toe.

9.3.3 Web Crushing

- How does the web crushing strength of a wall with boundary elements change with changes in the relative depth ratio, D_w/D_b?

While the UCSD shear model proved effective in evaluating the shear capacity of the test units, it did not properly evaluate the wall thickness of such sections. Web crushing capacity should also be checked based on one of the equations mentioned in Chapter 8. Classical models for web crushing do not account for the depth of the structural wall relative to the depth of the boundary elements. This ratio has been named to relative depth ratio, D_w/D_b and is thought to be a significant parameter in determining the web crushing strength of structural walls with boundary elements subjected to plastic deformations. Therefore, existing web crushing models based on an assumption of pure shear behavior may underestimate the web crushing capacity of bridge piers with large boundary elements placed relatively close together, such as piers for the East Bay Bridge viaduct. A new model for web crushing capacity was proposed as a function of the boundary element depth and the neutral axis depth. This model was discussed thoroughly in Chapter 8.

9.4 Future Work

With the shear transfer mechanisms for structural walls with boundary elements more clearly understood, it remains to generalize this understanding to three dimensions and apply it to the behavior of hollow rectangular bridge piers with highly-confined corner elements. Particularly under loads in the diagonal direction, these full rectangular sections still raise many unanswered questions with regard to the shear transfer between boundary elements through the structural walls.

The web crushing model proposed in Chapter 8 needs to be refined based on finite element and experimental parametric studies on boundary element depth, wall depth, wall thickness and concrete strength. The concrete strength reduction factor, k needs to be modified to reflect the 1986 model for compression softening [17], requiring accurate experimental estimates of the principal tensile strains ε_1 in the critical compression strut region of the plastic hinge.

The proposed equivalent plastic hinge length equation (Equation 9.1) must be refined based on more test results and detailed finite element parameter studies that investigate a variety of section depths, longitudinal reinforcement ratios, aspect ratios and levels of transverse reinforcement. Special attention should be paid to the vertical distribution of longitudinal strains in both the tests and the models, in order to explore the effects which these parameters have on tension shift.

Uncoupling of the structural wall from the boundary elements and subsequent vertical slippage between these elements may still be a possibility under large deformations in double bending, where such vertical slippage is allowed to occur unrestrained by a rigid boundary condition. This phenomenon could soften the force-deflection response of bridge piers in the longitudinal direction. Another equation, possibly based on a shear friction approach, is therefore needed to predict the uncoupling capacity of these bridge piers in double bending and should be added to the two existing equations (the three component shear assessment equation and the flexure-shear web crushing assessment model) designed to evaluate shear capacity.

Appendix A

Photos from Tests

This appendix contains photos from each of the five tests. The photos for each test in Phase I and for each test in Phase II correspond to similar levels of displacement and can therefore be directly compared with one another. Each photo is titled with a short description and the relevant level of force and displacement.

A.1 Unit 1A Test Photos

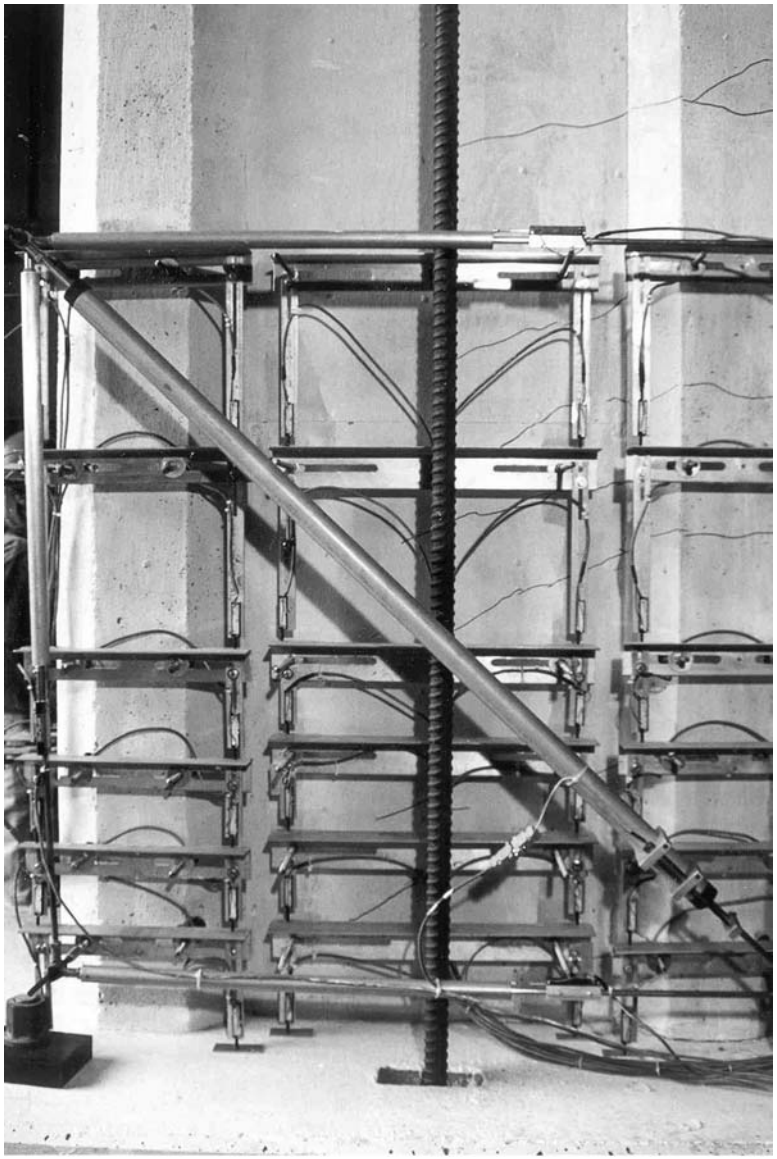

Figure A.1: Unit 1A; F_y; F=47.4kips [211kN]; Δ=0.81in. [21mm]: Cracks in the tension boundary element and wall at steel yield.

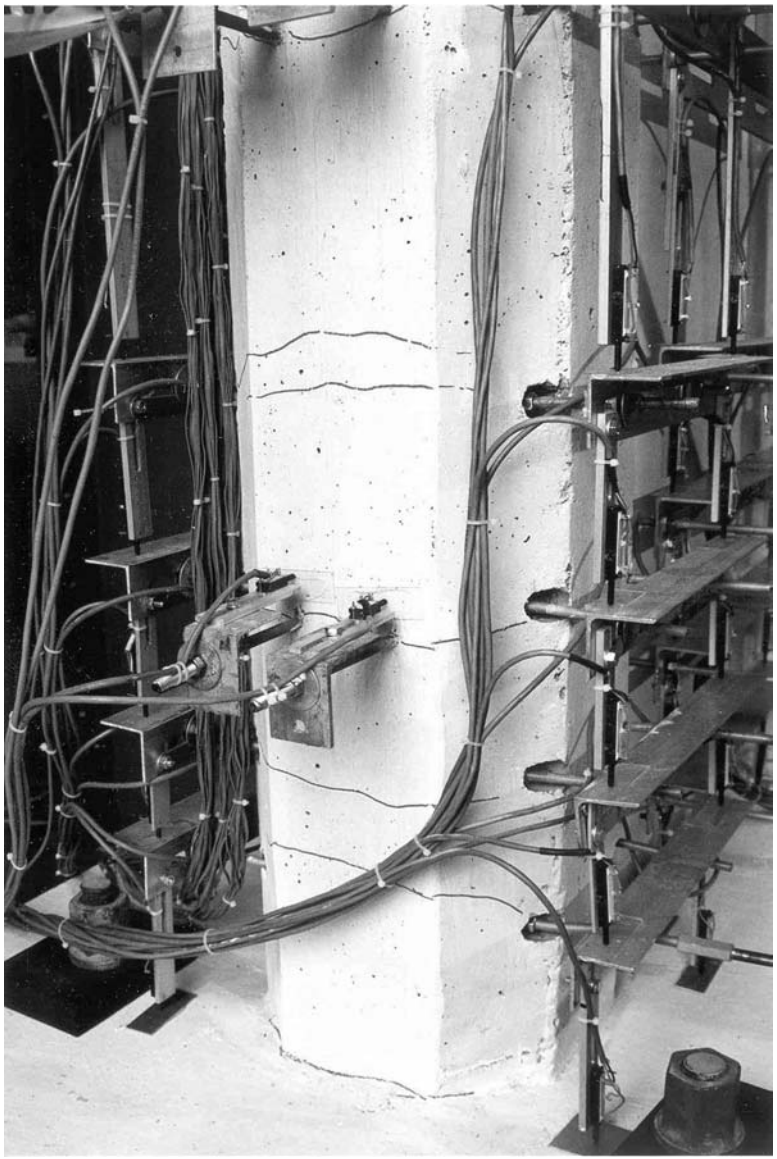

Figure A.2: Unit 1A; $-F_y$; F=-47.3kips [-210kN]; Δ=-0.86in. [-22mm]: Flexural cracks on the extreme face of the tension boundary element.

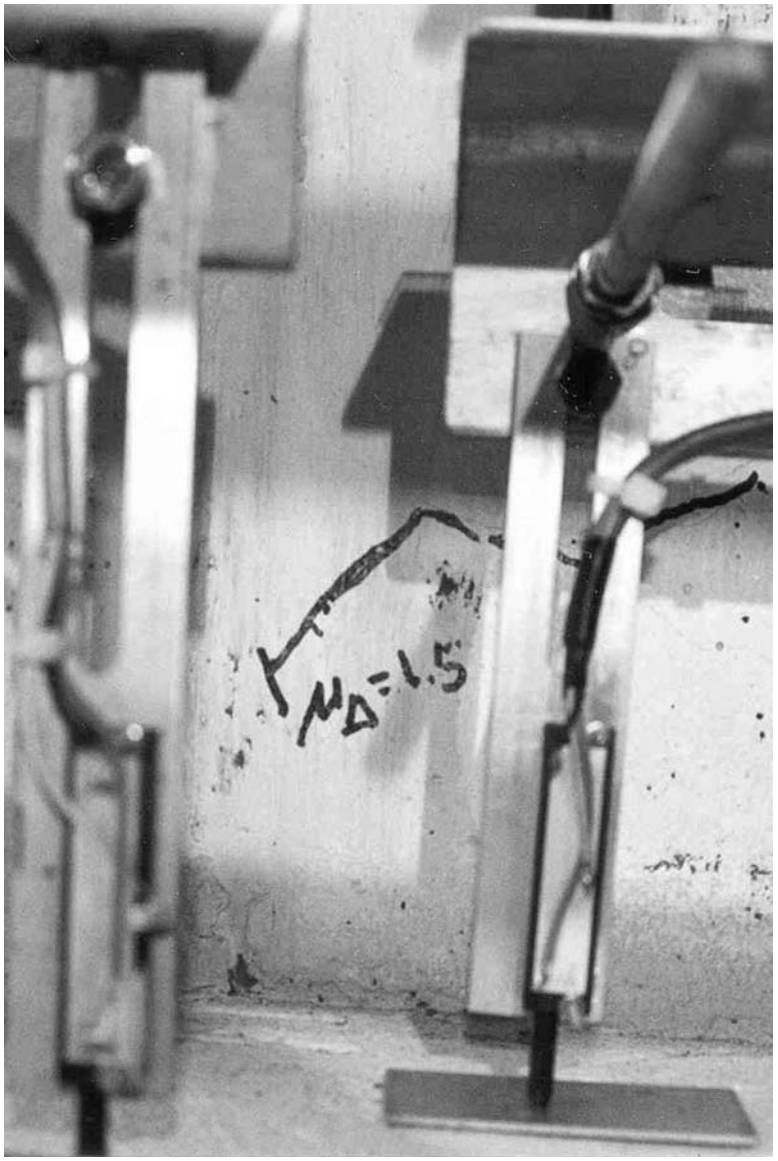

Figure A.3: Unit 1A; μ_Δ=1.5x1; F=63.1kips [281kN]; Δ=1.67in. [42mm]: Flexural cracks reach the edge of the compression boundary element.

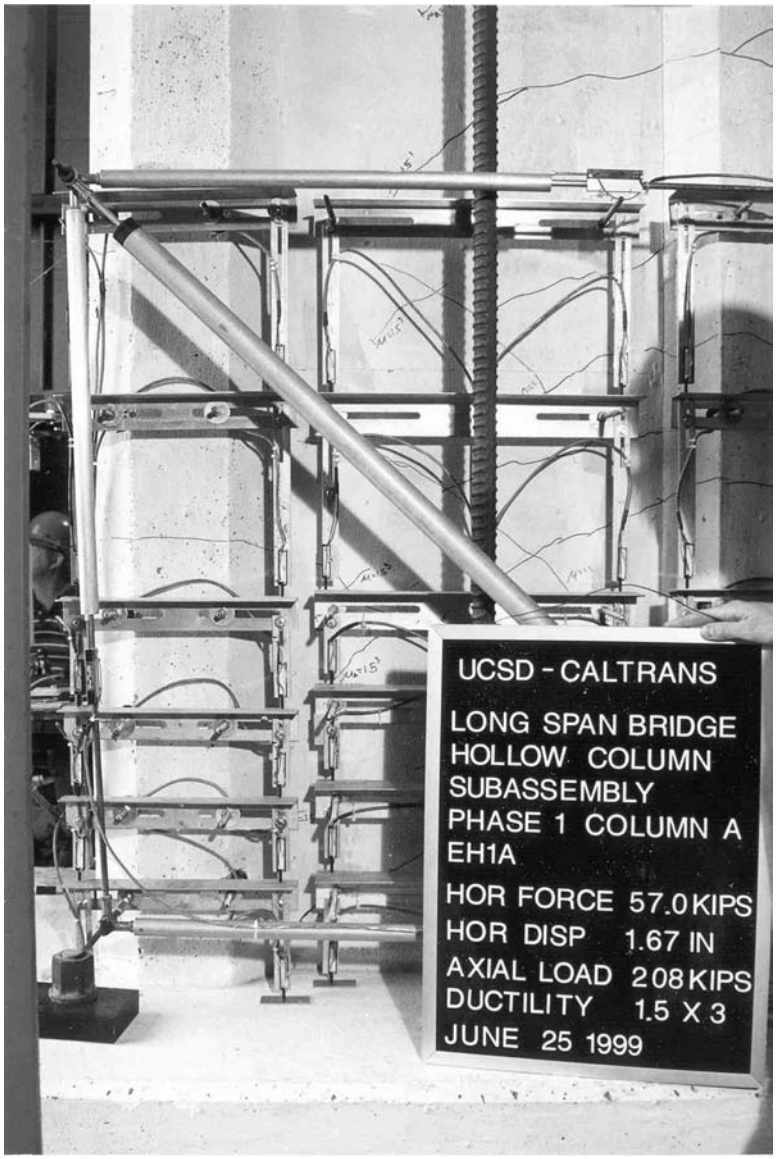

Figure A.4: Unit 1A; μ_Δ=1.5x3; F=57.0kips [254kN]; Δ=1.67in. [42mm]: Flexure-shear cracks propagate further into the wall.

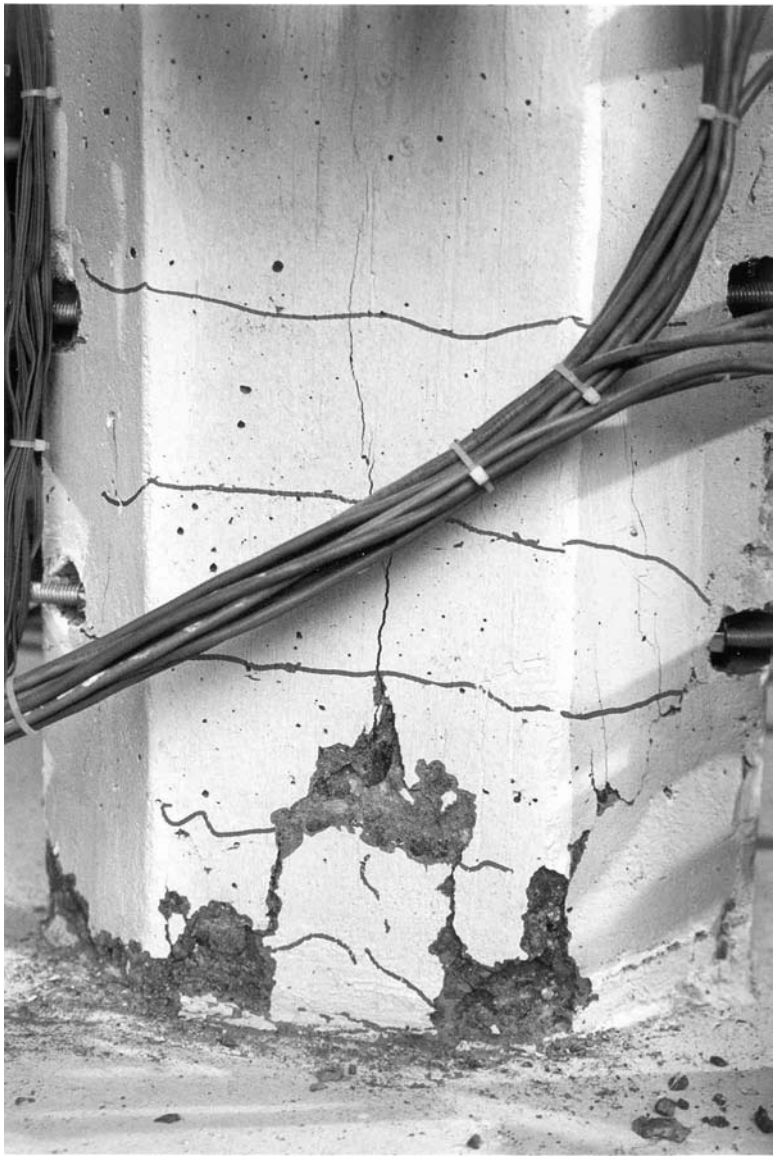

Figure A.5: Unit 1A; μ_Δ=3.0x1; F=66.0kips [294kN]; Δ=3.33in. [85mm]: Initiation of spalling in the compression boundary element (north).

Figure A.6: Unit 1A; μ_Δ=3.0x3; F=65.2kips [290kN]; Δ=3.34in. [85mm]: Well-developed spalled region at the base of the compression boundary element (south).

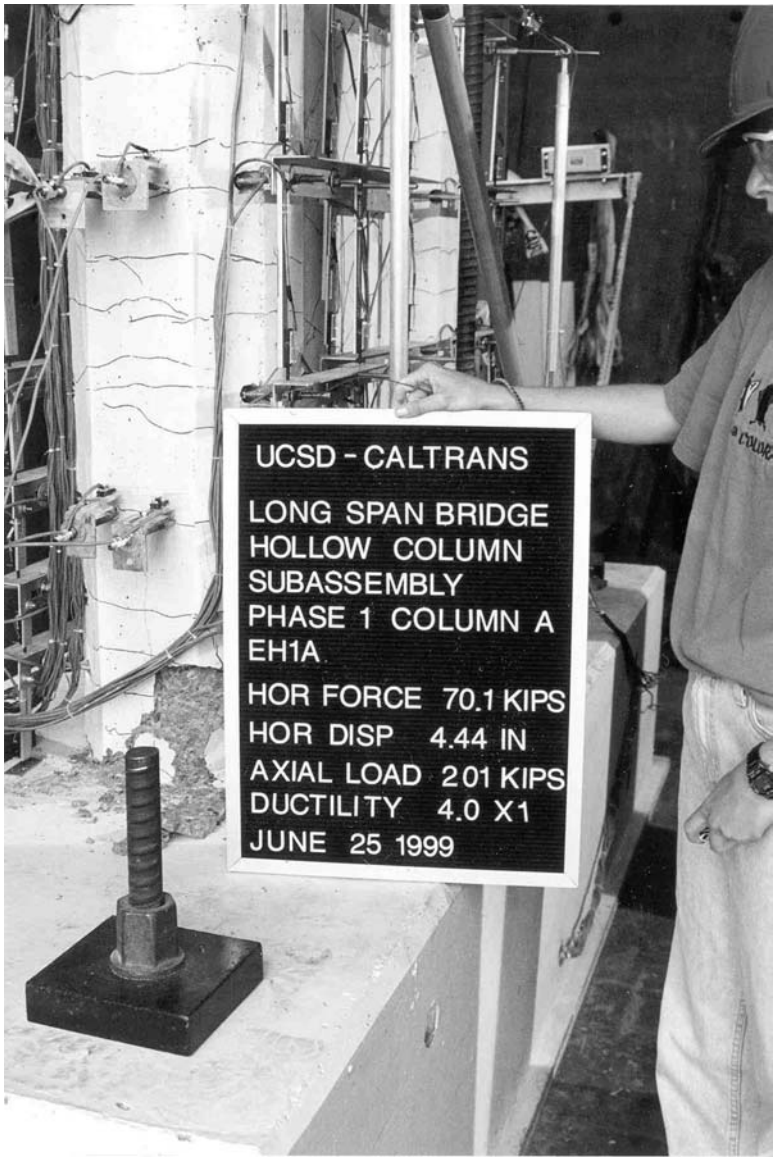

Figure A.7: Unit 1A; μ_Δ=4.0x3; F=70.1kips [312kN]; Δ=4.44in. [113mm]: Further development of spalled region at the base of the compression boundary element (north). The spalling on the north side is significantly less than that on the south side.

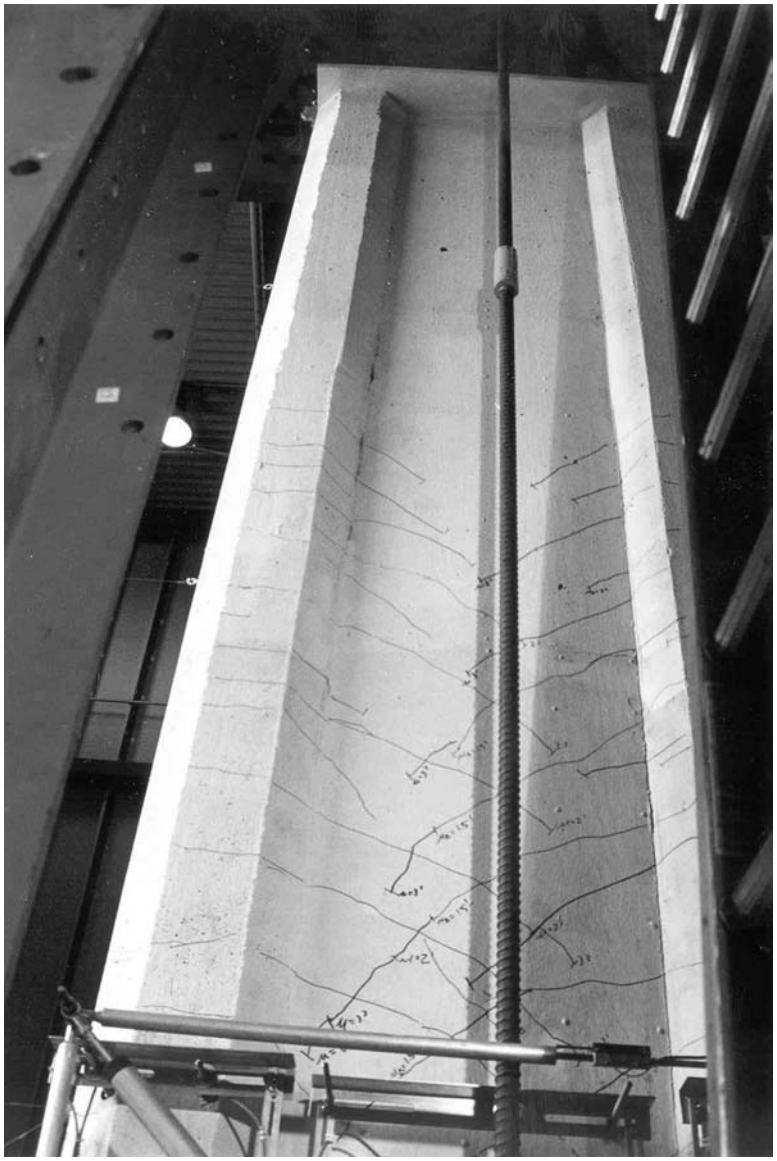

Figure A.8: Unit 1A; μ_Δ=6.0x1; F=72.5kips [323kN]; Δ=6.68in. [170mm]: Deformation and crack pattern up the column height.

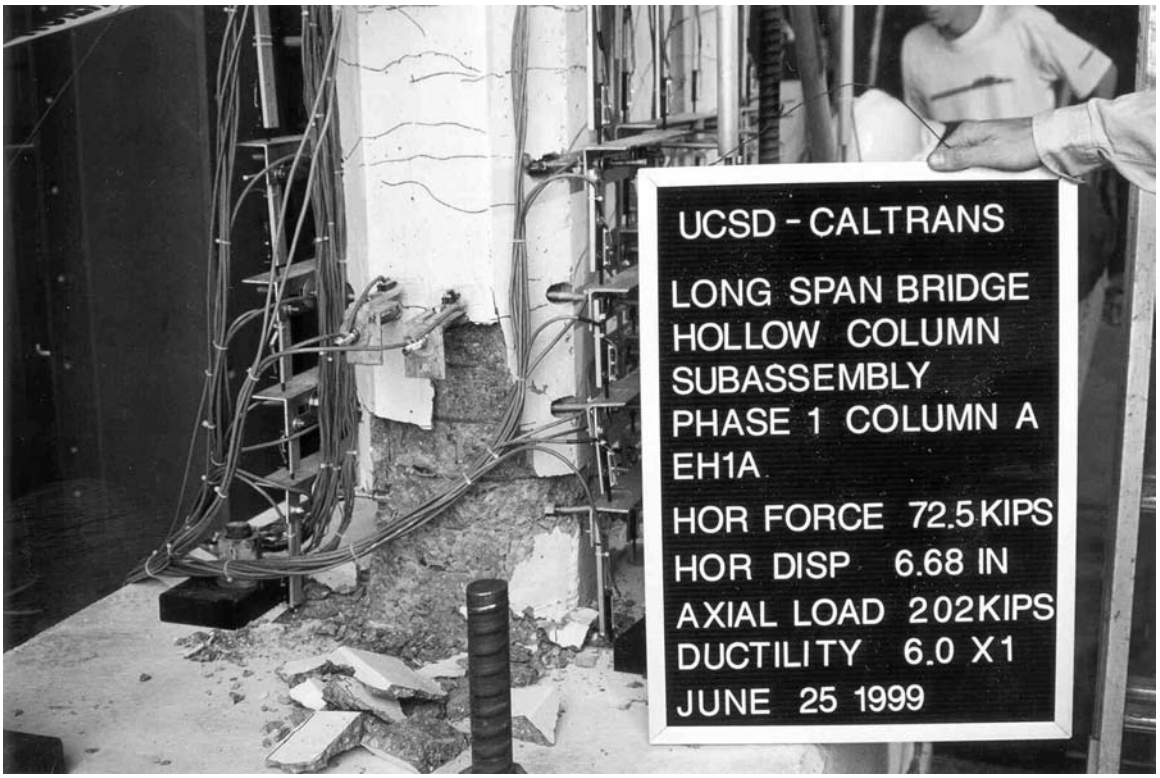

Figure A.9: Unit 1A; μ_Δ=6.0x1; F=72.5kips [323kN]; Δ=6.68in. [170mm]: Fully developed spalled region at the base of the compression boundary element (north).

Figure A.10: Unit 1A; μ_Δ=-6.0x1; F=-70.2kips [-312kN]; Δ=-6.68in. [-170kN]: incipient bar buckling in the compression boundary element (south).

Figure A.11: Unit 1A; μ_Δ=-8.0x1; F=-63.8kips [-284kN]; Δ=-8.82in. [-224mm]: Deformation and cracked pattern.

Figure A.12: Unit 1A; μ_Δ=8.0x3; F=42.8kips [190kN]; Δ=8.82in [224mm]: Fully developed failure of the tension boundary element (south) due to buckling and fracture of the longitudinal bars and subsequent crushing of the concrete core.

A.2 Unit 1B Test Photos

Figure A.13: Unit 1B; $3/4F_y$ F=33.5kips [149kN]; Δ=0.38in. [10mm]: Initial cracks remain primarily within the tension boundary element, and spread up to a height of 62in.

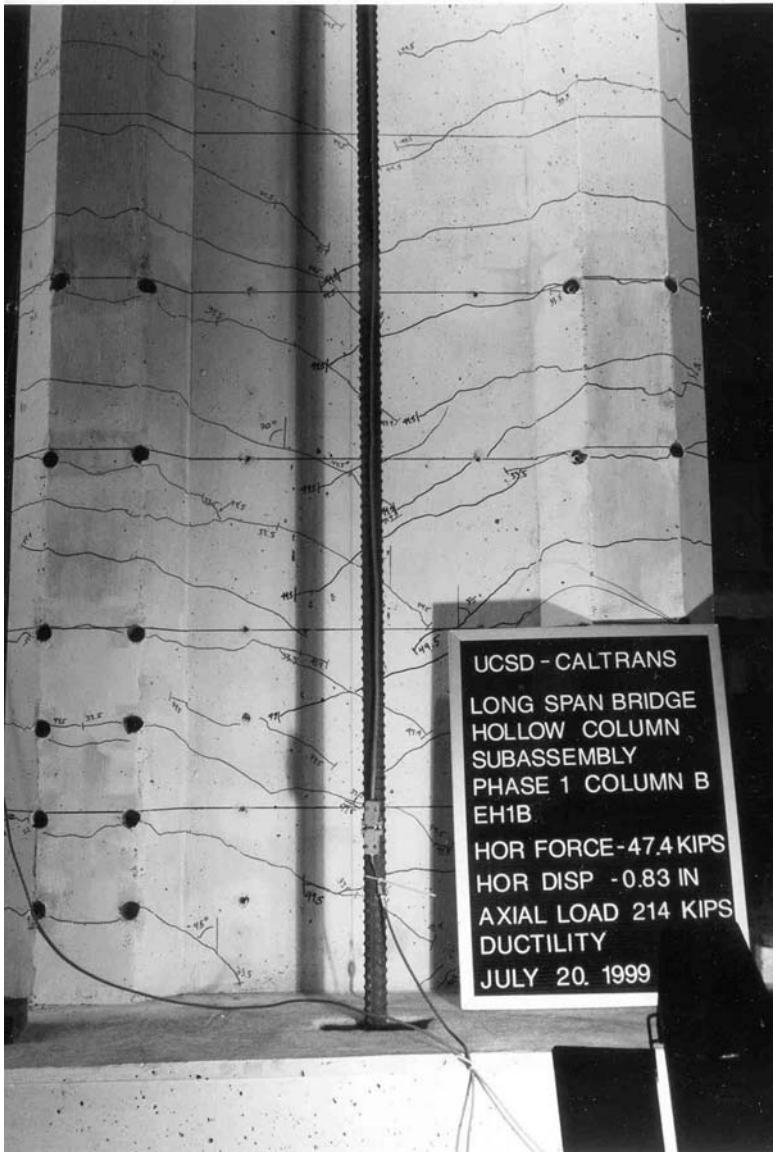

Figure A.14: Unit 1B; $-F_y$ F=-47.4kips [-211kN]; Δ=-0.83in. [-21mm]: Cracks propagate into the wall mostly as flexural cracks. There is some initial evidence of these cracks steepening.

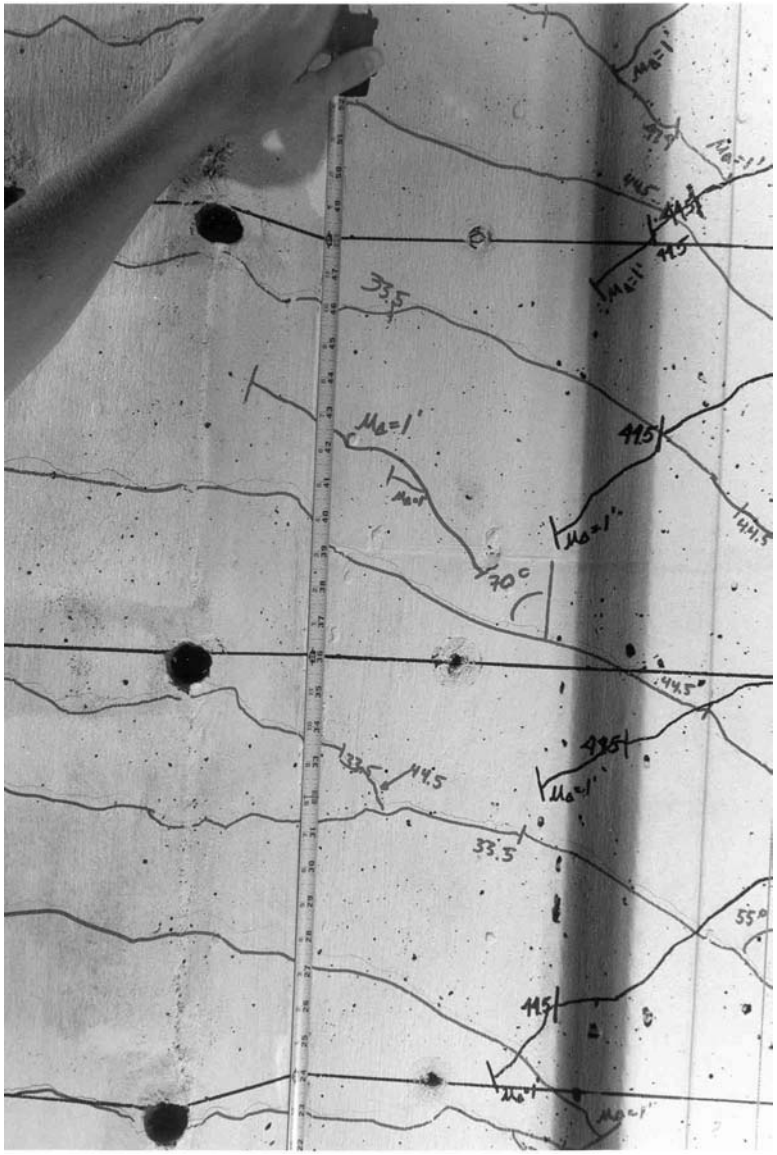

Figure A.15: Unit 1B; μ_Δ=-1.0x1; F=-54.1kips [-241kN]; Δ=-1.11in. [-28mm]: A shear crack forms from 38in. [965mm] to 44in. [1118mm] high across the tension boundary element/wall interface.

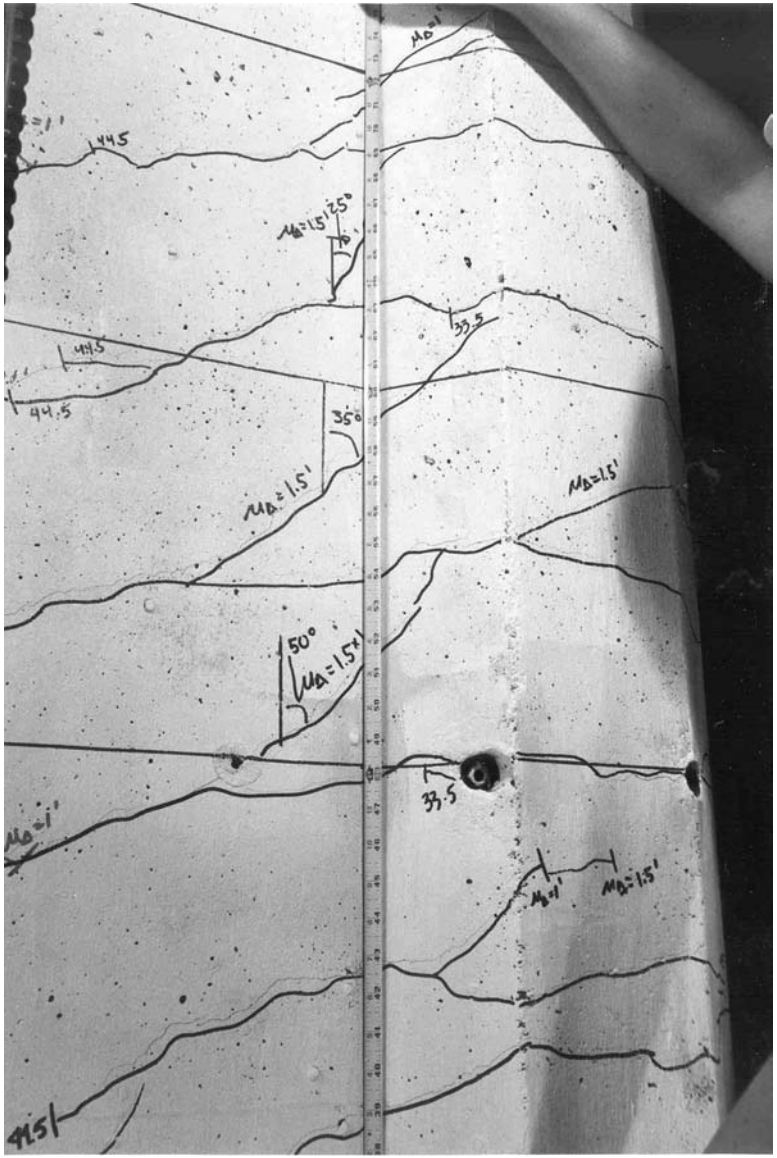

Figure A.16: Unit 1B; μ_Δ=1.5x1; F=62.2kips [277kN]; Δ=1.67in. [42mm]: New shear cracks connect existing flexural cracks across the tension boundary element inside chamfer from a height of 48in. [1219mm] to 72in. [1829mm]

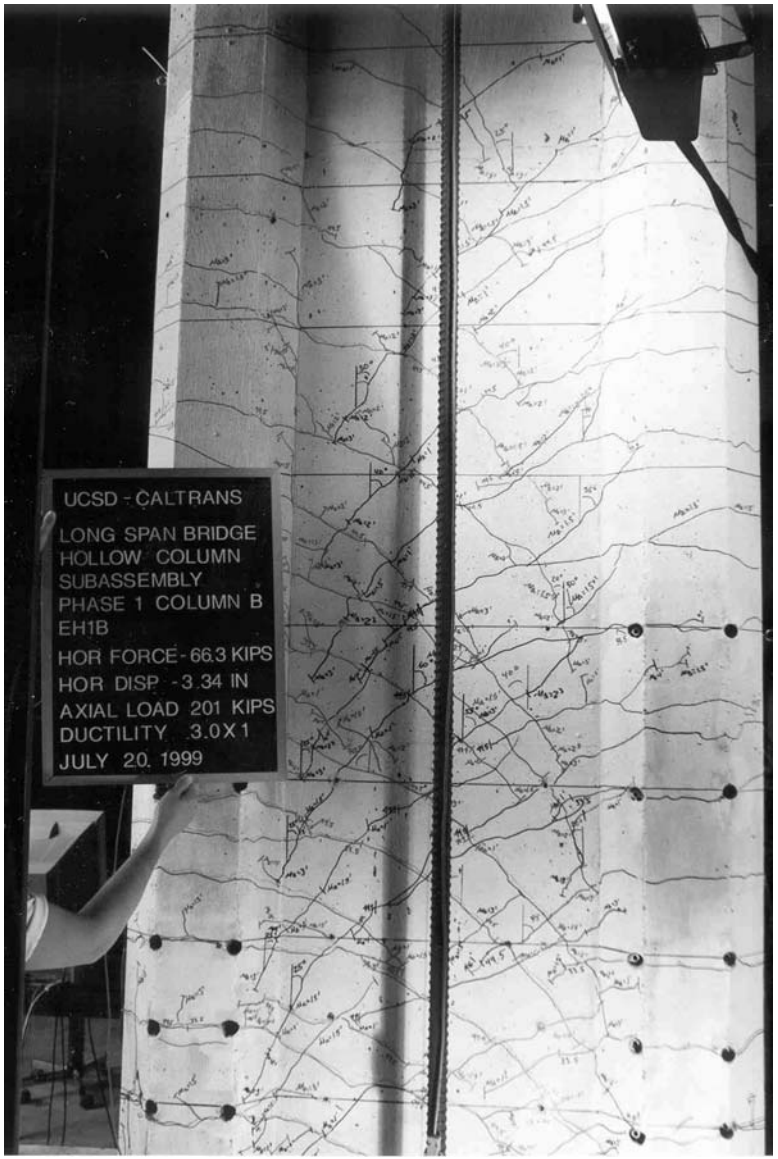

Figure A.17: Unit 1B; μ_Δ=-3.0x1; F=-66.3kips [-295kN]; Δ=-3.34in. [-85mm]: crack pattern.

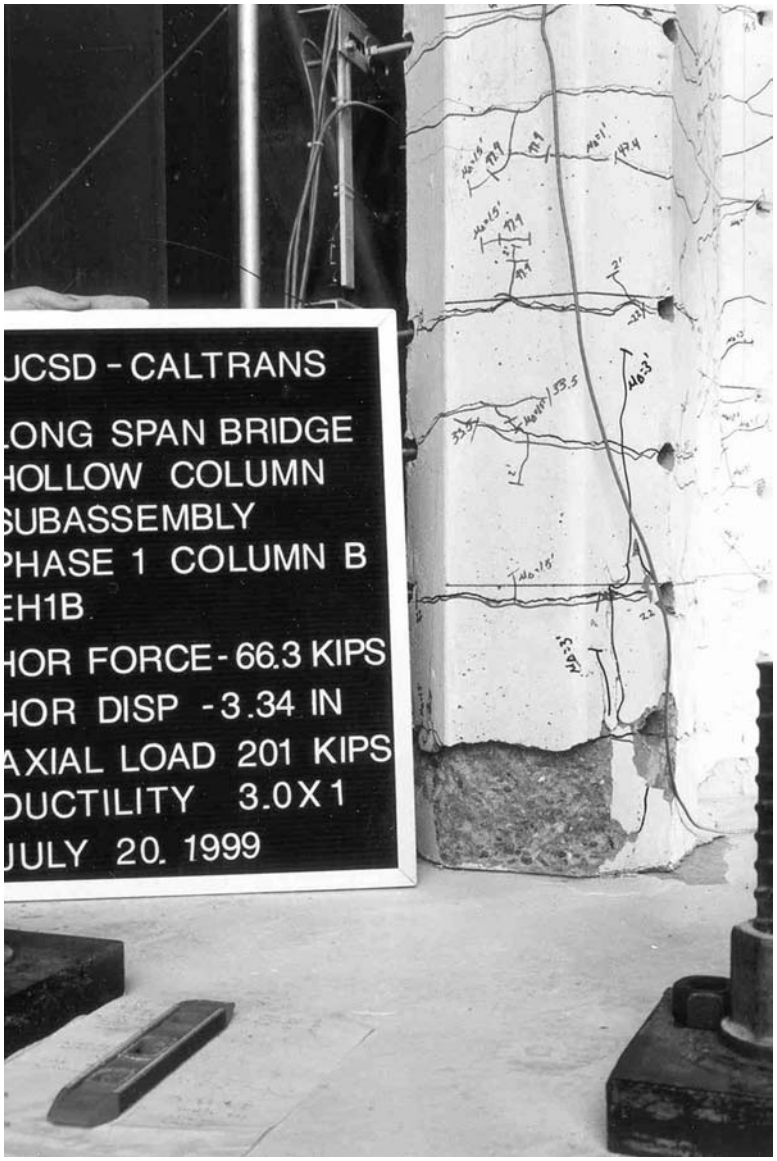

Figure A.18: Unit 1B; μ_Δ=-3.0x1; F=-66.3kips [-295kN]; Δ=-3.34in. [-85mm]: Onset of spalling in the tension boundary element (north).

Figure A.19: Unit 1B; μ_Δ=4.0x1; F=67.4kips [300kN]; Δ=4.45in. [113mm]: Further development of spalled region at the base of the compression boundary element (north). Spalled concrete comes off in large chunks, as it did in Unit 1A.

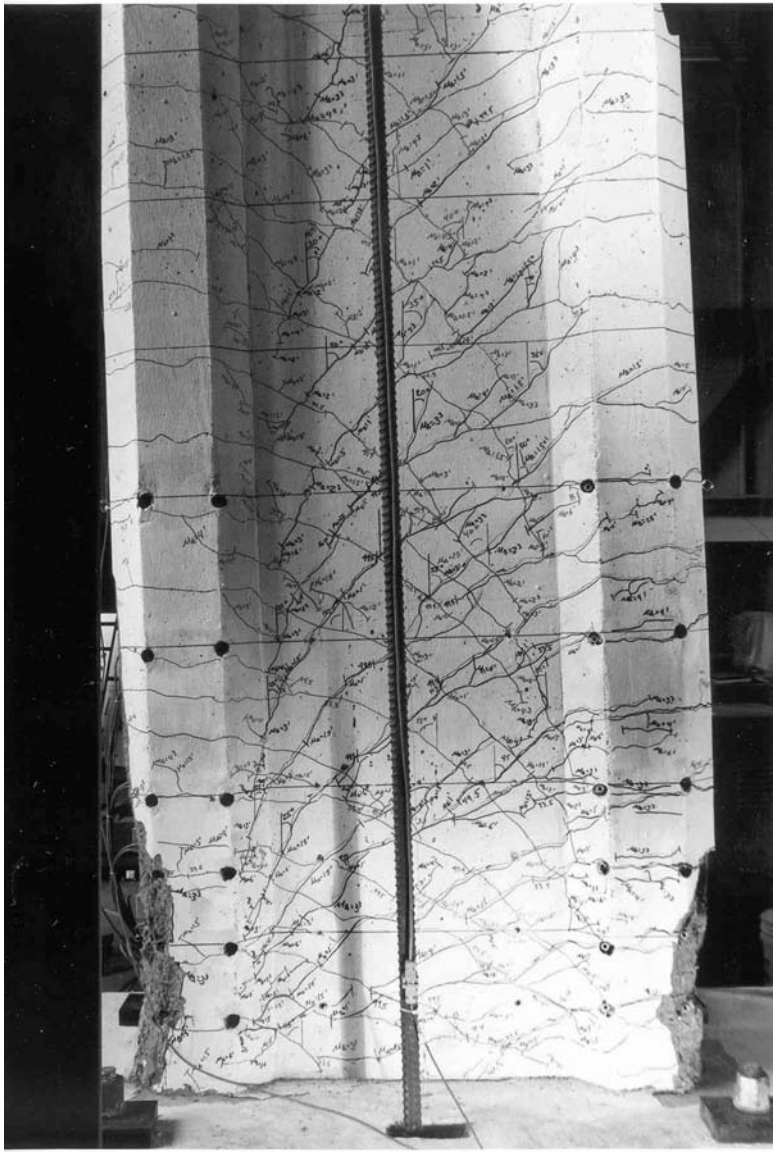

Figure A.20: Unit 1B; μ_Δ=6.0x1; F=69.6kips [310kN]; Δ=6.67in. [169mm]: Deformation and crack pattern 84in. up the column height. Spalled region on the compression boundary element (left) extends 24in. [610mm] up the column height.

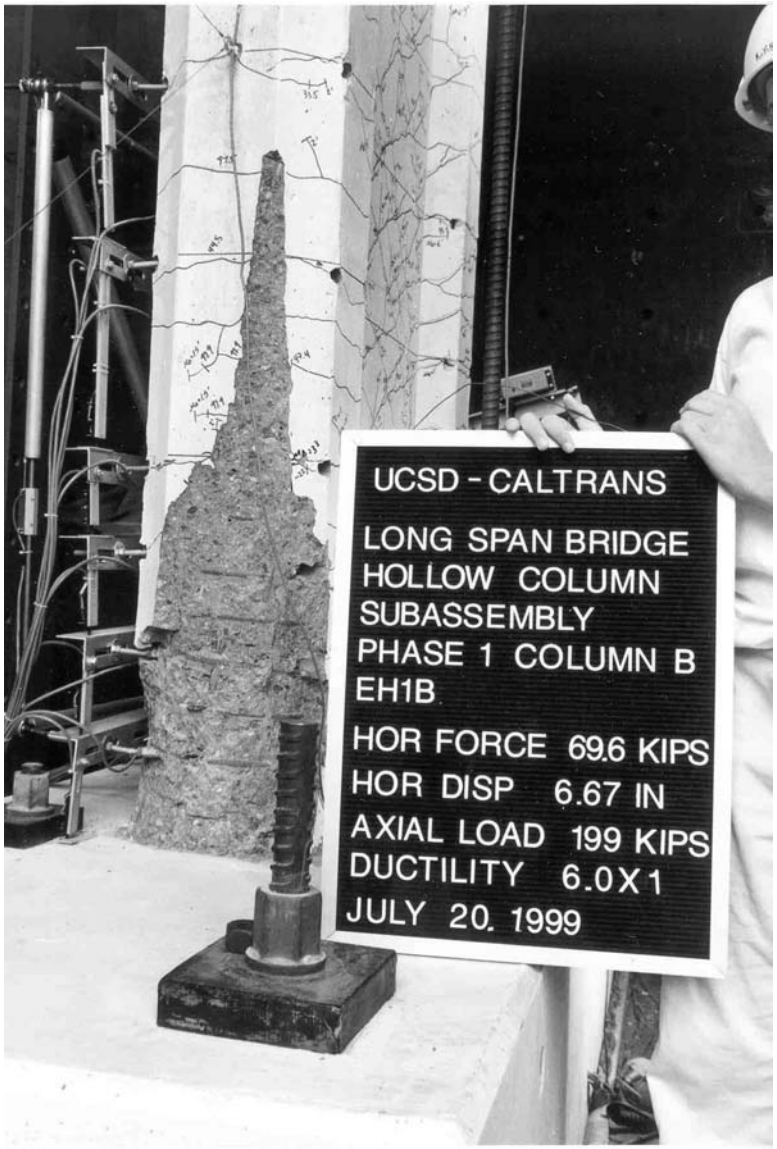

Figure A.21: Unit 1B; μ_Δ=6.0x1; F=69.6kips [310mm]; Δ=6.67in. [169mm]: Fully developed spalled region at the base of the compression boundary element (north). Major spalling extends 24in. [610mm] up the column height.

Figure A.22: Unit 1B; μ_Δ=-6.0x3; F=-65.7kips [-292kN]; Δ=-6.68in. [-170mm]: Incipient bar buckling in the compression boundary element (south).

Figure A.23: Unit 1B; μ_Δ=8.0x1; F=65.9kips [293kN]; Δ=8.88in. [226mm]: Column deformation.

Figure A.24: Unit 1B; μ_Δ=-8.0x2; F=-55.9kips [249kN]; Δ=-8.82in. [-224mm]: Fracture of three longitudinal bars in the tension boundary element (north).

A.3 Unit 2A Test Photos

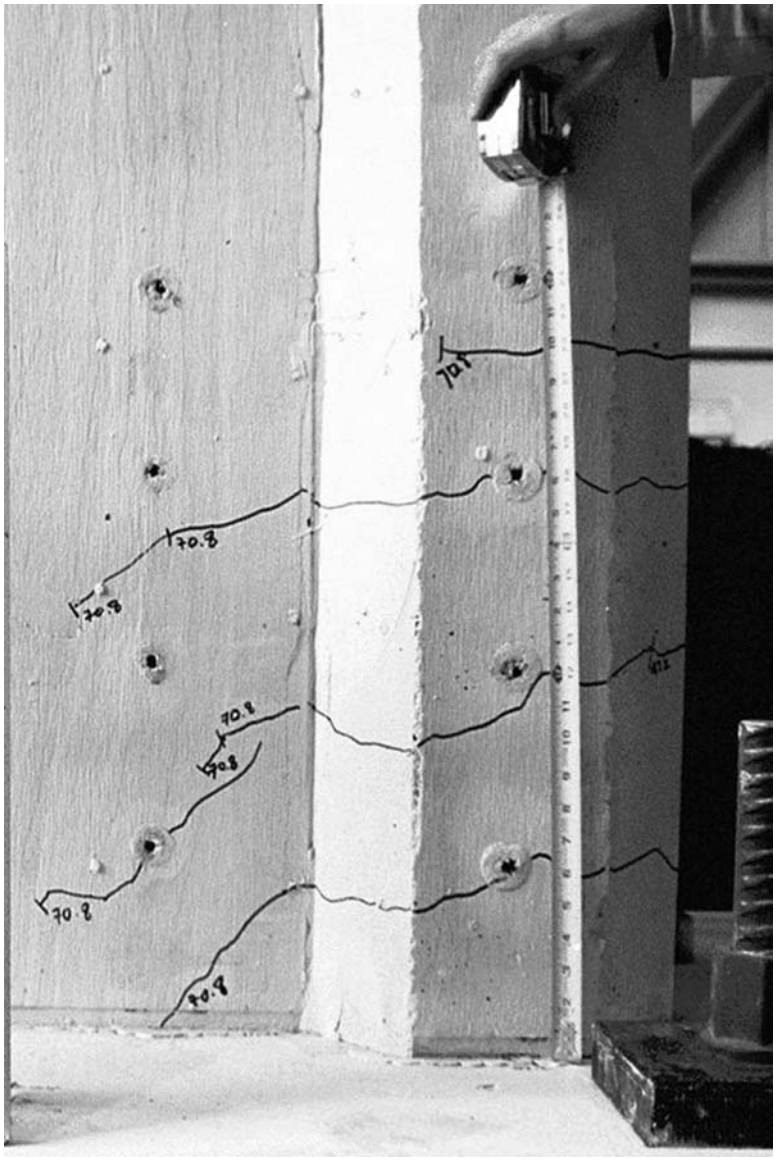

Figure A.25: Unit 2A; 3/4 F_y F=70.8kips [315kN]; Δ=0.14in. [4mm]: First cracks in the tension boundary element and wall.

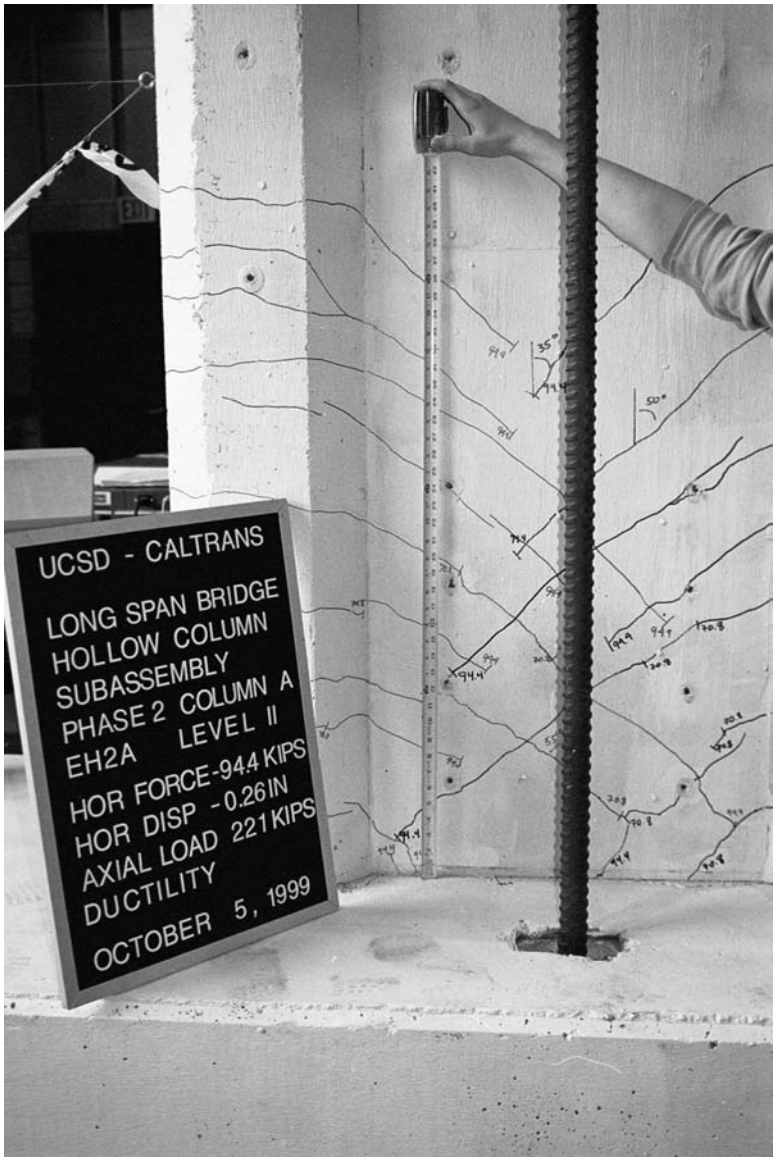

Figure A.26: Unit 2A; $-F_y$ F=-94.4kips [-420kN]; Δ=-0.26in. [-7mm]: Cracking up to a height of 40in. [1016mm] at first yield.

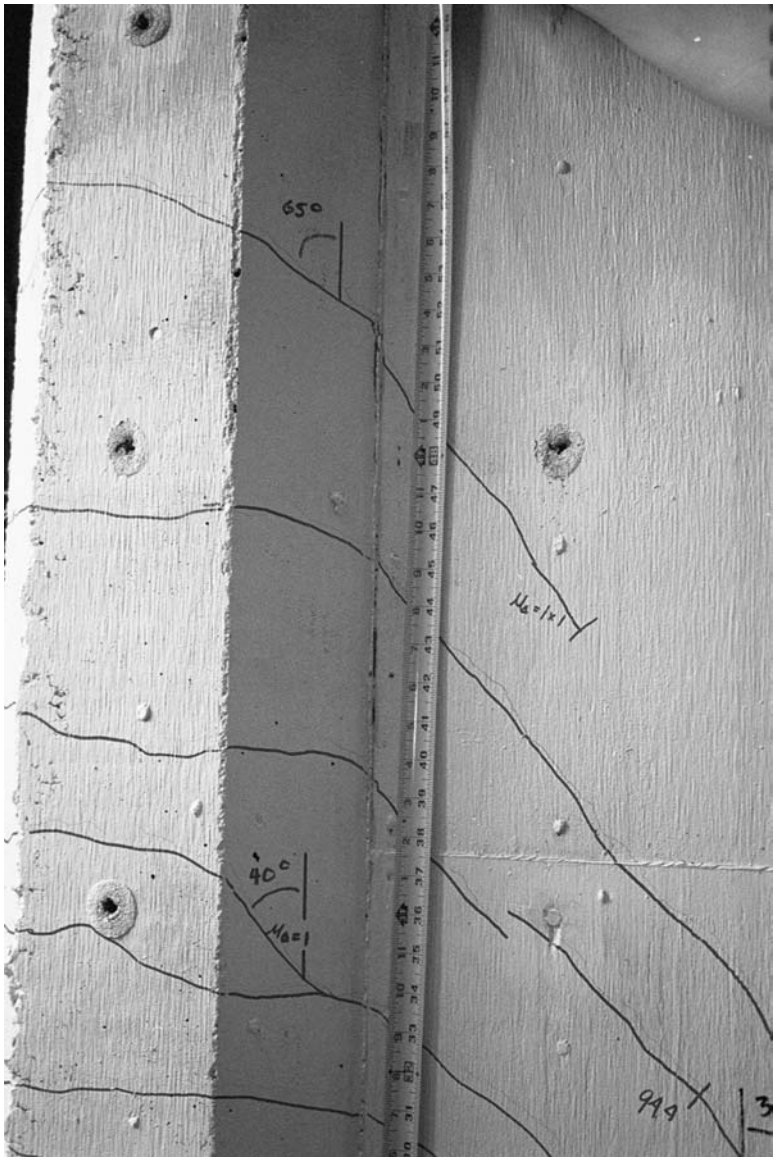

Figure A.27: Unit 2A; μ_Δ=-1.0x1; F=-105.4kips [-469kN]; Δ=-0.35in. [-9mm]: Flexural cracks steepen into shear cracks in the tension boundary elemen hamfer. The crack at 36in. [914mm] height is angled at 40° from the vertical.

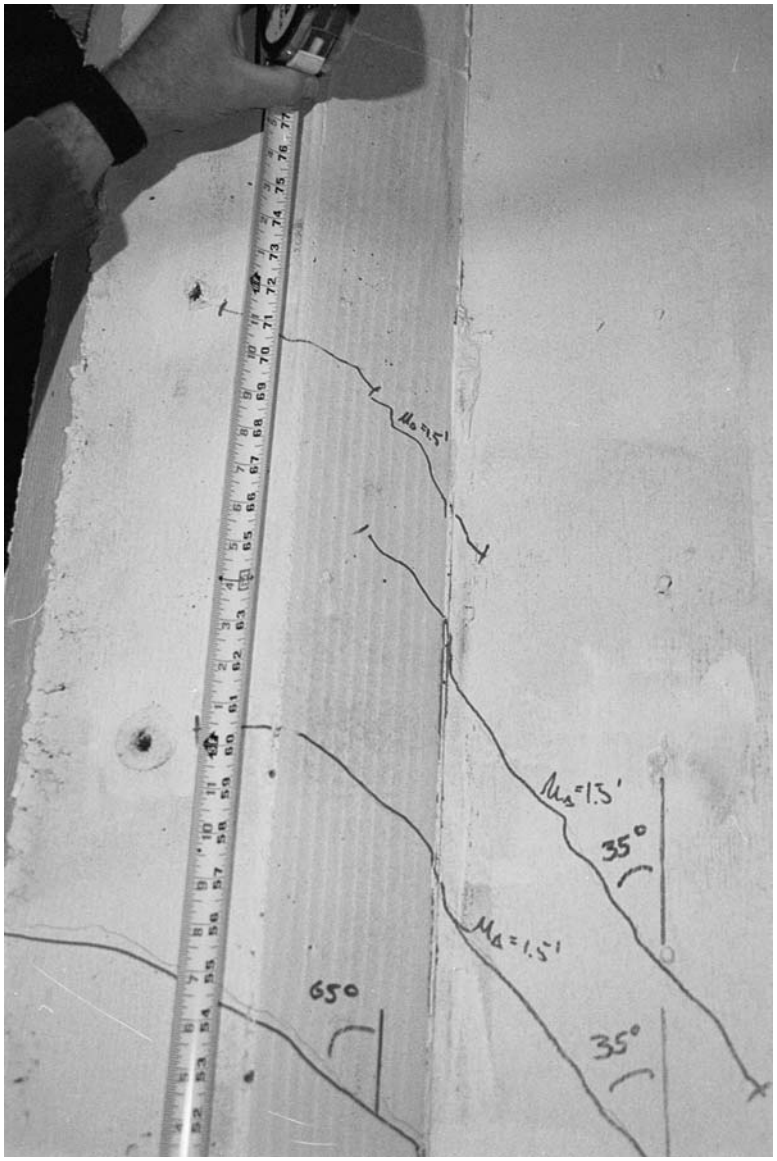

Figure A.28: Unit 2A; μ_Δ=-1.5x1; F=-121.4kips [-540kN]; Δ=-0.53in. [-13mm]: Shear cracks, angled 35° from the vertical form in the wall and in the tension boundary element from 55in. [1397mm] to 72in. [1829mm] high.

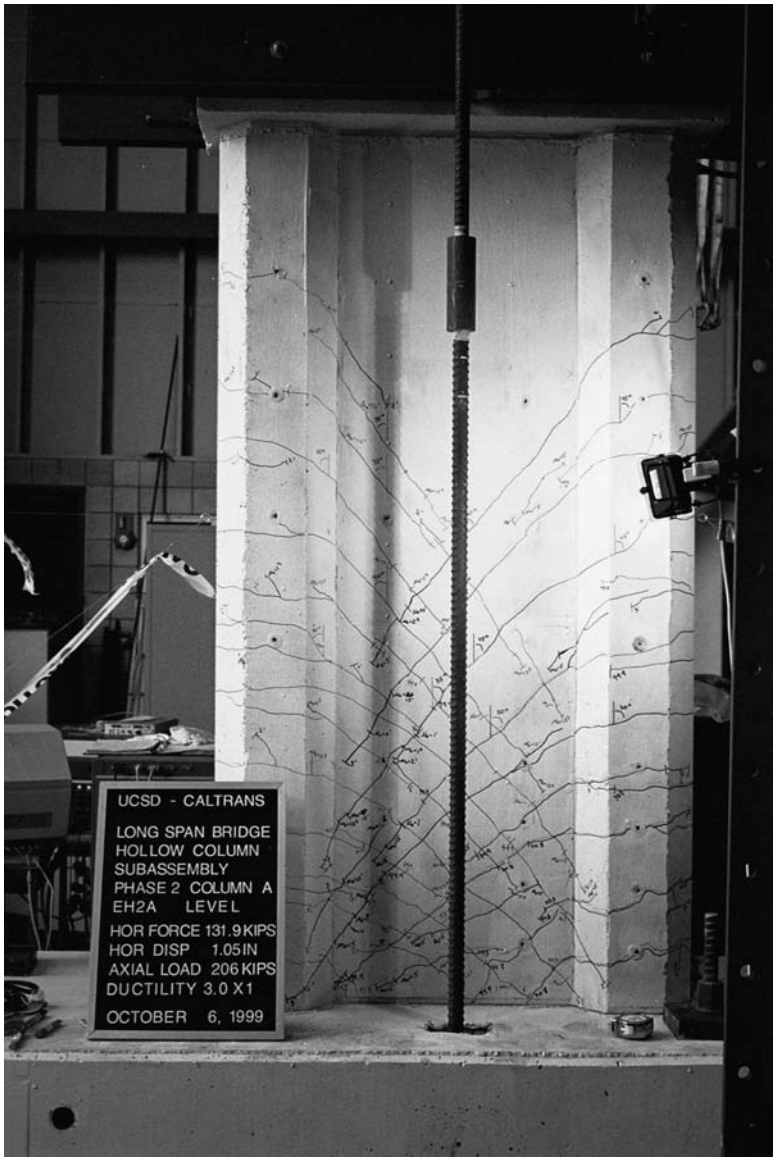

Figure A.29: Unit 2A; μ_Δ=3.0x1; F=131.9kips [587kN]; Δ=1.05in. [27mm]: Deformation and crack pattern.

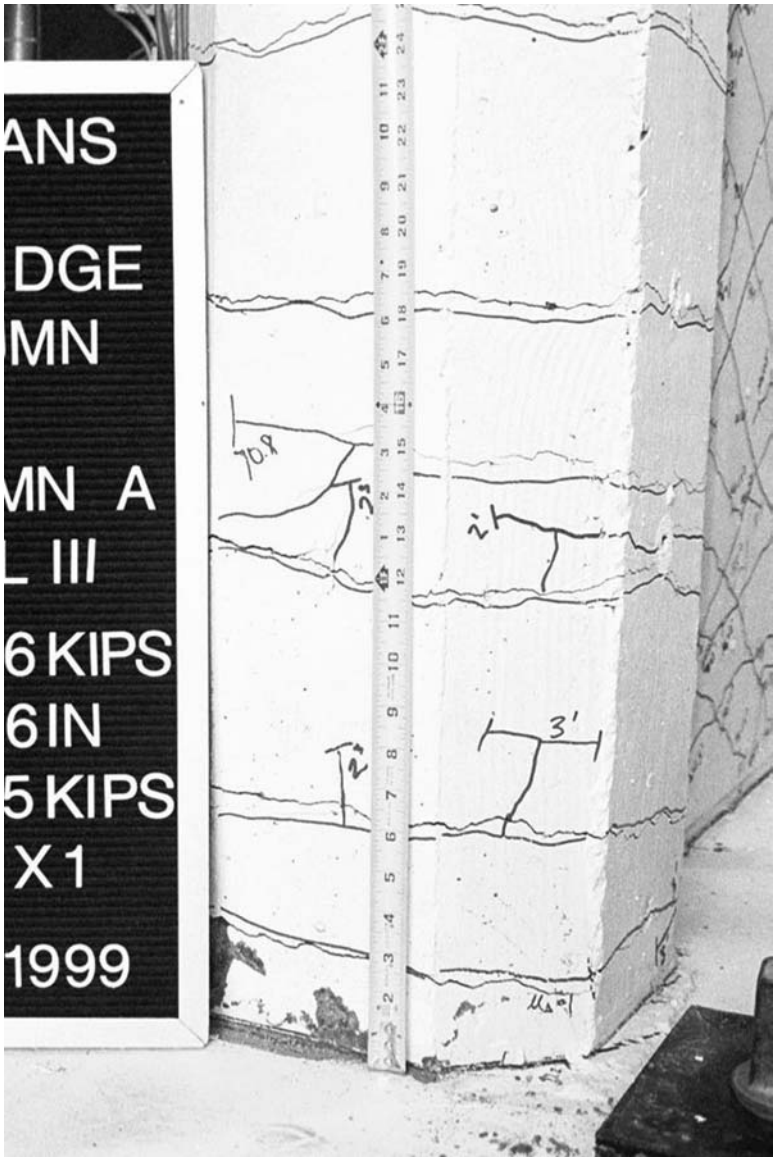

Figure A.30: Unit 2A; μ_Δ=-3.0x1; F=-127.6kips [-568kN]; Δ=-1.06in. [-27mm]: Incipient spalling at the base of the tension boundary element.

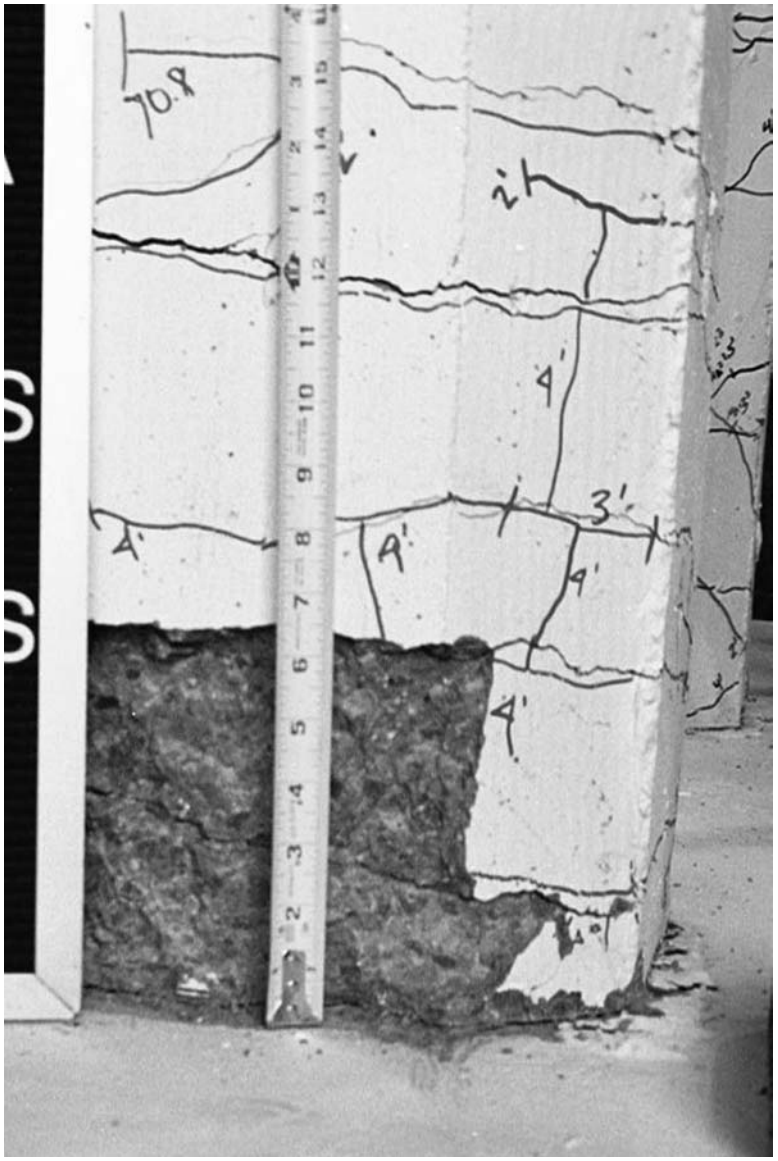

Figure A.31: Unit 2A; μ_Δ=-4.0x3; F=-121.2kips [-539kN]; Δ=-1.44in. [-37mm]: Partially developed spalled region at the base of the tension boundary element.

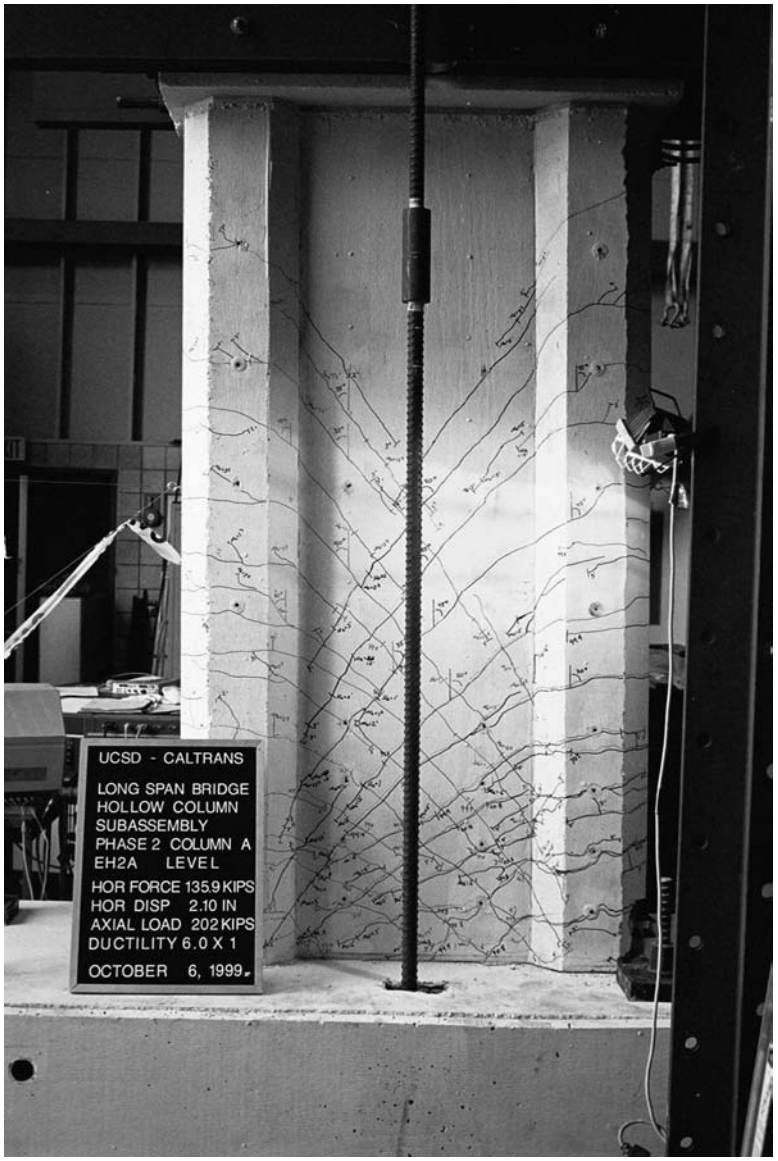

Figure A.32: Unit 2A; μ_Δ=6.0x1; F=135.9kips [605kN]; Δ=2.10in. [53mm]: Deformation and crack pattern.

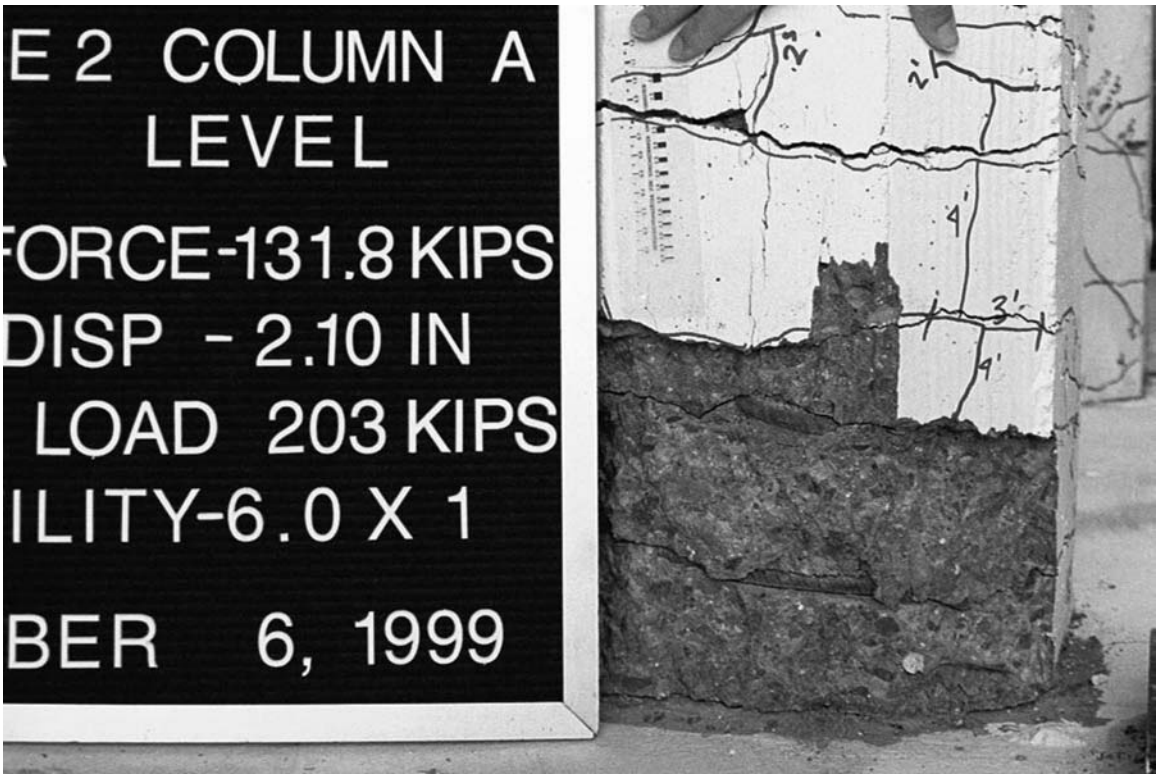

Figure A.33: Unit 2A; μ_Δ=-6.0x1; F=-131.8kips [-587kN]; Δ=-2.10in. [-53mm]: Fully developed spalled region at the base of the tension boundary element.

Figure A.34: Unit 2A; μ_Δ=-6.0x3; F=-125.8kips [-560kN]; Δ=-2.10in. [-53mm]: Bar buckling in the compression boundary element.

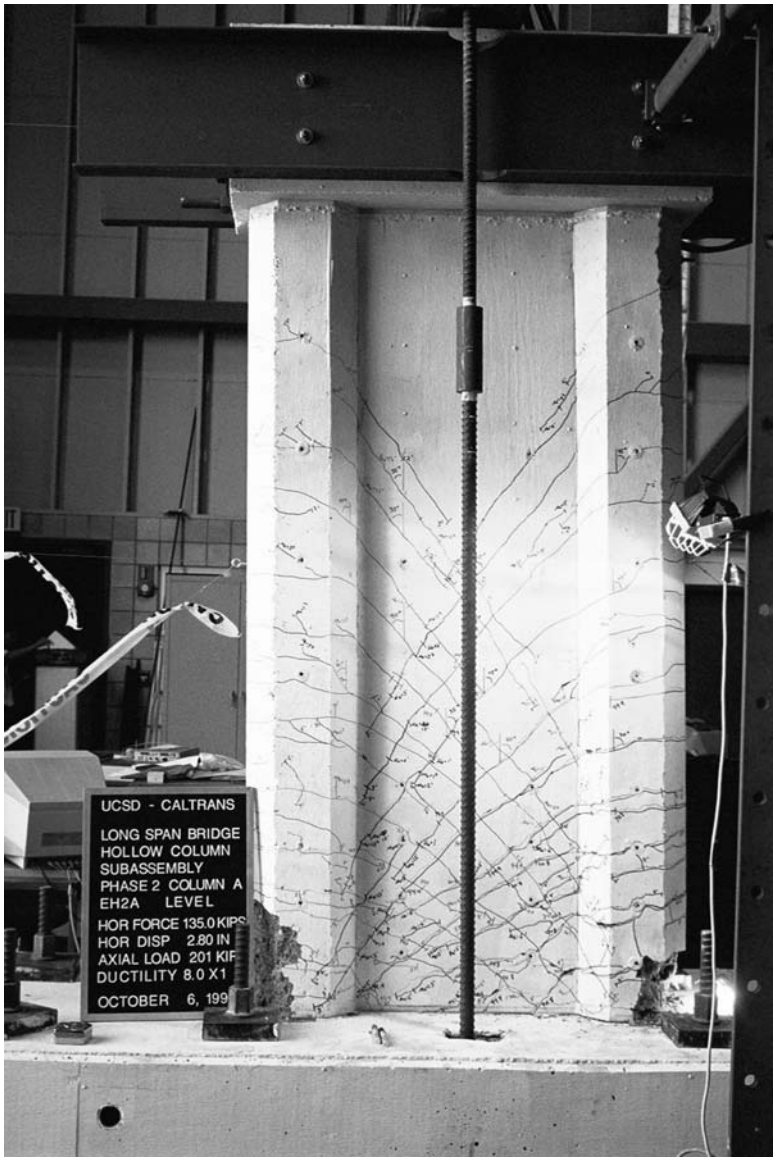

Figure A.35: Unit 2A; μ_Δ=8.0x1; F=135.0kips [601kN]; Δ=2.80in. [71mm]: Deformation and crack pattern.

Figure A.36: Unit 2A; μ_Δ=8.0x2; F=118.0kips [525kN]; Δ=2.80in. [71mm]: Fracture of a longitudinal reinforcing bar in the tension boundary element, signifying the onset of column failure.

A.4 Unit 2B Test Photos

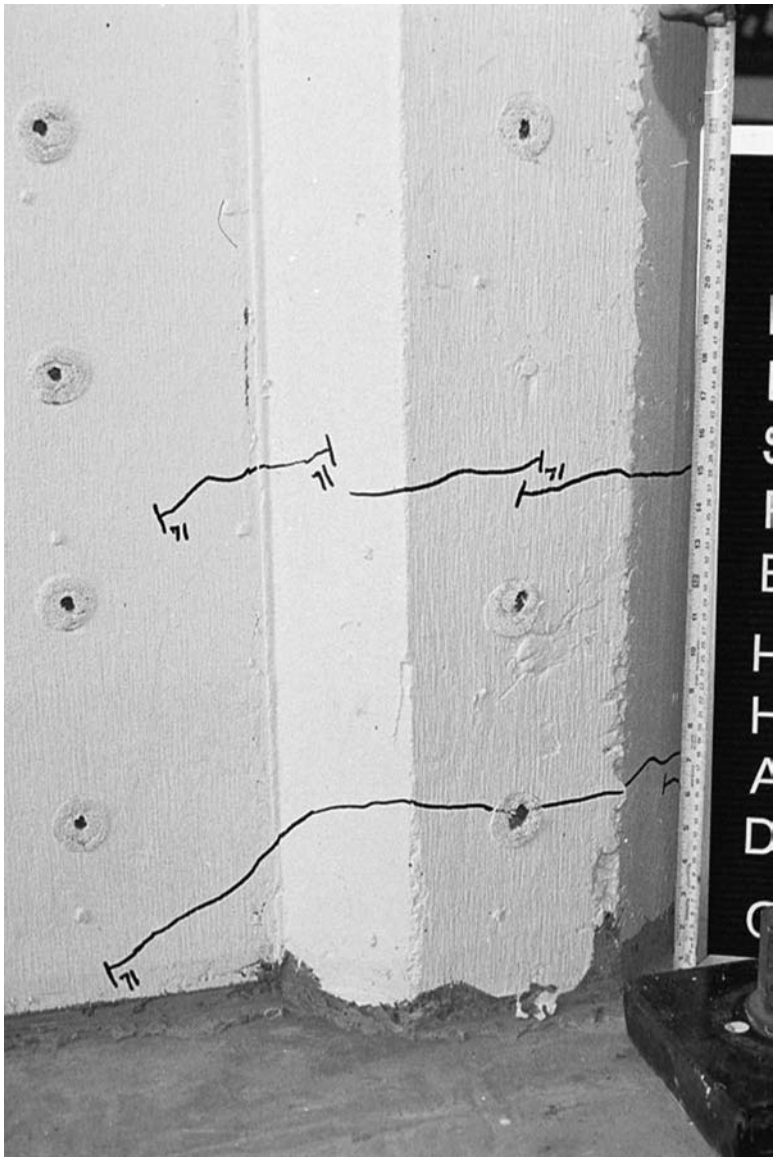

Figure A.37: Unit 2B; 3/4 F_y F=71.1kips [316kN]; Δ=0.12in. [3mm]: First cracks in the tension boundary element and wall.

Figure A.38: Unit 2B; $-F_y$ F=-94.6kips [-421kN]; Δ=-0.25in. [-6mm]: Cracking up to a height of 42in. [1067mm] at first yield.

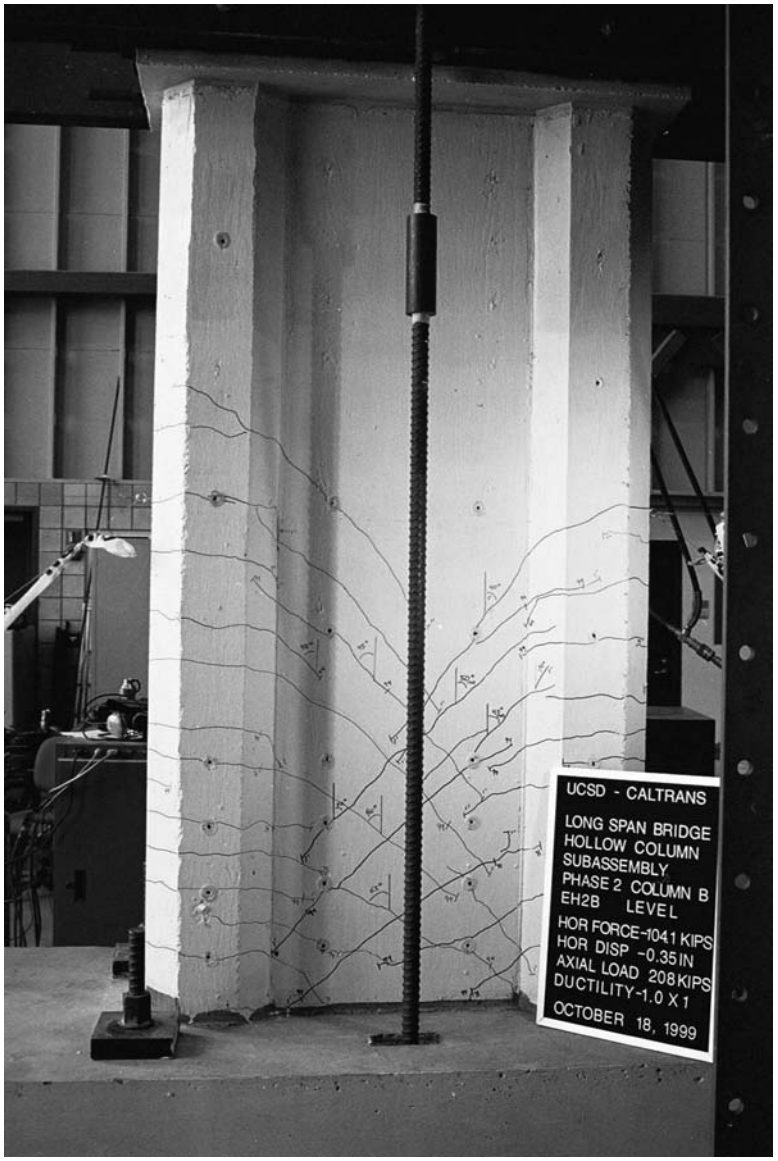

Figure A.39: Unit 2B; μ_Δ=-1.0x1; F=-104.1kips [-463kN]; Δ=-0.35in. [-9mm]: Flexural cracks steepen into shear cracks in the tension boundary elemen hamfer. The crack at 48in. [1219mm] height is vertical along the interface of the tension boundary element and wall.

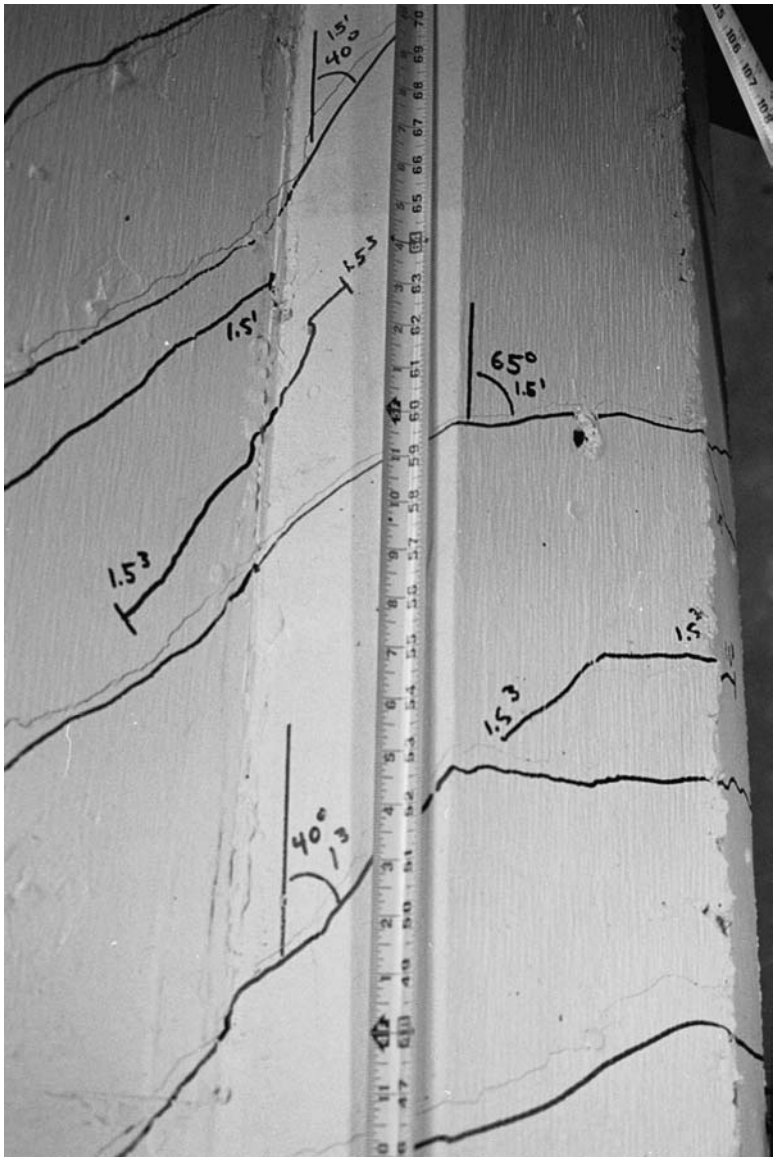

Figure A.40: Unit 2B; μ_Δ=1.5x3; F=112.4kips [500kN]; Δ=0.53in. [13mm]: Shear cracks, angled 40° from the vertical are shown forming in the wall and in the tension boundary element from 48in. [1219mm] to 69in. [1753mm] high.

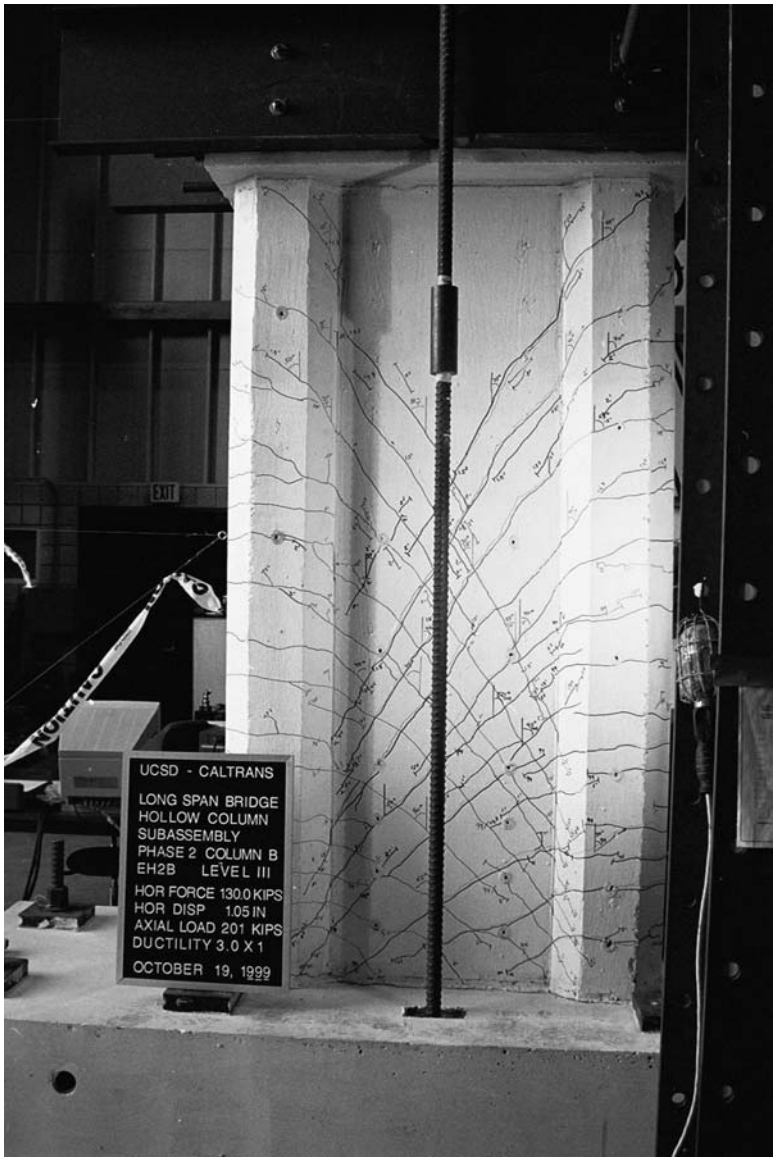

Figure A.41: Unit 2B; μ_Δ=3.0x1; F=130.0kips [579kN]; Δ=1.05in. [27mm]: Deformation and crack pattern.

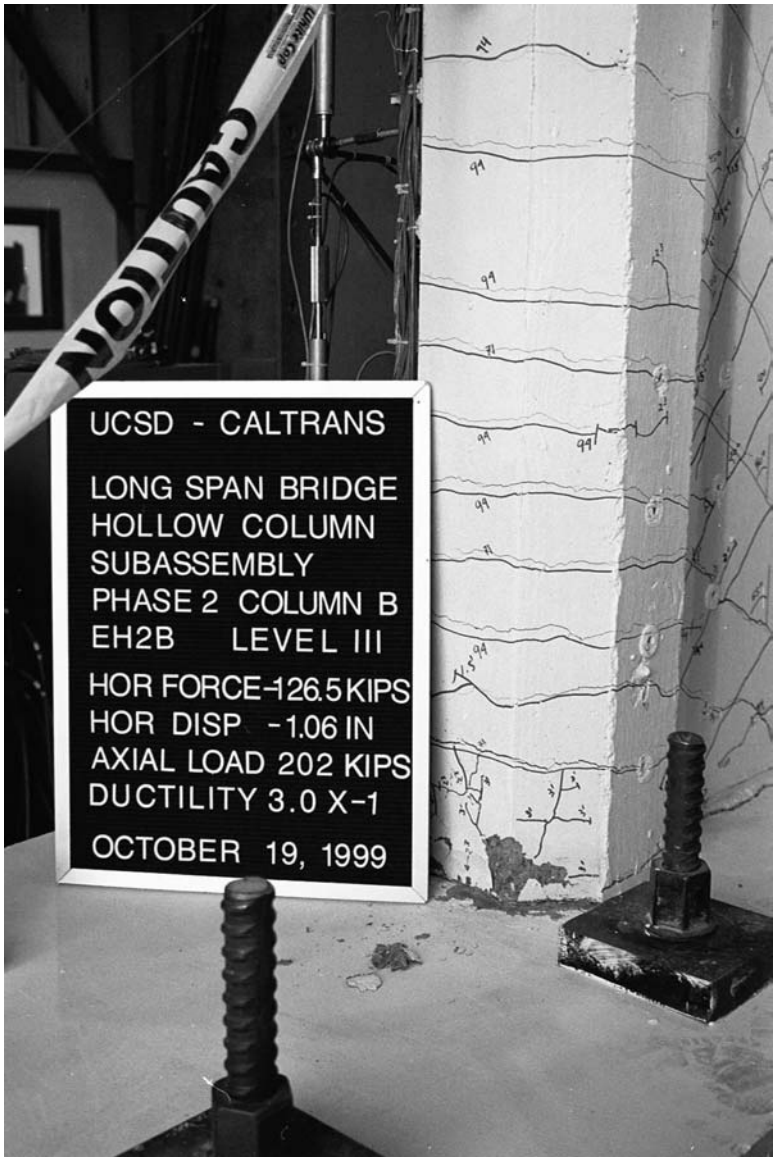

Figure A.42: Unit 2B; μ_Δ=-3.0x1; F=-126.5kips [-563kN]; Δ=-1.06in. [-27mm]: Incipient spalling at the base of the tension boundary element.

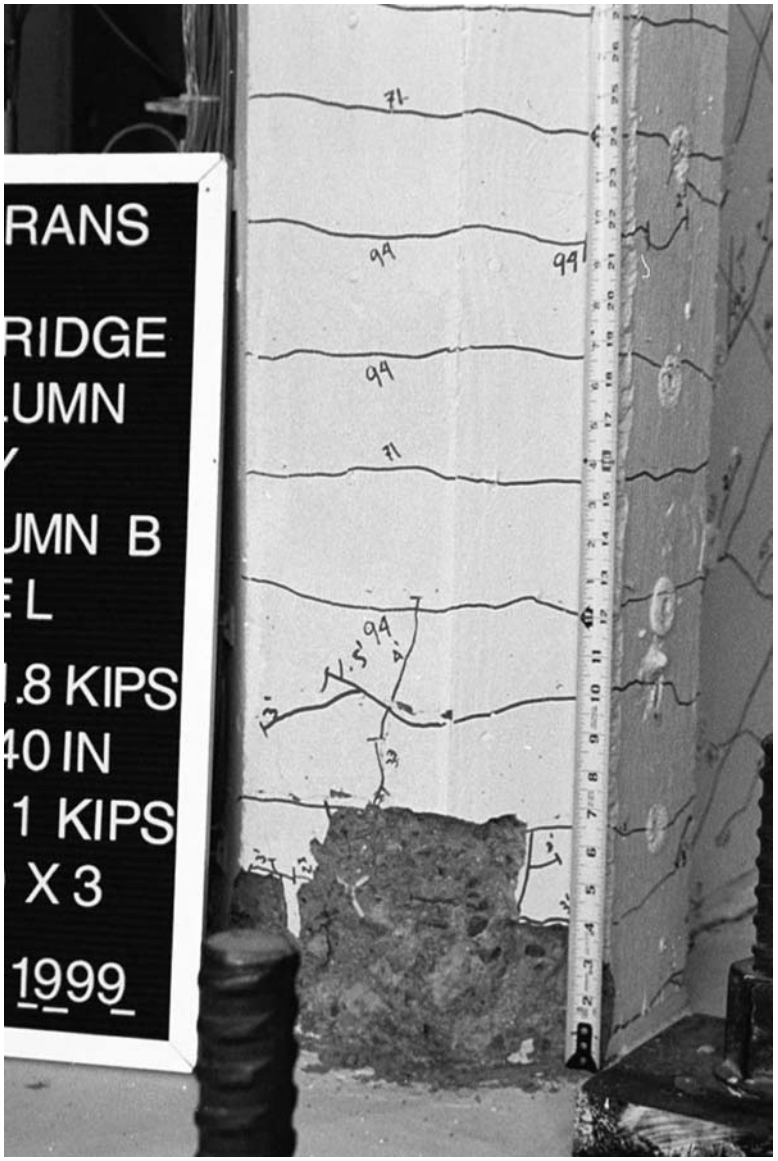

Figure A.43: Unit 2B; μ_Δ=4.0x3; F=121.8kips [542kN]; Δ=1.40in. [36mm]: Partially developed spalled region at the base of the compression boundary element.

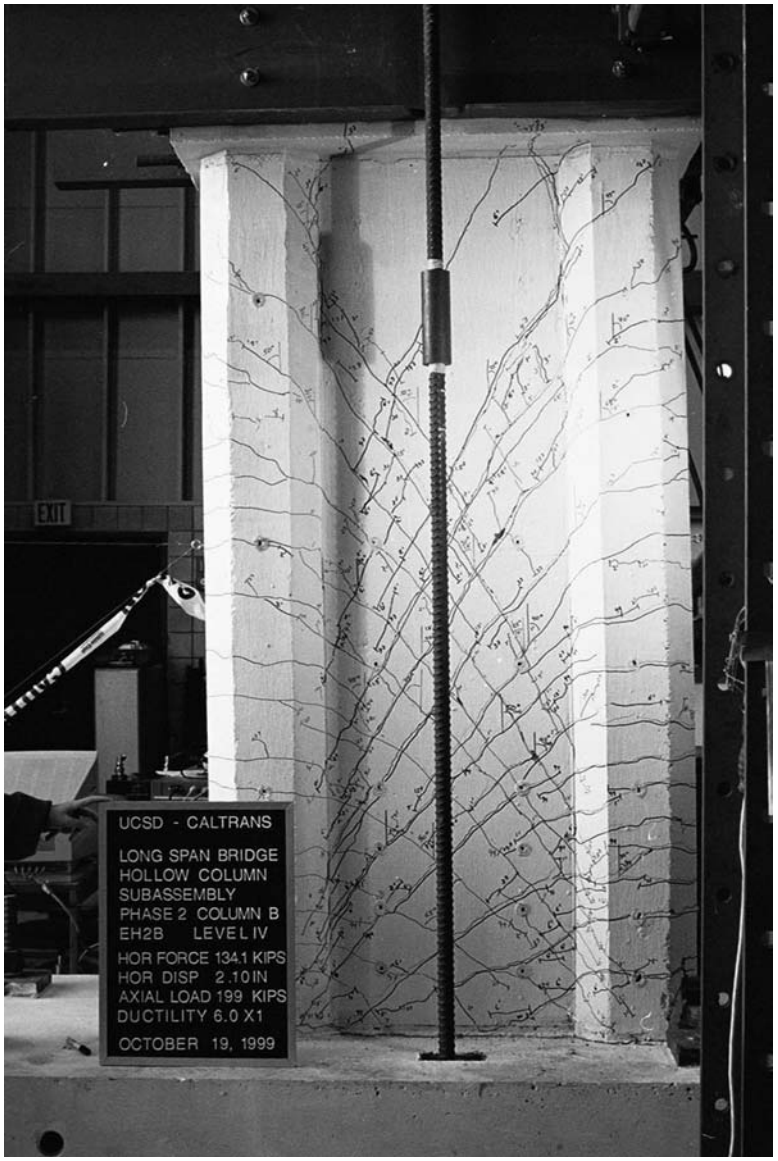

Figure A.44: Unit 2B; μ_Δ=6.0x1; F=134.1kips [597kN]; Δ=2.10in. [53mm]: Deformation and crack pattern.

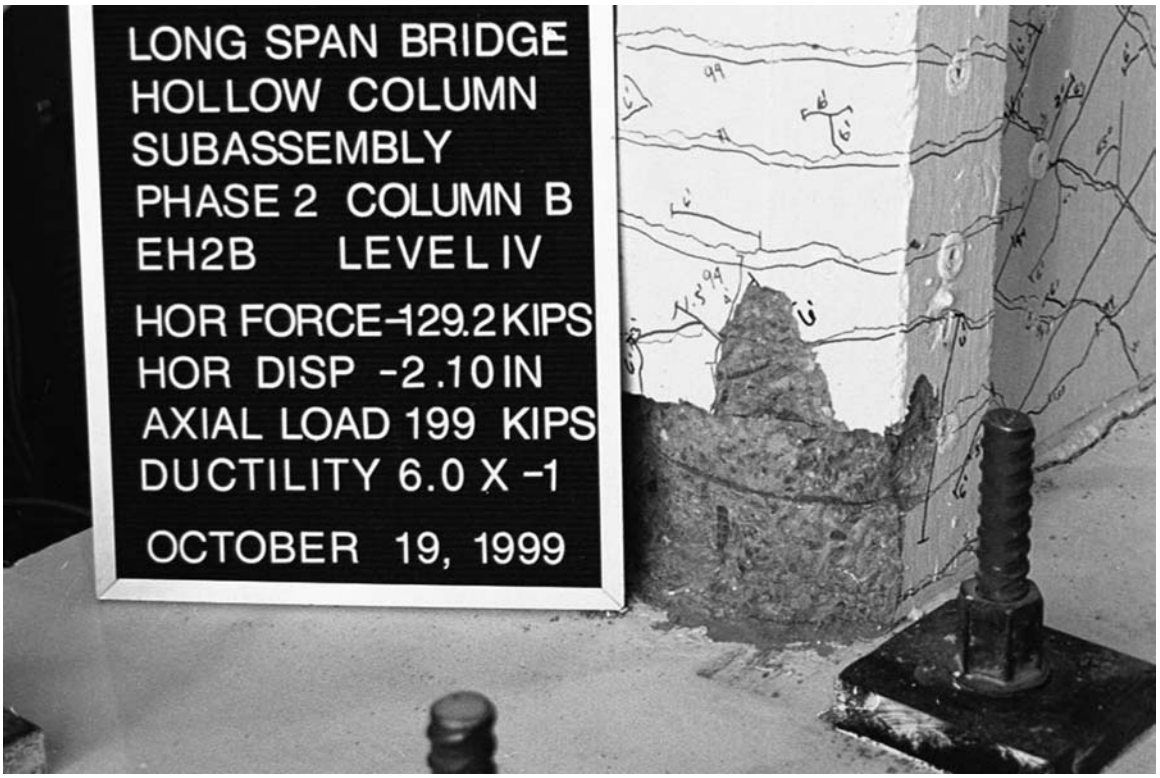

Figure A.45: Unit 2B; μ_Δ=-6.0x1; F=-129.2kips [-575kN]; Δ=-2.10in. [-53mm]: Fully developed spalled region at the base of the tension boundary element.

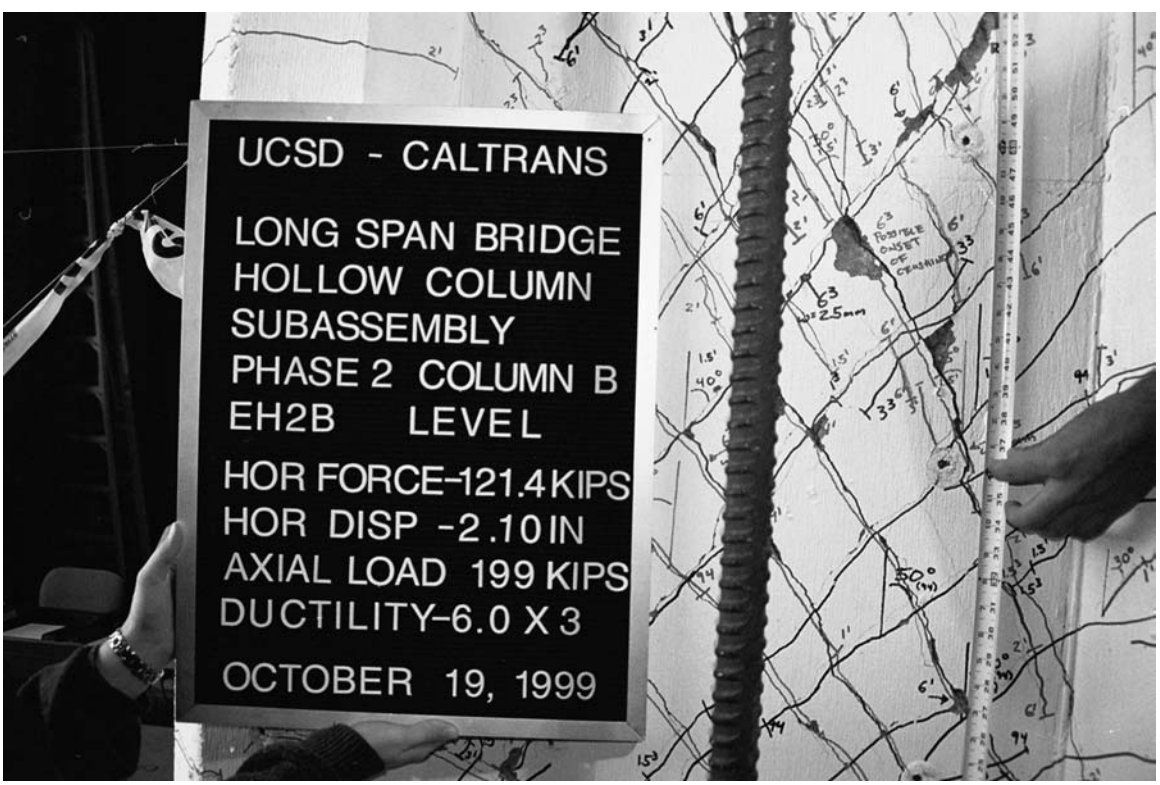

Figure A.46: Unit 2B; μ_Δ=-6.0x3; F=-121.4kips [-540kN]; Δ=-2.10in. [-53mm]: Onset of degradation in the wall from 39in. [991mm] to 52in. [1321mm] high.

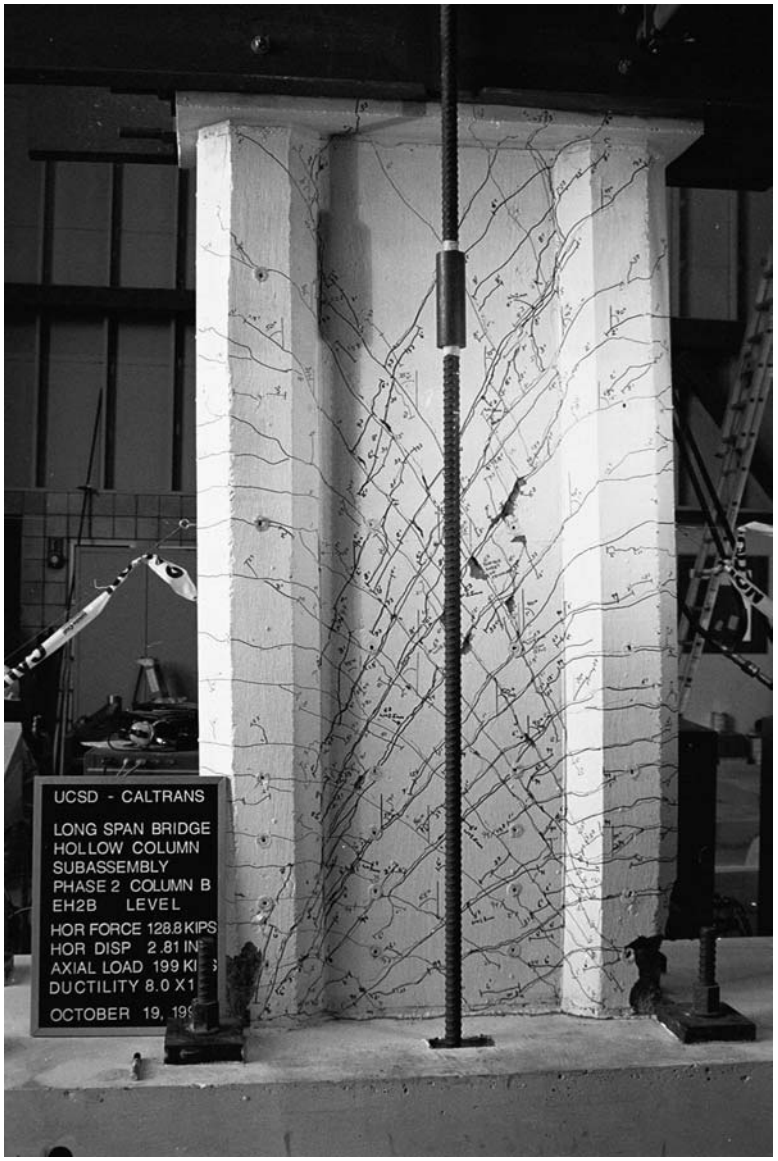

Figure A.47: Unit 2B; μ_Δ=8.0x1; F=128.8kips [573kN]; Δ=2.80in. [71mm]: Deformation and crack pattern.

Figure A.48: Unit 2B; μ_Δ=8.0x3; F=101.1kips [450kN]; Δ=2.80in. [71mm]: Shear failure in the wall, with visible transverse strains at column midheight.

A.5 Unit 2C Test Photos

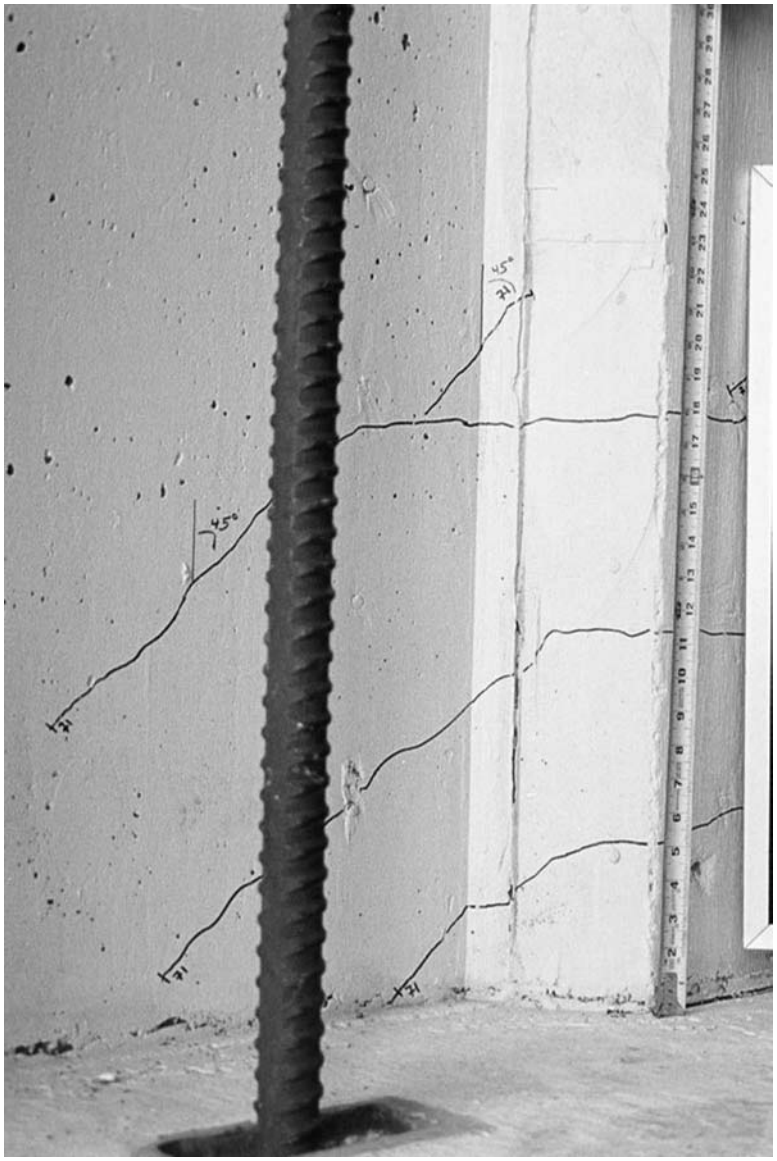

Figure A.49: Unit 2C; 3/4 F_y F=71.1kips [316kN]; Δ=0.12in. [3mm]: First cracks in the tension boundary element and wall.

Figure A.50: Unit 2C; $-F_y$ F=-94.6kips [-421kN]; Δ=-0.25in. [-6mm]: Cracking in the column up to a height of 42in. [1067mm] at first yield.

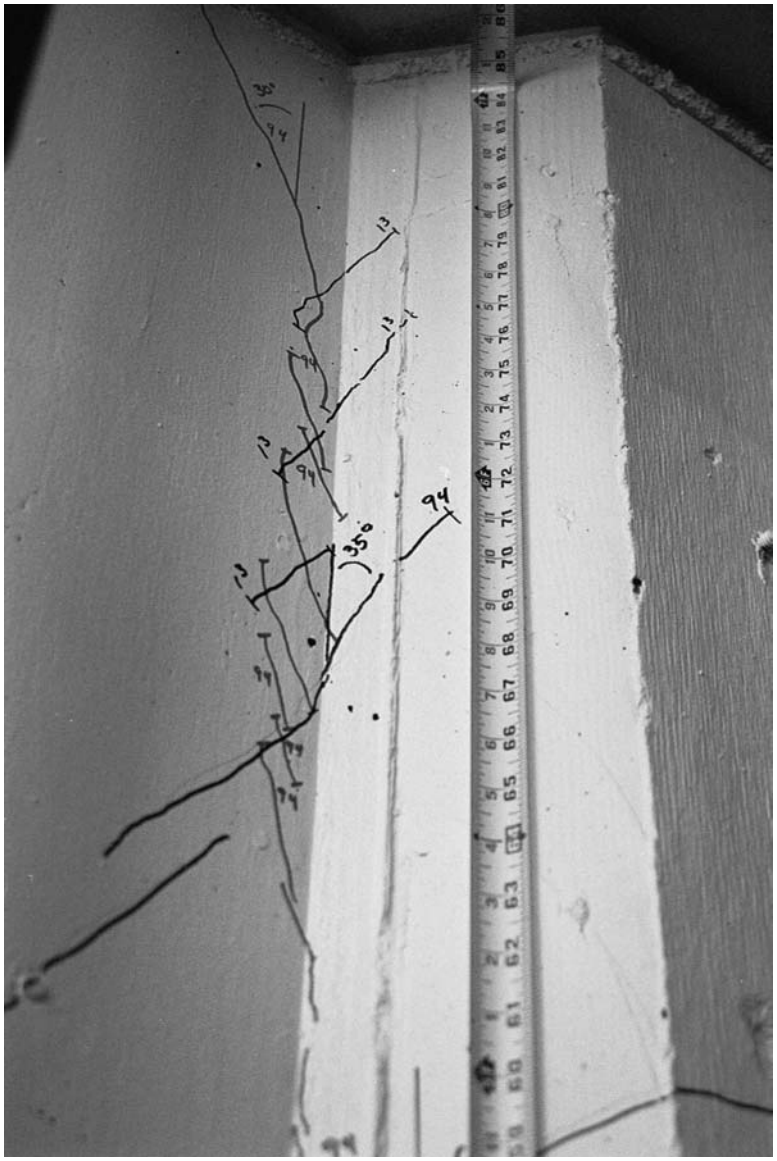

Figure A.51: Unit 2C; μ_Δ=-1.0x1; F=-104.1kips [-463kN]; Δ=-0.35in. [-9mm]: Flexural cracks steepen into shear cracks in the tension boundary elemen hamfer. The crack at 48in. [1219mm] height is vertical along the interface of the tension boundary element and wall.

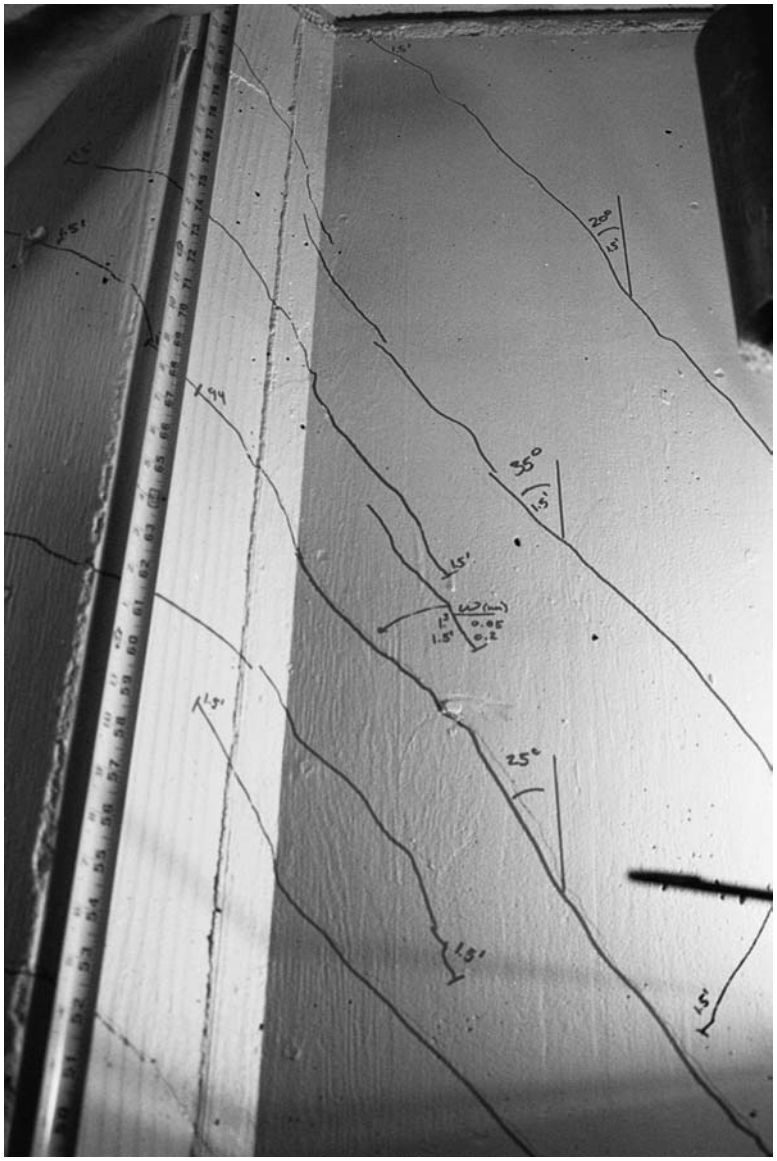

Figure A.52: Unit 2C; μ_Δ=1.5x3; F=112.4kips [500kN]; Δ=0.53in. [13mm]: Shear cracks, angled 40° from the vertical are shown forming in the wall and in the tension boundary element from 48in. [1219mm] to 69in. [1753mm] high.

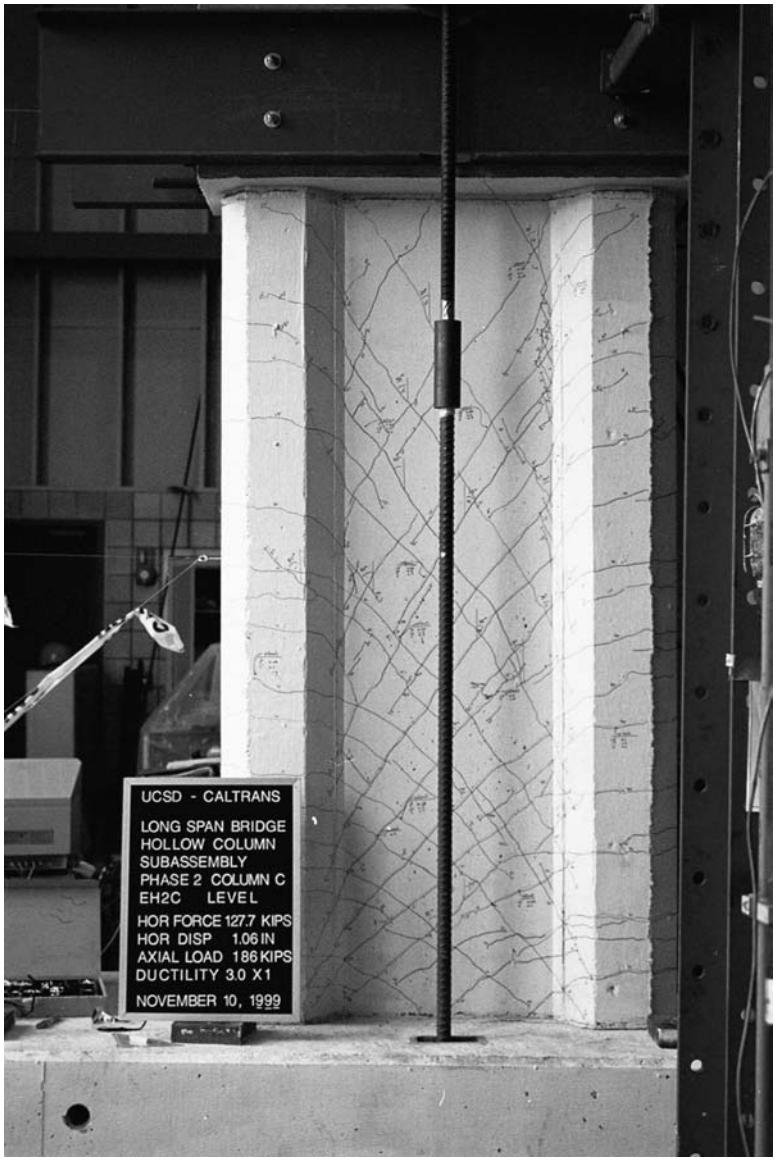

Figure A.53: Unit 2C; μ_Δ=3.0x1; F=130.0kips [579kN]; Δ=1.05in. [27mm]: Deformation and crack pattern.

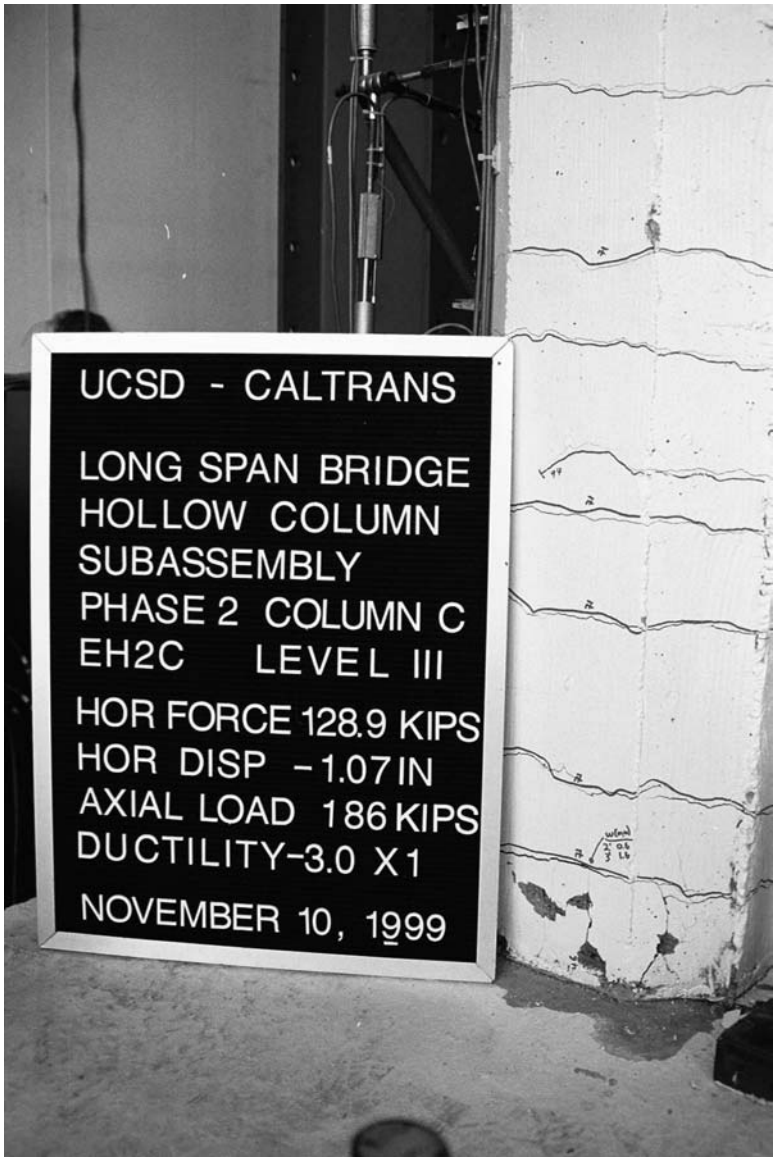

Figure A.54: Unit 2C; μ_Δ=-3.0x1; F=-126.5kips [-563kN]; Δ=-1.06in. [-27mm]: Incipient spalling at the base of the tension boundary element.

Figure A.55: Unit 2C; μ_Δ=4.0x3; F=121.8kips [542kN]; Δ=1.40in. [36mm]: Partially developed spalled region at the base of the compression boundary element.

Figure A.56: Unit 2C; μ_Δ=6.0x1; F=134.1kips [597kN]; Δ=2.10in. [53mm]: Deformation and crack pattern.

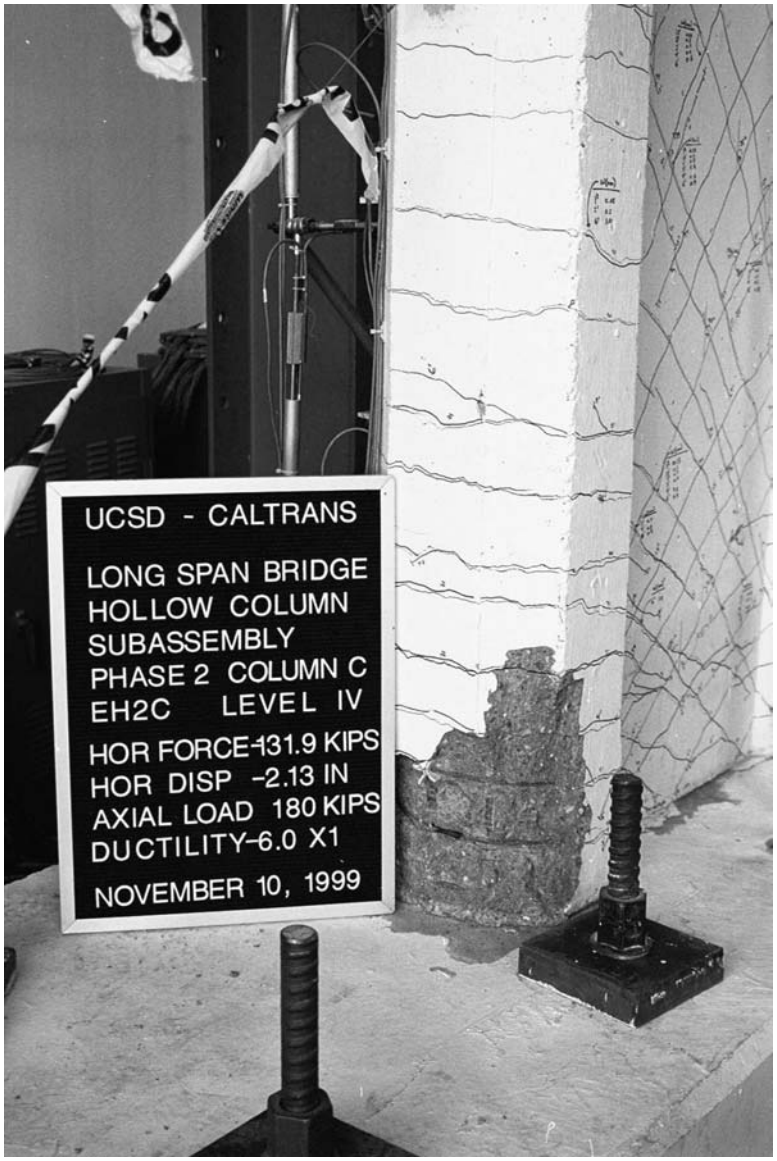

Figure A.57: Unit 2C; μ_Δ=-6.0x1; F=-129.2kips [-575kN]; Δ=-2.10in. [-53mm]: Fully developed spalled region at the base of the tension boundary element.

Figure A.58: Unit 2C; μ_Δ=6.0x3; F=121.4kips [540kN]; Δ=2.10in. [53mm]: Incipient bar buckling at 6in. [152mm] high in the compression boundary element (north).

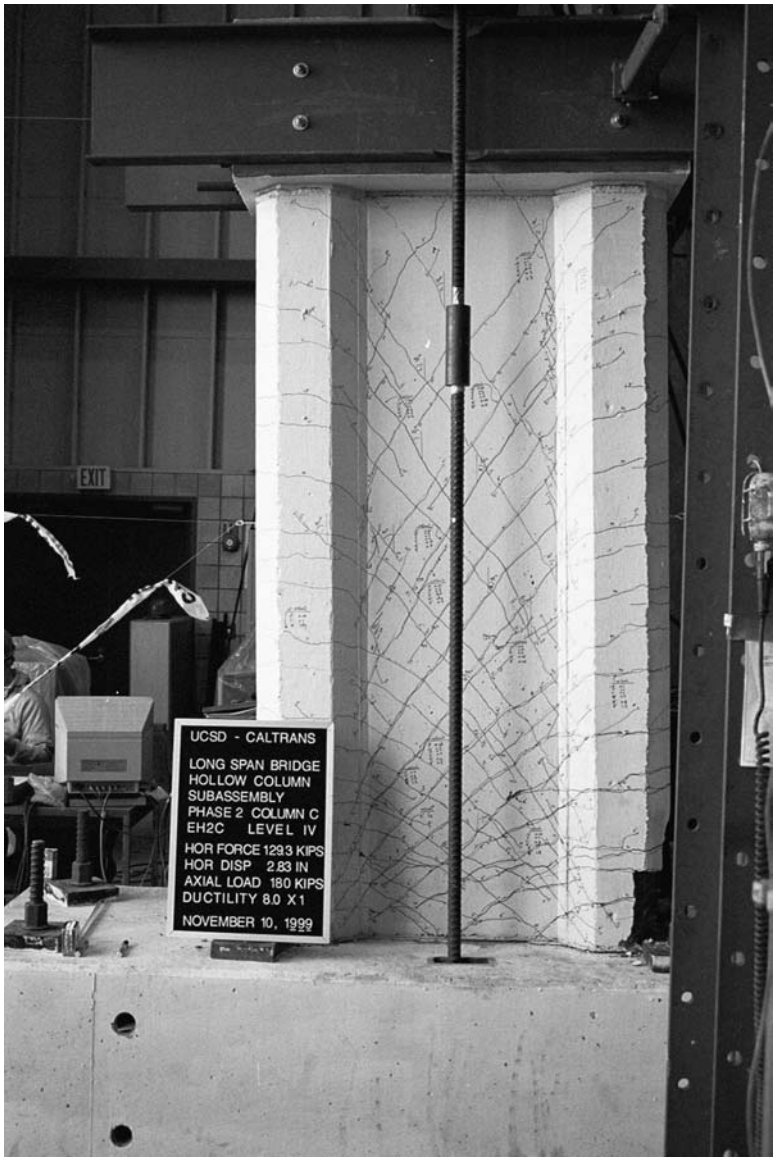

Figure A.59: Unit 2C; μ_Δ=8.0x1; F=128.8kips [573kN]; Δ=2.80in. [71mm]: Deformation and cracked pattern.

Figure A.60: Unit 2C; μ_Δ=8.0x3; F=104.5kips [465kN]; Δ=2.83in. [72mm]: Failure due to buckling and fracture of the longitudinal bars in the compression boundary element (north).

Appendix B

Test Unit 1A Results

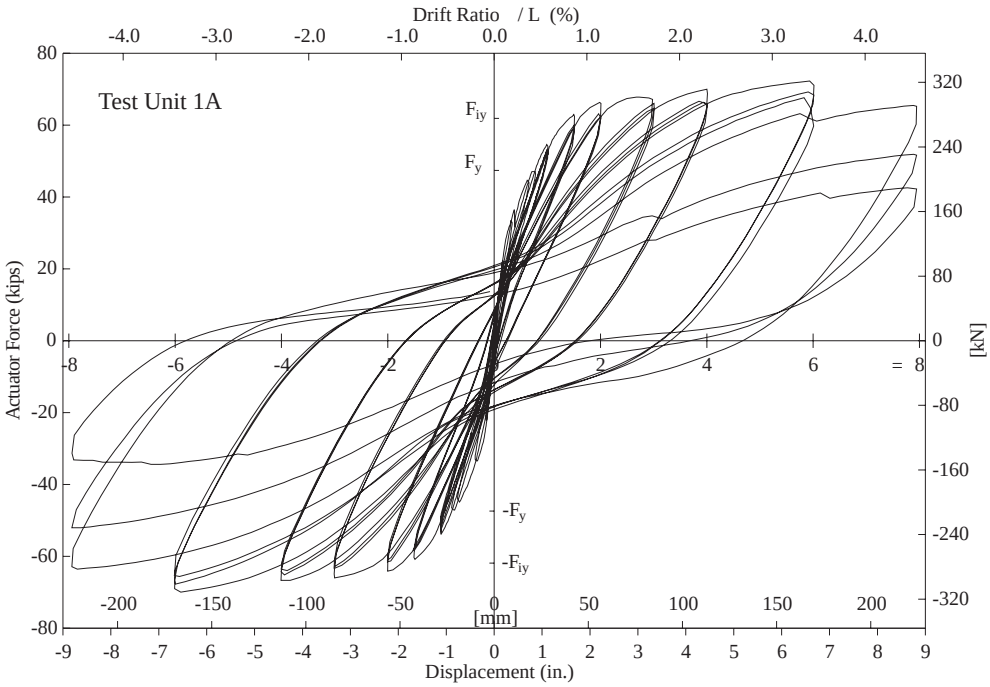

Figure B.1: Test Unit 1A hysteretic behavior.

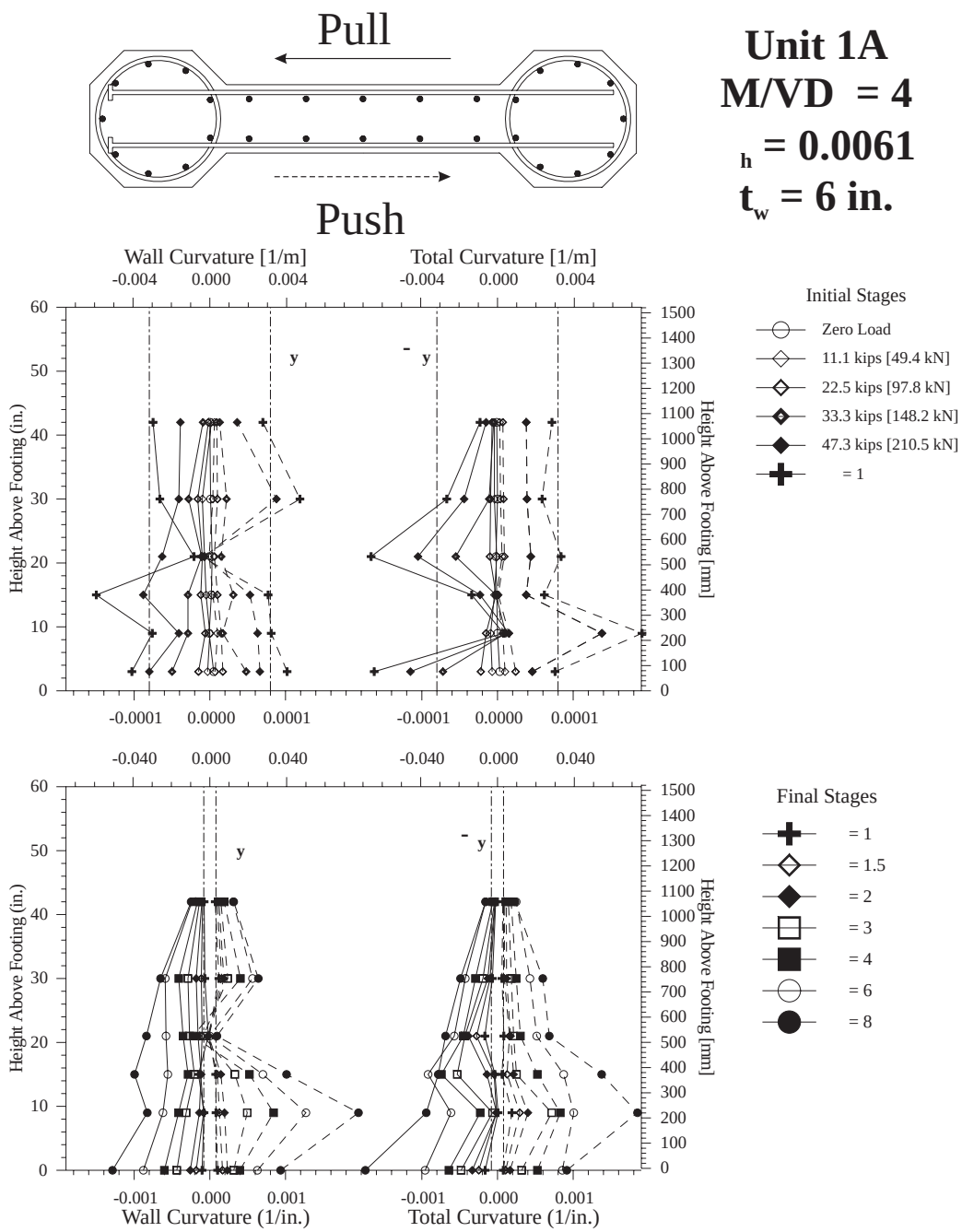

Figure B.2: Unit 1A: Curvature profiles for the wall (left) and for the total section (right).

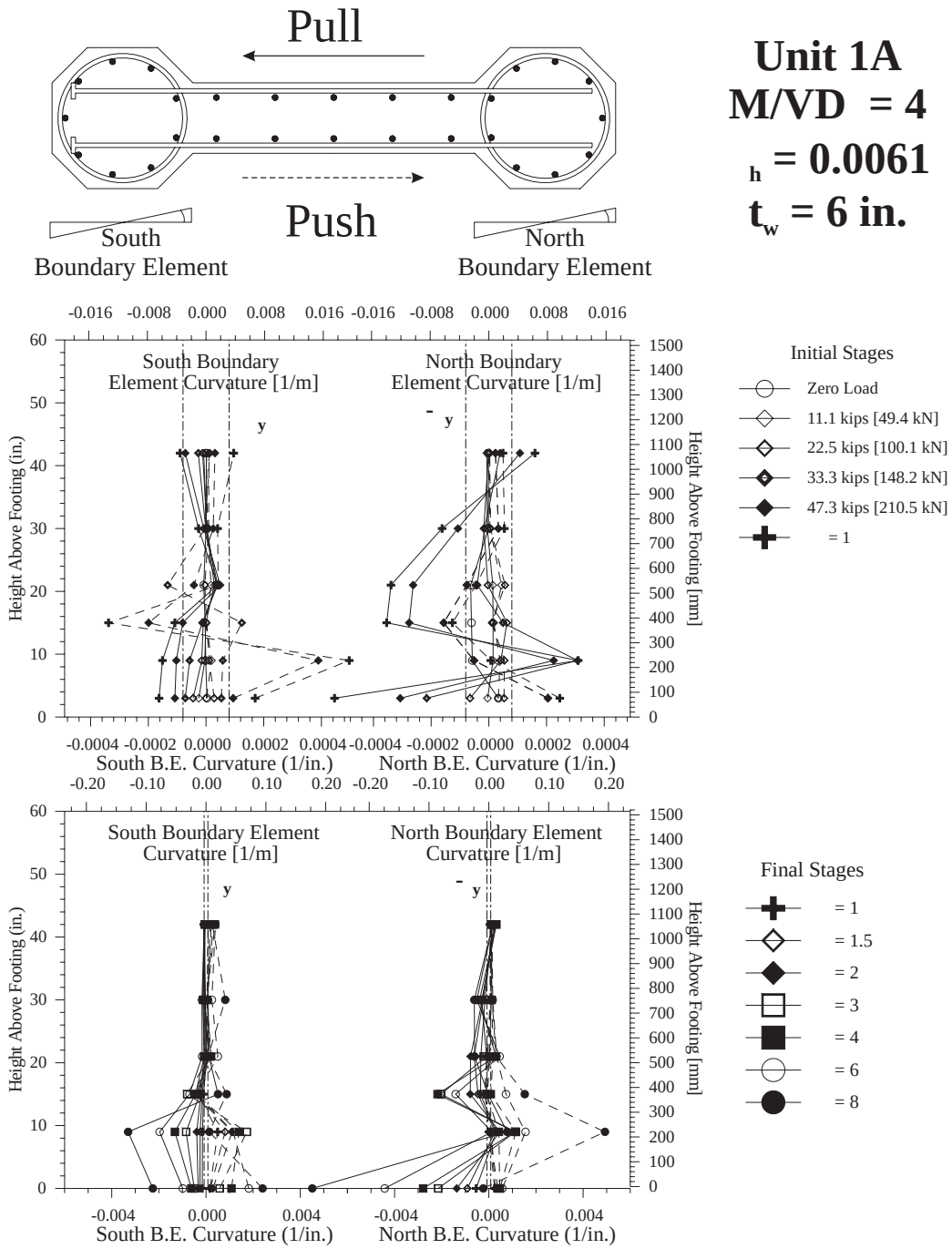

Figure B.3: Unit 1A: Curvature profiles for the south boundary element (left) and for the north boundary element (right).

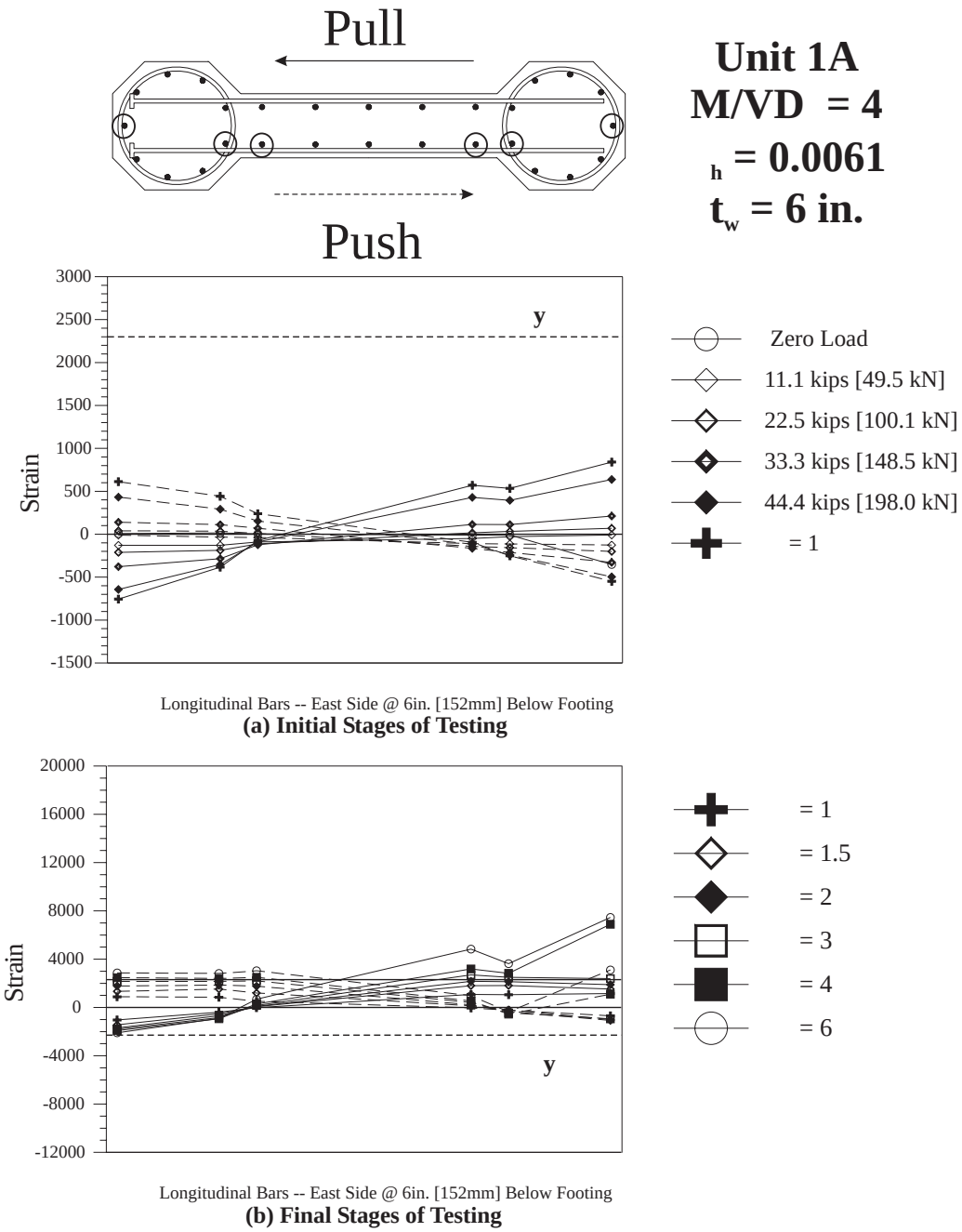

Figure B.4: Unit 1A: Longitudinal bar strain profiles at 6in. [152mm] below the footing surface.

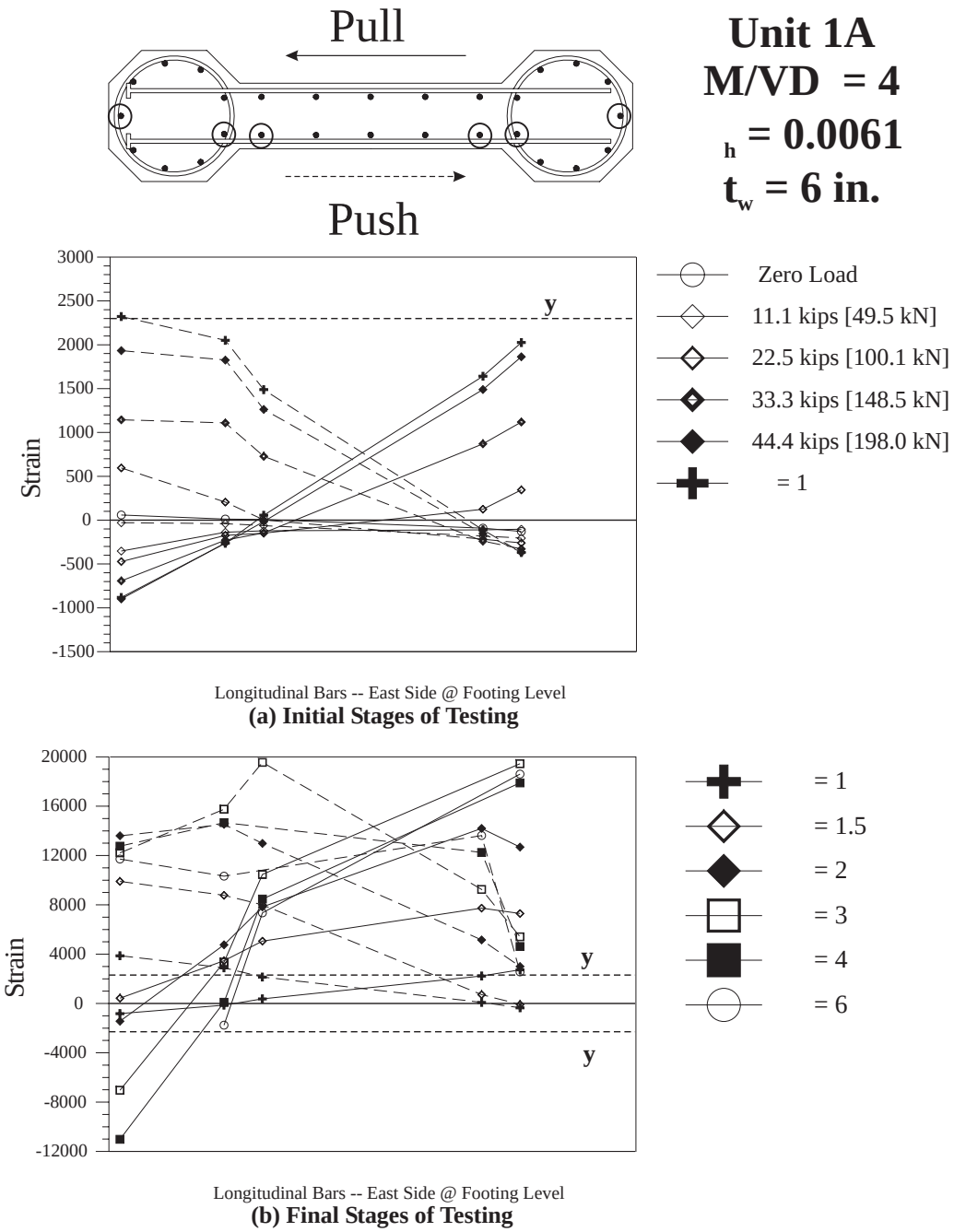

Figure B.5: Unit 1A: Longitudinal bar strain profiles at footing level.

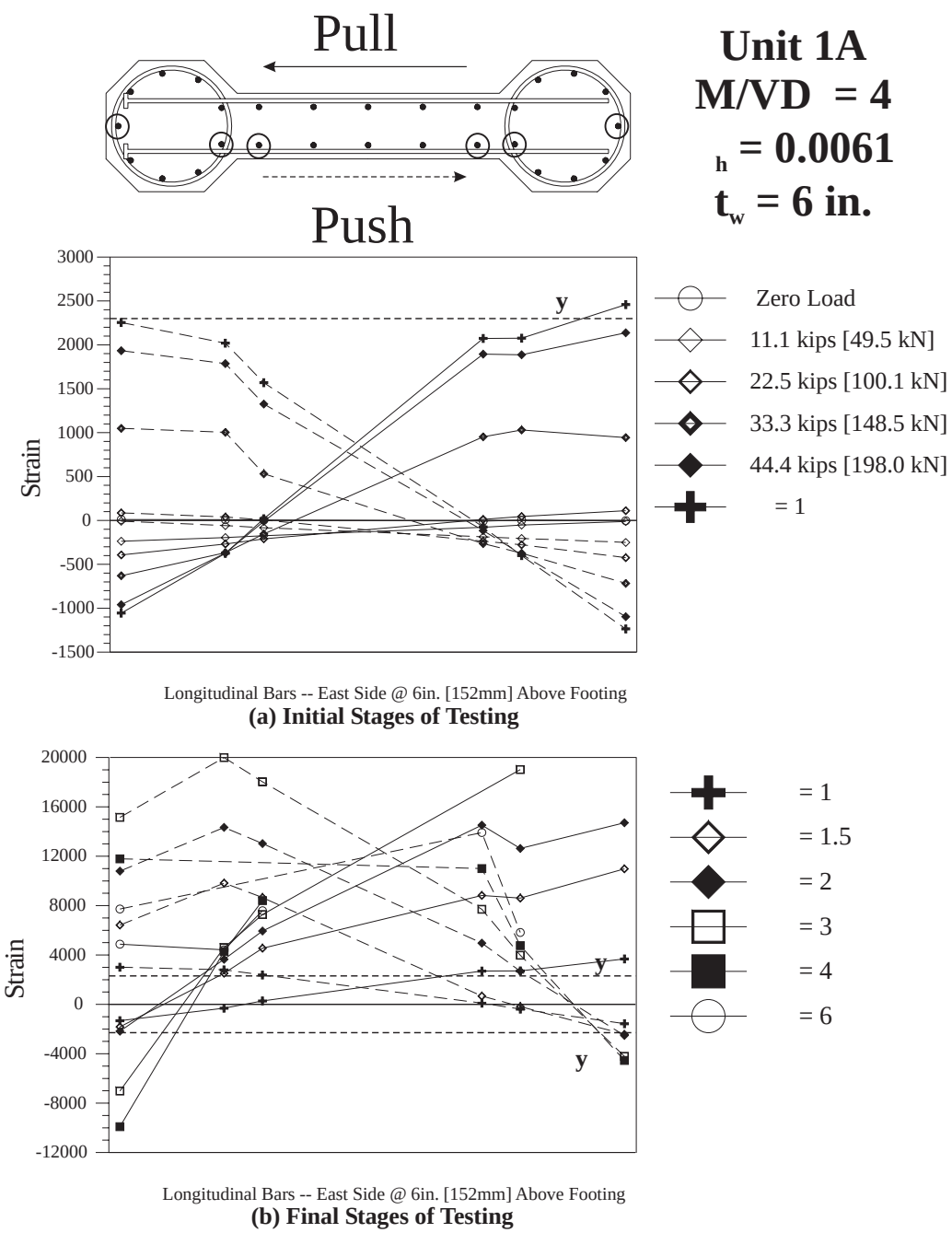

Figure B.6: Unit 1A: Longitudinal bar strain profiles at 6in. [152mm] above the footing.

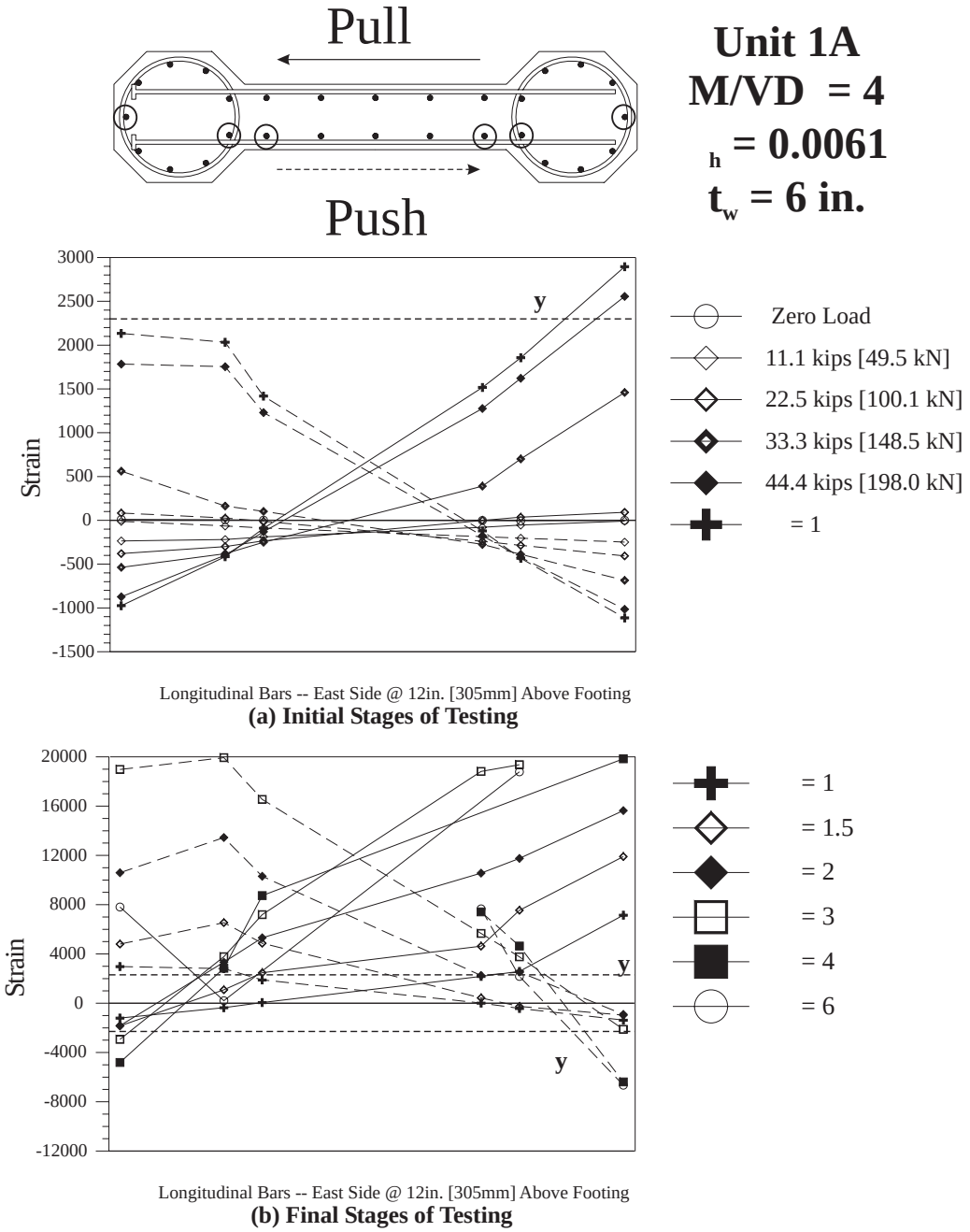

Figure B.7: Unit 1A: Longitudinal bar strain profiles at 12in. [305mm] above the footing.

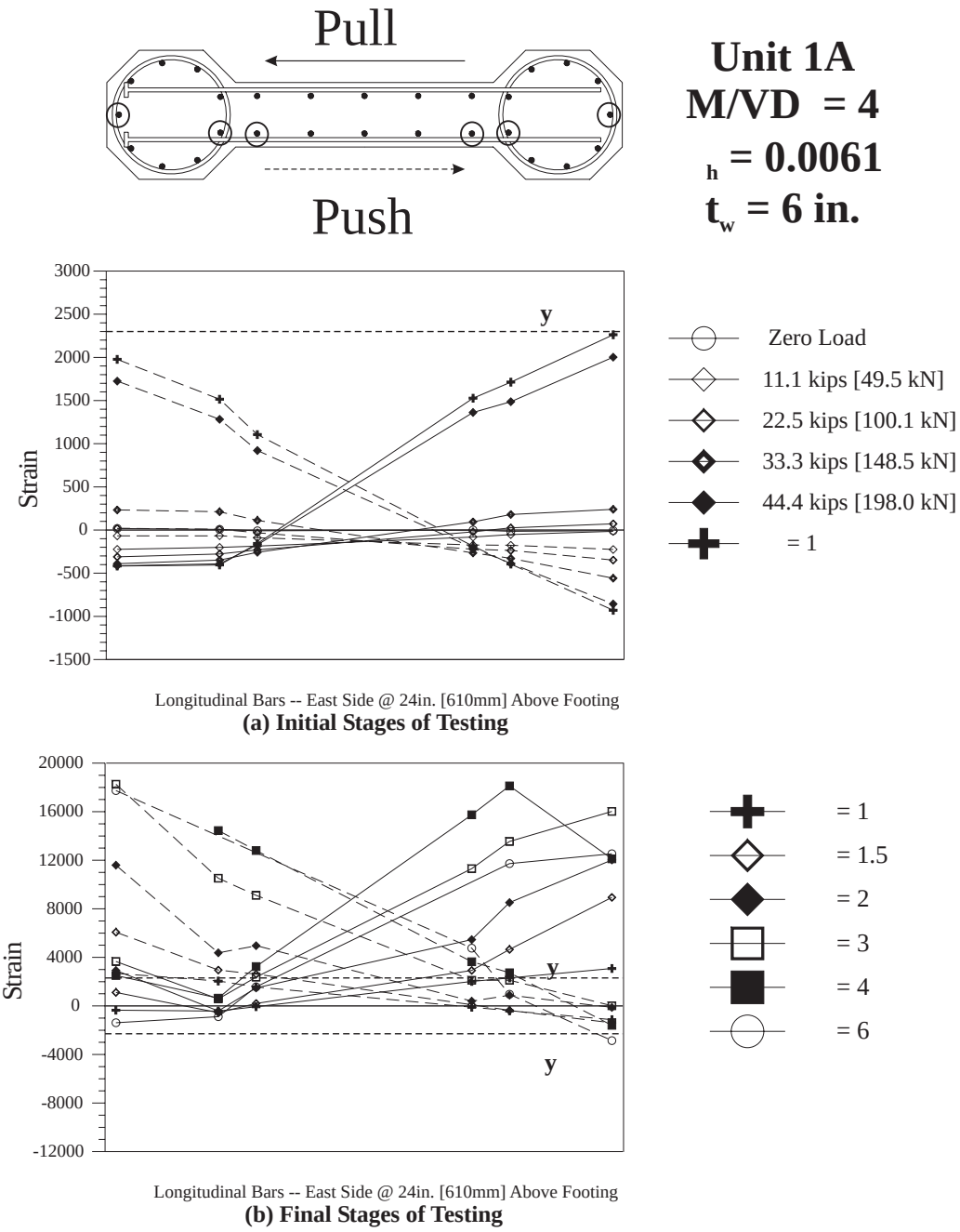

Figure B.8: Unit 1A: Longitudinal bar strain profiles at 24in. [610mm] above the footing.

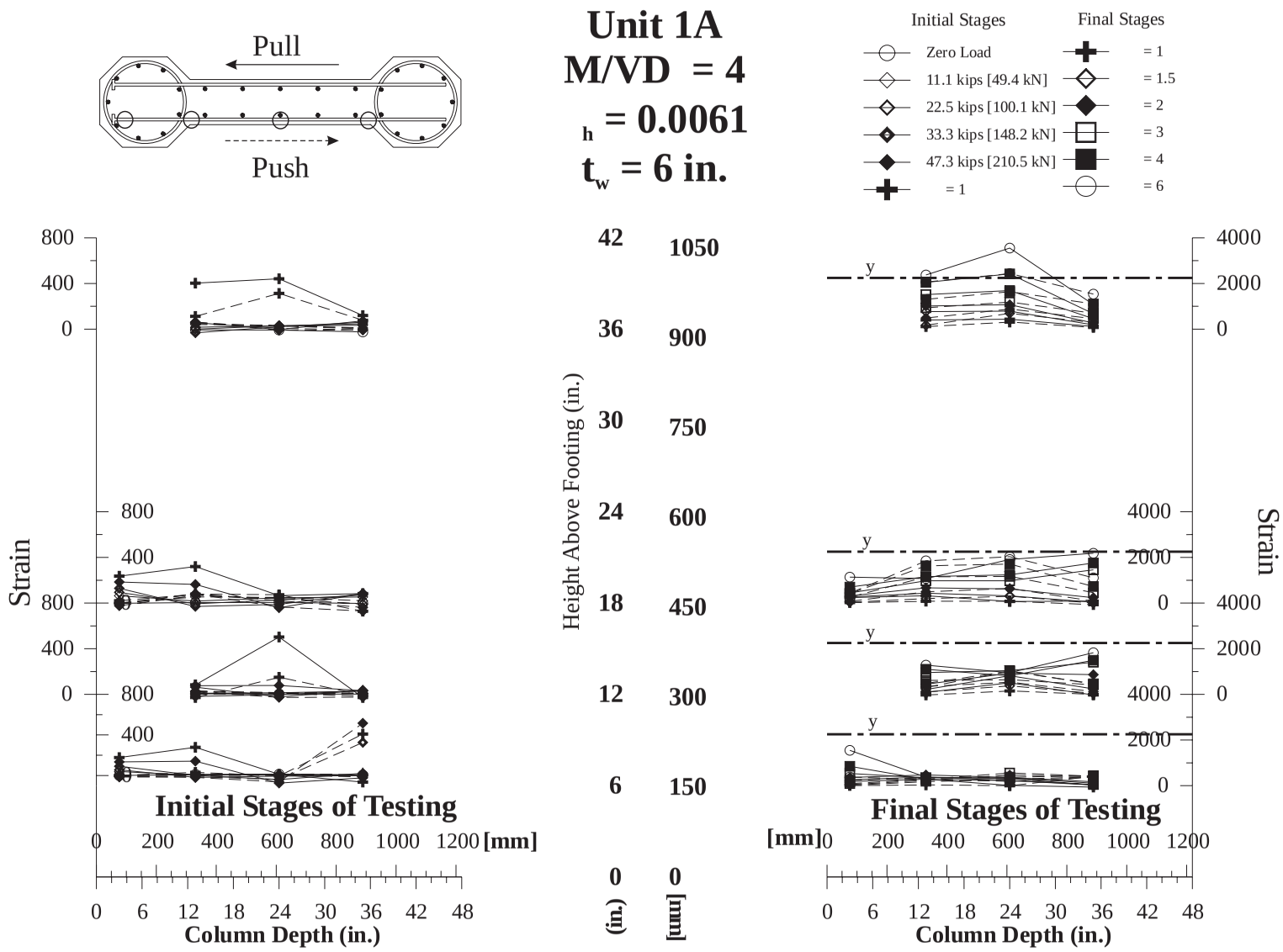

Figure B.9: Unit 1A: Strains on east transverse bars at initial and final testing stages.

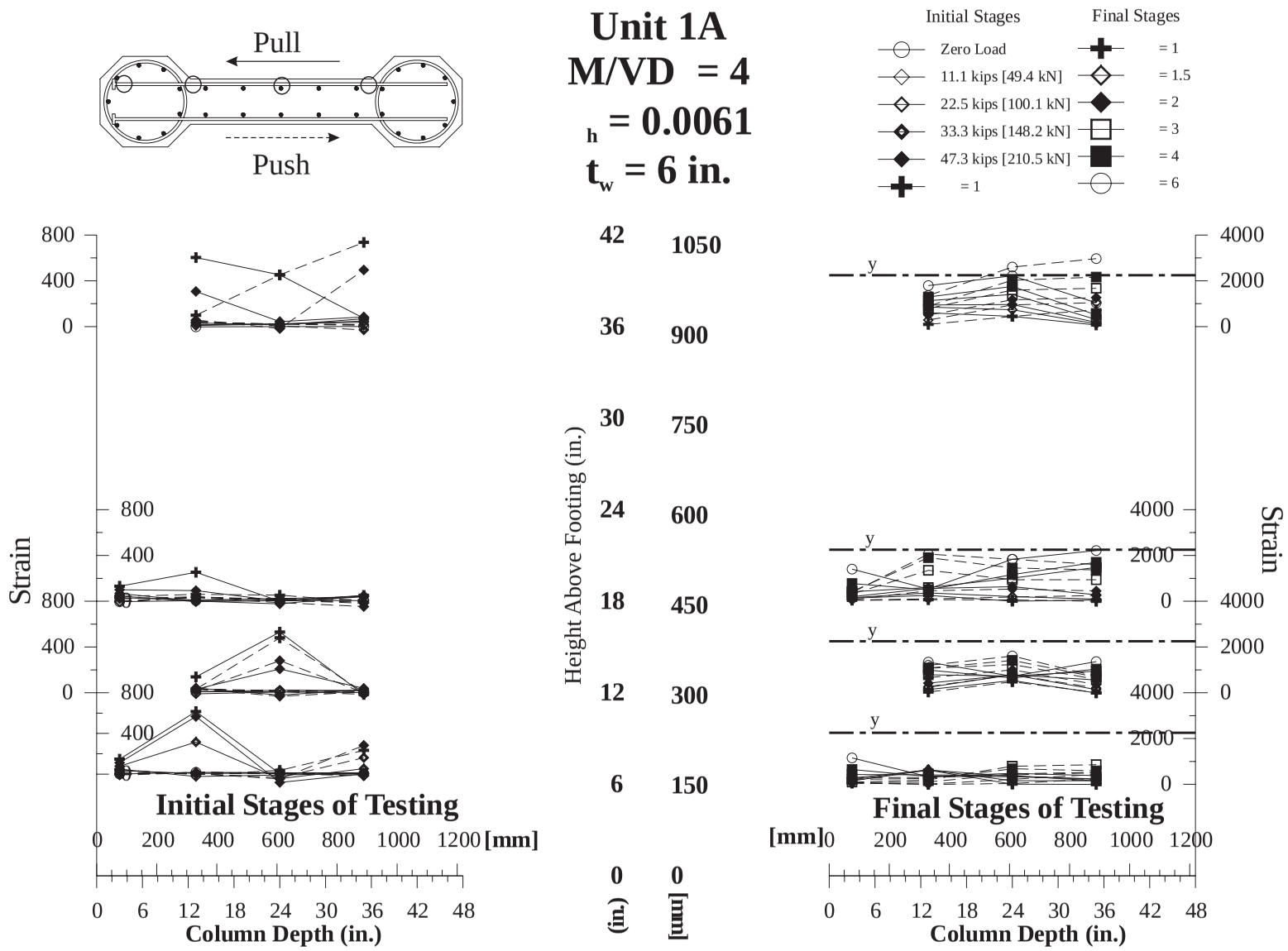

Figure B.10: Unit 1A: Strains on west transverse bars at initial and final testing stages.

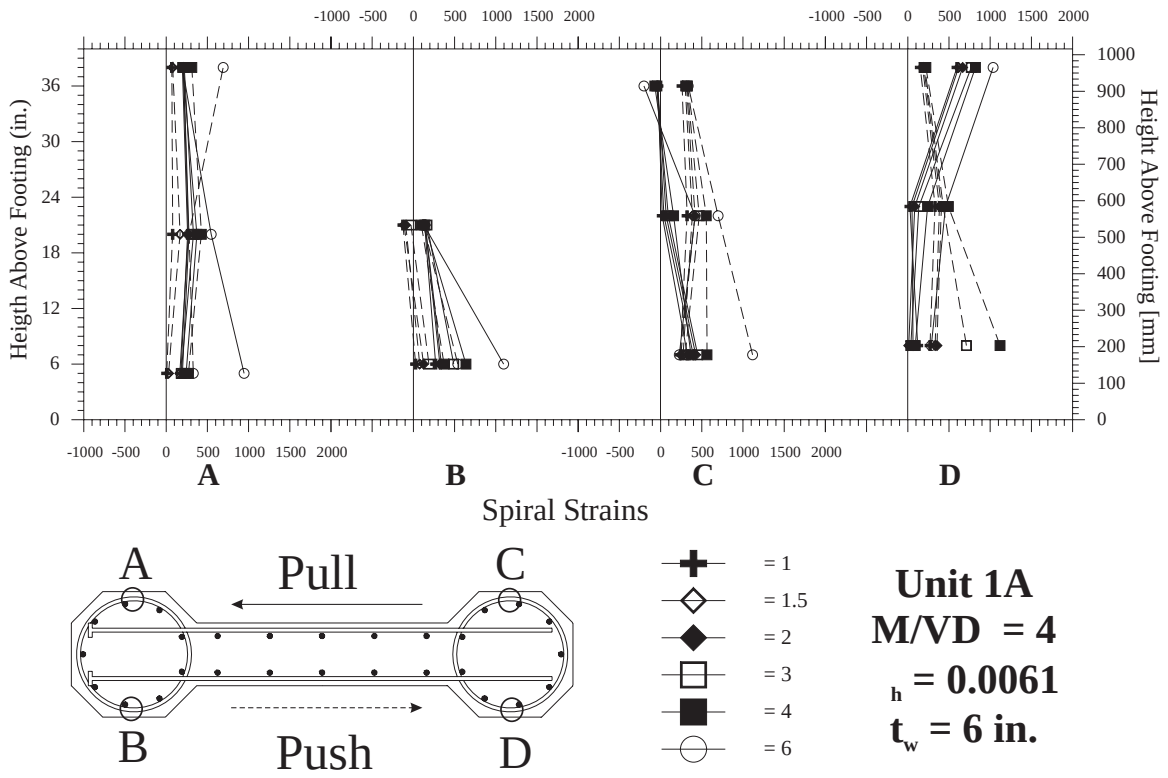

Figure B.11: Unit 1A: East and west spiral strains at final stages of loading.

Appendix C

Test Unit 1B Results

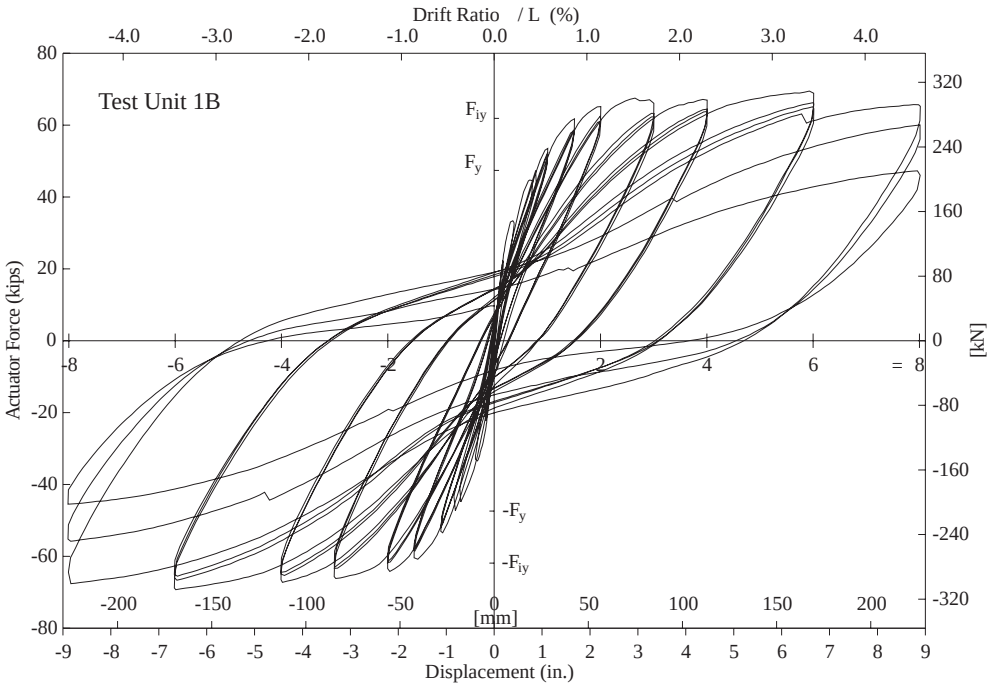

Figure C.1: Test Unit 1B hysteretic behavior.

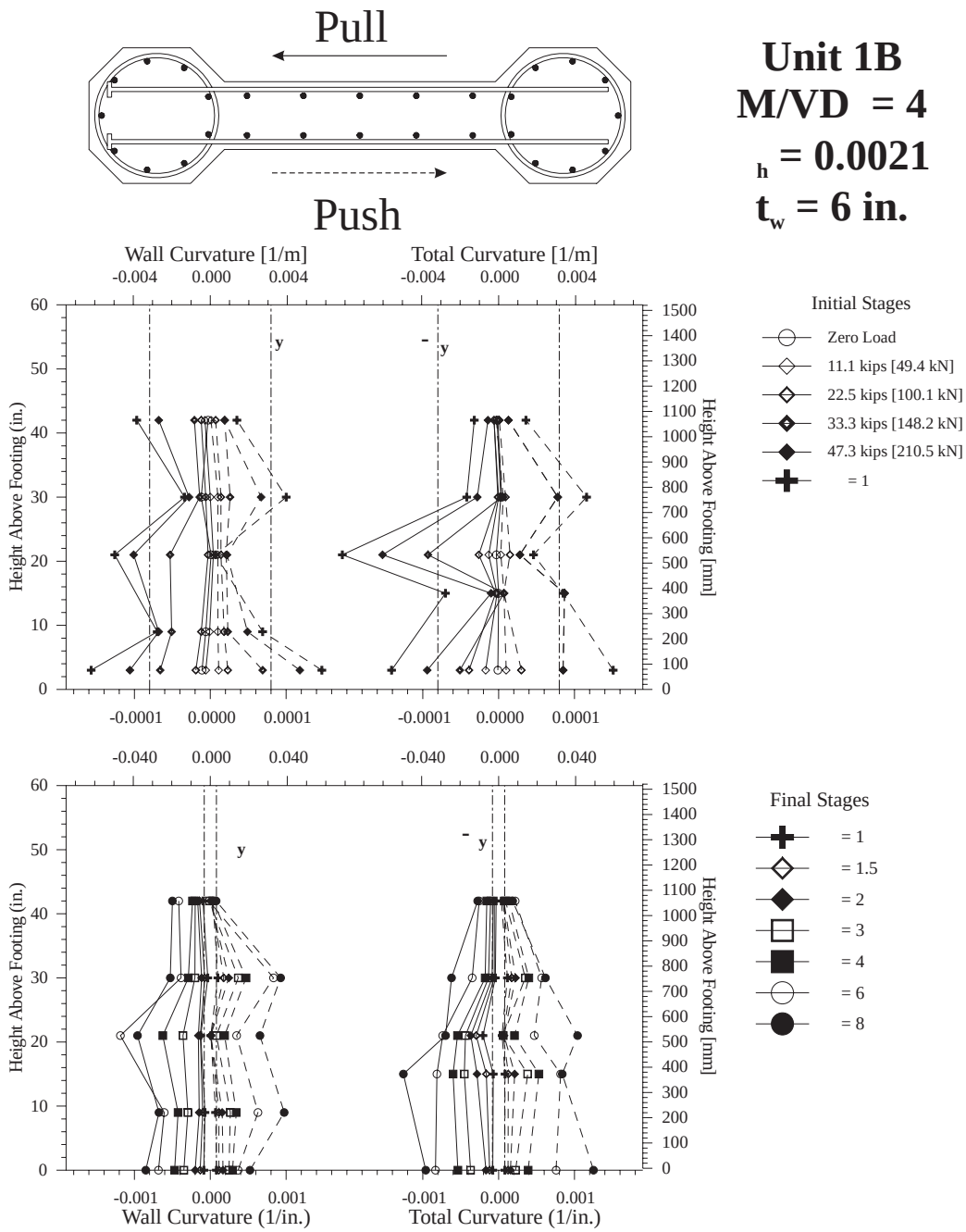

Figure C.2: Unit 1B: Curvature profiles for the wall (left) and for the total section (right).

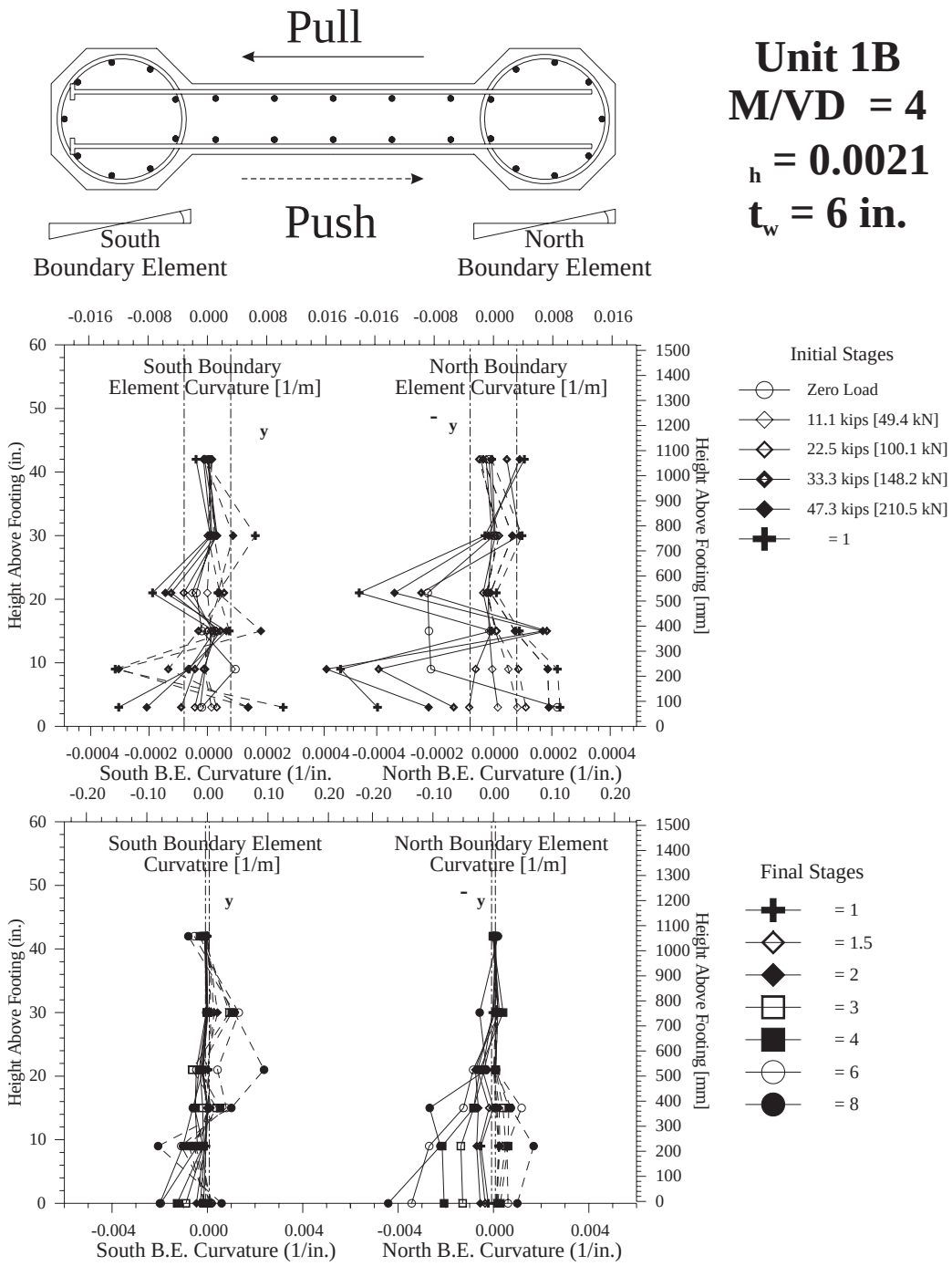

Figure C.3: Unit 1B: Curvature profiles for the south boundary element (left) and for the north boundary element (right).

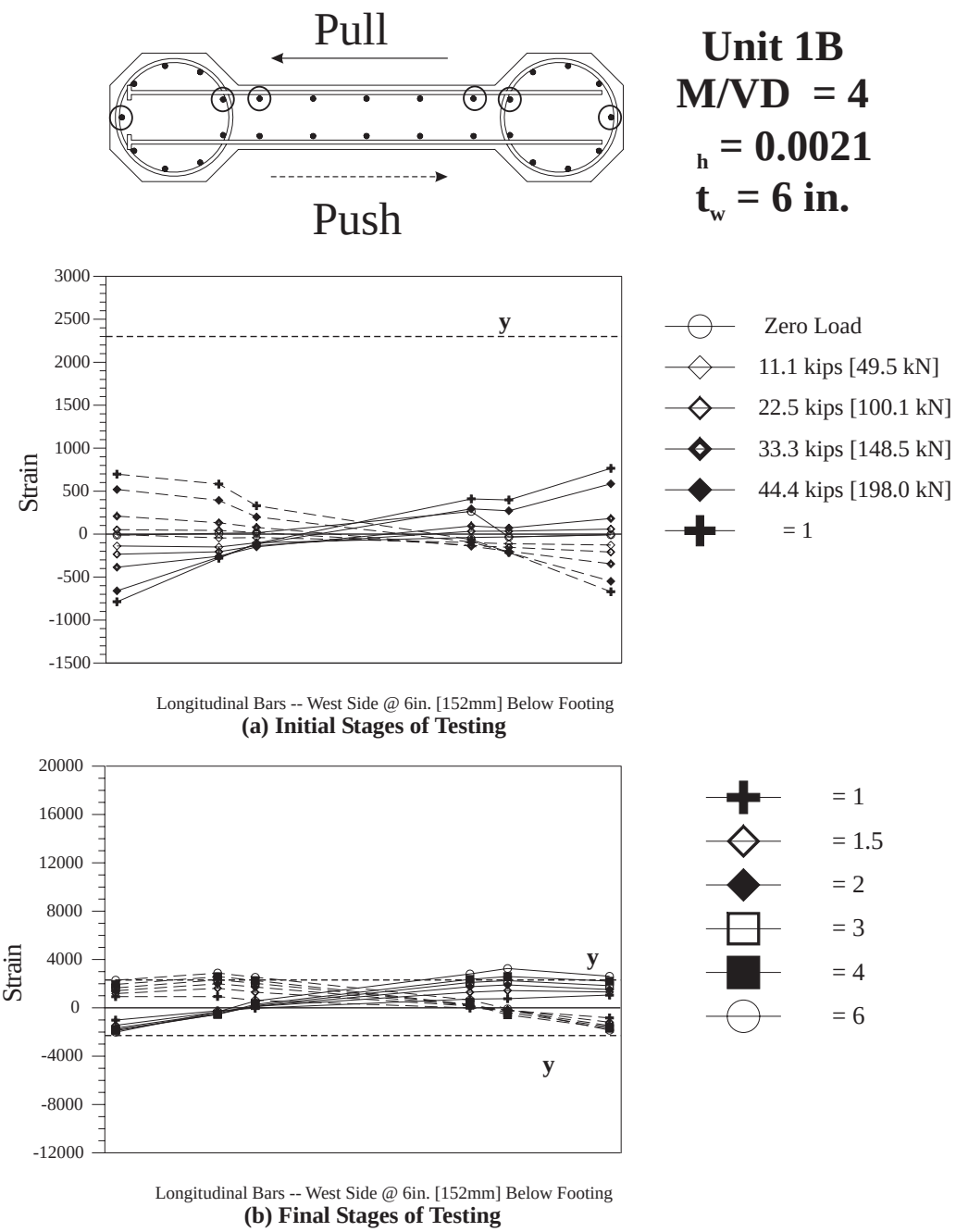

Figure C.4: Unit 1B: Longitudinal bar strain profiles at 6in. [152mm] below the footing surface.

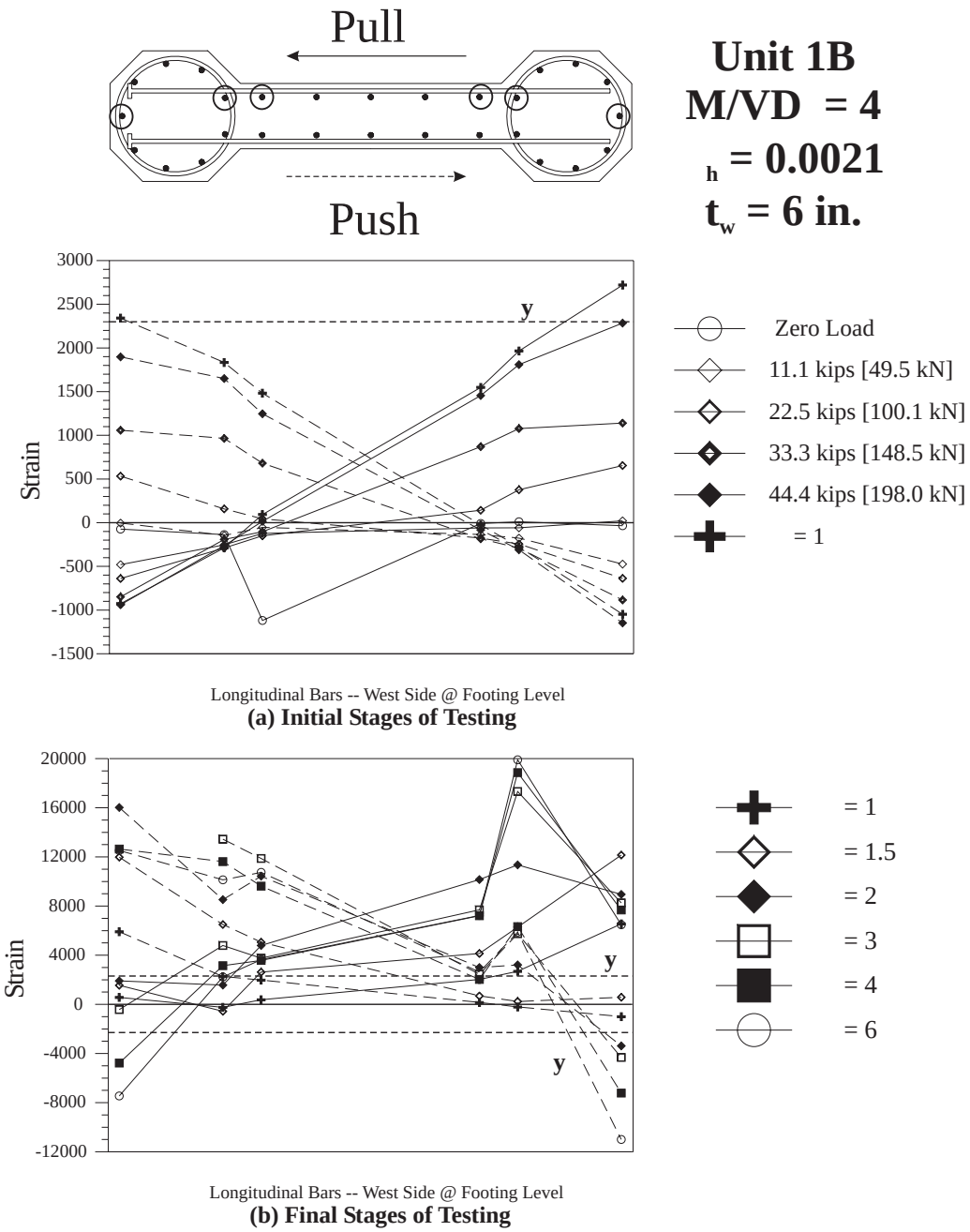

Figure C.5: Unit 1B: Longitudinal bar strain profiles at footing level.

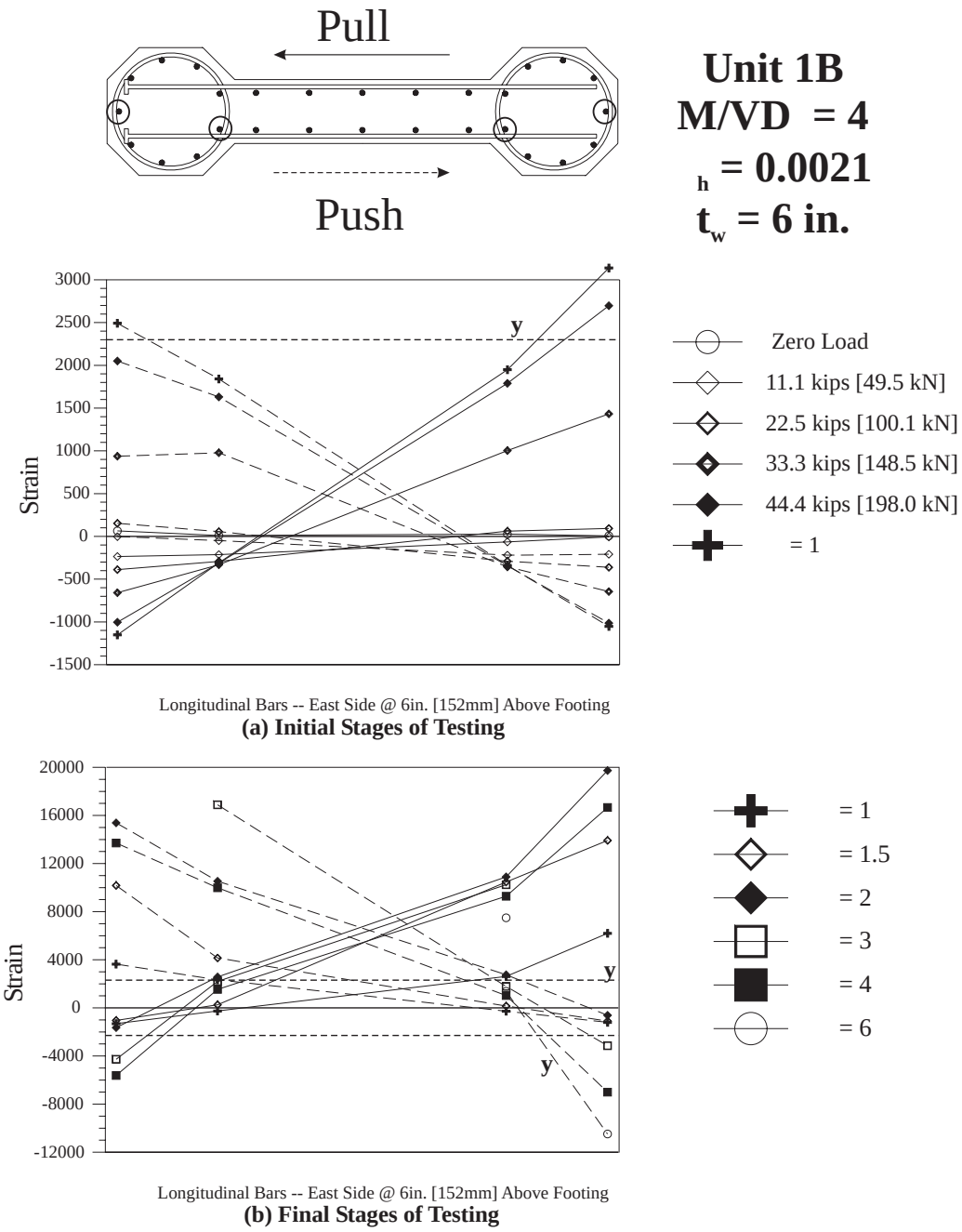

Figure C.6: Unit 1B: Longitudinal bar strain profiles at 6in. [152mm] above the footing.

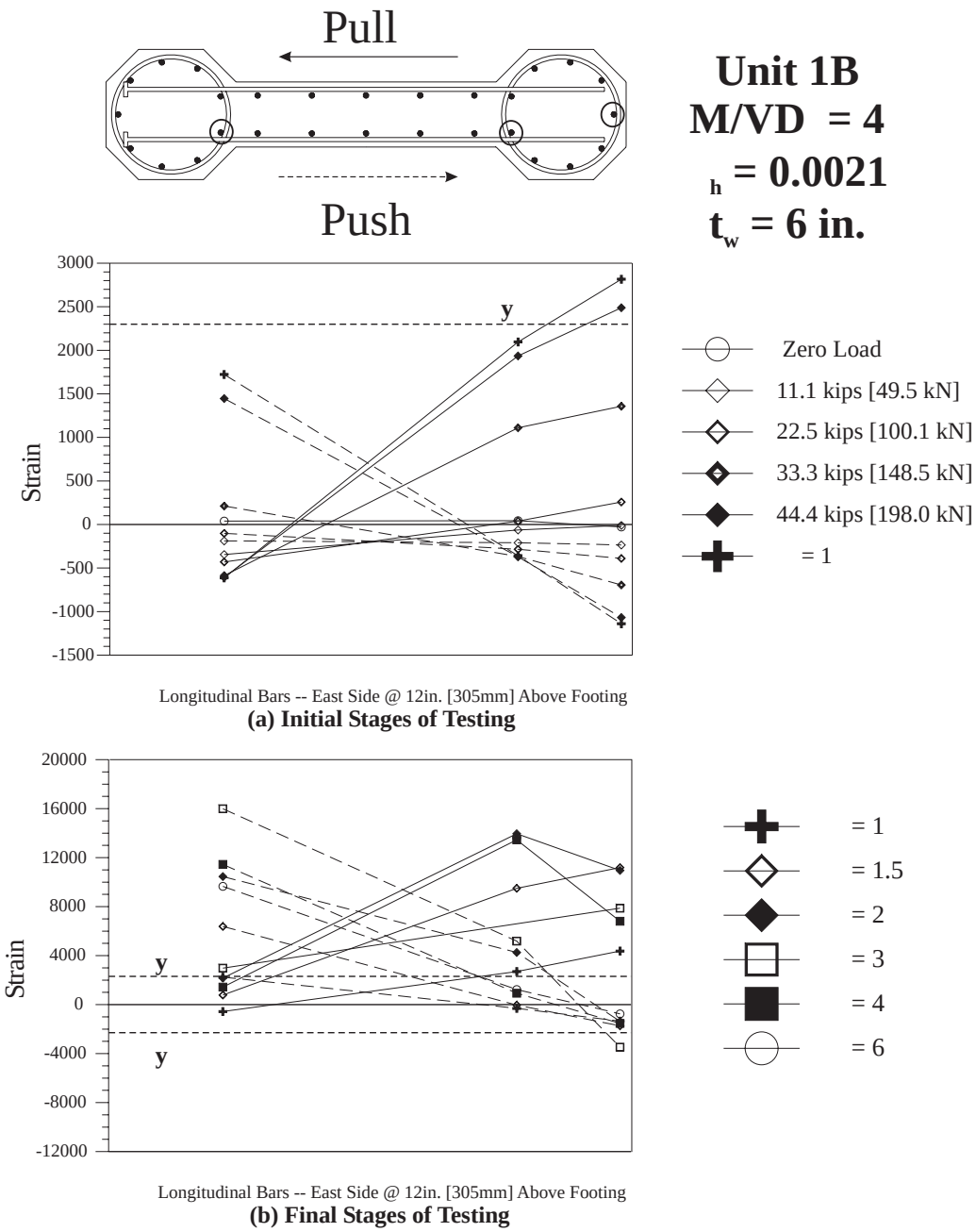

Figure C.7: Unit 1B: Longitudinal bar strain profiles at 12in. [305mm] above the footing.

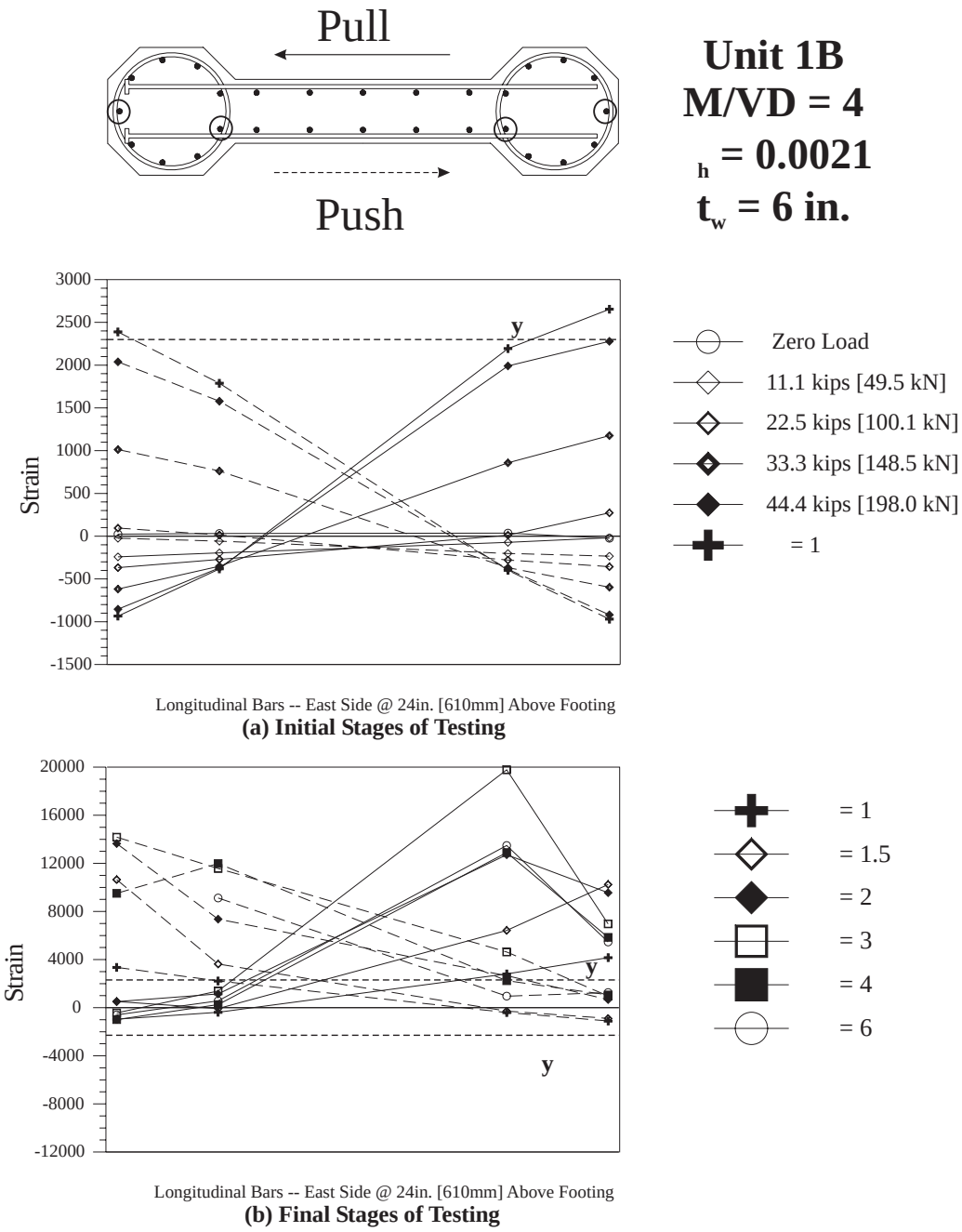

Figure C.8: Unit 1B: Longitudinal bar strain profiles at 24in. [610mm] above the footing.

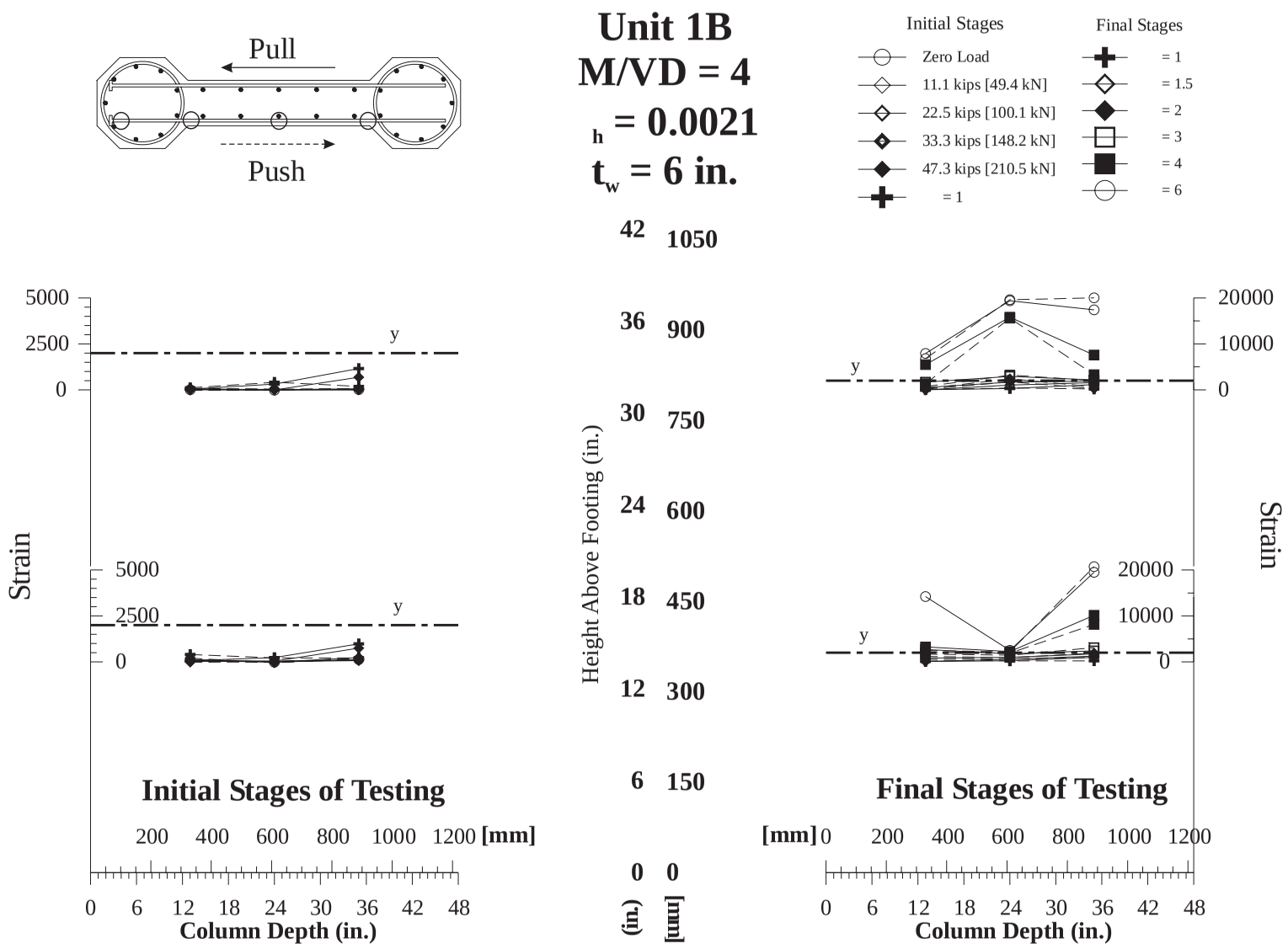

Figure C.9: Unit 1B: Strains on east transverse bars at initial and final testing stages.

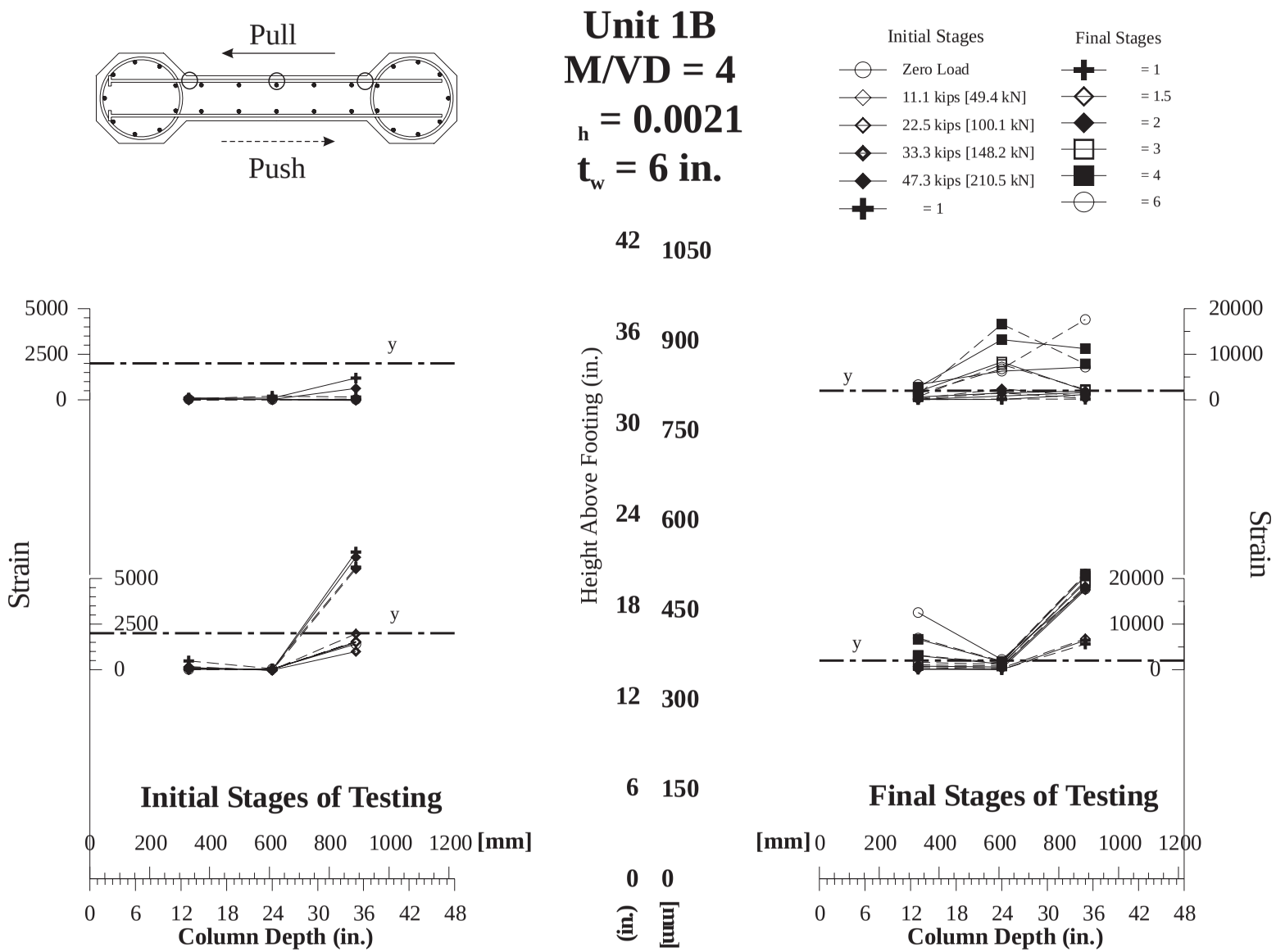

Figure C.10: Unit 1B: Strains on west transverse bars at initial and final testing stages.

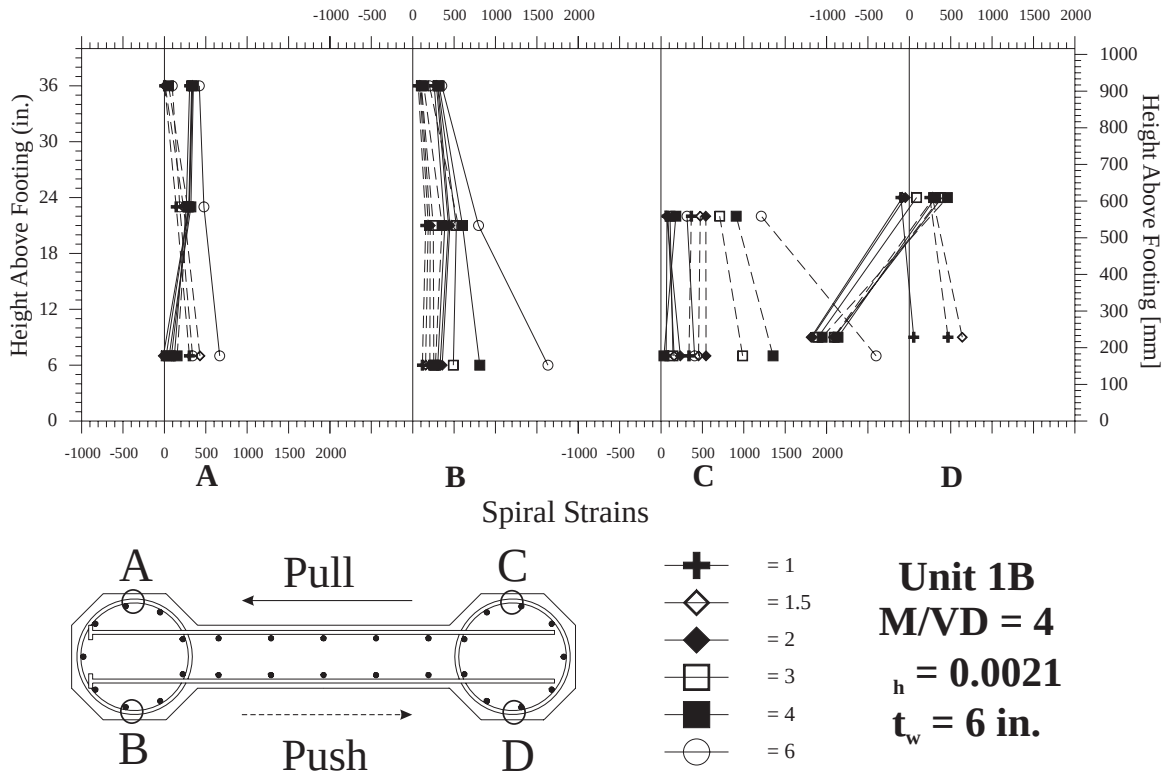

Figure C.11: Unit 1B: East and west spiral strains at final stages of loading.

Appendix D

Test Unit 2A Results

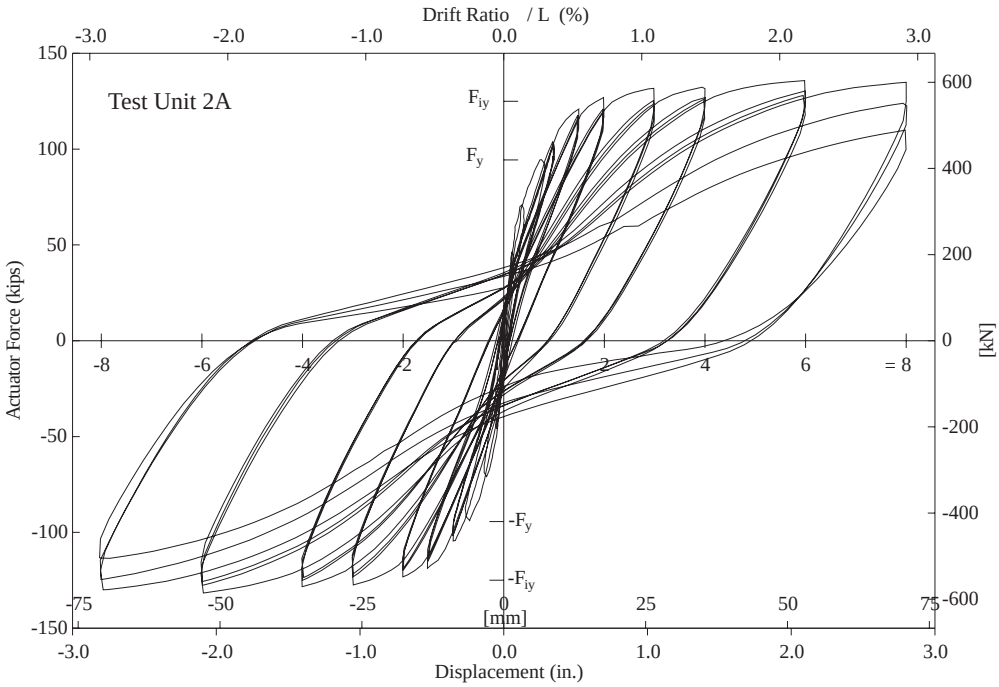

Figure D.1: Test Unit 2A hysteretic behavior.

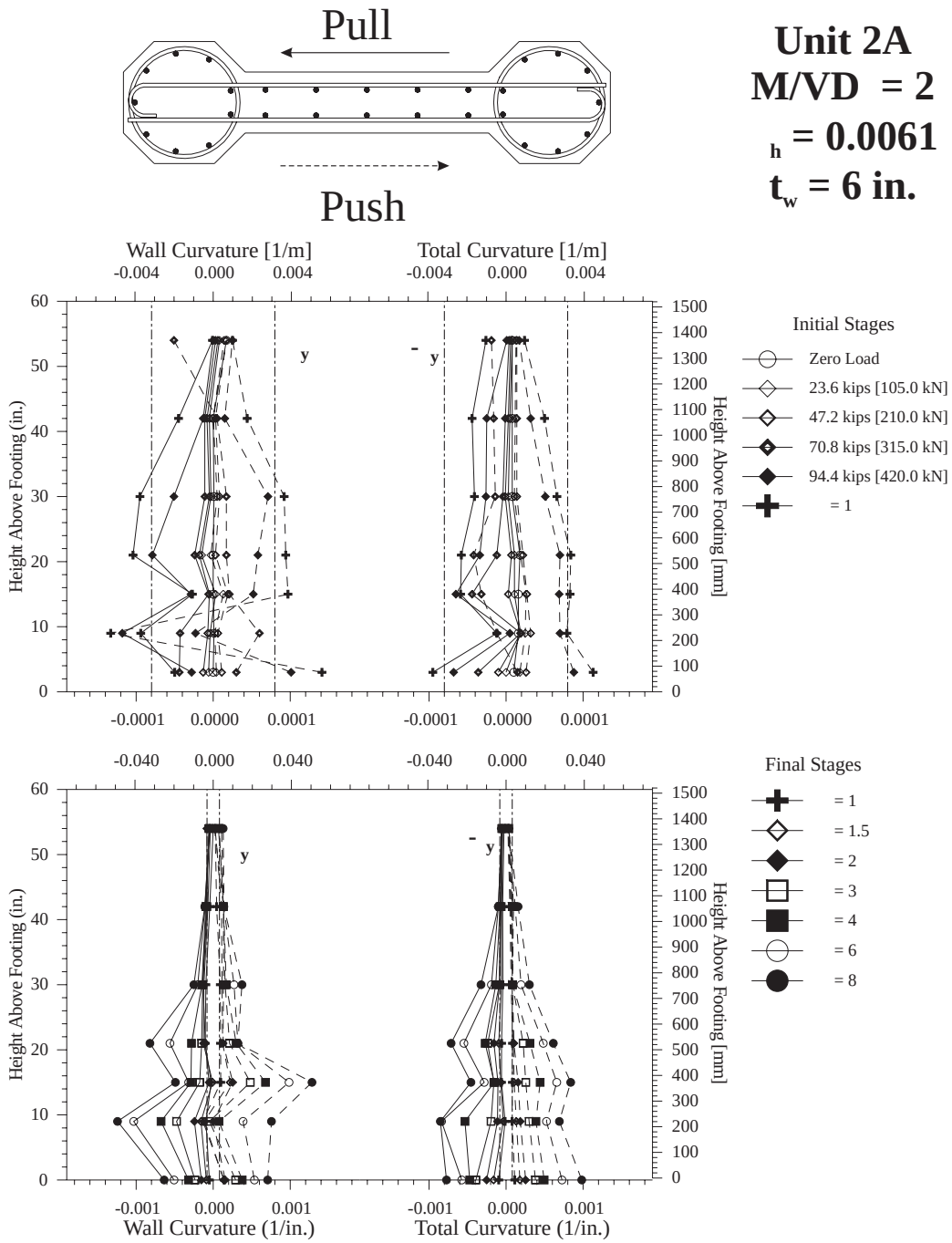

Figure D.2: Unit 2A: Curvature profiles for the wall (left) and for the total section (right).

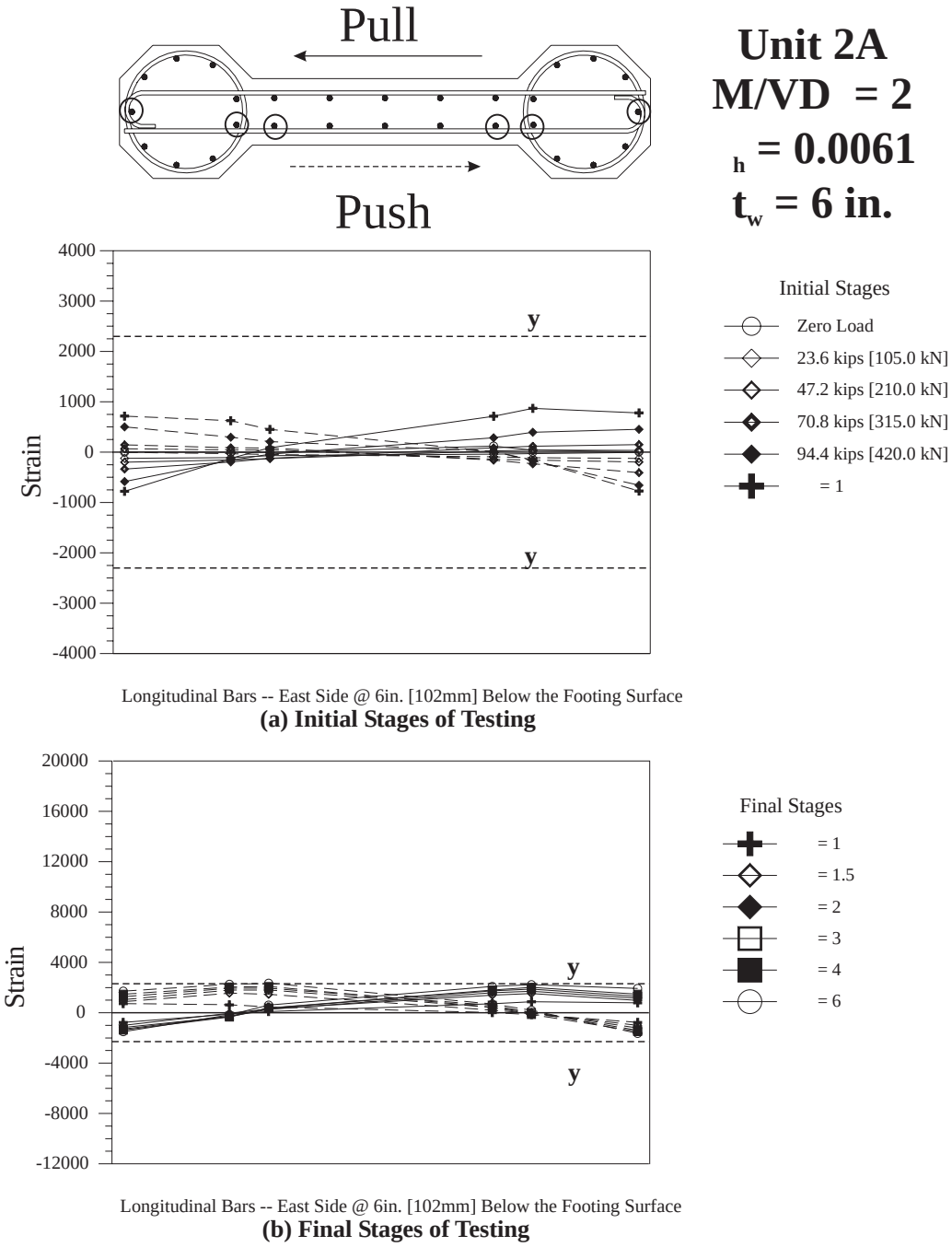

Figure D.3: Unit 2A: Longitudinal bar strain profiles at 6in. [152mm] below the footing surface.

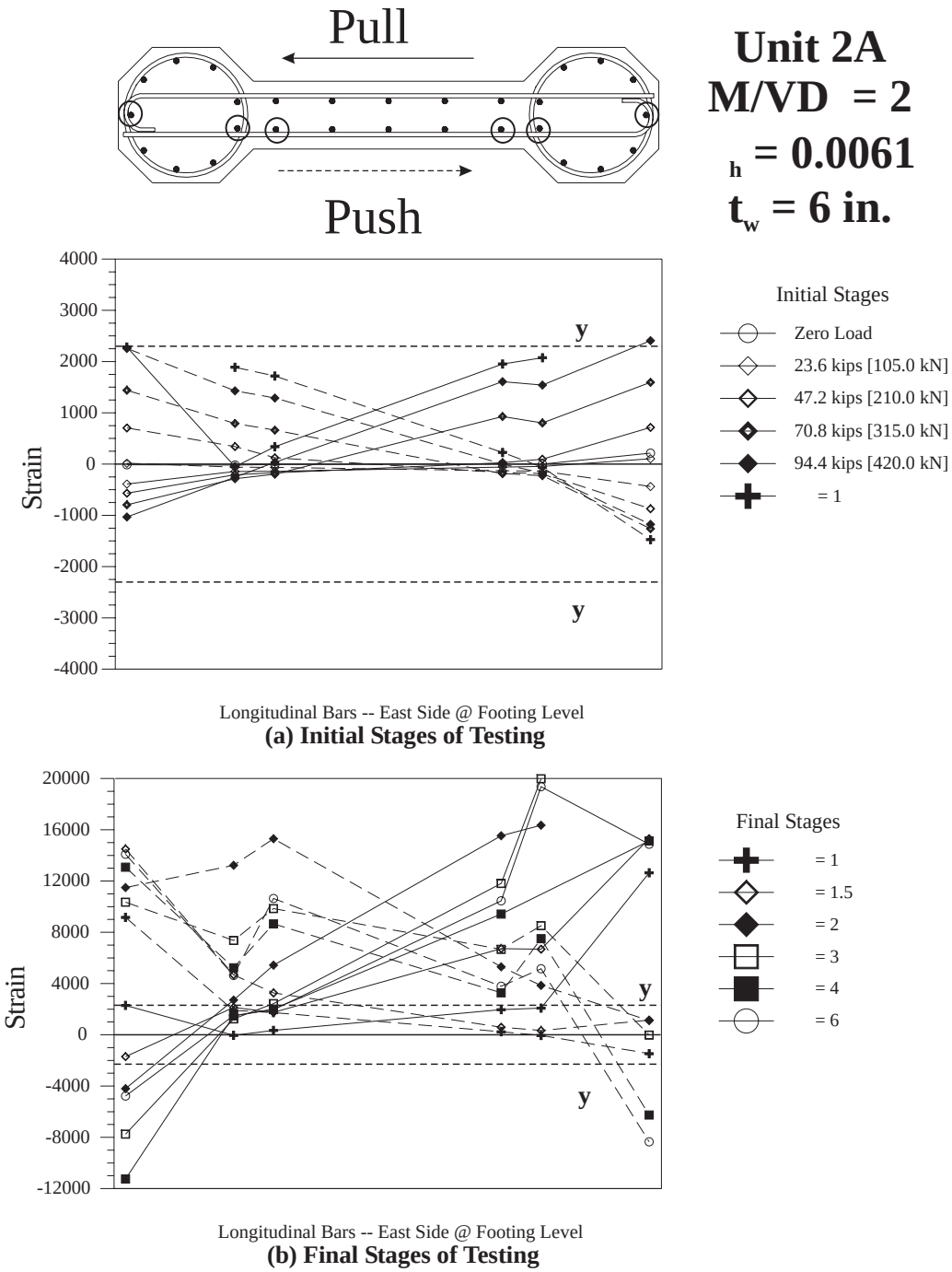

Figure D.4: Unit 2A: Longitudinal bar strain profiles at footing level.

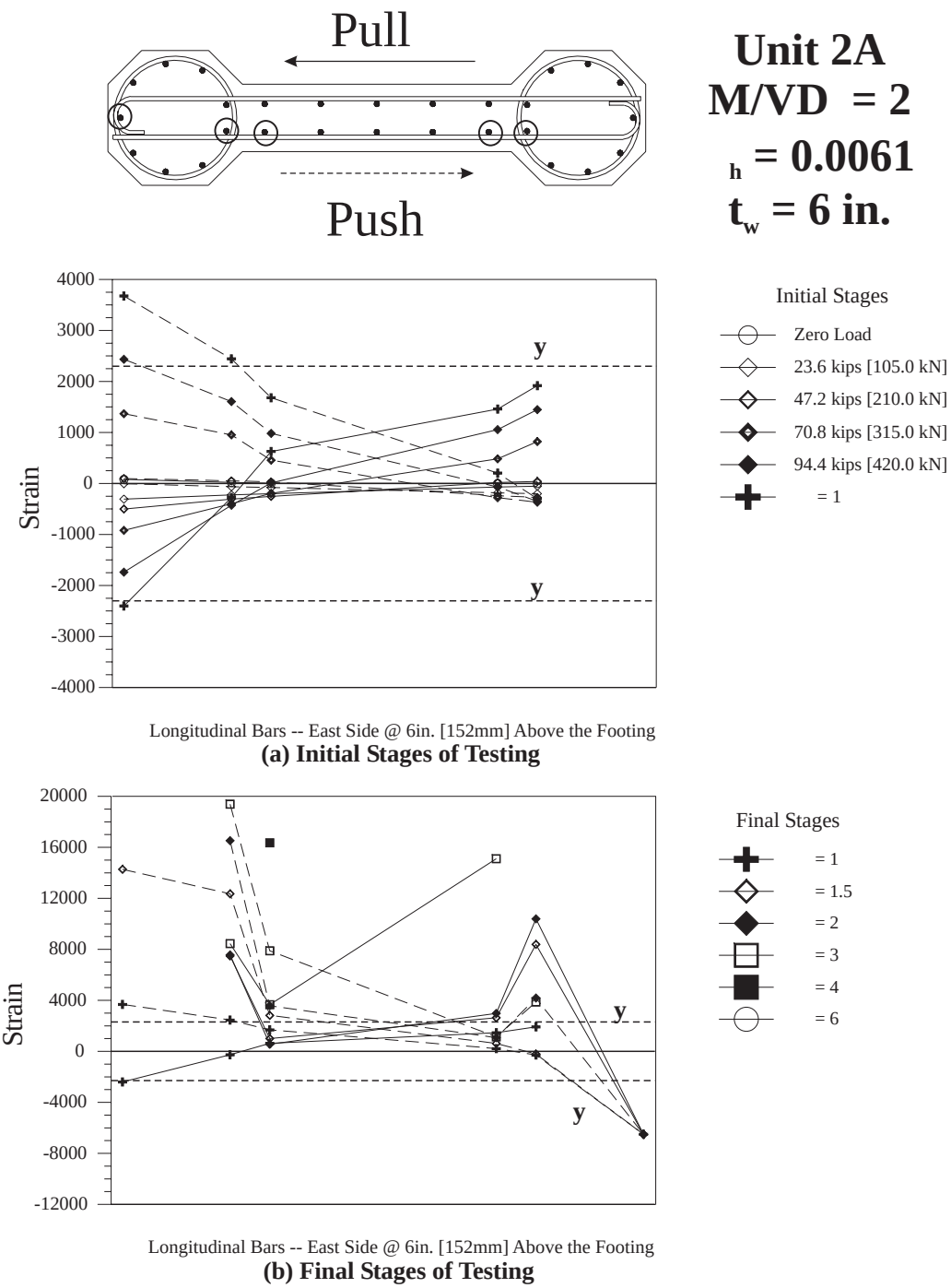

Figure D.5: Unit 2A: Longitudinal bar strain profiles at 6in. [152mm] above the footing.

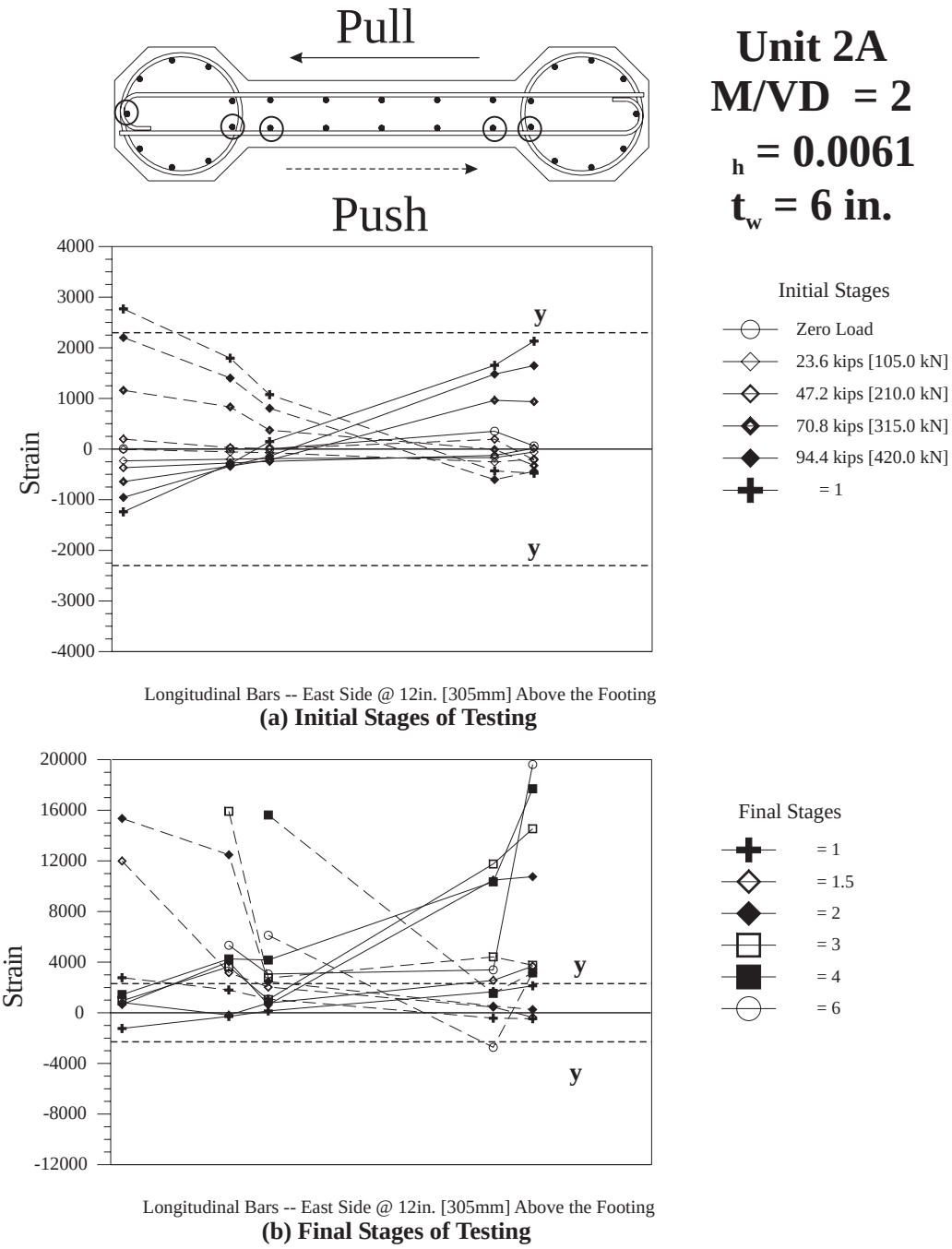

Figure D.6: Unit 2A: Longitudinal bar strain profiles at 12in. [305mm] above the footing.

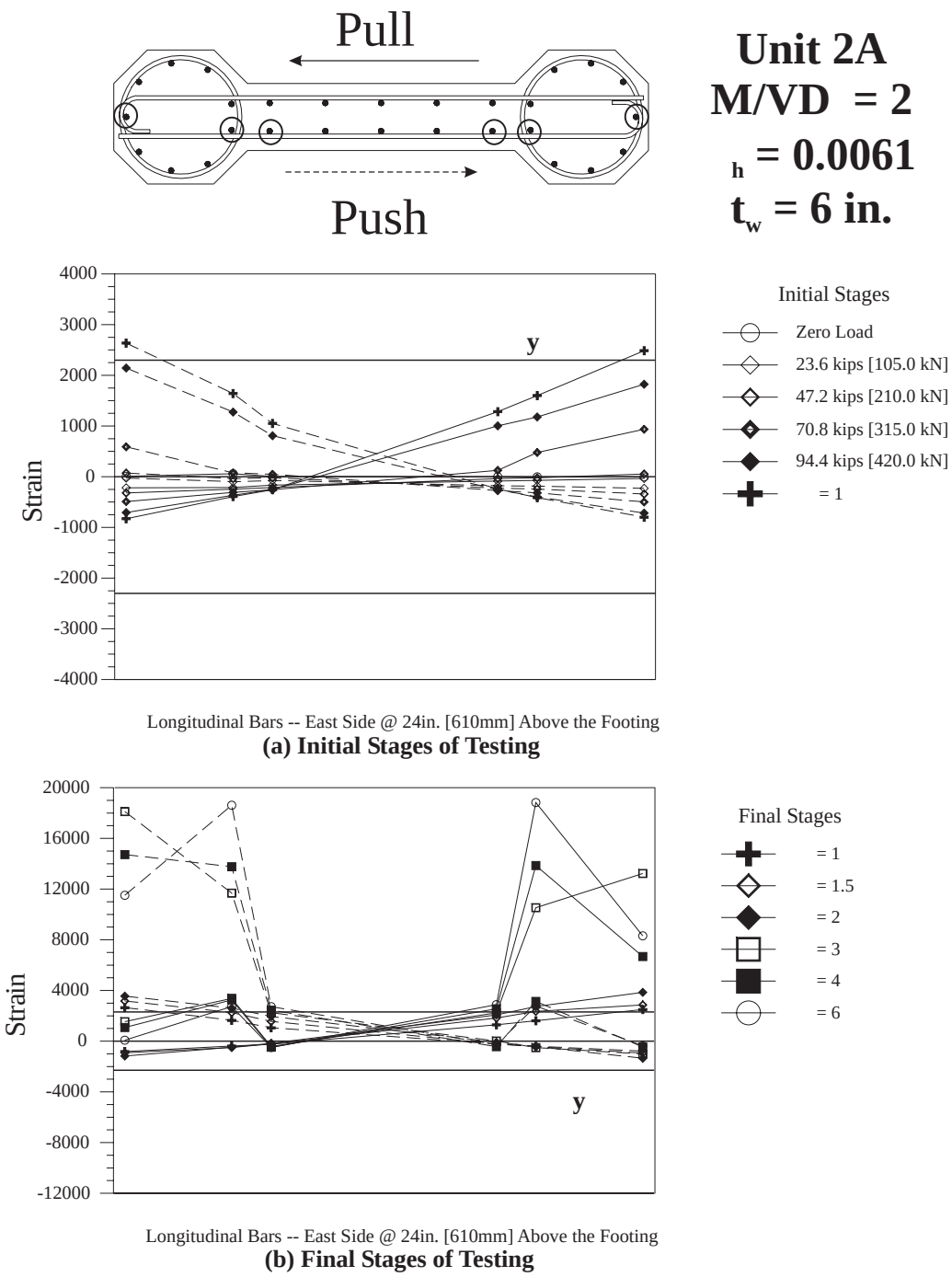

Figure D.7: Unit 2A: Longitudinal bar strain profiles at 24in. [610mm] above the footing.

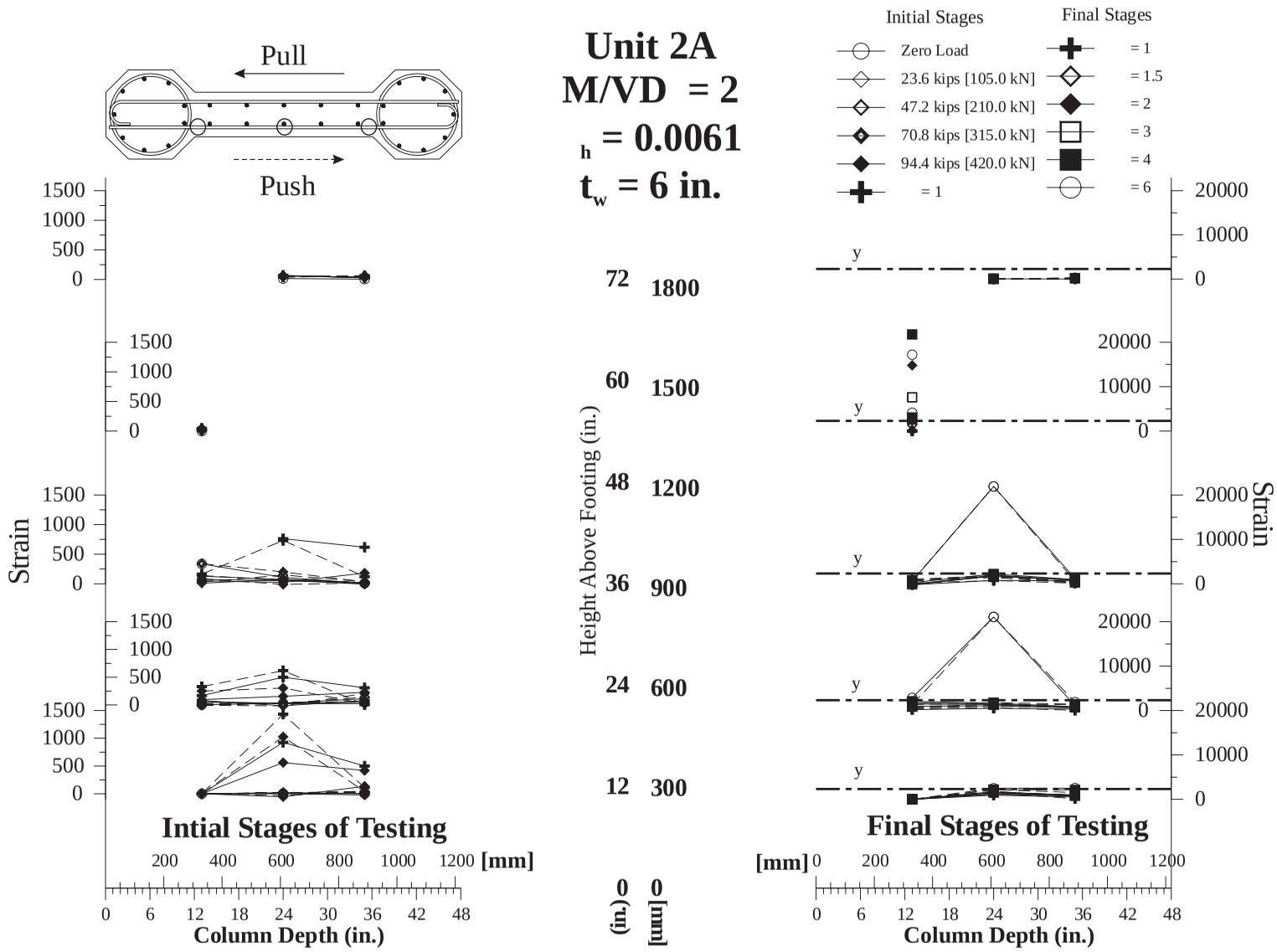

Figure D.8: Unit 2A: Strains on east transverse bars at initial and final testing stages.

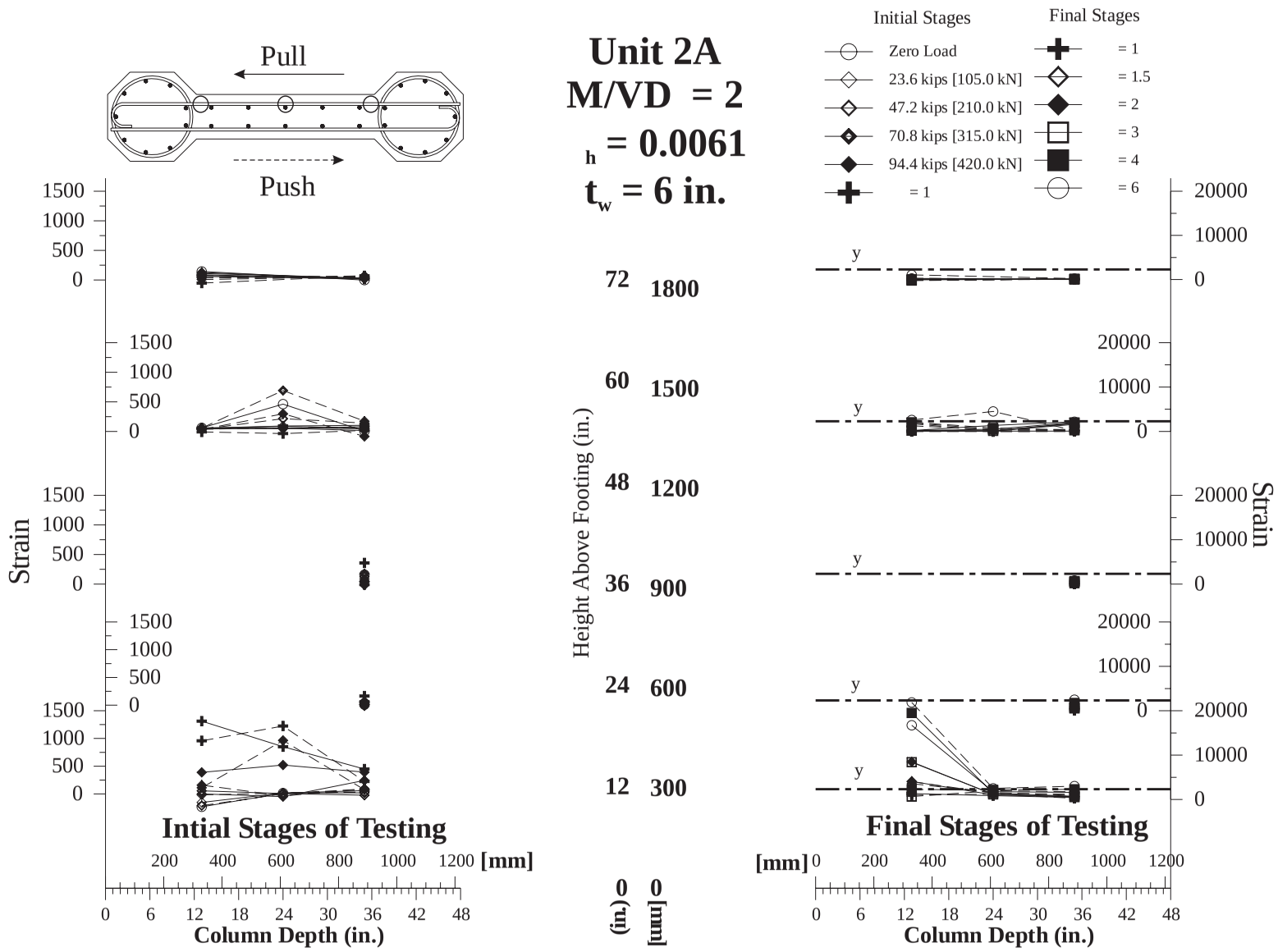

Figure D.9: Unit 2A: Strains on west transverse bars at initial and final testing stages.

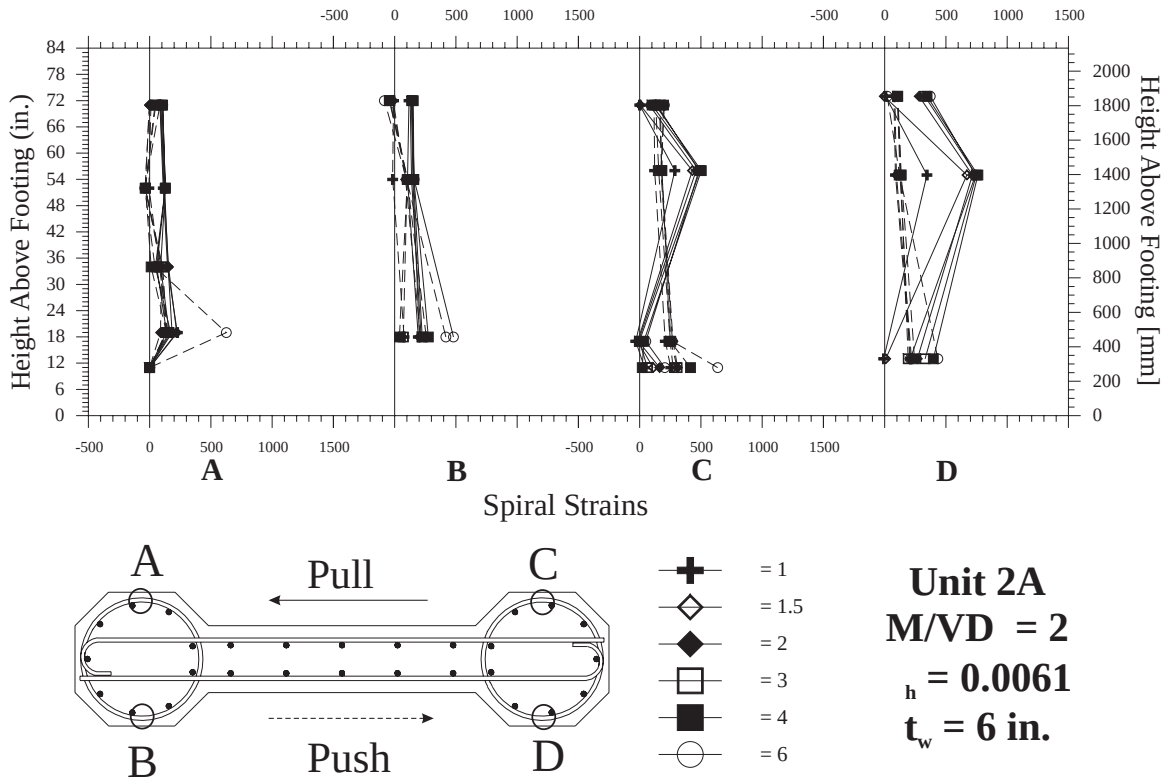

Figure D.10: Unit 2A: East and west spiral strains at final stages of loading.

Appendix E

Test Unit 2B Results

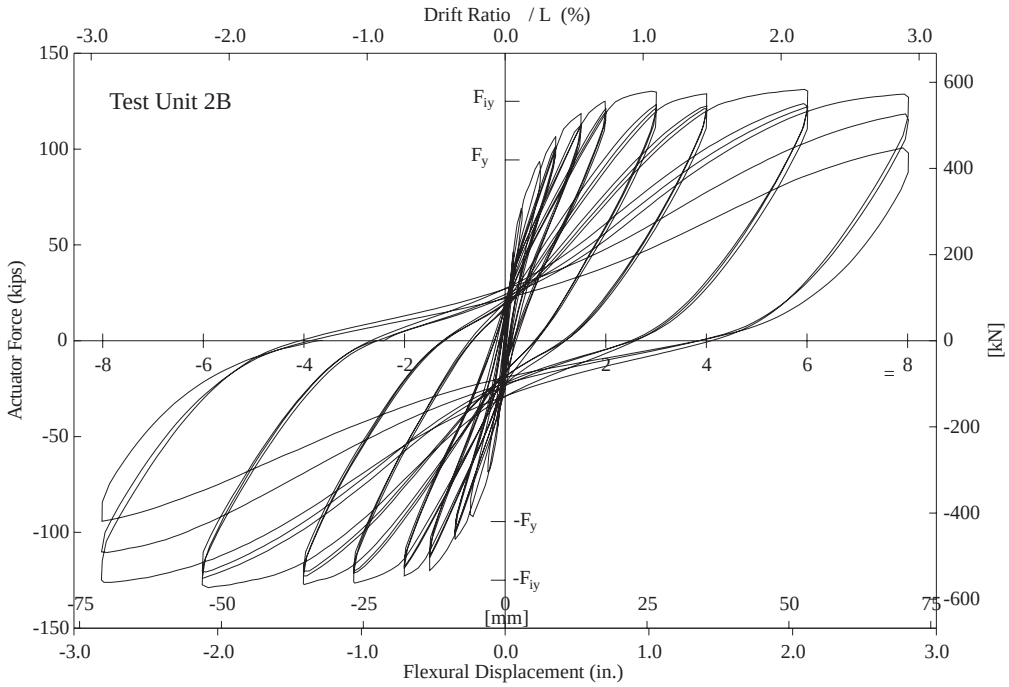

Figure E.1: Test Unit 2B hysteretic behavior.

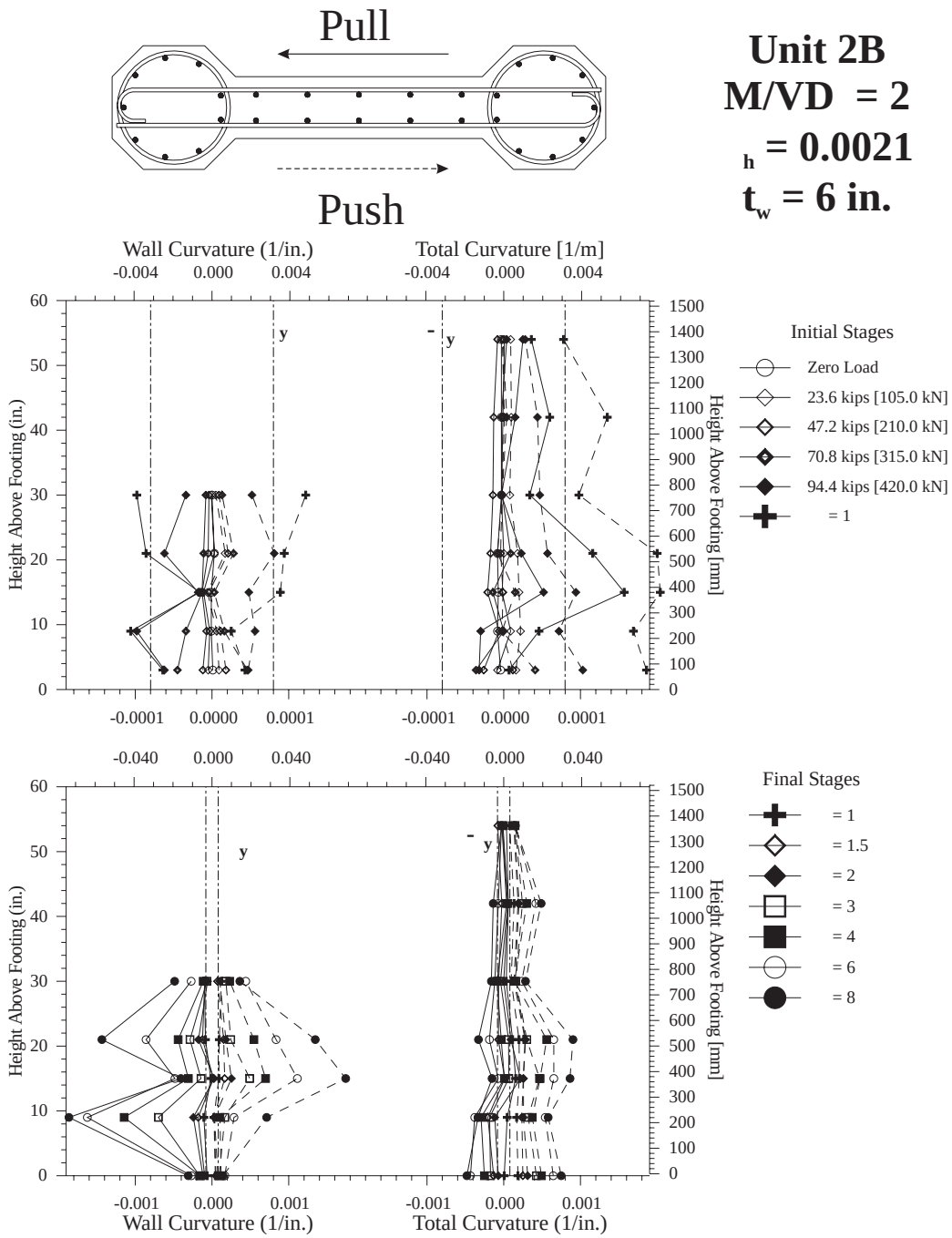

Figure E.2: Unit 2B: Curvature profiles for the wall (left) and for the total section (right).

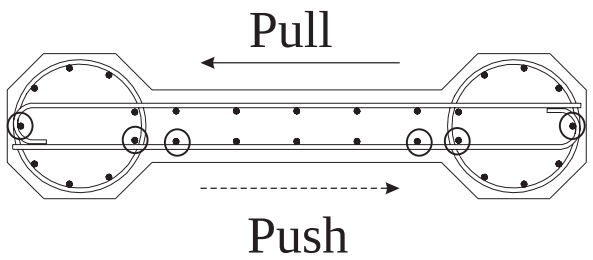

Unit 2B
M/VD = 2
$_h$ = 0.0021
t_w = 6 in.

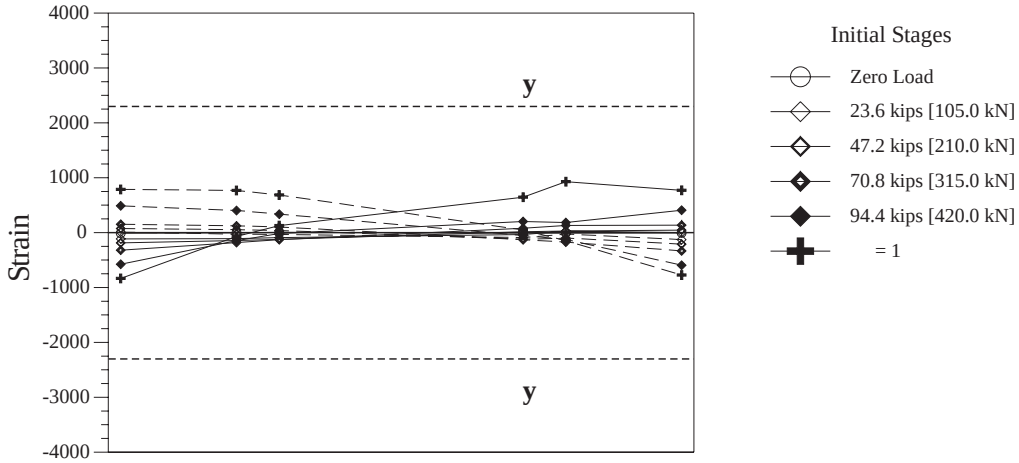

(a) Initial Stages of Testing

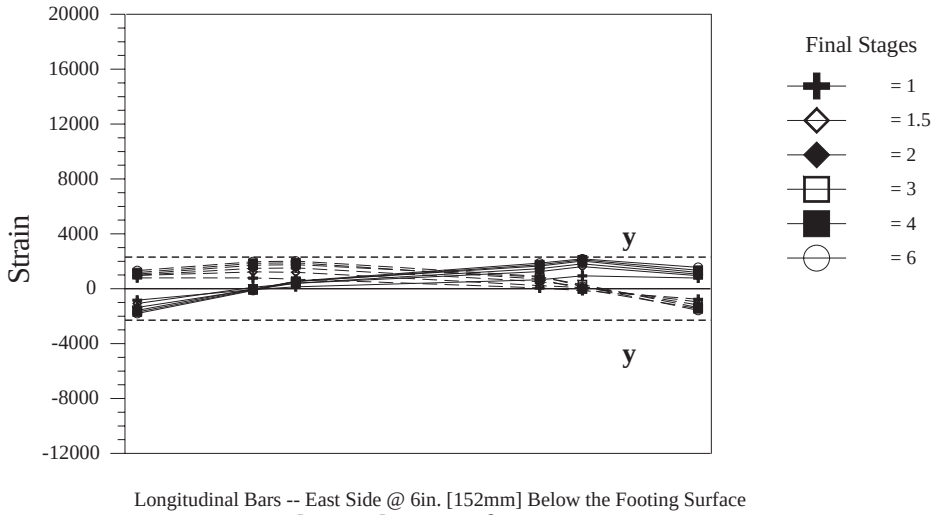

(b) Final Stages of Testing

Figure E.3: Unit 2B: Longitudinal bar strain profiles at 6in. [152mm] below the footing surface.

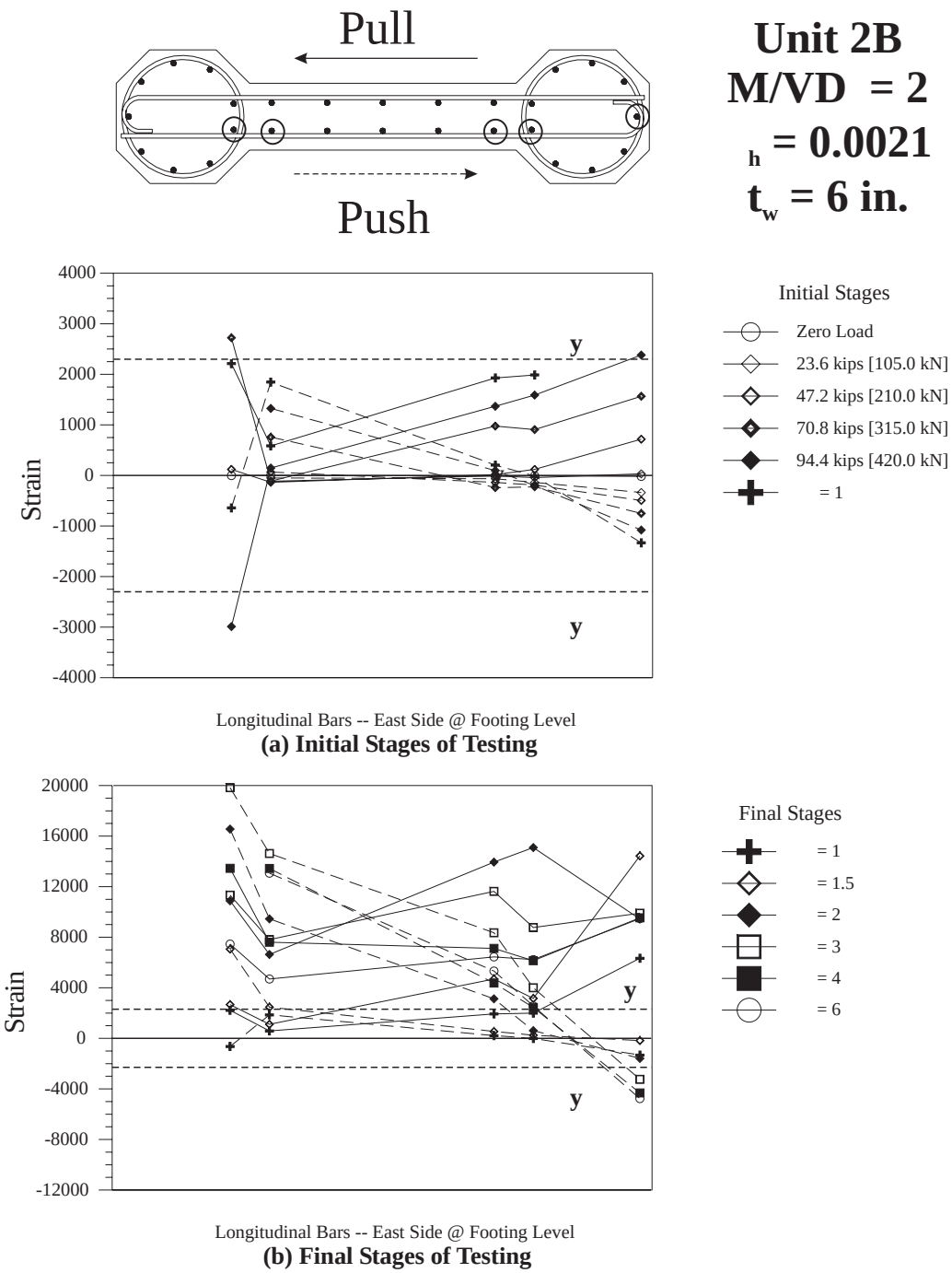

Figure E.4: Unit 2B: Longitudinal bar strain profiles at footing level.

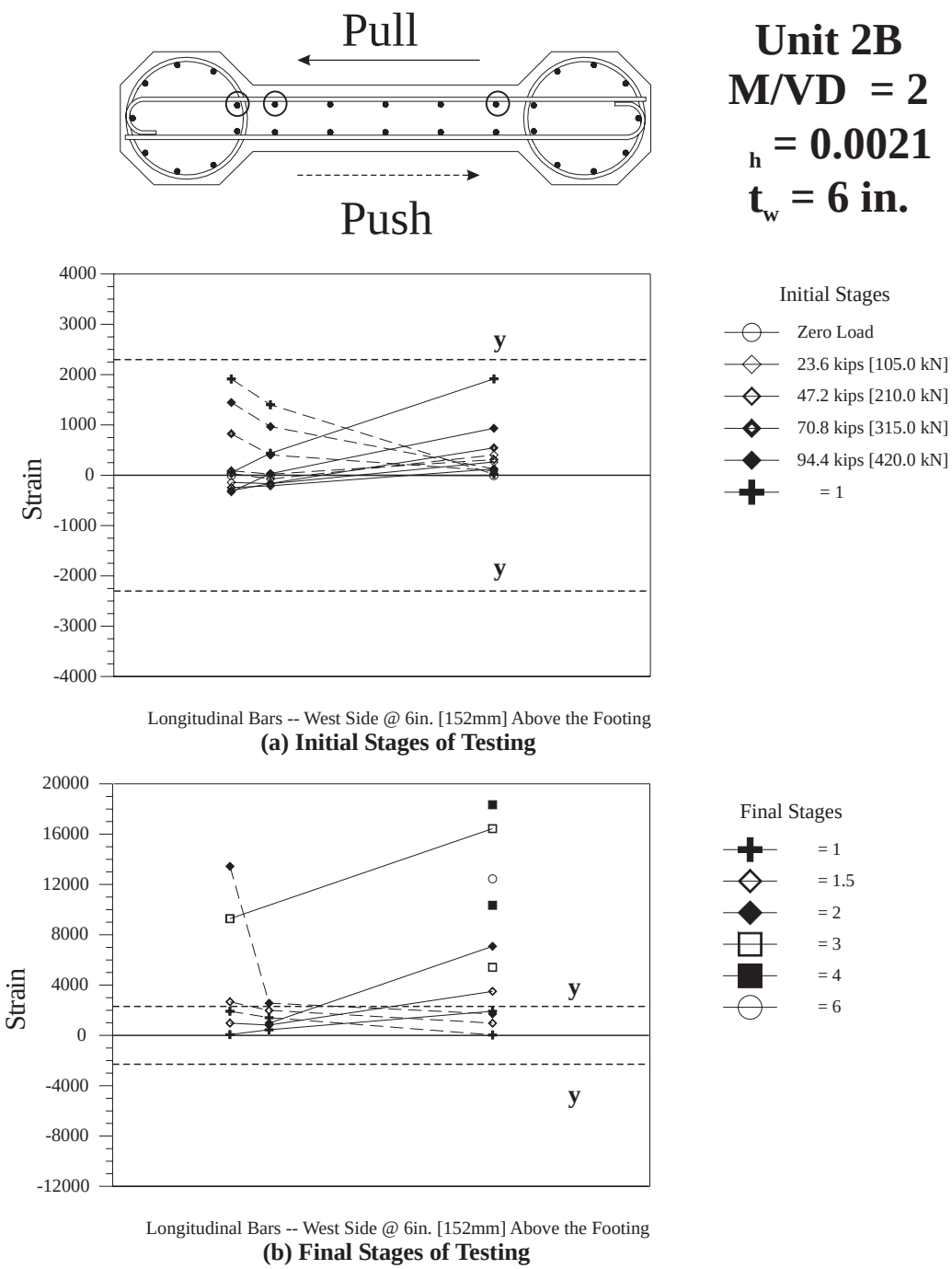

Figure E.5: Unit 2B: Longitudinal bar strain profiles at 6in. [152mm] above the footing.

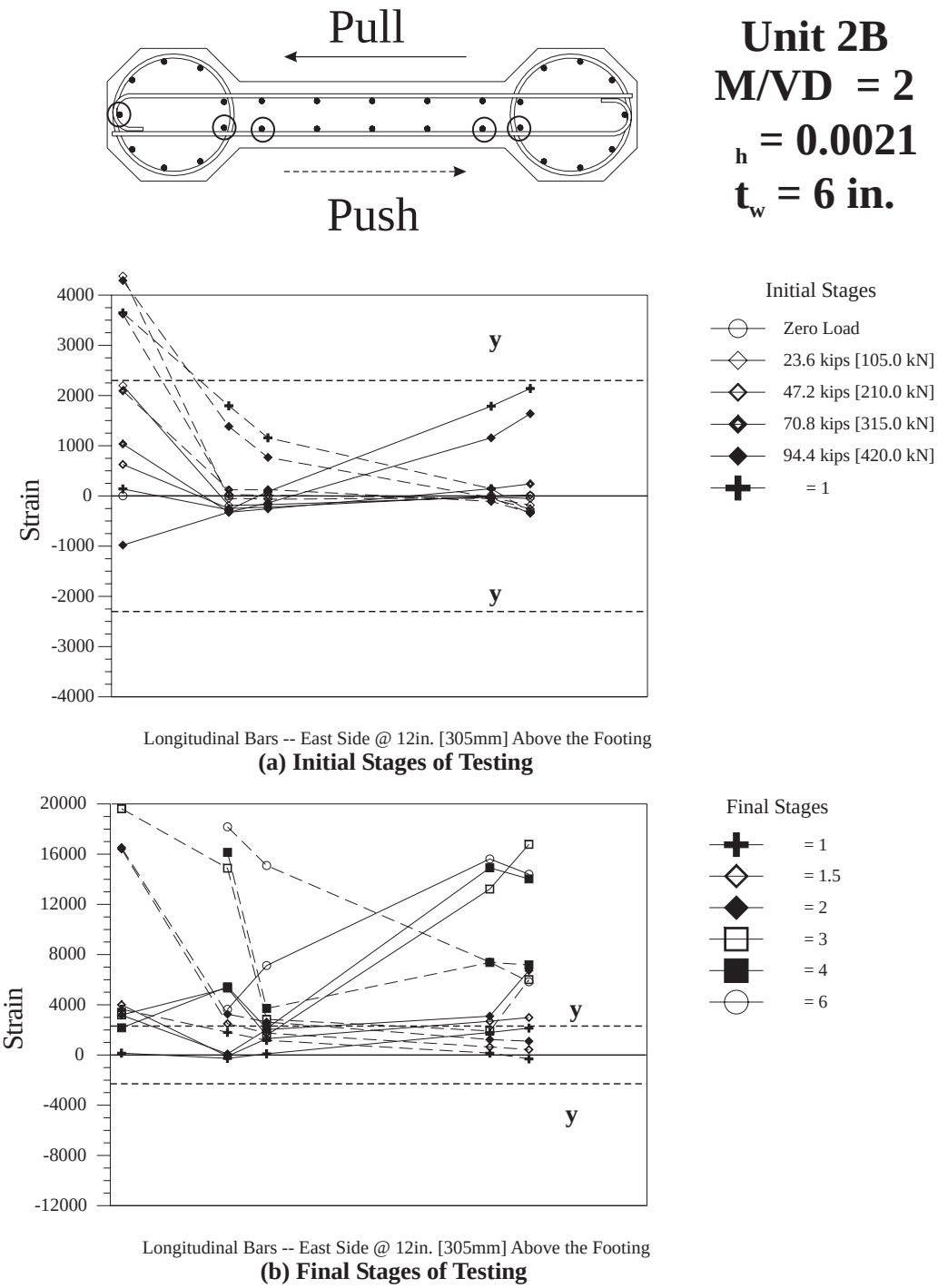

Figure E.6: Unit 2B: Longitudinal bar strain profiles at 12in. [305mm] above the footing.

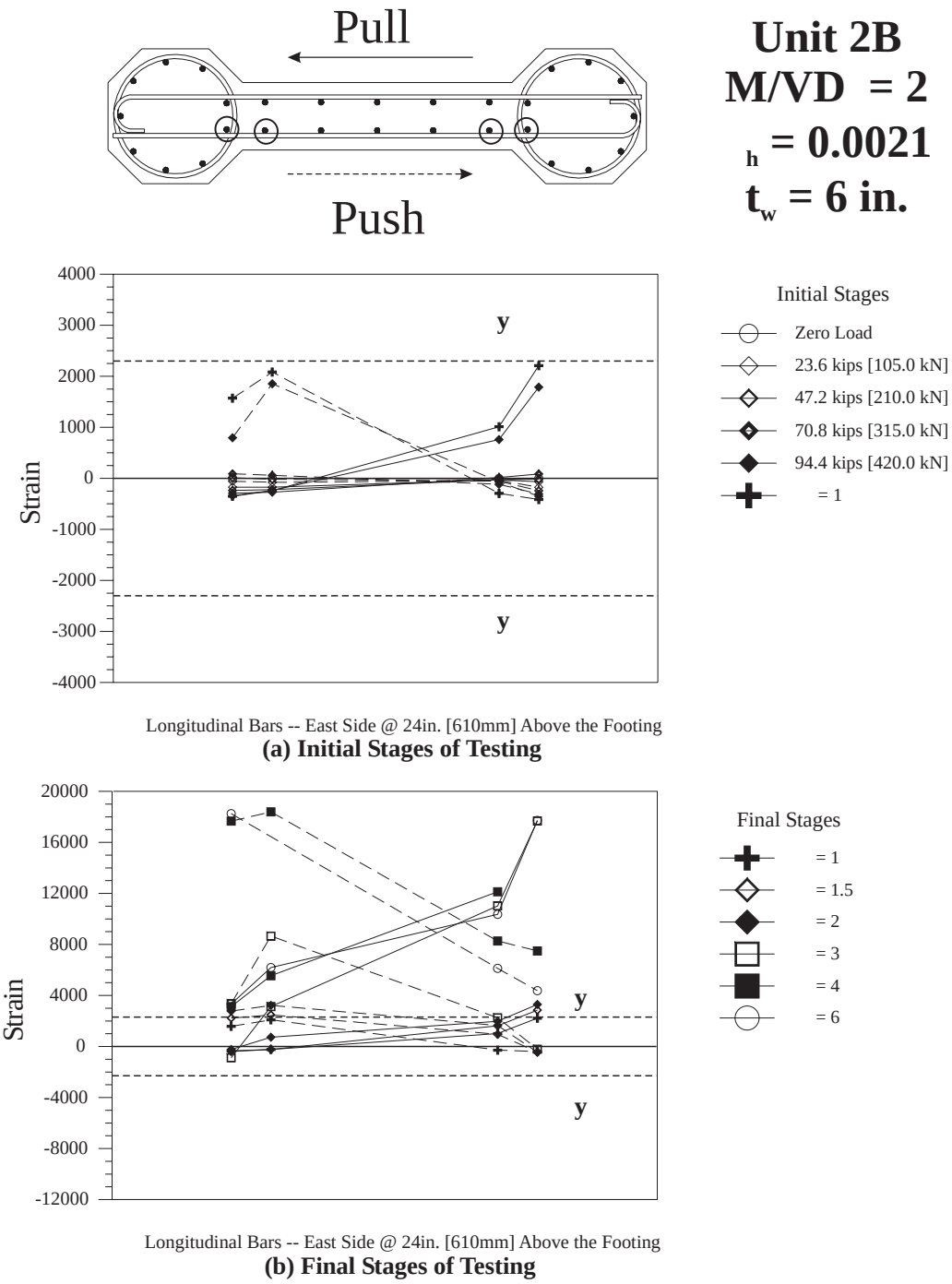

Figure E.7: Unit 2B: Longitudinal bar strain profiles at 24in. [610mm] above the footing.

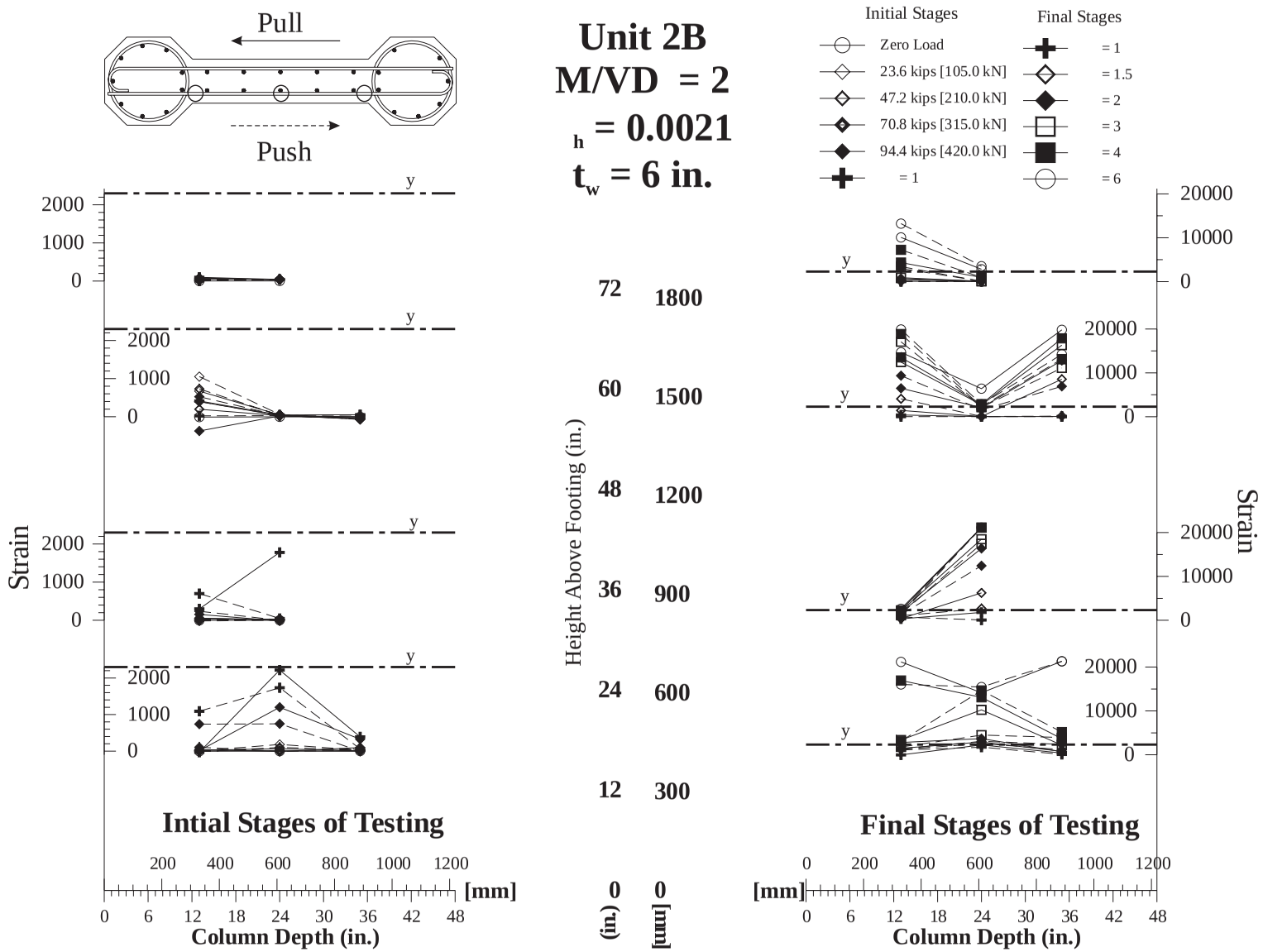

Figure E.8: Unit 2B: Strains on east transverse bars at initial and final testing stages.

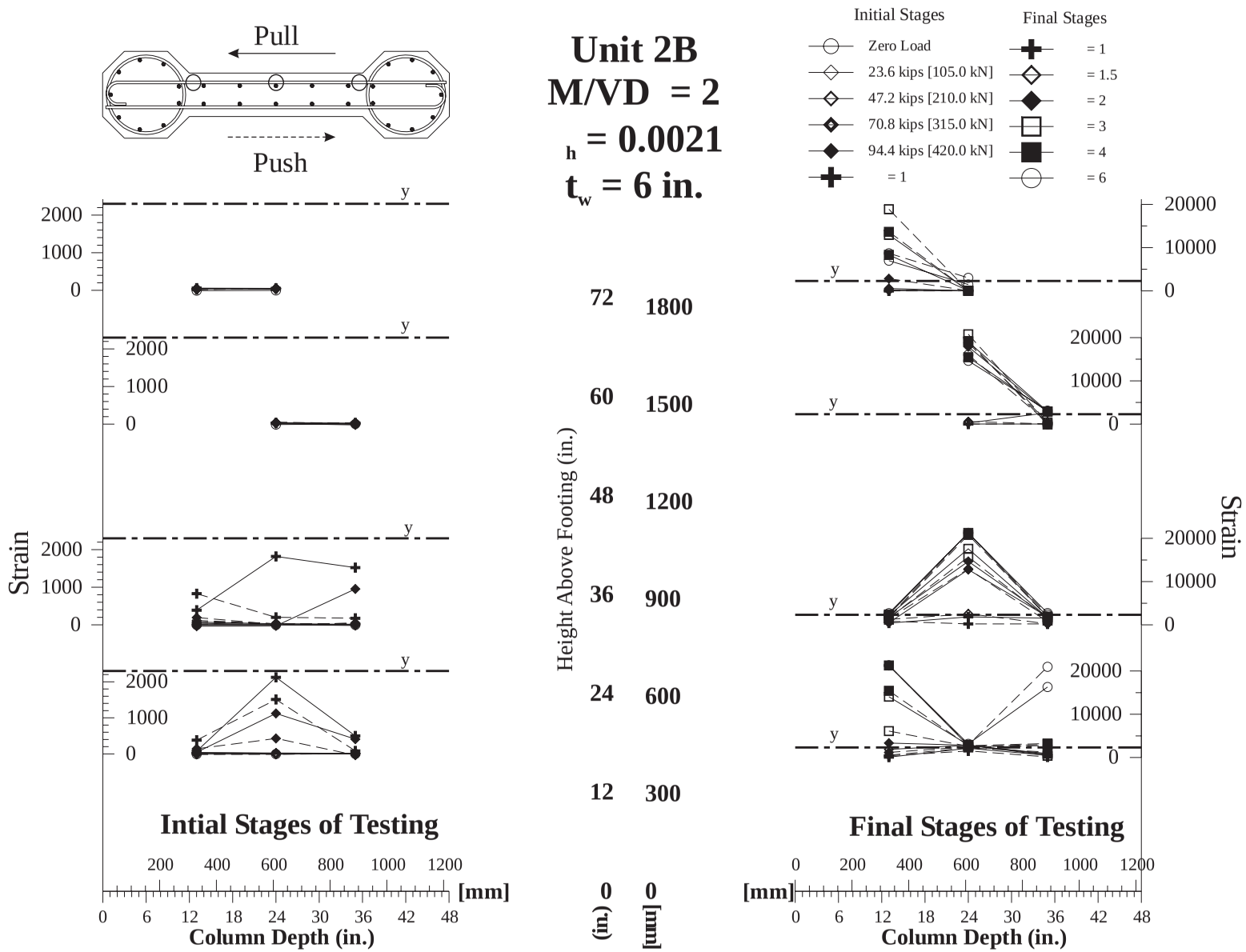

Figure E.9: Unit 2B: Strains on west transverse bars at initial and final testing stages.

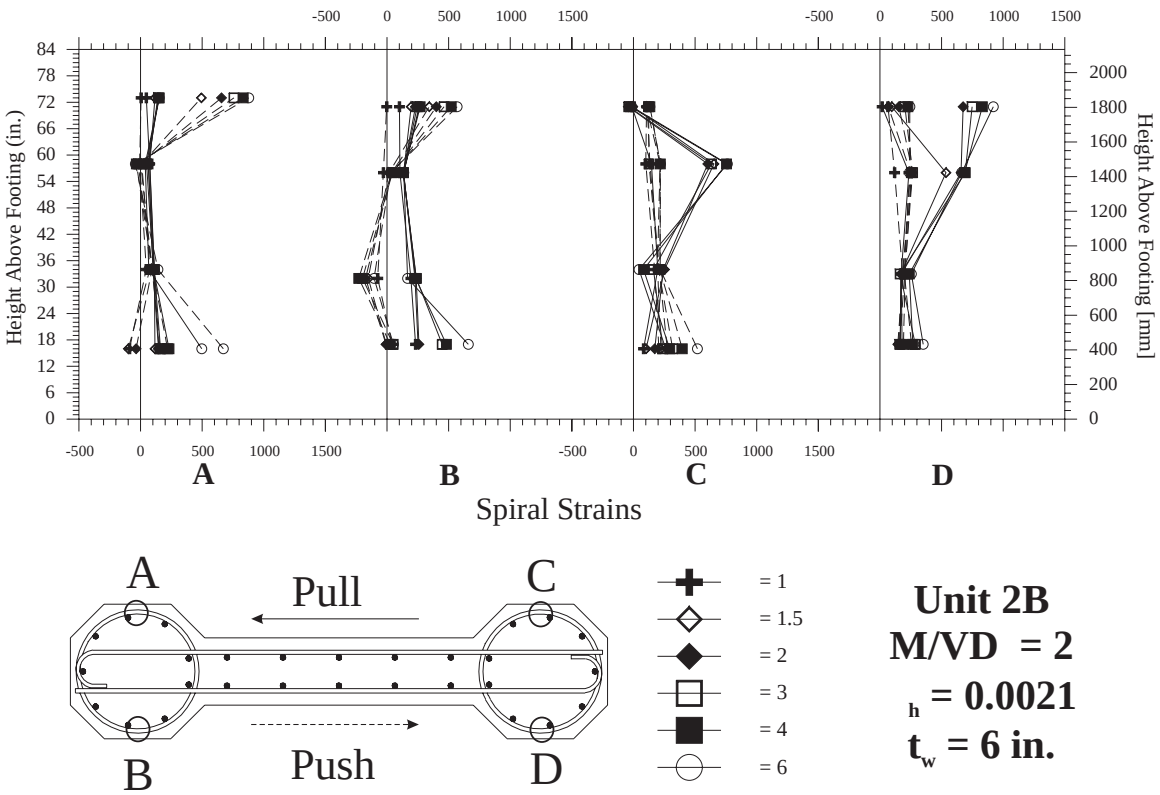

Figure E.10: Unit 2B: East and west spiral strains at final stages of loading.

Appendix F

Test Unit 2C Results

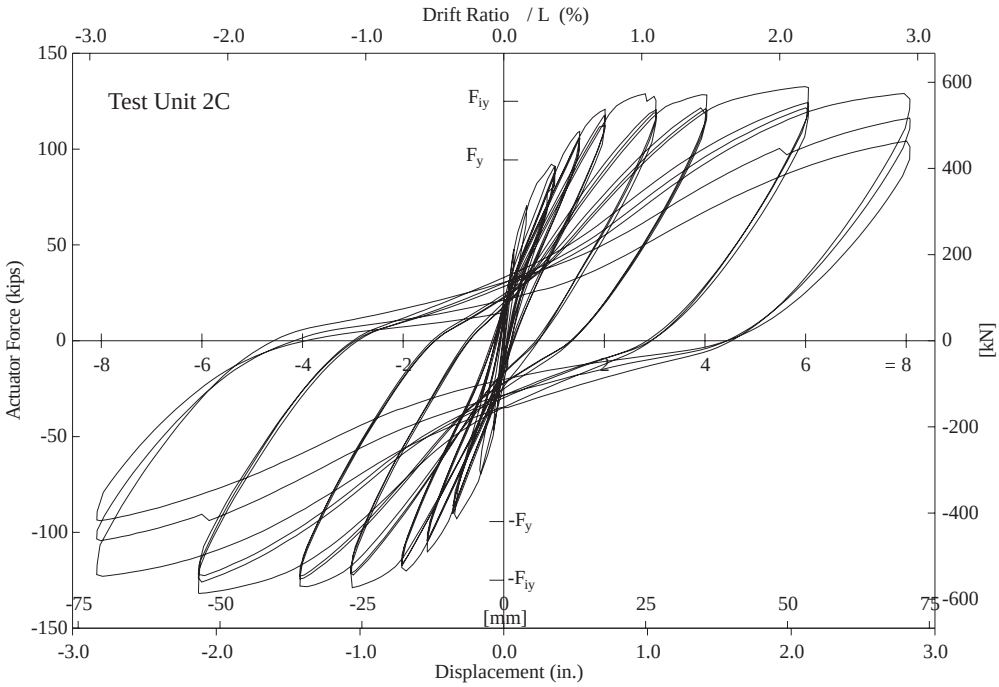

Figure F.1: Test Unit 2C hysteretic behavior.

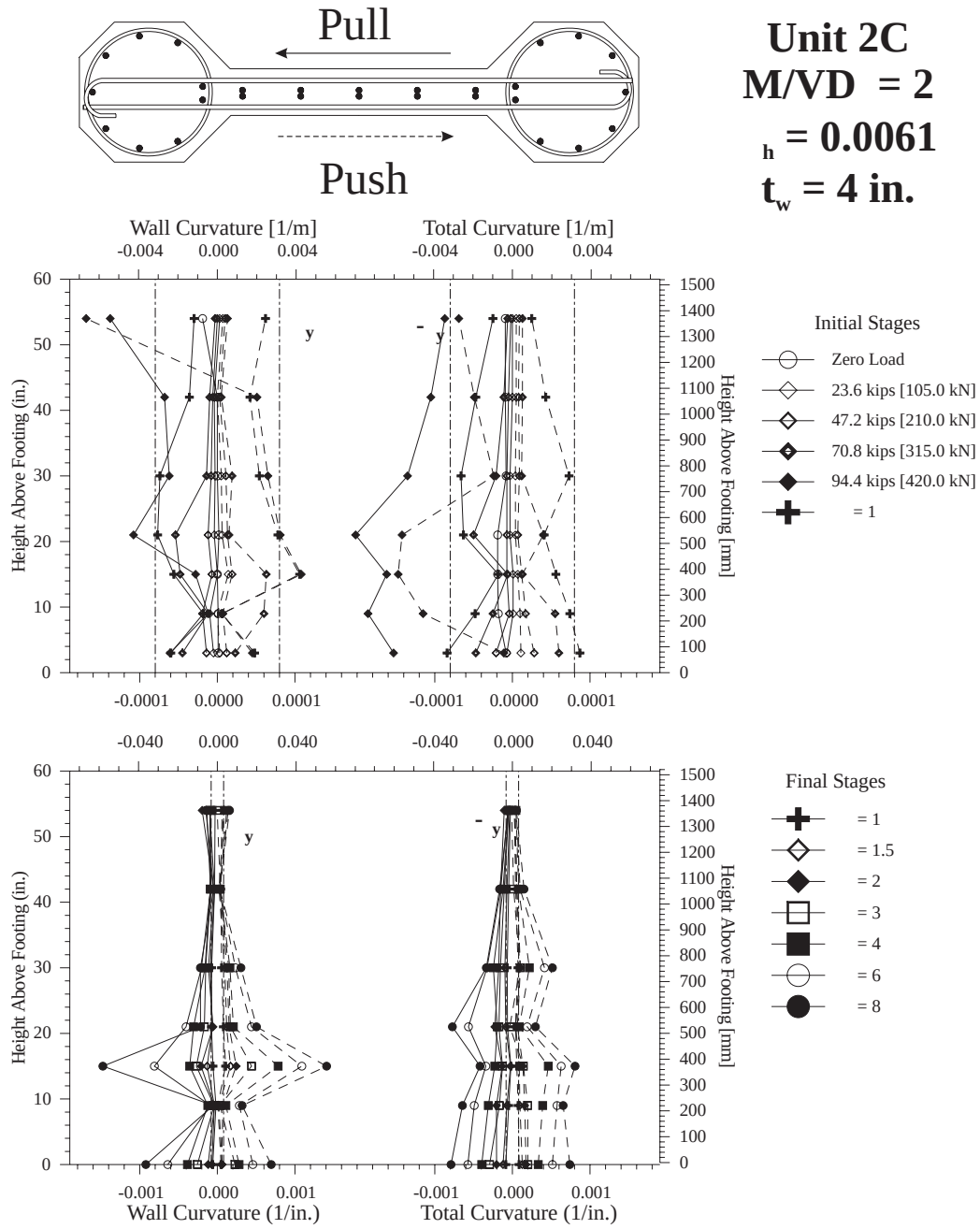

Figure F.2: Unit 2C: Curvature profiles for the wall (left) and for the total section (right).

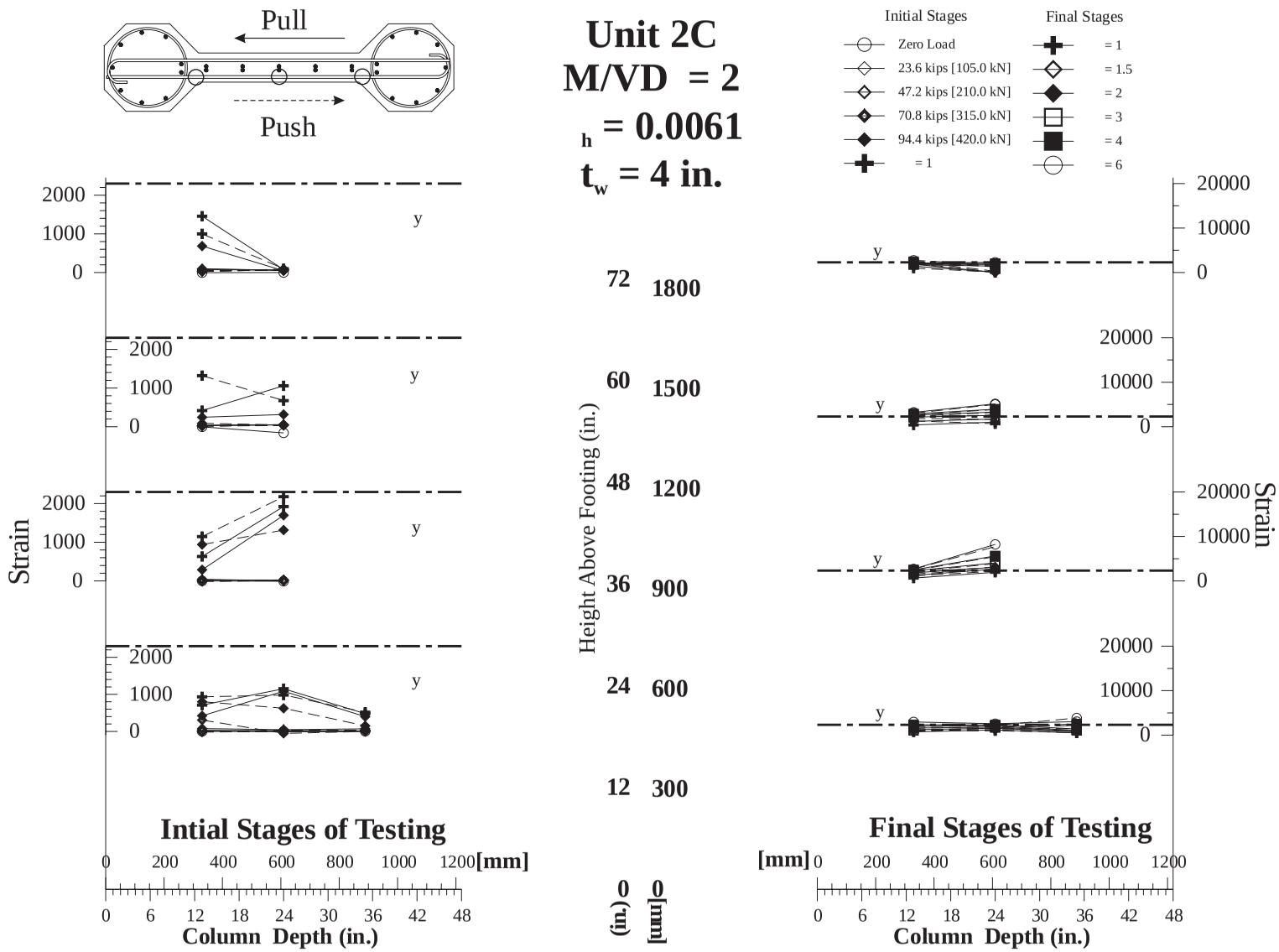

Figure F.3: Unit 2C: Strains on east transverse bars at initial and final testing stages.

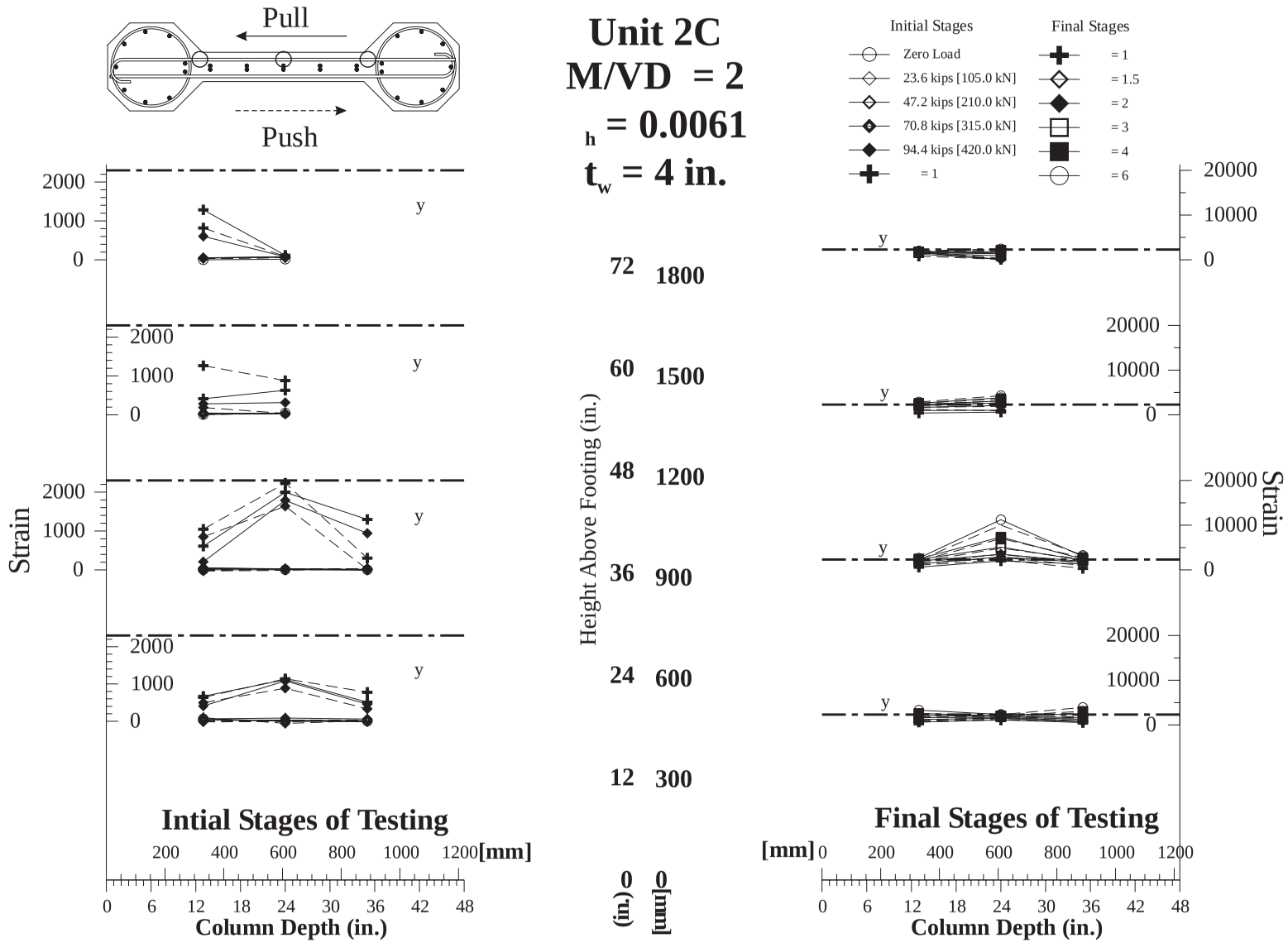

Figure F.4: Unit 2C: Strains on west transverse bars at initial and final testing stages.

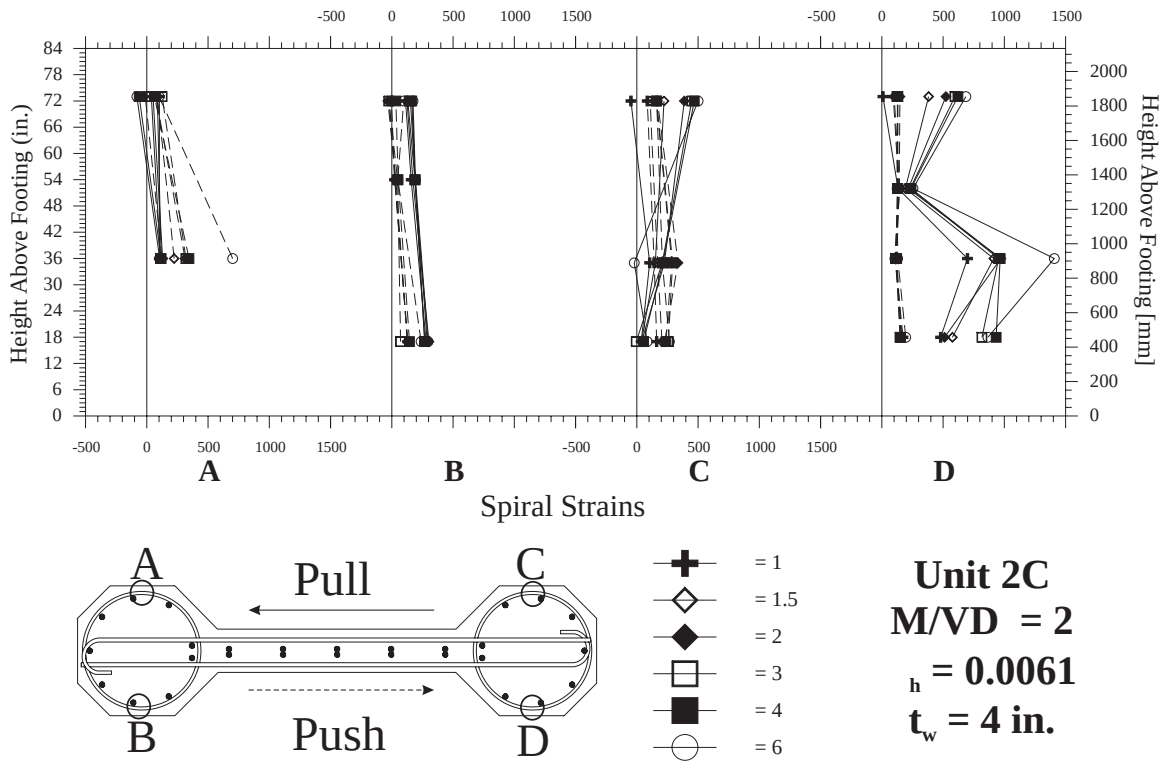

Figure F.5: Unit 2C: East and west spiral strains at final stages of loading.

References

[1] ACI. *Building Code Requirements for Reinforced Concrete.* American Concrete Institute, Detroit, MI, 1995.

[2] Caltrans. *Bridge Design Specifications.* California Department of Transportation, Sacramento, CA, 1993.

[3] M.P. Collins. "Towards a rational theory for RC members in shear". *ASCE Journal of the Structural Division*, 104(ST4):649–666, April 1978.

[4] M.J. Kowalsky and M.J.N. Priestley. "An improved analytical model for shear strength of circular RC columns in seismic regions". ACI Journal, 97(3):388–396, May-June 2000.

[5] J.B. Mander, M.J.N. Priestley, and R. Park. Theoretical stress-strain model for confined concrete. *ASCE Journal of Structural Engineering*, 114(8):1804–1826, August 1988.

[6] R.G. Oesterle, J.D. Ariztizabal-Ochoa, A.E. Fiorato, H.G. Russell, and W.G. Corley. Earthquake resistant structural walls–tests of isolated walls–Phase II. NSF Report ENV77-15333, Portland Cement Association, Skokie, IL, October 1979.

[7] R.G. Oesterle, A.E. Fiorato, and W.G. Corley. Web crushing of reinforced concrete structural walls. *ACI Journal*, 81(3):231–241, May-June 1984.

[8] R.G. Oesterle, A.E. Fiorato, L.S. Johal, J.E. Carpenter, H.G. Russell, and W.G. Corley. Earthquake resistant structural walls–tests of isolated walls. NSF Report GI-43880, Portland Cement Association, Skokie, IL, November 1976.

[9] T. Paulay and M.J.N. Priestley. *Seismic Design of Reinforced Concrete and Masonry Buildings.* Wiley, New York, 1992.

[10] M.J.N. Priestley, M.J. Kowalsky, N. Vu, and C. McDaniel. Comparison of recent shear strength provisions for circular bridge columns. In *5th Caltrans Seismic Research Workshop*, pages :session 9, paper 3, Sacramento, CA, June 1998.

[11] M.J.N. Priestley and R. Park. Bridge columns under seismic loading. *ACI Structural Journal*, 84(1):61–76, January-February 1987.

[12] M.J.N. Priestley, F. Seible, and Calvi G.M. *Seismic Design and Retrofit of Bridges.* Wiley, New York, 1996.

[13] Y.R. et al. Rashid. *Constitutive Modeling of Reinforced Concrete and Steel.* ANATECH Corp., San Diego, CA, 1996.

[14] C. Sittipunt and S. Wood. Finite element analysis of reinforced concrete shear walls. NSF Report BCS 89-12992, University of Illinois, Urbana-Champaign, IL, December 1993.

[15] S. Sritharan, M.J.N. Priestley, and F. Seible. Seismic design and performance of concrete multi-column bents for bridges. Structural Systems Research Project 97/03, University of California, San Diego, La Jolla, CA, June 1997.

[16] J.M. Vallenas, V.V. Bertero, and E.P. Popov. Hysteretic behaviour of reinforced concrete structural walls. Earthquake Engineering Research Center Report EERC 79/20, University of California, Berkeley, Berkeley, CA, August 1979.

[17] F.J. Vecchio and M.P. Collins. "The Modified Compression-Field Theory for reinforced concrete elements subjected to shear". *ACI Journal*, 83(22):219–231, March–April 1986.

[18] T.Y. Wang, V.V. Bertero, and E.P. Popov. Hysteretic behavior of reinforced concrete framed walls. Earthquake Engineering Research Center Report EERC 75/23, University of California, Berkeley, Berkeley, CA, December 1975.